The propagation of ultrasonic waves in mercury telluride

Turban Alper

Alper, Turban (1968) The propagation of ultrasonic waves in mercury telluride. Doctoral thesis, Durham University.

THE PROPAGATION OF ULTRASONIC WAVES IN MERCURY TELLURIDE

A thesis submitted to the University of Durham
for the Degree of
Doctor of Philosophy

by

Turhan Alper

Department of Applied Physics,
Science Laboratories,
South Road,
Durham.

November, 1968.

ABSTRACT

The propagation of ultrasonic waves in single crystals of mercury telluride has been studied on a broad front between 1·2°K and 380°K. Measurements have been made by the pulse-echo technique for ultrasonic waves (frequency 10 MHz to 300 MHz) directed along the [100], [110] and [111] crystallographic directions.

The large mercury telluride single crystals, required for the ultrasonic measurements, have been grown by the Bridgman technique from either stoichiometric melts or from off-stoichiometric, tellurium-rich, melts.

The elastic constants C_{11}, C_{12} and C_{44} of mercury telluride have been measured as a function of temperature between 1·2°K and 300°K, attention being paid to possible effects of non-stoichiometry in the crystals, and the results correlated with ultrasound attenuation data. Results are discussed in terms of the crystalline interatomic forces and are compared with those of other II-VI and III-V compounds with the zinc blende structure, together with group IV, elemental semiconductors and I-VII compounds: elastic properties of mercury telluride correspond closely to those of cubic zinc sulphide and fall into the general scheme presented by the related compounds. From the Szigeti relationship, the ionicity e^* is estimated as $0{\cdot}65 \pm 0{\cdot}05e$ and the fundamental lattice absorption (restrahlen) frequency as $(4{\cdot}1 \pm 0{\cdot}1) \times 10^{12}$ Hz. The Debye temperature, calculated from the elastic constant data, is 141 ± 4°K.

Anelastic properties of mercury telluride have been deduced from the temperature (1·2°K to 300°K), frequency (10 MHz to 300 MHz) and applied stress dependences of ultrasound attenuation measurements. The important ultrasound dissipation mechanisms include the viscous drag of lattice phonons and forced dislocation motion.

Theoretical assessments of piezoelectric coupling on sound attenuation and thermoelastic loss, show that the effect of both are negligible.

One of the main sound energy dissipation mechanisms is due to the lattice phonon-ultrasonic phonon interaction. Attenuation due to this effect exhibits characteristic features at low temperatures. These have been found in mercury telluride. The effect is larger than observed in other materials because the Debye velocity is lower and can therefore be observed at relatively low frequencies.

Another loss mechanism arises from forced vibration of dislocation segments. At 4·2°K a maximum has been observed in the frequency dependence of attenuation. The results have been accounted for by the vibrating string model. The resonance frequency is 220 MHz. The dislocation drag coefficient is $2{\cdot}3 \times 10^{-5}$ dyn.sec.cm^{-2} at 4·2°K and loop length is about 3×10^{-4} cm. Data for the ultrasonic wave velocity and attenuation before and after annealing and under stress are in agreement with the dislocation mechanism.

In the region 170°K to 260°K peaks are found in the attenuation which show characteristics of those of Bordoni. The activation energy is about 0·15 eV and the attempt frequency about 4×10^{9} Hz.

ACKNOWLEDGMENTS

I am grateful to Dr. G.A. Saunders for his constant encouragement and guidance in supervising this research programme.

I wish to thank Professor D.A. Wright for the use of his laboratory facilities and the Turkish NATO Science Committee and the Scientific and Technical Research Council of Turkey for their financial support.

I also wish to acknowledge the technical assistance given by the departmental workshop staff headed by Mr. F. Spence.

Finally, I would like to thank Mrs. K.J. Barker for her careful typing of the manuscript.

CONTENTS

CHAPTER 4. ELASTIC CONSTANTS OF MERCURY TELLURIDE

CHAPTER 5. ULTRASOUND ATTENUATION IN MERCURY TELLURIDE: RESULTS

CHAPTER 6. MECHANISM CONTRIBUTING TO ULTRASONIC ATTENUATION IN MERCURY TELLURIDE

CHAPTER 7. ULTRASONIC WAVE INTERACTION WITH THERMAL ELASTIC WAVES: THE ULTRASONIC PHONON-THERMAL PHONON INTERACTIONS

CHAPTER 8. DISLOCATION CONTRIBUTION TO THE MEASURED ATTENUATION IN MERCURY TELLURIDE

CHAPTER 1

INTRODUCTION

Ultrasonic velocity and attenuation measurements provide valuable information about the nature of materials. Yet few details are available for compound semiconductors or semimetals. While II-VI compounds exhibit many useful and interesting ultrasonic phenomena, no studies have been previously reported for the mercury chalcogenides, a group whose properties span from semimetals to wide gap semiconductors. The present concern has been a study on a broad front of ultrasonic wave propagation in the semimetal mercury telluride. The principal objectives were to asses both intrinsic properties and the effects of material imperfections.

Before discussion of ultrasonic wave propagation in mercury telluride, let us discuss sound wave motion in elastic and anelastic solids in general.

1.1 PROPAGATION OF ELASTIC WAVES IN ELASTIC AND ANELASTIC SOLIDS

An "elastic" solid may be defined as one in which the stress σ is proportional to the strain ϵ. Thus the stress-strain relation can be written for an elastic, linear, one dimensional solid in the following form.

$$\sigma = M.\epsilon \tag{1.1}$$

This is Hooke's law. Here the proportionality constant M is a real number and is defined as an elastic modulus. In an anisotropic solid σ and ϵ are second rank tensors and M is fourth rank tensor. This is the case for all single crystals and will be discussed later, in particular for cubic crystals. In most real solids, Hooke's law of elasticity is not obeyed, even for the smallest stress. Deviations from Hooke's law give rise to the elastic after-effects shown by anelastic or viscoelastic solids.

A modification of Hooke's law to contain the anelastic behaviour was proposed by Zener (1948), who gave an expansion in terms of the time derivatives of the stress and strain and retained only the first derivatives $\dot{\sigma}$ and $\dot{\epsilon}$

$$\sigma + \tau\dot{\sigma} = M_1\epsilon + \tau M_0\dot{\epsilon} \tag{1.2}$$

Here M_0 is the true or unrelaxed modulus, M_1 is the time dependent or relaxed modulus and τ is the stress relaxation time.

In a one-dimensional solid the strain in terms of displacement gradient is

$$\epsilon = \frac{\delta S}{\delta X} \tag{1.3}$$

and the equation of motion is

$$\rho\ddot{S} = \frac{\delta\sigma}{\delta X} \tag{1.4}$$

Here $\underline{S}$ is the displacement vector, $\underline{X}$ is the position vector, $\ddot{S}$ is the second derivative with time of the position vector, that is the acceleration, and ρ is the density of the solid. Then on combining Equations (1.4) and (1.3) with (1.2), one obtains the following equation:

$$\frac{1}{\tau}\frac{\delta^2\sigma}{\delta t^2} + \frac{\delta^3\sigma}{\delta t^3} = \frac{M_1}{\tau\rho}\frac{\delta^2\sigma}{\delta X^2} + \frac{M_0}{\rho}\frac{\delta^3\sigma}{\delta X^2\delta t} \tag{1.5}$$

This equation admits solutions of the form

$$\sigma = Ae^{-\alpha X} \cos (kX - \omega t) \tag{1.6}$$

or

$$\sigma = Ae^{-\alpha' X} \cos (kX) \cos (\omega t) \tag{1.7}$$

where

$$\alpha v = \alpha'$$

which define an attenuated travelling wave and an attenuated standing wave. Here α is the attenuation, ω is the angular frequency and k is the propagation vector for the X direction. Introducing Equations (1.6) and (1.7) into (1.5) leads to following expressions for attenuation (Lücke 1956).

$$\alpha' = \frac{1}{2\tau} \frac{\Delta M}{M} \frac{\omega^2\tau^2}{1+\omega^2\tau^2} \tag{1.8}$$

and for velocity

$$V = \frac{M_o}{\rho} \left\{ 1 - \frac{\Delta M}{2M} \frac{1}{1+\omega^2\tau^2} \left(1 - \frac{2\omega^2\tau^2}{1+\omega^2\tau^2} \right) \right\} \tag{1.9}$$

The frequency dependences of α' and V given by Equations (1.8) and (1.9) are shown in Figure (1.1). In the figure V is the group velocity, v is the phase velocity, α is the attenuation coefficient and Δ is the logarithmic decrement ($\Delta \propto \alpha/f$). From this it may be concluded that in an enelastic solid, sound waves are attenuated, and velocities are frequency dependent, that is the solid is dispersive. For $\omega\tau \ll 1$ Equations (1.8 and 1.9) lead to $\alpha' \simeq 0$ and $M \simeq \rho V^2$; therefore, for $\omega\tau \ll 1$ a solid does not absorb elastic waves and velocities are independent

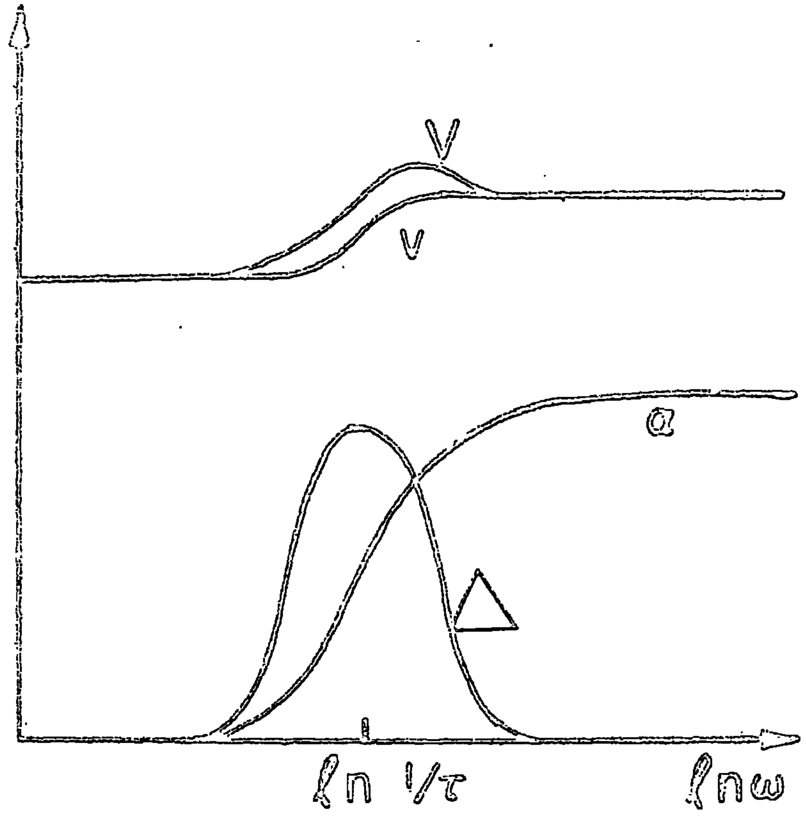

FIGURE (1.1) Logarithmic decrement (Δ), phase velocity (v), group velocity (V) and attenuation (α) of a sound wave in a standard linear body as a function of frequency (Lücke,1956).

of frequency. This case, also shown Figure (1.1), is the Hooke's law approximation.

Before discussing the ultrasonic wave propagation in mercury telluride, it is necessary to describe the crystal structure and relevant details of thermal and elastic properties of mercury telluride.

1.2 PROPERTIES OF MERCURY TELLURIDE

Mercury telluride is formed from the group II element mercury and the group VI element tellurium. Like the semiconducting group IV elements, the III-V compounds and several of the wider band gap II-VI compounds, mercury telluride possesses the zinc-blende structure. The point group is $\bar{4}3m$. The zinc-blende structure, like the diamond structure, is composed of two face centred cubic lattices displaced from each other by one-quarter of a body diagonal (see Figure 1.2). The zinc-blende structure is derived from the diamond structure simply by placing A atoms on one face-centred sublattice and B atoms on the other interpenetrating face-centred sublattice. There are four each of mercury and tellurium atoms in a unit cell; all atoms occupy spatial positions with the coordinates:

Four mercury atoms at (0,0,0); (0,1/2,1/2); (1/2,0,1/2); (1/2,1/2,0) and

Four tellurium atoms at (1/4,1/4,1/4); (1/4,3/4,3/4); (3/4,1/4,3/4); (3/4,3/4,1/4).

Each mercury atoms has four nearest neighbours, which are tellurium atoms,

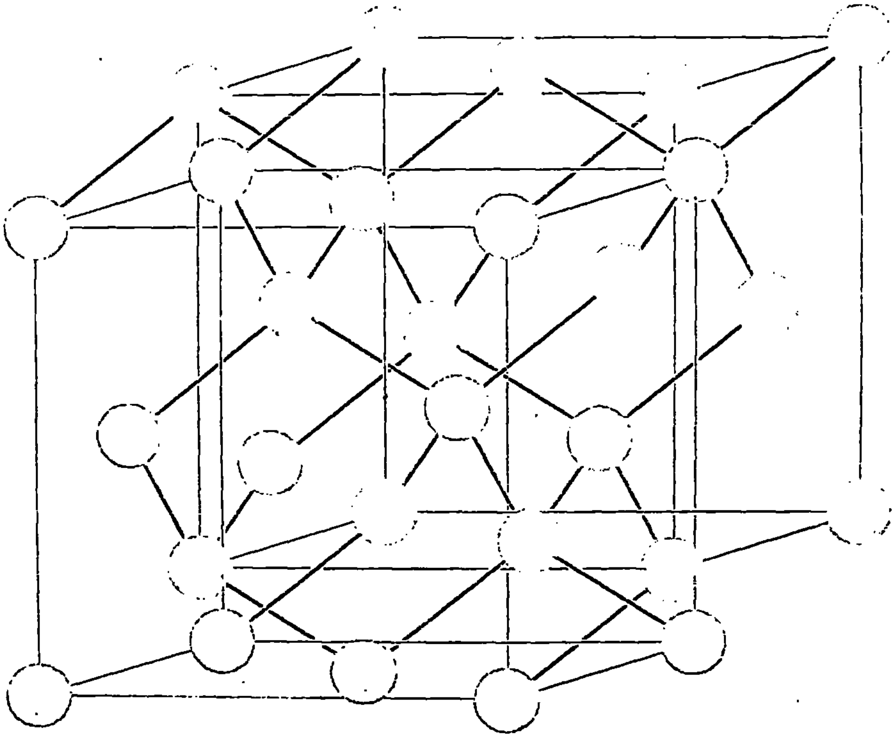

FIGURE (1.2) Zinc-blende lattice. The elementary cubes of the two interpenetrating face-centred cubic lattices are shown.

at a distance of $\frac{1}{4}\sqrt{3}\ a_o$, at the corners of regular tetrahedron, where a_o is the cubic lattice parameter. There are twelve next-nearest neighbour of atoms of the same kind at the distance $\frac{1}{2}\sqrt{2}\ a_o$.

An important aspect of the zinc-blende structure is the absence of a centre of symmetry or inversion. As illustrated in Figure (1.3a) and (1.3b), the mercury-tellurium layers have unique orientations along the [111] direction. As a result, mercury telluride like other zinc-blende crystals is polar and is piezoelectric. The opposed (hkl) and $(\overline{h}\overline{k}\overline{l})$ faces and opposed [hkl] and $[\overline{h}\overline{k}\overline{l}]$ directions have different physical and chemical properties. The intensity of diffracted X-rays from an ideal lattice will be different for the (hkl) and $(\overline{h}\overline{k}\overline{l})$ crystal faces. The effect is small but Warekois et al., (1962) have been able to establish that the intensities for the (111) and $(\overline{1}\overline{1}\overline{1})$ faces are not the same. The higher intensities are characteristic of the surface plane consisting of mercury atoms. These workers have also reported the etching characteristics of mercury telluride. The behaviour for pit producing etchants was correlated with the X-ray data. It was found that etch pits were formed on the mercury surface of mercury telluride.

Mercury telluride, like other II-IV compounds, forms a link between semiconducting elements of the fourth column of the periodic table and the I-VII compounds. The situation is illustrated schematically in Figures (1.3b) (1.3c) and (1.3d). Consequently, it is useful to compare the properties of mercury telluride with those of the neighbouring substances.

The nature of the bond in mercury telluride is a mixture of ionic

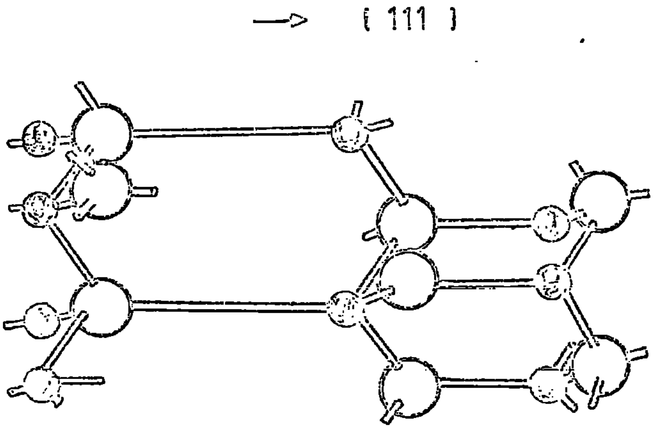

(a)

3-Dim. model of zinc-blende lattices

(b)

Zinc-blende structure

(c)

Diamond structure

(d)

Rock-salt structure

FIGURE (1.3)

and covalent bonds. Wolff and Broder (1959), from cleavage experiments have concluded that the ionic character of mercury telluride is slightly greater than 50%.

Unlike the other II-VI compounds, mercury telluride is a semimetal with overlapping valence and conduction bands (Harman 1967, p.790).

The lattice and thermal properties of mercury telluride have not been studied extensively. Measurements of those lattice and thermal properties relevant to an understanding of ultrasonic wave propagation are collected in Appendix A.

1.3 THE PLAN OF THE WORK

The primary object of the measurements reported here was to develop an understanding of the elastic and anelastic properties of mercury telluride. Like other compounds, preparation of stoichiometric mercury telluride presents a problem and attention has been paid to effects of non-stoichiometry: a wide variety of crystals have been studied. Effects, which could play a role in the absorption of ultrasonic waves, include dislocation damping, the viscous drag of lattice phonons, the thermoelastic loss, electronic interactions and piezoelectric coupling, have been studied. Contributions from different absorption mechanisms are often difficult to distinguish because predicted attenuations are of the same order of magnitude. To facilitate separation of possible interactions, measurements have been made over a wide range of temperature ($1{\cdot}2^{\circ}$K to 400°K) and frequencies (10 MHz to 300 MHz).

After details of the crystal growth and the specifications of the specimens used have been given, ultrasonic wave propagation in single crystal of mercury telluride will be discussed in detail. First the velocity and elastic constants will be considered, followed by the absorption of ultrasonic waves.

CHAPTER 2

PREPARATION AND EXAMINATION OF SPECIMENS

2.1 INTRODUCTION

Stoichiometry plays an important role in the electronic properties of compounds, particularly those containing volatile components. Excess atoms act like foreign impurities in the materials. Knowledge of the phase diagram is useful for preparing crystals with controlled stoichiometry. An incomplete phase diagram of the mercury-tellurium system is given by Hansen (1958, p.840). The complete liquidus curve has been obtained by Delves and Lewis (1963) and Strauss and Brebrick (1965). The phase diagram of the mercury-tellurium system, like other III-V, II-VI systems exhibits a maximum melting point (See Fig. 2.1a) higher than that of either components. The melting points of mercury and tellurium are -38·9°C and 453°C respectively (Hansen 1958, p.840), while the melting point of mercury telluride is 670°±1°C (Delves and Lewis, 1963). Delves and Lewis (1963) have stated that the maximum in the liquidus lies on the tellurium rich-side, between 2·5 and 4 at.%. However, Brebrick and Strauss (1965) have concluded from the results of their electrical measurements on annealed mercury telluride that the deviation is at most 0·01 at.%, much smaller than their upper limit of 0·60 at.% obtained by partial pressure measurements.

Crystal growth of mercury telluride from the melt can be approached

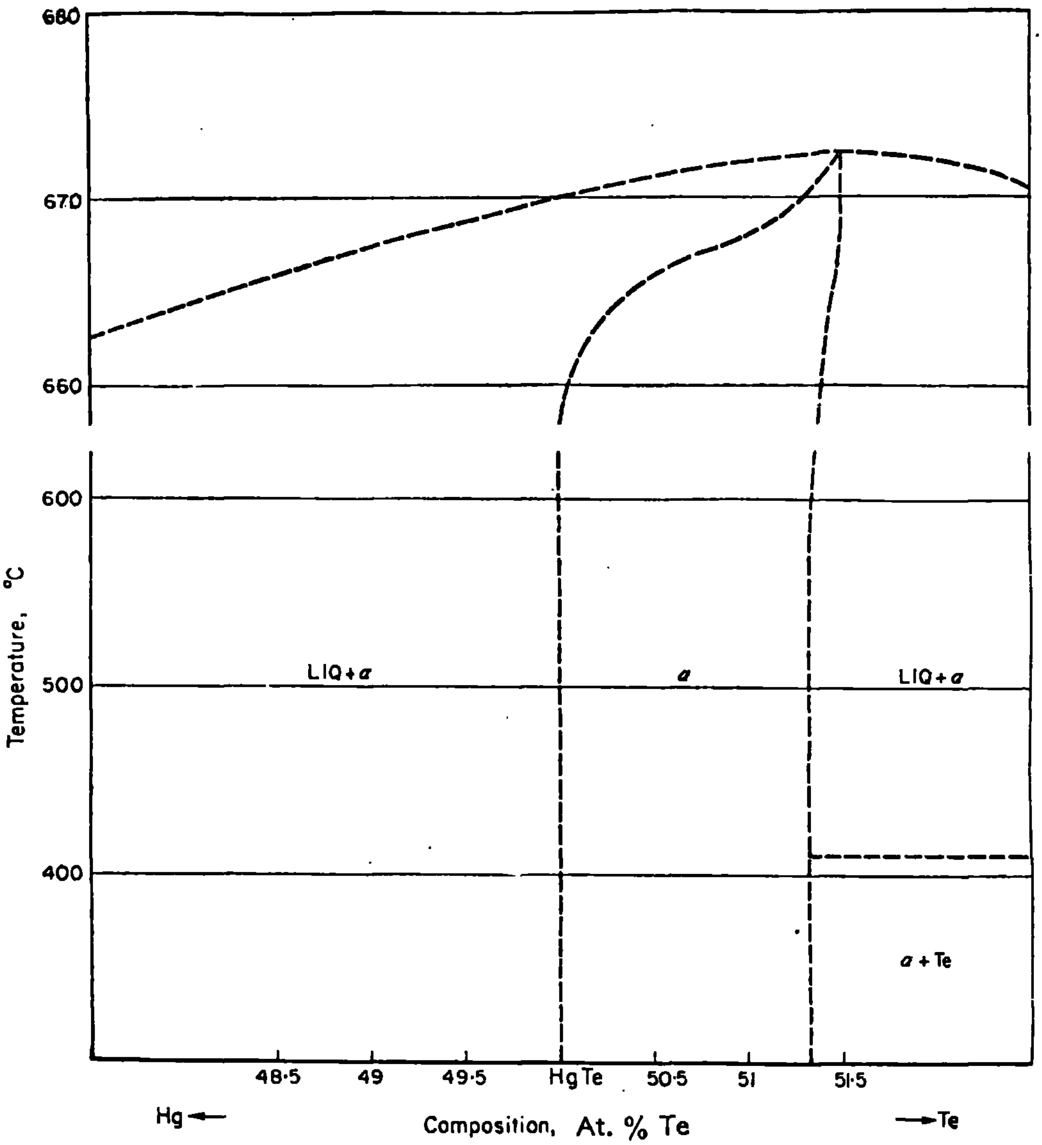

FIGURE (2.1a). Schematic phase diagram for the system Hg-Te near the stoichiometric composition (After Delves and Lewis 1963).

in two different ways: first, crystal formation from stoichiometric or near-stoichiometric melts, and second from off-stoichiometric melts. Although most workers have grown mercury telluride from near-stoichiometric melts, the relatively high mercury vapour pressure does create some technical difficulties in achieving stoichiometric and well-formed monocrystals and the results are erratic. Brebrick and Strauss (1965) have found that the pressure of mercury over mercury saturated mercury telluride at the melting point is 12·5 atm. and is 19 atm. between 643° and 656°C. Thus a considerable quantity of mercury is lost from the liquid phase to the vapour phase under the crystal growing conditions a further complication is that the system often has to be heated considerably above the melting point to assure a completely liquified system. Giriat (1964) and others have demonstrated that the properties of as grown mercury telluride vary from sample to sample. For example, the Hall coefficient at 77°K ranged from +1 cm^3/C to -9 cm^3/C in samples grown under apparently identical conditions. Harman (1967, p.778), using excess mercury, observed even larger variations of the Hall coefficient between +1 cm^3/C to -100 cm^3/C. These variations were attributed to slight differences in the cooling process, growth conditions and melt composition.

Some of these problems may be overcome by growth from off-stoichiometric melts. Delves (1965) has predicted that the mercury-tellurium phase diagram near the stoichiometric composition there could be a region of two immiscible liquids, between about $Hg_{1\cdot0}$ $Te_{1\cdot12}$ and

and $Hg_{1.0}$ $Te_{1.25}$, (see Figure 2.1b). He has shown that in a binary system it is possible to grow single crystals from the monotectic point Y, where solid is in equilibrium with the two immiscible liquids. At this point the composition of the solid is fixed. On cooling the first liquid solidifies and the second liquid, carrying the excess tellurium is rejected from the freezing interface.

Growth of single crystals from the monotectic by this method of Delves (1965), has certain advantages, namely

1. There is no segregation.

2. Constitutional supercooling will not occur provided that certain conditions are obeyed. These will be discussed later.

3. The solidification temperature is lower than that of the stoichiometric composition, which is at the maximum melting point in the phase diagram.

The large single crystals required for the ultrasonic measurements were grown by the Bridgman technique from either stoichiometric or off-stoichiometric melt, in sealed quartz crucibles.

2.2 DESCRIPTION OF THE CRYSTAL GROWTH FURNACE

The furnace, shown in Figure (2.2) used to grow HgTe single crystals consisting of a vertically mounted, 79 cm long, 4 cm bore, mullite tube inside a rectangular (78 x 40 x 40 cm^3) sindanyo box. To increase the temperature gradient, the furnace was constructed in two sections, only the top half being well-insulated by vermiculate. Three windings of

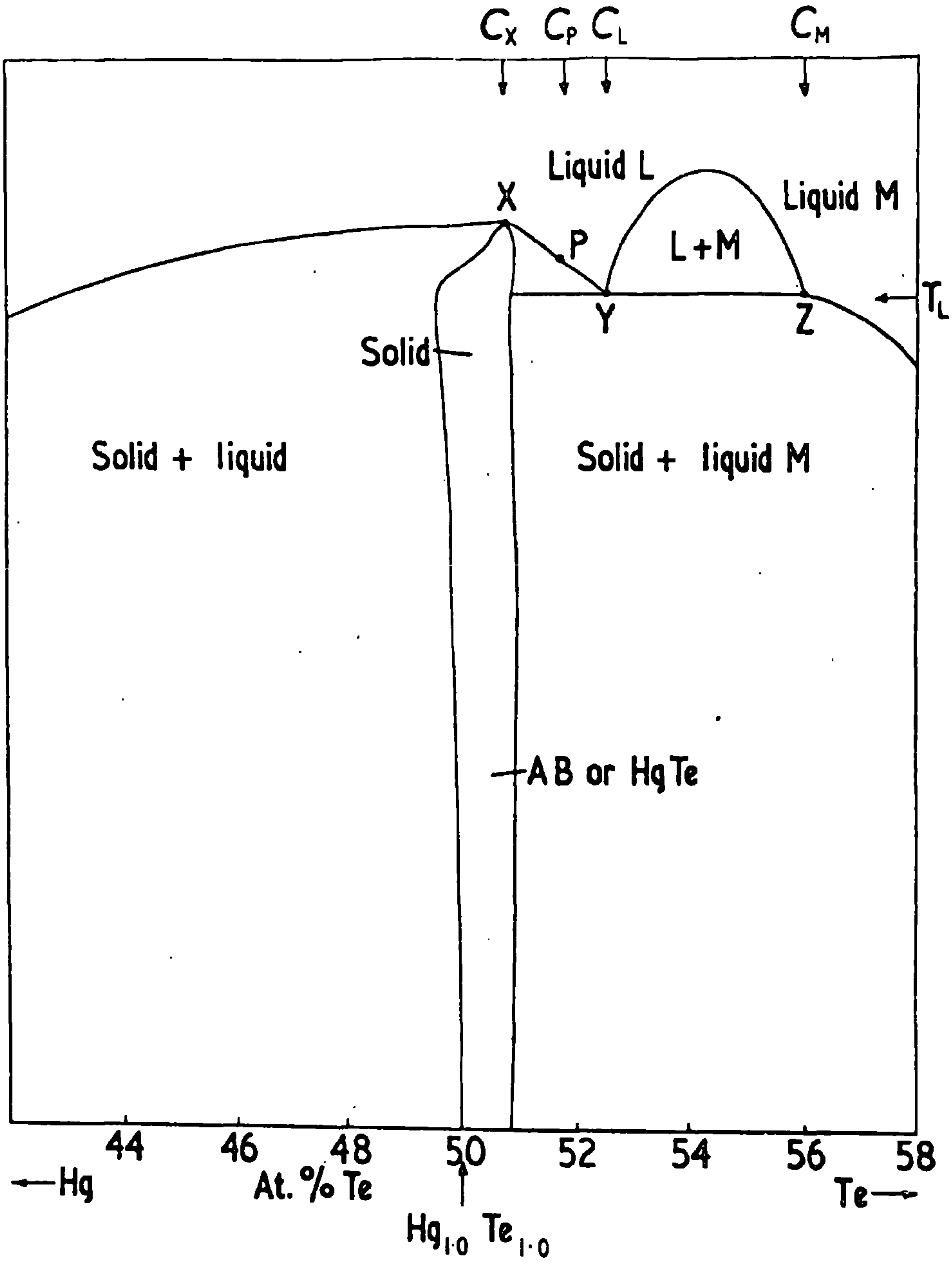

FIGURE (2.1b). Schematic phase diagram for Hg-Te near the stoichiometric composition, showing a region with two immiscible liquids (After Delves 1965).

FIGURE (2.2). CRYSTAL GROWTH FURNACE

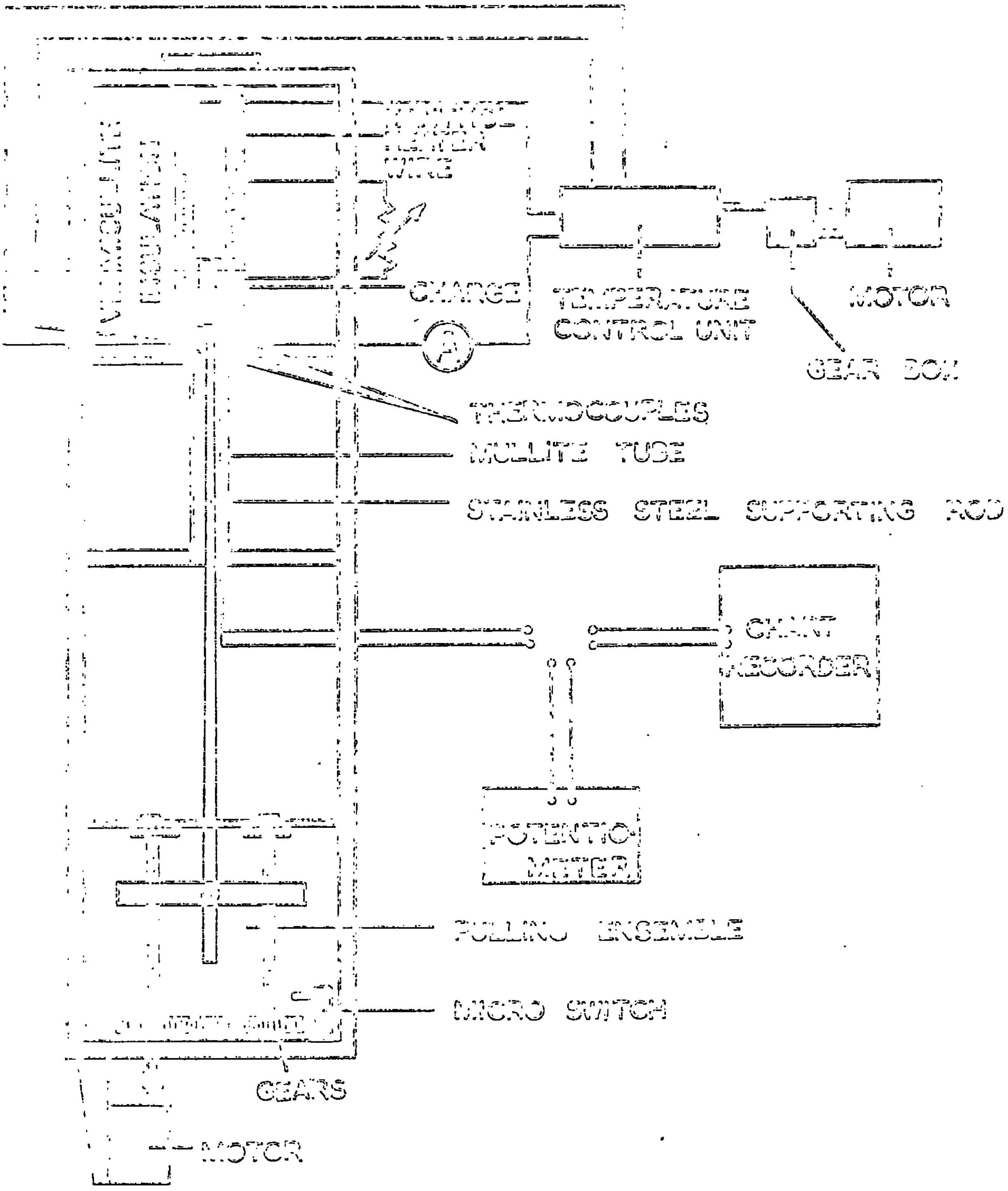

kanthal wire, independently controlled to facilitate minimization of the temperature humps in the high temperature region, were wound onto the upper part of the mullite tube. To prevent the coils from slipping together, the heater wires were held in position with alumina cement.

A potentiometric, proportional, Eurotherm controller was employed to control the furnace temperature. The voltage difference between a measuring thermocouple sited in the furnace and the reference setting on the controller is amplified and fed back into the heater windings. The external resistances used to control the heater currents were wound non-inductively to avoid any disturbance of the controller. The true temperature of the charge was measured by another thermocouple whose potential could be recorded during the growth process. Platinum versus 13% rhodium-platinum thermocouples were used throughout. The junctions were made by twisting cleaned ends of the appropriate wires together and fusing them with oxygen-gas flame.

The growth furnace temperature profile, shown in Figure (2.3), has two major features, a sharp gradient and a slightly humped plateau. The temperature gradient was found to be 35°C per cm at the growing interface.

The furnace was designed to allow crystal growth from the melt either by pulling the charge through the temperature gradient or keeping the charge still in the furnace while lowering the whole temperature profile. In the latter case mechanical vibrations were eliminated. Smooth lowering of the charge at a rate of 3 mm per hr. was obtained (see Figure 2.2), through a stainless steel rod driven by motor rotated,

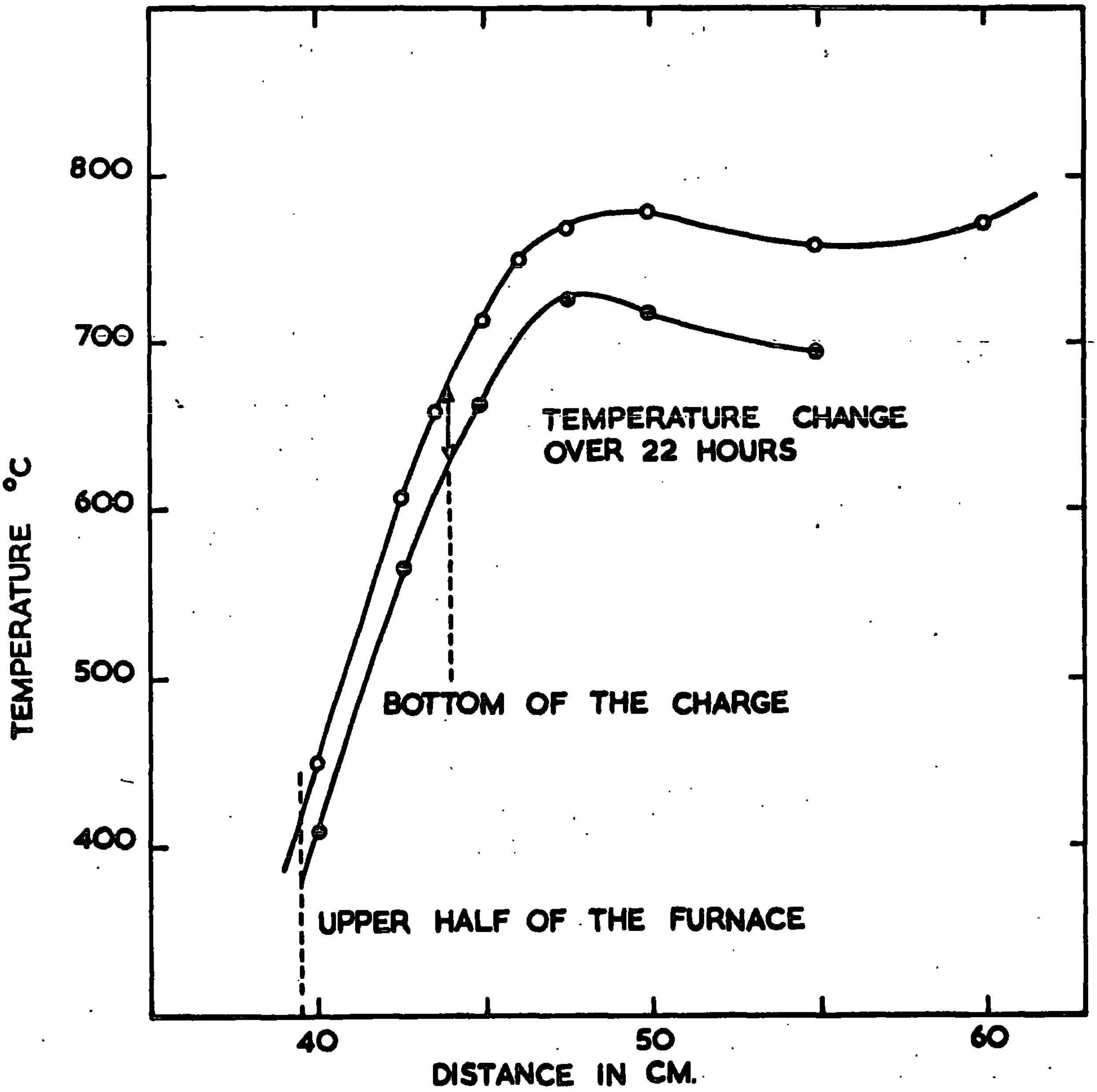

FIGURE (2.3). TEMPERATURE PROFILE IN THE FURNACE screw legs. For the other method the whole temperature gradient was lowered at 2°C per hr. using a geared down, slow motor driving an appropriate potentiometer in the controller. (Figure 2.2).

2.3 PREPARATION OF THE CHARGE AND CRYSTAL GROWTH

Crystals were grown in quartz crucibles whose shape differed for the pulling technique and the temperature profile lowering method. Crucibles used in the pulling technique were made from 13 mm bore 1·5 mm wall-thickness quartz tubing. In the temperature profile lowering method, not only the freezing interface but also the charge ought to lie completely in the temperature gradient. Therefore to avoid heating the charge too much, shorter length crucibles were used in this method. These were made from 24 mm bore 1·5 mm wall thickness: no preferred orientation of mercury telluride during the growth was observed and to prepare samples of desired orientation and sizes large crystals were required.

Both types of crucibles have similar features. To facilitate seed crystals formation, the bottom ends were conical in shape ($\sim 70^\circ$) (see Figure 2.4).

The tubes were cleaned with hot chromic acid, followed by distilled water and heating under vacuum. To prevent the sample sticking to the tube surface, the crucibles were then carbon coated, by burning a few drops of acetone in them using an oxygen-gas flame.

Single crystals were grown from either stoichiometric $Hg_{1\cdot00}\ Te_{1\cdot00}$ or non-stoichiometric $H_{1\cdot00}\ Te_{1\cdot12}$ melts (Delves' method). The crucible was charged with the prerequisite amounts of (99·9999% purity) mercury and (99·999% purity) tellurium obtained from Koch-Light Co.Ltd. The charged crucibles were evacuated for several hours under the 10^{-4} torr pressure, and occasionally the charge was warmed slightly to remove any trapped air. Tubes were sealed off under vacuum at the construction using an oxygen-gas flame. To ensure that the materials were not heated during the quartz fusion, the lower part of the tube was wetted to cool it down. For safety from possible explosion at high temperatures, which could rise from the high vapour pressure of mercury (the vapour pressure of mercury at 700°C is approximately 70 atm.) crucible was placed in a stainless steel bomb, sealed by a copper gasket.

The charged crucible inside its stainless steel bomb was located on the top of the pulling bar in the furnace (see Figure 2.2). The position of the charge in the temperature profile was such that, the conical tip of the crucible was approximately 15°C above the melting point of mercury telluride.

The furnace temperature was increased gradually over three days to the working conditions. Crystals were then usually grown by the method of lowering the temperature gradient slowly. In the samples which were solidified with high growth rates (10°C per hour), or with a small temperature gradient (5°C per cm) constitutional supercooling was observed. An interesting example of polycrystalline growth arising from fast growth rate, illustrated in Figure (2.5). Here the core was supercooled due to poor heat conductance of the solid, especially important in that wide samples and froze out rapidly to give small grains.

Large and well-formed single crystals of mercury telluride grew when the temperature gradient decrease did not exceed 2°C per hour.

2.4 EXAMINATION OF THE SINGLE CRYSTALS

To take out the sample the top end of the quartz crucible was cut with a water cooled, grinding wheel. The sample then slid out easily. To reveal of the grain boundaries, specimens were etched with freshly prepared concentrated one part nitric, one part hydrochloric acids and two parts water, followed by re-etching with concentrated hydrochloric acid and washed with distilled water. Monocrystallinity of the solid was further inspected using the X-ray back reflection Laue technique. Laue photographs were taken at translational intervals along a face of the sample and after 180° rotation. The sample to film distance (3 cm) and the angular orientation were held constant during this process; if the sample was a single crystal, all of the photographs were identical.

Usually one complete single crystal grew. In Delves' method (1965) an abrupt line, marking growth from melts with a large excess of tellurium, was extant towards the top of the boule, as shown in Figure (2.4). The tellurium-rich upper portion was removed by spark erosion and not examined fully; in X-ray powder photographs a few extra lines, in addition to mercury telluride lines, were observed, and X-ray back reflection photographs showed this portion to be single crystal. The specimen from the main bulk of the boule showed no cellular structure, and as evidenced on back-reflection Laue photographs by a complete lack of spot splitting or spreading, no mosaic structure or strain. Examples of back-reflection Laue photographs are shown in Figures (2.6a,b and c) which were taken along [001] (four fold symmetry), [110] (2m symmetry) and [111] (three fold symmetry).

Etch pits in mercury telluride

Etch pits formation was examined on (111) surfaces prepared first by spark cutting, followed by mechanical polishing. Warekois et al., (1962) have described upon the etching characteristics of the mercury telluride. Their polishing etchant (see Table 2.1) has been used in the present work for chemical polishing. To reveal the pits, an etchant suggested by Delves seen in the same table (private communication) was used.

The mercury and tellurium surfaces along the (111) direction have been explained in more detail in Chapter (1, page 5). The triangular pits, which appear on the mercury surface, were examined under a vertically illuminated, metallurgical microscope. Examples of photographs are shown in Figure (2.7). The magnification was calculated from photographs of a graduated scale enlarged under the same conditions. The number of dislocation etch pits was found to be about 10^7 pits per cm^2 both for samples grown by Delves' method and for samples grown from stoichiometric melts. No figures are available in the literature for comparison.

TABLE (2.1). Polishing and structure etchant for mercury telluride

Composition of etchant	Etching Condition	Results on (111) and $(\bar{1}\bar{1}\bar{1})$ surface
6:1:1 HNO_3 = HCl = H_2O	25°C, 10-15 min.	Pitless polish on both surface .
1:1:2 HNO_3 = HCl = H_2O	Use freshly, after a few min. rinse with HCl, followed by water	Pits on mercury surface.

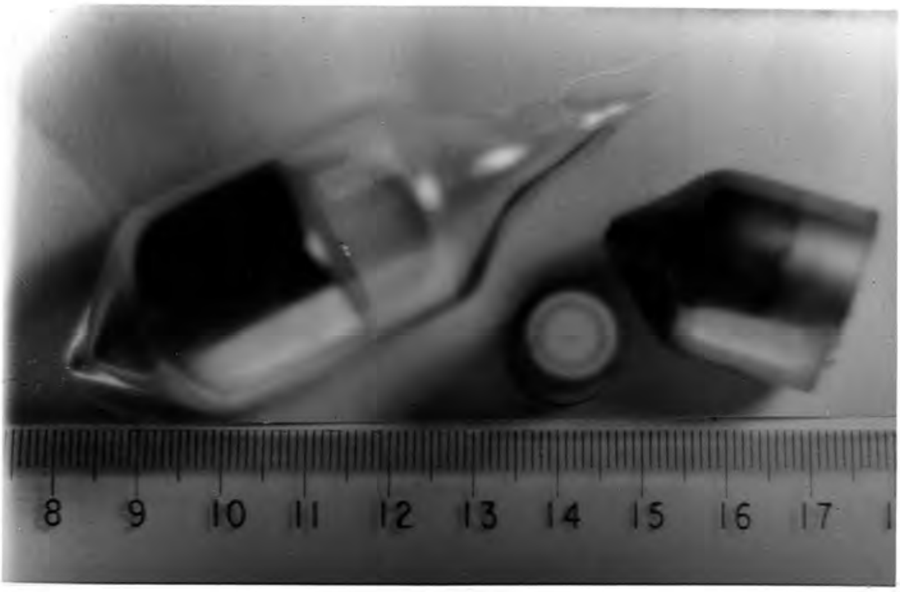

FIGURE (2.4). Ingot in the quartz crucible (left). Mercury telluride specimen with the transducer attached. Abrupt line on the ingot, marking growth from melt with a large excess of telluride (right).

FIGURE (2.5). Cross section of a supercooled mercury telluride sample.

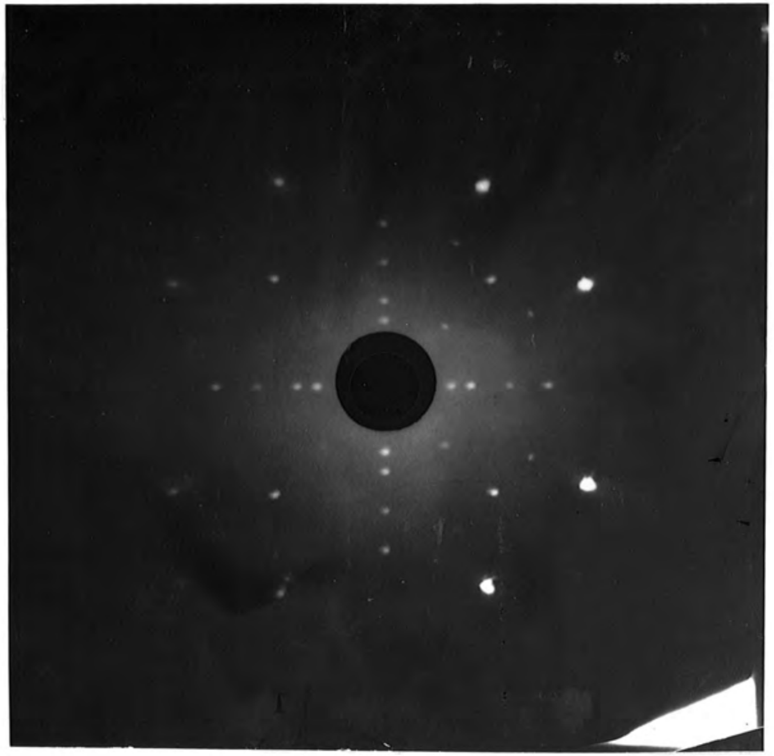

FIGURE (2.6a). X-ray photograph taken along the [001] axis (four-fold symmetry).

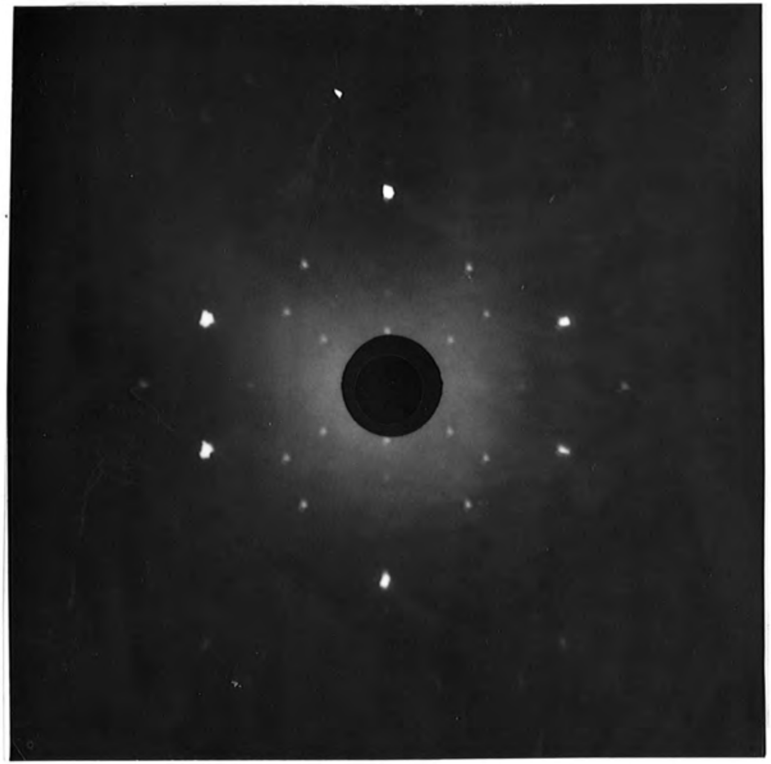

FIGURE (2.6b). X-ray photograph taken along the [110] axis (2m symmetry).

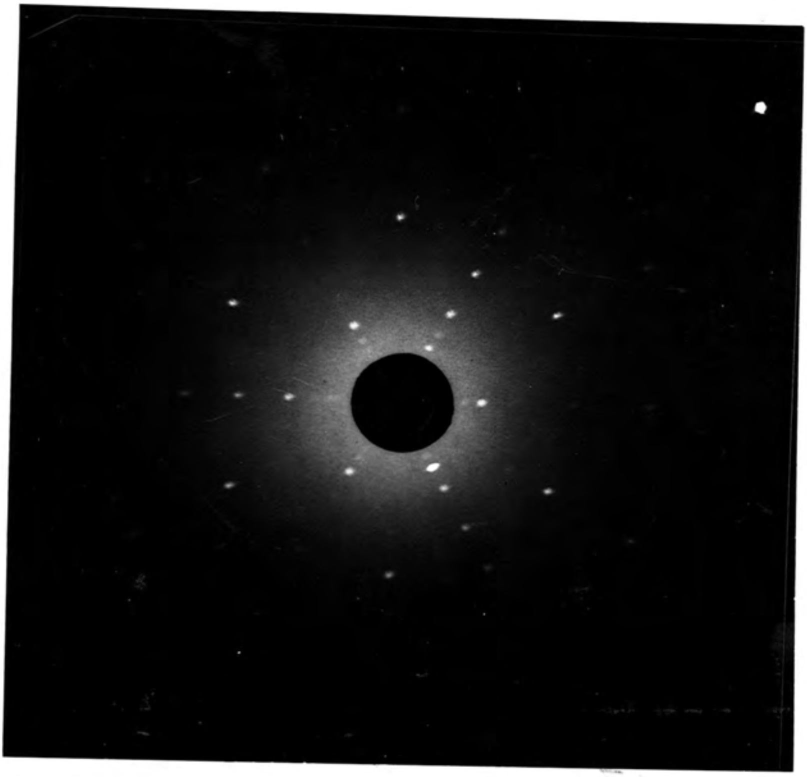

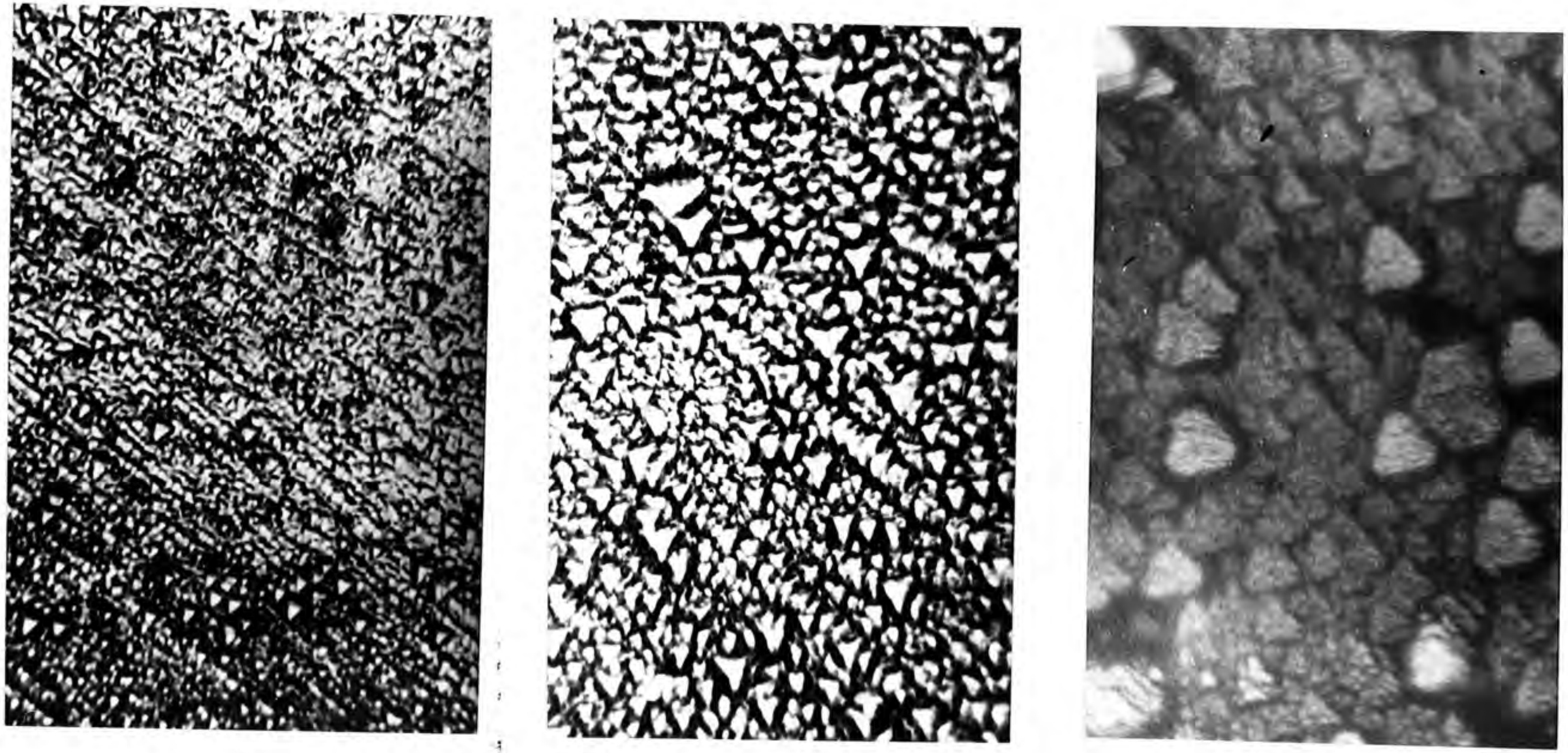

⟶ (increasing magnification)

FIGURE (2.7). Triangular etch pits obtainable on the (111) plane of mercury telluride.

2.5 MEASUREMENTS OF LATTICE SPACING AND DENSITY OF HgTe

The lattice spacing of HgTe was measured by the powder method. Sufficiently fine powder was fixed by collodion to the glass fibre, which was then located along the axis of a Philips Debye-Scherrer camera of circumference 360 mm. Nickel filtered X-rays from a copper target were employed. A twenty hour exposure was found satisfactory to resolve the singlets at the low θ end. The accurate lattice spacing was measured through the doublets at the high θ end. To make them clear, the exposure time was increased to two days, in this case the singlets were almost lost in the background. The angles θ between the reflected X-ray beam and the atomic planes were deduced from the ring diameter on the films, which were measured with accuracy of an $\pm$ 0·05 mm by a Hilger and Watt illuminated scale. The θ values were used to calculate d-spacing and the lattice spacing a_o from Bragg law by the standard procedure.

An accurate lattice spacing a_o can be obtained if measurements are made on the spectra that are reflected almost back into the incident beam, since large Bragg angles are very sensitive to small change in cell dimensions. This can be seen by differentiating the Bragg equation to obtain

$$\delta d = -d \cot \theta \, \delta \theta \tag{2.1}$$

because cot θ tends to zero as θ tends to 90^o, therefore, a small error in θ should produce a vanishingly small error in d as θ approaches 90^o, and all the systematic errors such as non-coincidence of the axis of the camera and the rotation axis of the specimen, should be zero. Although this is impossible to achieve, since a Bragg angle of 90° corresponds with reflection directed back into the X-ray beam, it can be done in effect by determining d from several reflections having different θ 's and extrapolating the result to $\theta = 90^\circ$. This can be done in several ways. The method used in the present instance was that developed by Nelson and Riley (1945). In Figure (2.8) the plot of the lattice spacing of both as grown and annealed HgTe (100 hours at 300°C in mercury vapour) against $1/2(\cos^2\theta/\sin\theta + \cos^2\theta/\theta)$ is shown. From this figure the lattice spacing, extrapolated to $\theta = 90^\circ$ was deduced to be

$a_o = 6{\cdot}463 \pm 0{\cdot}001$ Å for annealed HgTe, and

$a_o = 6{\cdot}461 \pm 0{\cdot}001$ Å for as grown material;

Annealing does not alter the lattice spacing within experimental error. These results agree with the quoted (6·462 Å) by Woolley and Ray (1960) and others.

The theoretical X-ray density was calculated in the following way. The density of the cell is (Mass of cell)/(Volume of cell). Cell volume is a_o^3, if it is considered that there are four mercury and four tellurium atoms per cell. The mass of the cell is $(4\,A_{Te} + 4\,A_{Hg})/N$ where the A's are the atomic weights of mercury and tellurium and N is Avogadro's number. Therefore, the density is

$$\rho = \frac{4(A_{Te} + A_{Hg})}{N\,a_o^3} \qquad (2.2)$$

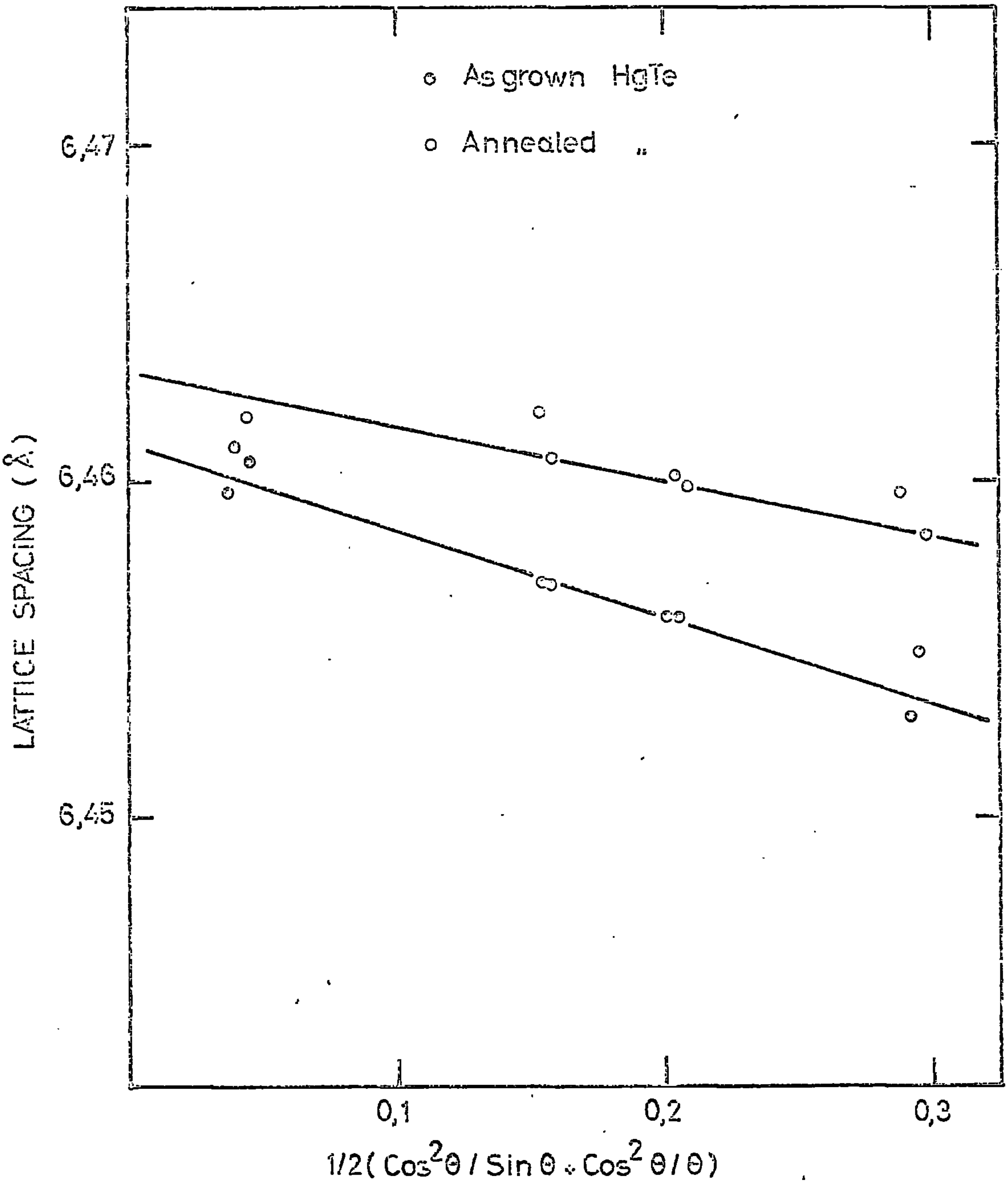

FIGURE (2.8). Nelson-Riley extrapolation curve for the accurate determination of the lattice parameter of HgTe at room temperature.

and using 6·462 Å for a_o turns out to be 8·079 gm/cm^3. Densities measured by Archimedes' principle, of both as grown and annealed crystals, were found to be 8·08 ± 0·01 gm/cm^3. These results support the conclusion of Brebrick and Strauss (1965) that the deviation of the maximum in the liquidus on the phase diagram from 50-50 at % point is very small.

2.6 COMPARISON BETWEEN THE CRYSTALS GROWN FOR THE PRESENT EXPERIMENTS AND THOSE OF OTHER WORKERS

A good way to compare materials grown by different methods is to examine the electrical properties, which are very sensitive to excess of either elements in compounds. In Table (2.2) measurements of thermoelectric power, conductivity, Hall coefficient, mobility and the number of carriers are tabulated for two selected temperatures (77°-300°K). In Figure (2.9) the temperature variation of these properties are presented. The units of each property can be obtained from Table (2.2). We are grateful to Dr. Dahake for permission to present these data. Sample (1) was grown by Dahake from the stoichiometric melt which was unannealed. Sample (2) was the same but annealed for 70 hours at 300°C in mercury vapour. Sample (3) was reannealed for 180 hours at 300°C in mercury vapour. Sample (4) was cut out of the same Delves' type boule from which some samples for ultrasonic measurements were prepared. This sample was annealed for 100 hours at 300°C in mercury vapour. Sample (5) was the same as (4) but it was reannealed for 150 hours at 300°C in mercury vapour.

TABLE (2.2). Comparison between electrical properties of HgTe crystals grown from stoichiometric and non-stoichiometric melts.

Sample Number	Electrical Conductivity (b) ohm^{-1} cm^{-1}		Hall Coefficient (R_H) cm^3 $coulomb^{-1}$		Mobility $\mu_H = R_H \cdot b$ cm^2 v^{-1} sec^{-1}		Carrier Density $cm^{-3} \times 10^{17}$		Seebeck Coefficient μV $^{\circ}K^{-1}$	
	77°K	300°K	77°K	300°K	77°K	300°K	77°K	300°K	77°K	300°K
1	72	780	-21·5	-21	1500	16200	3·4	3·3	+160	-136
2	255	520	+5·5	-22		11500	13·4	3·4	+60	-360
3	160	420	+2·0	-25		10600	36·8	2·9	+170	-136
4	86	1100	-76	-18·5	7000	19500	0·97	4·0	0	-140
5	160	440	+2	-25		10800	13·4	2·9	+170	-136

Remarks: Sample 1 was grown from a stoichiometric melt. Sample 2 is the same sample annealed for 70 hours in Hg vapour at 300°C. A further anneal for 180 hours at 300°C gave Sample 3. Sample 4 was grown from a tellurium-rich melt and annealed for 100 hours at 300°C. Sample 5 resulted from annealing, sample 4 for 150 hours at 300°C.

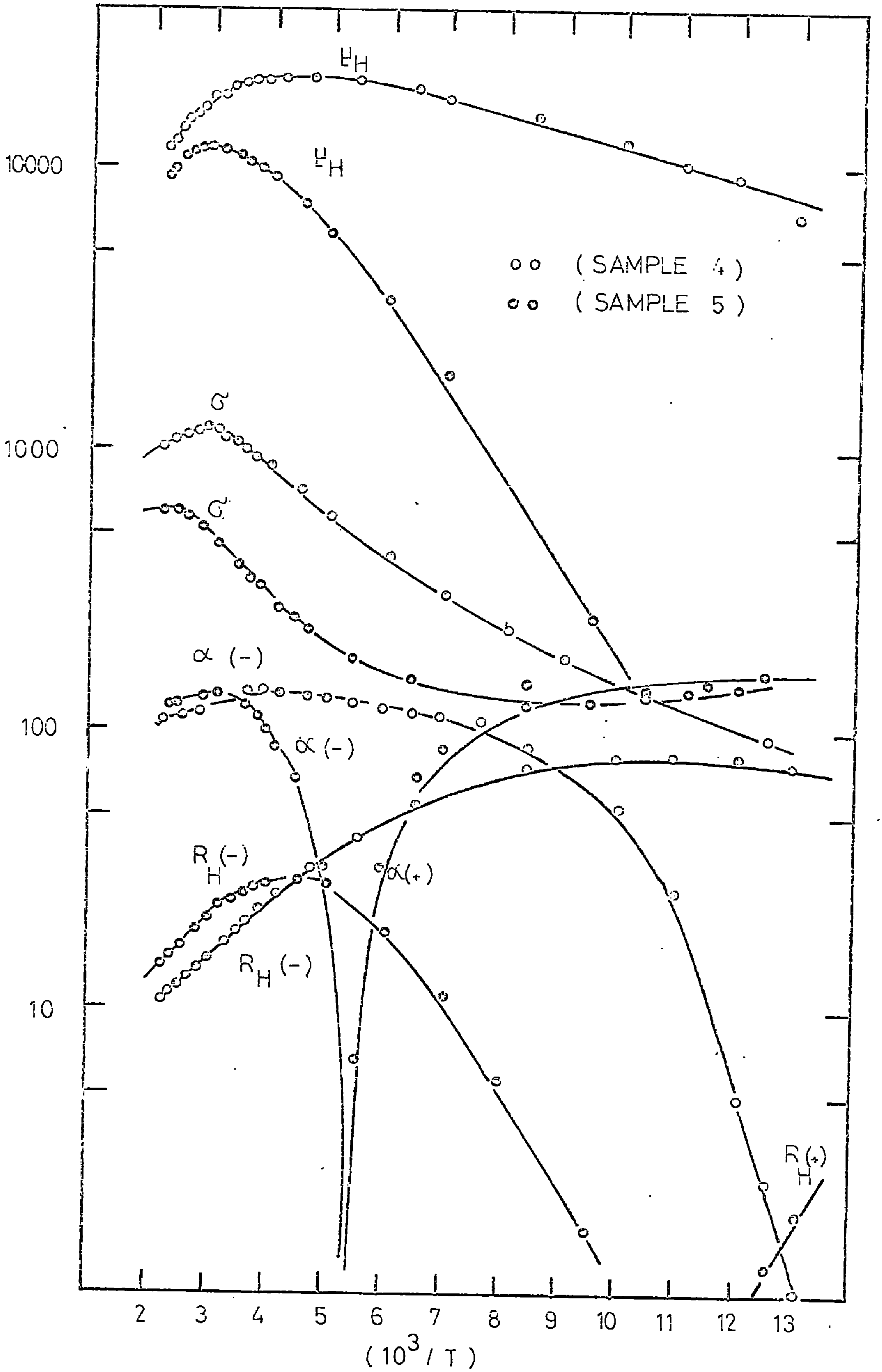

FIGURE (2.9). Temperature variation of electrical properties of mercury telluride.

Harman et al.(1958), Rodot and Triboulet (1962), Giriat (1964) and the others have shown that annealing of as grown mercury telluride in mercury vapour at different temperatures from 630°C to as low as 250°C profoundly alters the electrical properties. Giriat (1964) from the variation in electrical properties with annealing time and temperature, concluded that in the annealing process two, possibly three reactions take place. In the first reaction microheterogeneous precipitates are dissolved. In the second, mercury atoms diffuse in to the mercury telluride from the vapour. This process ultimately makes the mercury telluride stoichiometric. In the third process further diffusion of mercury atoms occurs. This reaction leads to the observed increase in electron concentration. Further annealing beyond the stoichiometric composition creates excess mercury samples.

The Hall coefficient of sample (4) is negative and shows a broad maximum of 80 cm^3/C at 91°K (see Figure 2.9). The electron mobility reaches a maximum of 21000 $cm^2/V.sec.$ at 240°K. The results for sample (5) are identical with those for sample (3) and confirm that HgTe becomes more p-type as a result of annealing and that the Delves' material closely resembles the other grown from the stoichiometric melts: again evidence for the phase diagram of Brebrick and Strauss (1965).

2.7 PREPARATION OF THE SPECIMENS FOR ULTRASONIC MEASUREMENTS

The samples were oriented by use of Laue back reflection photographs. The goniometer, with the crystal fixed on it, was located on an aligned track in the spark cutting machine. The track axis was normal to the crystallographic plane down which the cut was made by a brass plate electrode. After cutting, the orientation of the spark eroded face was reinspected by X-ray diffraction. The same procedure was repeated to prepare the other sample face. The maximum error was estimated to be less than 1°. The faces were spark planed to achieve accurate parallelism. The planing disk of the spark machine was first used to plane a brass reference surface onto which one flat face of the specimen was then fixed. Both faces of the specimen were planed in the same conditions. The parallelism of the faces were checked with dial gauge capable of measuring 0·005" after accurate planing no response could be seen on this gauge. Although the (100) and (111) faces were easily planed easy cleavage of the (110) face made this face somewhat more difficult. Cylindrical specimens (one of them can be seen in Figure 2.4) were obtained by spark cutting with a cylindrical electrode. The planed faces were polished with 3μ followed by 1μ diamond powder.

CHAPTER 3

VELOCITY AND ATTENUATION MEASUREMENTS

3.1 THE UNITS OF ATTENUATION.

The attenuation of elastic waves having an infinite plane wavefront, may be written in the following form:

$$\sigma(X) = \sigma_0 \, e^{-\alpha X} \tag{3.1}$$

here $\sigma(X)$ and $\sigma(0)$ are the amplitudes of sound waves at two different positions and α in the attenuation coefficient. For two different points, from the solution of Equation (3.1), α turns out to be

$$\alpha = - \frac{d}{dX} [\ln \sigma(X)] \tag{3.2}$$

or

$$\alpha = \frac{1}{X_2 - X_1} \ln \frac{\sigma(X_1)}{\sigma(X_2)} \quad \text{(nepers/cm)} \tag{3.3}$$

here ln is the natural logarithm. The units of α is "neper/cm" (sometimes just written as "cm^{-1}"). Power attenuation is conventionally expressed in 'decibel' ('dB'). The definition of "dB" is:

$$10.\log_{10} \frac{(\text{Power})_1}{(\text{Power})_2} \quad \text{(dB)} \tag{3.4}$$

Therefore α , the attenuation coefficient, in terms of "dB/cm" can be written, since power is proportional to the square of the amplitude, as:

$$\alpha = \frac{1}{X_2 - X_1} \; 20 \log_{10} \frac{\sigma(X_1)}{\sigma(X_2)} \quad \text{(dB/cm)} \tag{3.5}$$

interconversion, between Equations (3.3) and (3.5) using the relation of ($\ln X = 2\cdot3026 \log_{10} X$)

$$1 \text{ neper} = 8\cdot686 \text{ dB} \tag{3.6}$$

Another commonly used unit in the attenuation measurements is: "dB/μsec", which is given from:

$$\alpha(\text{dB}/\mu\text{sec}) = 10^{-6}\, v(\text{cm}/\text{sec})\alpha(\text{dB}/\text{cm}) \tag{3.7}$$

Yet another expression for energy loss is that of "logarithmic decrement" ("Δ"), which is defined for a harmonically oscillating system as

$$\Delta = \frac{W}{2E} \tag{3.8}$$

here W is the energy loss per cycle in the specimen, and E is the total vibrational energy stored in the specimen. It turns out that

$$\Delta(\text{nepers}) = \alpha(\text{nepers}/\text{cm}) \ \ \lambda\ (\text{cm}) \tag{3.9}$$

here λ is the wavelength of the sound waves. The expression for conversion to "Δ" is:

$$\Delta = \frac{\alpha(\text{dB}/\mu\text{sec})}{8\cdot686.f(\text{MHz})} \tag{3.10}$$

There is, the equivalent measure of dissipation called the "Q^{-1}" of a system, which is defined as

$$Q^{-1} = 2\pi \frac{E}{W} \tag{3.11}$$

where E and W are as defined above. From the definition of Q^{-1} and Δ it is seen that from Equations (3.8) and (3.11),

$$Q^{-1}\ \Delta = \pi \tag{3.12}$$

3.2 THE BASIC PRINCIPLES OF THE PULSE-ECHO TECHNIQUE.

The sound attenuation can be measured by a variety of techniques, whose value depends upon the physical situation (a comprehensive review may be found in McSkimin 1964). In the present experiments the "pulse-echo technique" was used for measuring both the velocity (v) and the attenuation (α) of ultrasonic waves in mercury telluride.

A plot of σ against distance X using Equation (3.1) is shown in Figure (3.1a). It can be seen that a knowledge of only the amplitude of the sound waves at two different positions is sufficient to give the attenuation coefficient. For gases and liquids the amplitude of the sound waves, can be easily measured, at any desired position, but for solids, the measuring technique is rather more difficult. Here the pulse-echo technique is particularly valuable.

The practice almost invariably to produce the high frequency in an electrical circuit and then to convert the electrical oscillations to mechanical vibrations. A device producing this conversion is termed a transducer. In the pulse-echo technique, the transducer, bonded to the specimen, is excited by a wave packet of electrical oscillations of the desired frequency, and the wave packet of sound, generated by the transducer, travels through the material. The reflected beam is detected and reconverted to electrical oscillations by the same transducer in the single-ended method. The wave packet of sound travels through the material by successive reflections, while the amplitude dies off according to Equation (3.1). Figure (3.1b) gives a schematic of the situation. Here

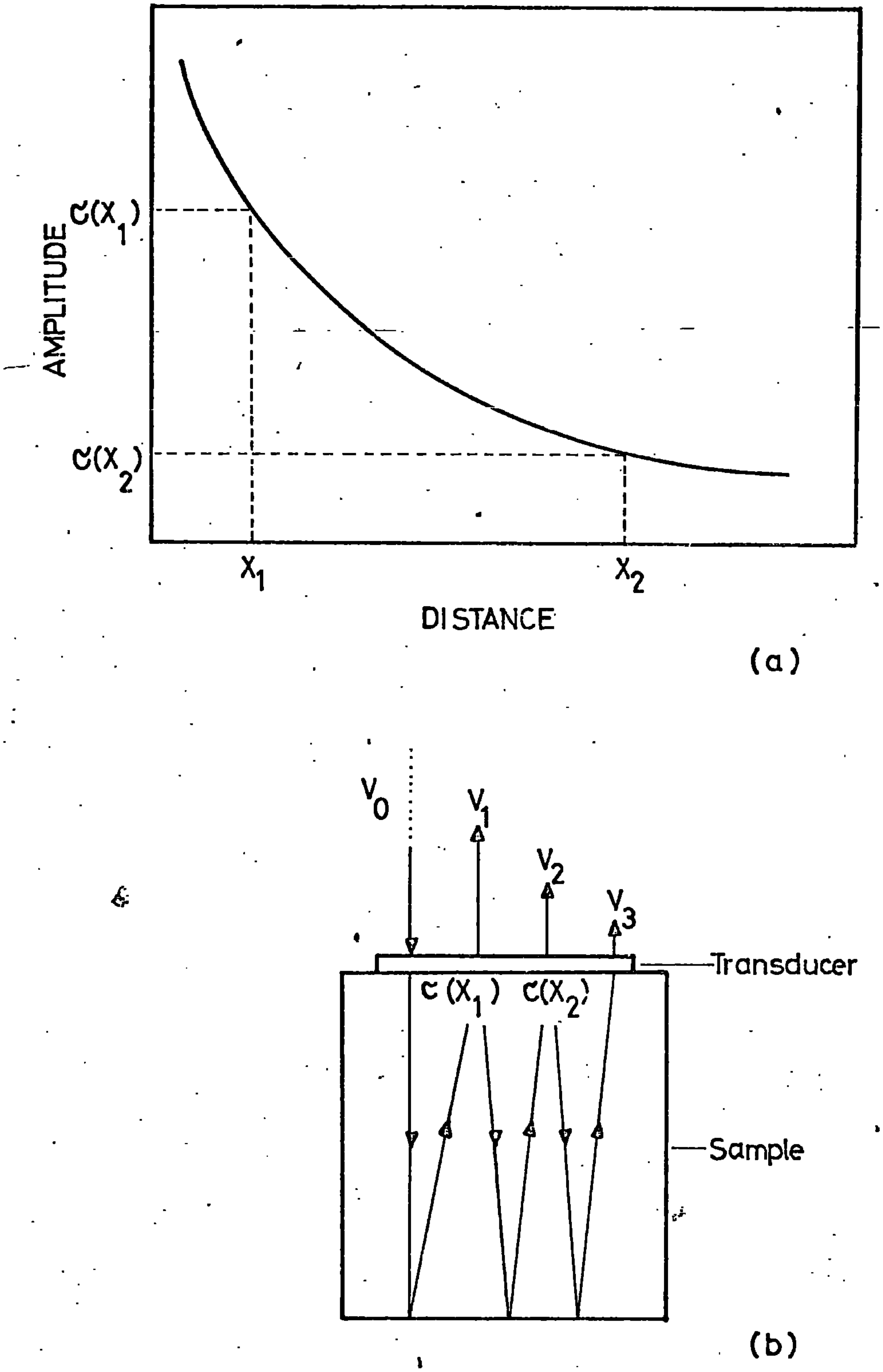

FIGURE (3.1). Physical basis of attenuation measurements.

V_o is the amplitude of the electrical oscillation exciting the transducer, $\sigma(X_1)$ and $\sigma(X_2)$ are the amplitudes of the sound waves at the transducer-specimen boundary, and V_1 and V_2, the amplitudes of the electrical oscillations, are proportional to the $\sigma(X_1)$ and $\sigma(X_2)$ (the proportionality factor includes terms such as the transducer efficiency and losses at the interfaces). As may be seen from the same figure, the distance between X_2 and X_1 is twice the specimen length, and, therefore, Equation (3.3) can be rewritten as:

$$\alpha = \frac{1}{2L} \ln \frac{V_1}{V_2} \qquad (3.13)$$

Thus, measurement of V_1 and V_2 and the specimen length give the sound attenuation. Further the time delay measurement between V_1 and V_2, gives the velocity of sound, which is $2L/t$ because within the time interval t, waves travel twice the sample length. The measurement of amplitudes and the transit time will now be described.

3.3 DESCRIPTION OF THE MEASURING EQUIPMENT

The velocity and attenuation of ultrasonic waves in mercury telluride were measured by the single-ended pulse-echo technique shown in Figure (3.2). A Matec, inc., Attenuation comparator, Model 9000 employing Model 96 R.F. Plug-in unit, was used. Pulsed electrical oscillations of frequencies between 10 MHz and 310 MHz continuously tunable, generated in the R.F. plug-in, are applied to the appropriate transducer and the resulting ultrasonic energy coupled in to the specimen. The pulse width

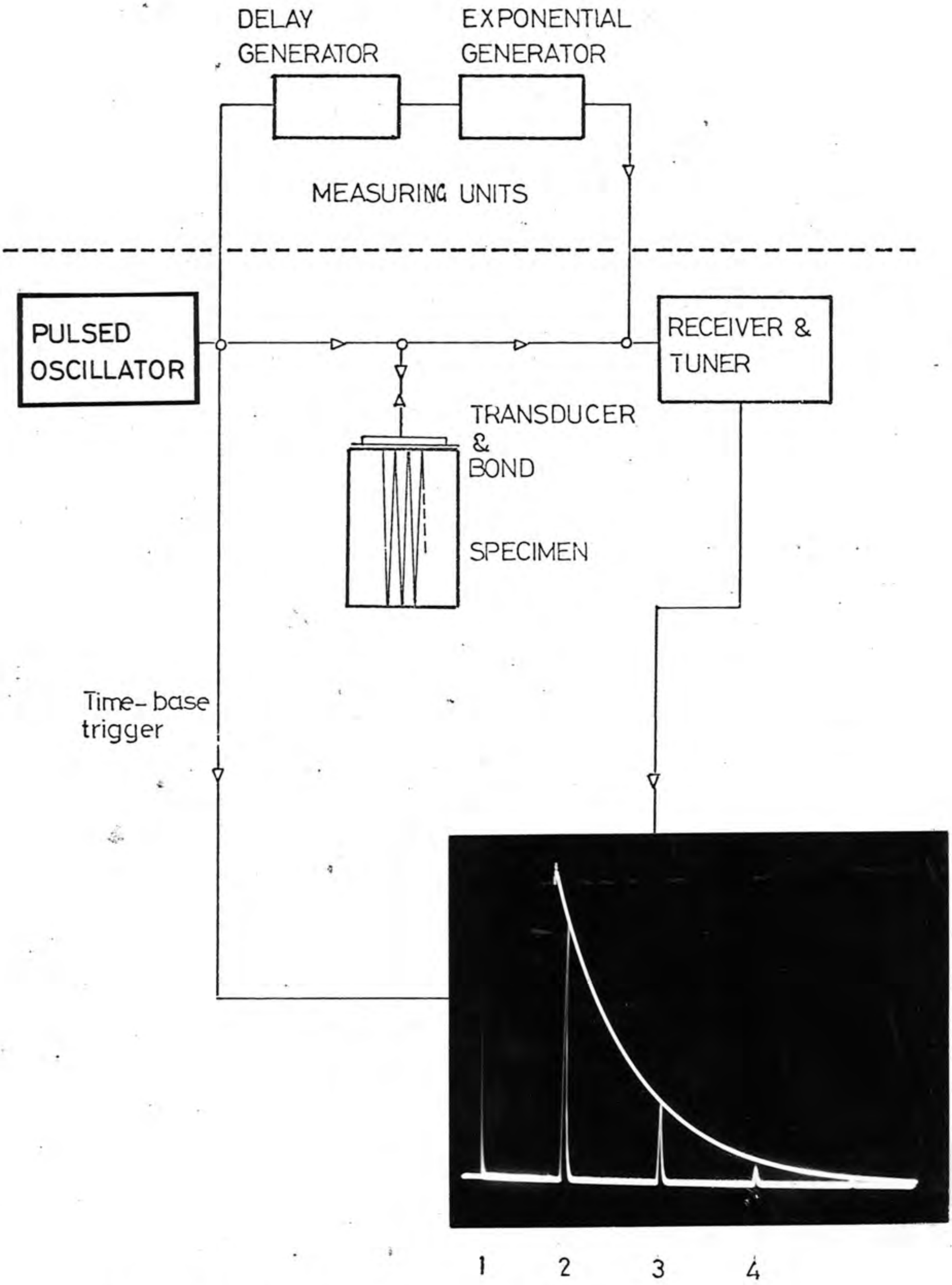

FIGURE (3.2). Block diagram of apparatus.

can be varied between 0·5 and 5 μsec. The pulse amplitude is continuously variable and has a maximum of 3KV peak-to-peak at 10 MHz which decreases a little at higher frequencies. The pulse repetition rate can be varied between 10 and 1,000 pulses $\sec^{-1}$. The R.F. pulse is tuned to the fundamental or an odd harmonic of the transducer. At each echo a small electrical signal reaches the originating transducer. These electrical signals are coupled to a high gain receiver for amplification. The bandwidth of the receiver is 4 MHz and the maximum gain 80 dB. The frequency range covered is again 10 MHz to 310 MHz with continuous tuning. These are then detected and filtered and the resulting video envelope displayed on an oscilloscope. A photographs the echoes and the exponential wave form is presented in Figure (3.2). The first peak (a) results from leakage of the R.F. power through the sample holder; the second peak (b) and subsequent peaks (c,d etc.) are the echoes propagated through the specimen twice, four times and six times respectively. Since the absorption rate of ultrasound is characteristically exponential, a calibrated, continuously variable exponential waveform generator is employed for measurements. By matching the exponential waveform to the peaks of the echoes and using this exponential decay generator, it is possible to obtain directly the value of attenuation in "dB/μsec." from calibration curves. The time delay between successive echoes on the oscilloscope is the time taken for the pulse to pass twice through the specimen. Velocity measurements may be readily obtained to within 1% by measuring the round trip time between echoes and measuring sample length. The transit time measurement is obtained by using calibrated delay generator.

3.4 GENERATION AND DETECTION OF ULTRASOUND: THE QUARTZ CRYSTAL TRANSDUCER.

Quartz transducers were used to convert to electrical oscillations into mechanical vibrations and vice versa. These transducers are based on the piezoelectric effect. Quartz (SiO_2) crystallizes in the trigonal system, forming a hexagonal prism with two rhombohedric ends (see Figure 3.3a). The "X" aces connecting opposite corners of a cross-section of the prism are called piezoelectric axes. The axes normal to the prism faces are the mechanical or "Y" axes. In Figure (3.3b) only one each of the "X" and "Y" axes are shown. Each of these axes has two identical axes obtainable by rotations of $\pm 120^{\circ}$.

The long axes of the prism is an axes of optical symmetry and is called the optical or "Z" axes, this is also shown in Figure (3.3a) and (3.3b). The "X", "Y" and "Z" axes form an orthogonal set.

In Figure (3.3c) a simple diagram of the quartz crystal lattice is shown. In the undeformed lattice, the negative ionic charge of oxygen and the positive charge of silicon neutralize each other. When a tensional stress is applied to a flat plate along the "X" direction, then, due to the resulting strain, the positive silicon ions are shifted towards the one surface and the negative oxygen ions towards the other surface. The disturbance of the electrical equilibrium leads a potential difference

FIGURE (3.3) Showing how transducers - are cut from quartz.

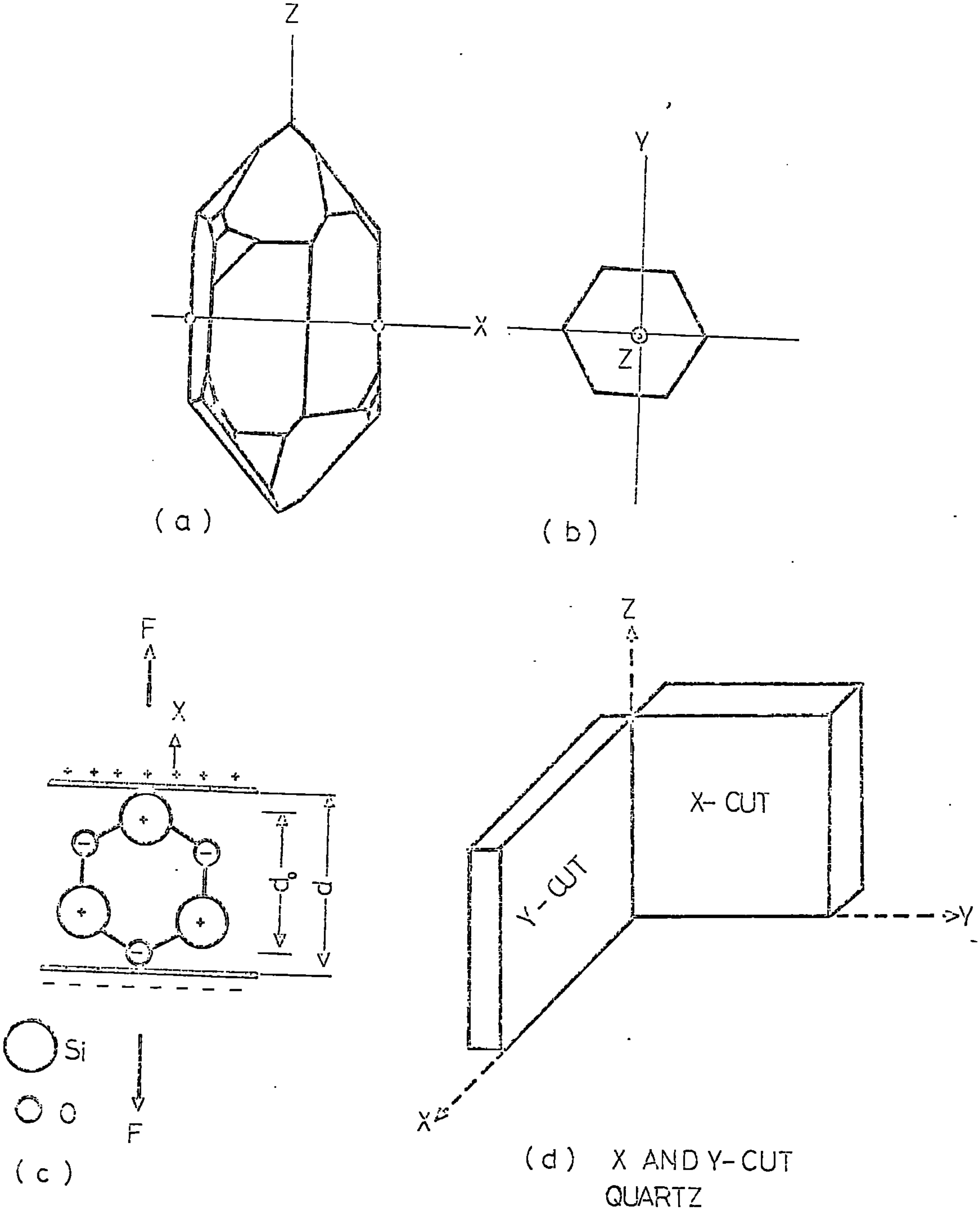

(a)

(b)

(c)

(d) X AND Y- CUT QUARTZ

"V" between the electrodes. If the direction of stress is inverted, the sign of the strain is also inverted and the charge on the electrodes changes sign, and the potential difference becomes "-V" for the same stress. A quartz slab under the tensional stress is shown in Figure (3.3c). A charge distribution also results if tension or compression is applied at right angles to "X" (i.e. in direction "Y"); this is the transverse piezoelectric effect. Conversely, if the quartz slab is subjected to an electric field in the "X" direction by applying a potential difference between the electrodes, ionic charges are caused to move in the direction of the field, giving rise to a strain. This effect is called the reciprocal piezoelectric effect.

To generate longitudinal and transverse waves, the transducer plate is cut from the crystal at a right angles to one of the piezoelectric axes "X-cut", and the one of the mechanical axes "Y-cut" respectively. A schematic diagram of the two methods of cutting out transducers is shown in Figure (3.3d), Opposite faces are coated with a thin gold layer to form electrodes. In Figures (2.4) and (3.9) a picture of a transducer, and its electrode is shown.

In operation the transducer is excited to one of its mechanical normal modes. Because an X-cut plate is vibrating in the direction of thickness, the natural frequency of the transducer is that when there is maximum elongation of the faces in the two opposite directions, a situation described by a standing elastic wave with displacement antinodes on both faces. In the case of the first normal mode of vibration there is only a single nodal plane, and the transducer thickness is equal to half a wavelength. When a quartz slab is excited at its nth harmonic, its thickness is devided into n equal parts with compressions and expansions taking place in adjoining sections. When n is even, compression occurs in n/2 of the sections and expansions occur in the remaining sections; thus there is no net strain in the crystal: the even harmonics cannot be used. When n is odd, however, (n-1)2 compressions neutralize the same number of expansions, leaving either a compression or an expansion is left in the remaining section. During the measurements, frequencies out to 290 MHz have been generated from transducers of fundemental frequency 10 MHz.

3.5 TRANSDUCER-SPECIMEN COUPLING.

Successful use of the pulse-echo ultrasonic method depends critically on the nature of the seal between the transducer and the specimen. The character of the seal becomes increasingly important at higher frequencies (shorter wave-length). At room temperature there are many choices for a bonding material, but at liquid helium temperatures the choice is limited. Any material used will become a solid before liquid helium temperature is reached and differential thermal expansions cause a considerable change in the nature of the seal during cooling.

Requirements in choosing the correct material and in preparation of a good bond are:

1. The seal should be uniform and a thin fraction of the ultrasound wave-length.

2. All particles and air bubbles should be excluded.

3. In temperature dependent measurements seal should stay on the sample, and keep a good match between specimen and transducer.

During the present work from experiment, a few bonding materials have been found to give satisfactory performance at low temperatures. The most successful bonding has been achieved by 250,000 centistoke silicone fluid obtained from "Hopkin and Williams Ltd., Chadwell Heath, Essex," for X-cut transducer, in the temperature range between 1·2 to 390°K. Also useful is 1,000,000 centistoke silicone fluid. However Y-cut transducers tended to break away above about 250°K for the propagation directions [100] and [110]. Near room temperature paraffin wax or phenyl salicylate (salol) was found to be satisfactory.

The following steps were followed to bond the transducer to the specimen with silicone fluids:

1. The transducer and specimen faces were cleaned with acetone and dried.

2. A small drop of fluid was put on the cleaned face of transducer and specimen.

3. To remove any trapped air bubbles in the fluid, the transducer and the specimen were kept in a vacuum for a few hours.

4. The transducer was pressed onto the sample and rung onto give a homogeneous, thin seal.

5. Uniformity and thinness of the seal was ensured by leaving a weight of approximately 30 gm on the transducer for about a day.

Paraffin wax and phenyl salicylate bonds were prepared by heating the specimen on a hot plate and following the above procedure. Phenyl salicylate gave the better bonds. On mechanically polished specimen faces with a mirror finish the bond tended to break away. The good adhesion was achieved on such faces by slightly etching them.

The quality of the bond was checked by the echo pattern on the oscilloscope.

3.6 SOURCES OF ERRORS.

3.6.1. Errors in the attenuation measurements.

In single crystals, the measured attenuation includes, in addition to the intrinsic absorption in the material, a) the loss due to diffraction of the sound beam, b) the loss due to phase sensitivity of the transducer, c) the loss due to slight misorientation of the specimen, d) the loss due to dissipation of the sound energy in the bond. These will be considered in turn.

a) diffraction effect: The sound wave is not a true plane wave as it leaves the quartz transducer but rather a diverging wave, and this contributes an apparent attenuation, which at low frequencies can be a dominating effect. Applying the results found for a liquid, an estimate of the diffraction contribution to the attenuation is given by (Granato and Truell 1956).

$$1 \text{ dB per } a^2/\lambda$$

here a is the radius of the transducer and λ is the wavelength of the sound wave. Thus, the diffraction loss varies inversely with frequency.

b) phase sensitivity of the transducer: A plane wave reflected back and forth within a specimen with nonparallel face will have its wave fronts distorted, so that the part of the wave falling on one side of a transducer will be out of phase with that striking another part. The situation is shown schematically in Figure (3.4). The transducer integrates the pressure signal over its surface and interference and apparent attenuation results. This value of this attenuation is given by (Granato and Truell 1956).

$$\alpha_{\text{error}} = \frac{8{\cdot}68\, \pi^2 f^2 a^2 \theta^2 n}{Lv} \quad (\text{dB}/\mu\text{sec}) \qquad (3.14)$$

here f is the sound wave frequency, a is the transducer radius θ is the angular deviation from parallel, n is the echo number, L is the specimen length, and v is the velocity of sound in the material.

For example, in order to insure that the loss due to this effect is less than 10% of the measured value of mercury telluride at 100 MHz, the required parallelness can be estimated from a numerical example. Typical numbers are:

$\alpha \simeq 1{\cdot}7$ dB/μsec (at 77°K, along the [110] direction for 100 MHz, i.e.

$\alpha_{\text{error}} = 0{\cdot}17$ dB/μsec)

$L = 1$ cm

$a = 0{\cdot}6$ cm

$n = 4$ echoes

$v = {\cdot}295$ (cm/μsec)

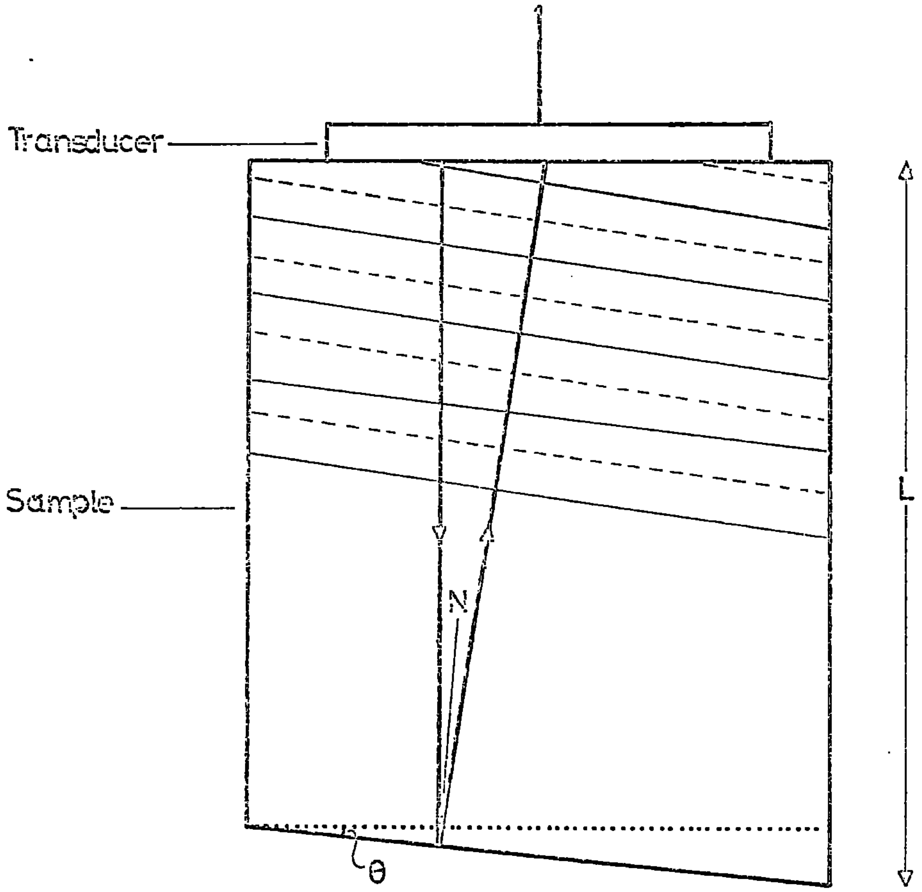

FIGURE (3.4). A plane sound wave reflected back and forth within a specimen with nonparallel face will have its wave fronts distorted, so that the part of the wave falling on one side of the transducer will be out of phase with that striking another part.

substituting these numbers into the Equation (3.14), on finds that the deviation angle θ must be less than 2×10^{-4} radians.

The best way of checking parallelism, other than direct measurement, is from exponential character of the echo train. In Figure (3.5) an echo display of one of the spark-planed mercury telluride specimens, is shown. From this evidence, it has been found that tolerances of better than 10^{-4} radians are readily obtained by the spark-planing technique, provided that, the conditions which were explained in Section (2.7) are all obeyed.

As seen from Equation (3.14) the effect becomes more important at high frequencies; this can be reduced by using a small diameter transducer and a long specimen. The limitation in choosing the transducer diameter is the diffraction loss, which is larger for smaller transducers. The specimen length is limited both by the difficulties of growing larger single crystals and the measurement of the attenuation.

c) the effect due to specimen misorientation: Misorientation results in mode conversion of the sound waves, which leads an ultrasonic attenuation.

d) the loss in the bond: There is little available data in the literature about the attenuation in the bonding material. Bobylev and Kravchenko (1967) found experimentally that the loss in the coupling film is about 8×10^{-3} (dB/μsec) per reflection at 150 MHz. The loss of sound energy in very thin seals of bonding materials is negligible.

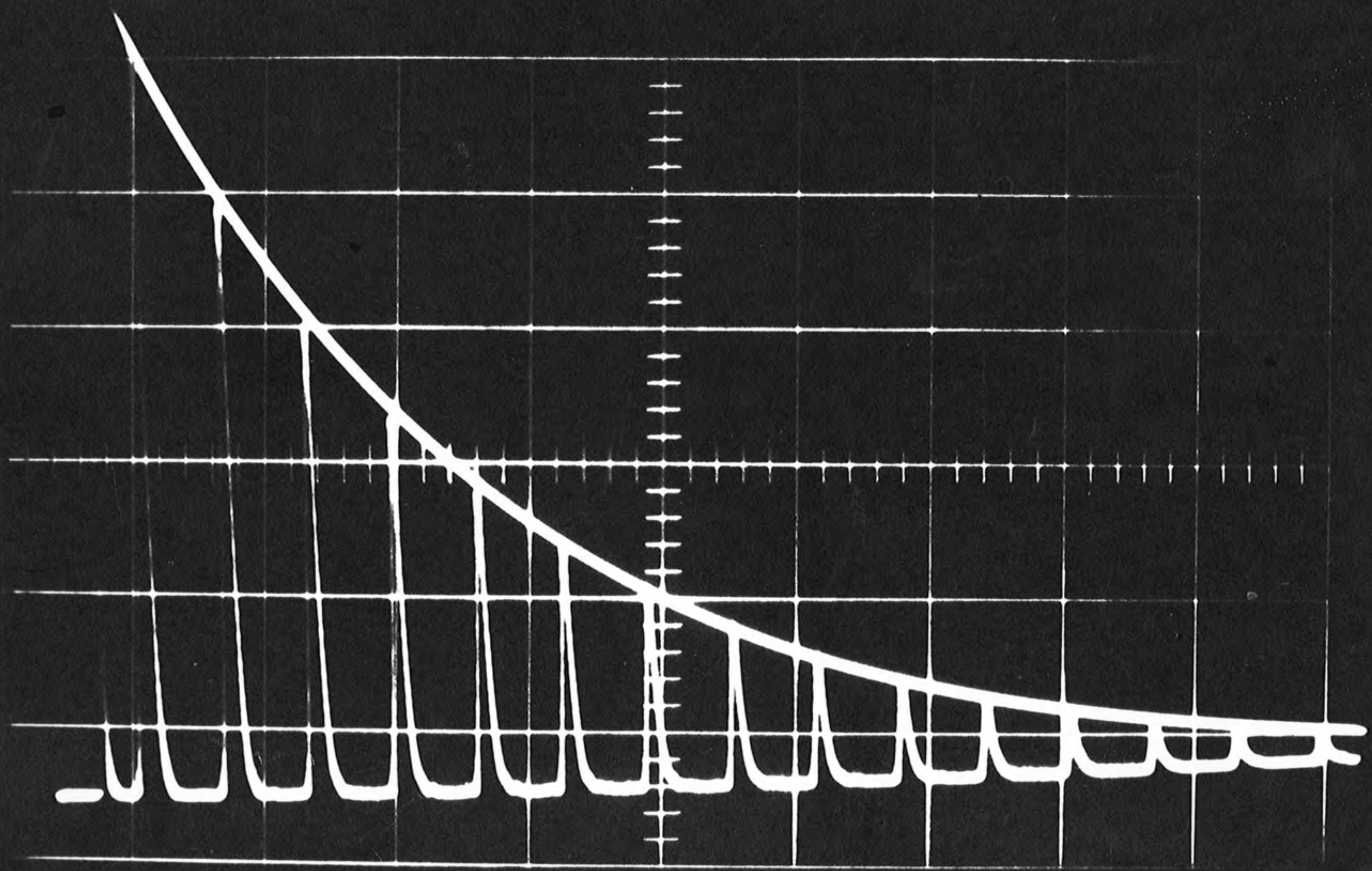

FIGURE (3.5). Pulse echo display.

In the present experiments the maximum relative error of the attenuation measurements did not exceed 10% except at low frequencies ($\sim$10 MHz) for small transducer when diffraction losses were appreciable.

3.6.2. Errors in the velocity measurements.

The main error in the present velocity measurements comes from the measurements of the transit time ($\sim$ 1%). The error in the measurement of sample length by a micrometer is about 0·2%. Other sources of error are negligible when compared with that in transit time measurement. For example, Waterman (1959) finds that the error introduced in velocity measurements on cubic crystals depends on the square of the misorientation angle. For silicon, for a one degree misorientation, he concluded that for shear wave propagation in a [100] direction

$$\frac{\Delta v}{v} = -2{\cdot}8 \times 10^{-4}$$

In Figure (3.6), C_{44} of mercury telluride calculated from shear wave propagation in a [100] direction for three temperatures, is presented. The velocities, in this figure were measured on the same specimen, using different bonding material. The maximum error, obtained from the scattering of the experimental points, is 2% on elastic constant, and 1% on velocity measurements ($C_{ij} \propto v^2$) which is, exactly, equal to quoted errors in transit time. Therefore, it may be concluded that the errors in elastic constants measurements are (remembering that elastic constants are proportional to density and the square of the velocity $C_{ij} \propto \rho v^2$ or $C_{ij} \propto \rho \frac{L^2}{t^2}$):

FIGURE (3.6). Errors in elastic constant measurements.

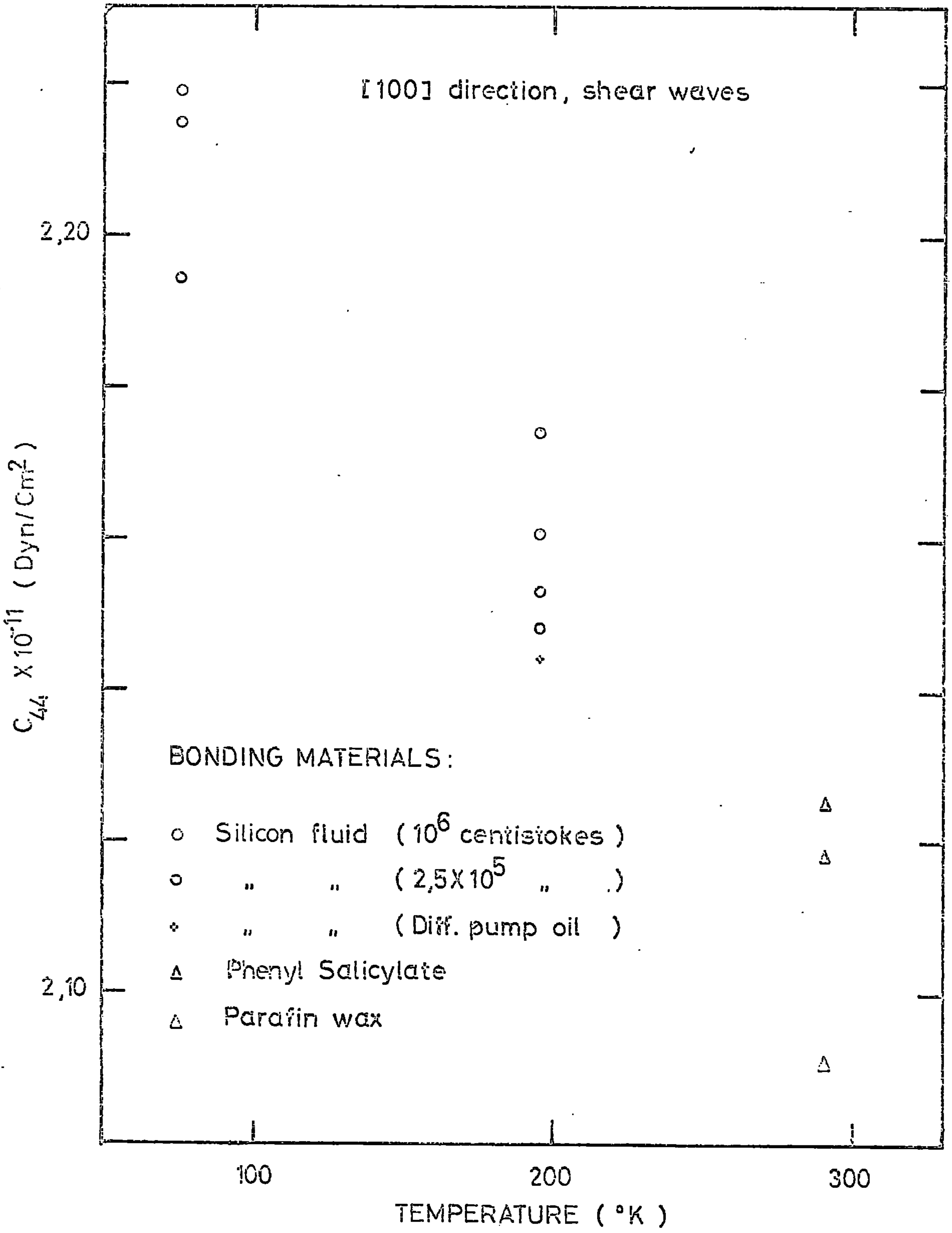

Error in the X-ray density: 0·075%

Error in the length measurements: 2 x 0·2%

Error in the transit time: 2 x 1%

i.e. total error in elastic constants: 2·5%

To estimate the error due to thermal expansion, the thermal expansivity of mercury telluride was measured (see Figure 3.7) with a simple quartz dilatometer, employing a dial gauge capable of reading 1/10000". The measured thermal expansivity of mercury telluride, together with the calculated thermal expansivity from the thermal expansion data, measured by Novikova and Abrikosov (1964) is shown in the Figure (3.8). The maximum error in velocity, at 77°K, calculated using room temperature length is 0·06%, $(\Delta L/L)_{77} \simeq 6 \times 10^{-4}$) which is also negligible among the other sources of error and can readily be corrected for.

3.7 THE SAMPLE HOLDER AND CRYOSTAT USED FOR ULTRASONIC MEASUREMENTS

The sample holder was designed to operate over a wide temperature range between 1·2°K to 450°K without altering the sample's position. To allow for different thermal expansions between the sample and the materials used in the sample holder construction spring adjustments and contacts were used.

As shown in Figure (3.9), the platform, upon which the sample is placed, can be driven upwards by compressing three springs by altering the position of a lower platform by a screw. The springs and the two

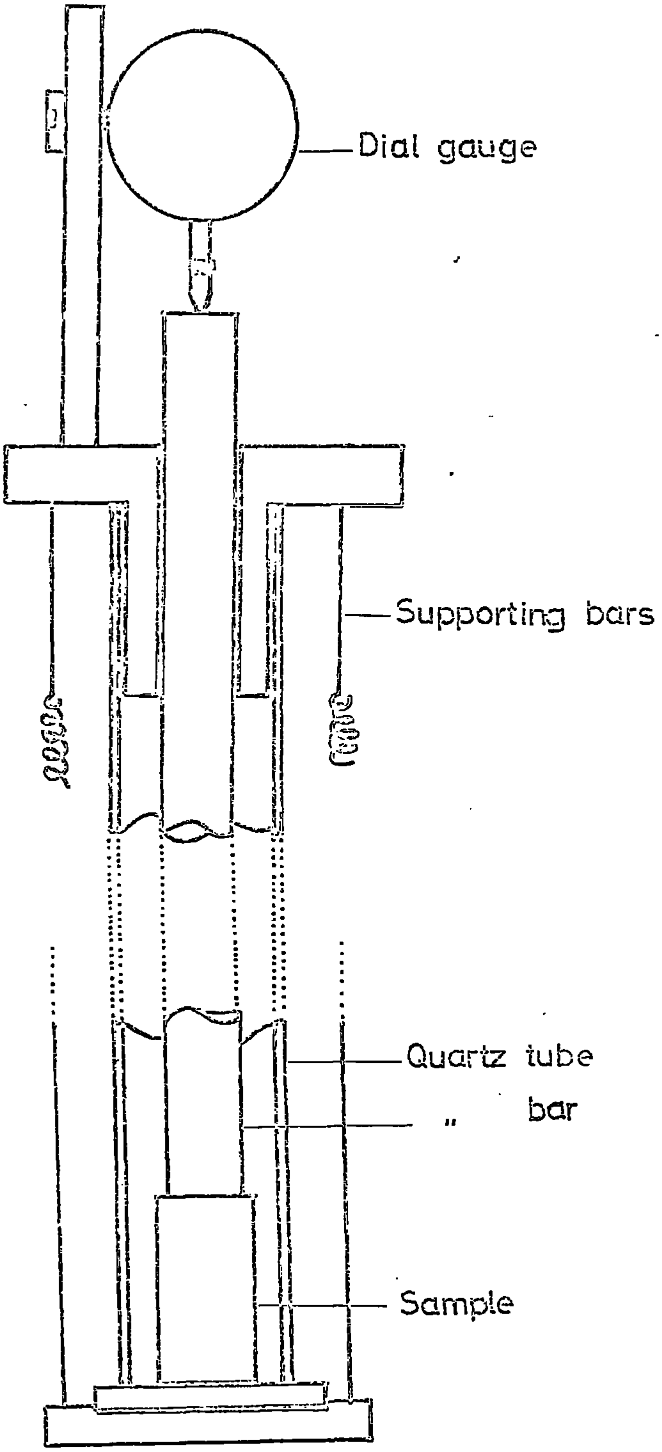

FIGURE (3.7). The quartz dilatometer.

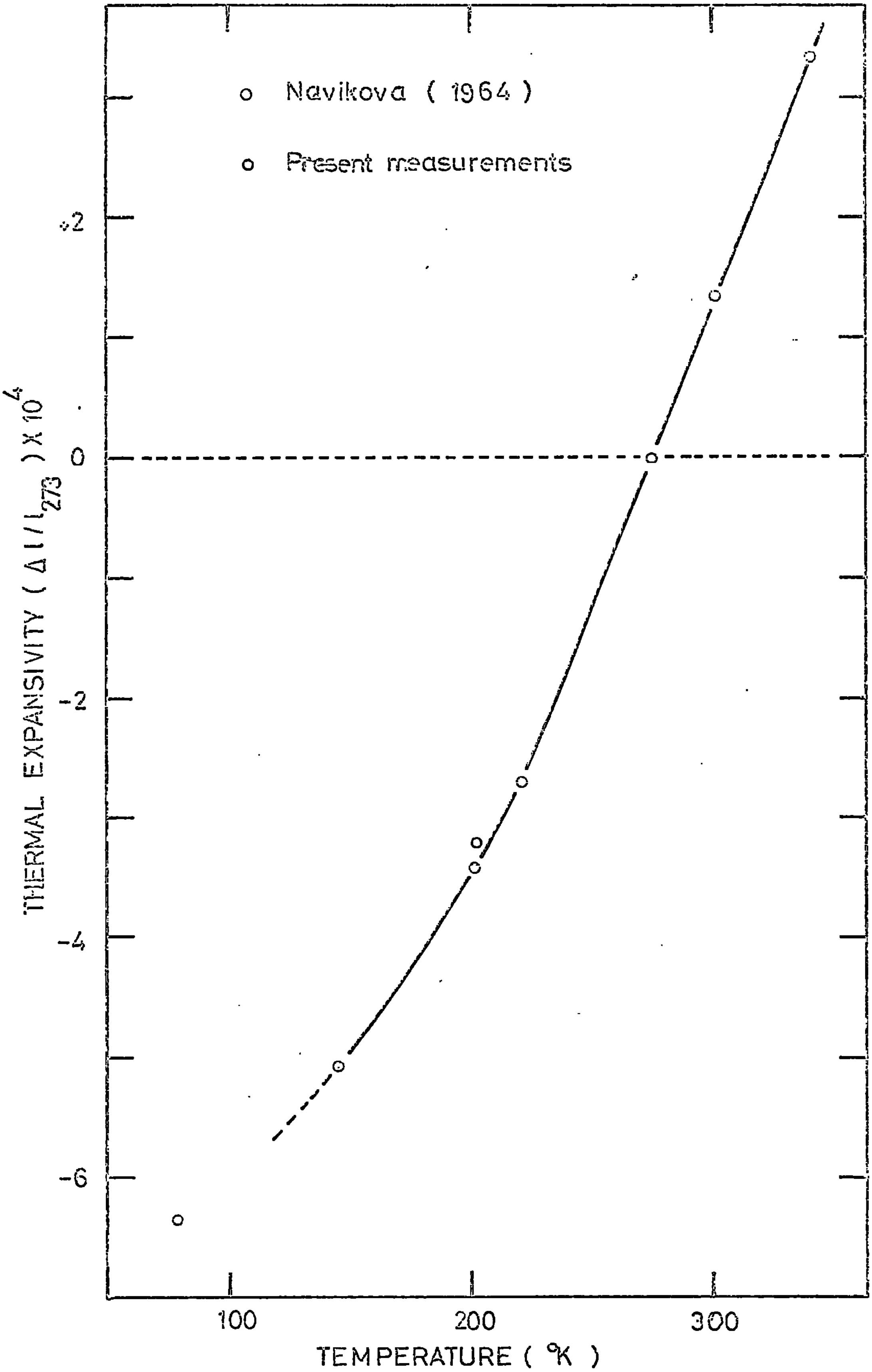

FIGURE (3.8). Thermal expansivity of mercury telluride.

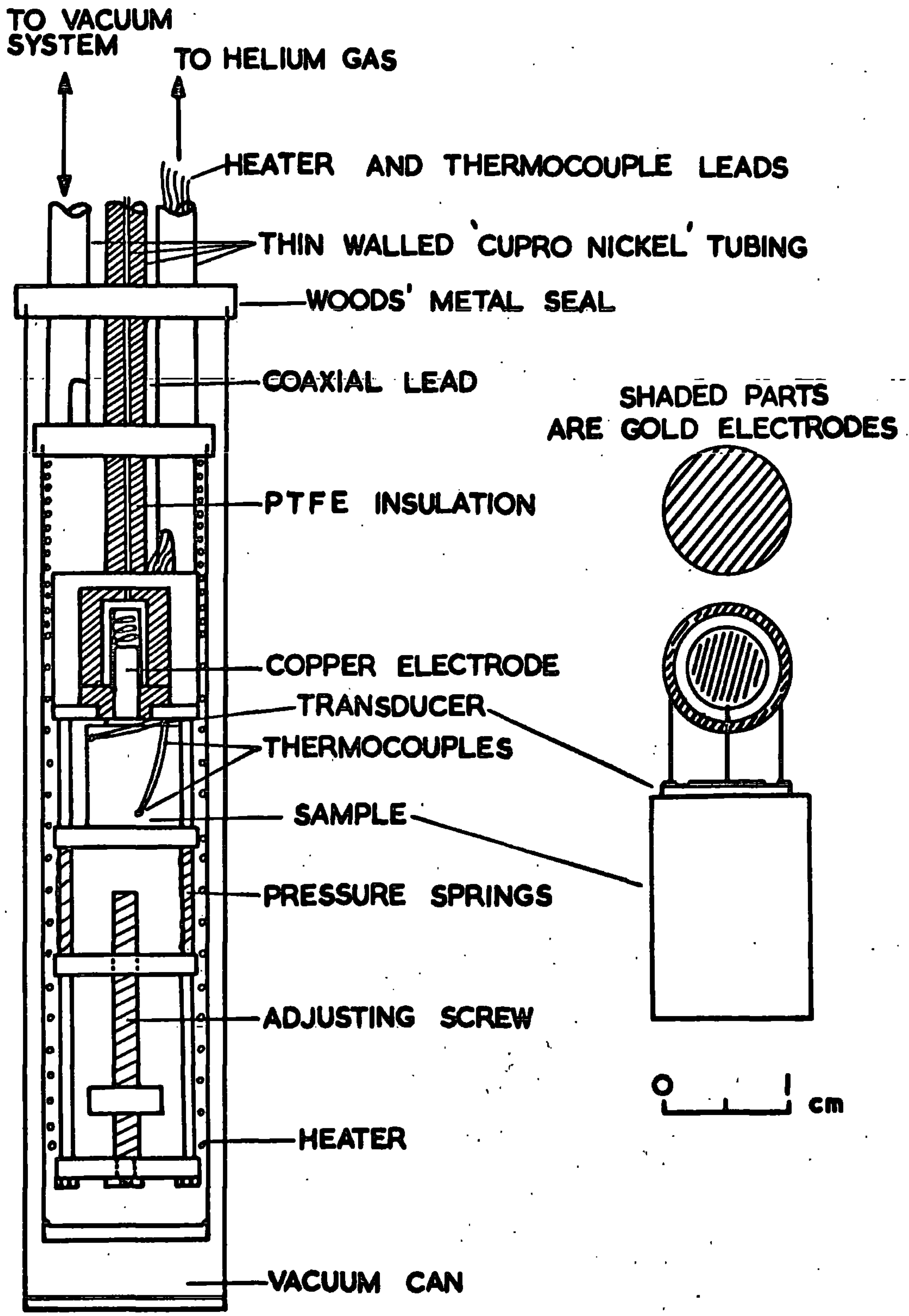

FIGURE (3.9).

SAMPLE HOLDER (Actual Size)

platforms were guided by three vertical brass bars, which were screwed to the sample holder head. For simplicity, in Figure (3.9), only two of these bars are shown. A spring loaded, guided, copper plunger was used to obtain contact with the inner electrode of the quartz transducer. The outer electrode was earthed by a brass ring with same internal diameter, connected to the sample holder head. The spring contacts used were successful in preventing contact breaking due to thermal expansion.

P.T.F.E. was used as the electrical insulation within the sample holder head the coaxial line, carrying R.F. power. Thin walled (0·1 mm), cupro-nickel tubing was used to make this coaxial line; sizes were outer diameter 6·0 mm and inner diameter 1·0 mm. The space between the lines was filled with P.T.F.E. sleeving. The inner line was soldered to the top of a copper case, which contained a spring-loaded copper plunger as the inner electrode.

The actual sample holder was isolated from the refrigerant liquid by two thin walled vacuum cans. As shown in Figure (3.9), these cans were connected separately to a vacuum system by two thin walled, cupro-nickel tubes.

All the joints, except for those of the two concentric vacuum cans, were hard soldered. To avoid damage of the inner components of the sample holder the two vacuum cans were soldered, just before starting each experiment, with "Wood's metal", which melts at about 65-70°C, using "killed spirit" as flux. The methods of soldering vacuum can joints are illustrated in Figure (3.10a); these gave completely

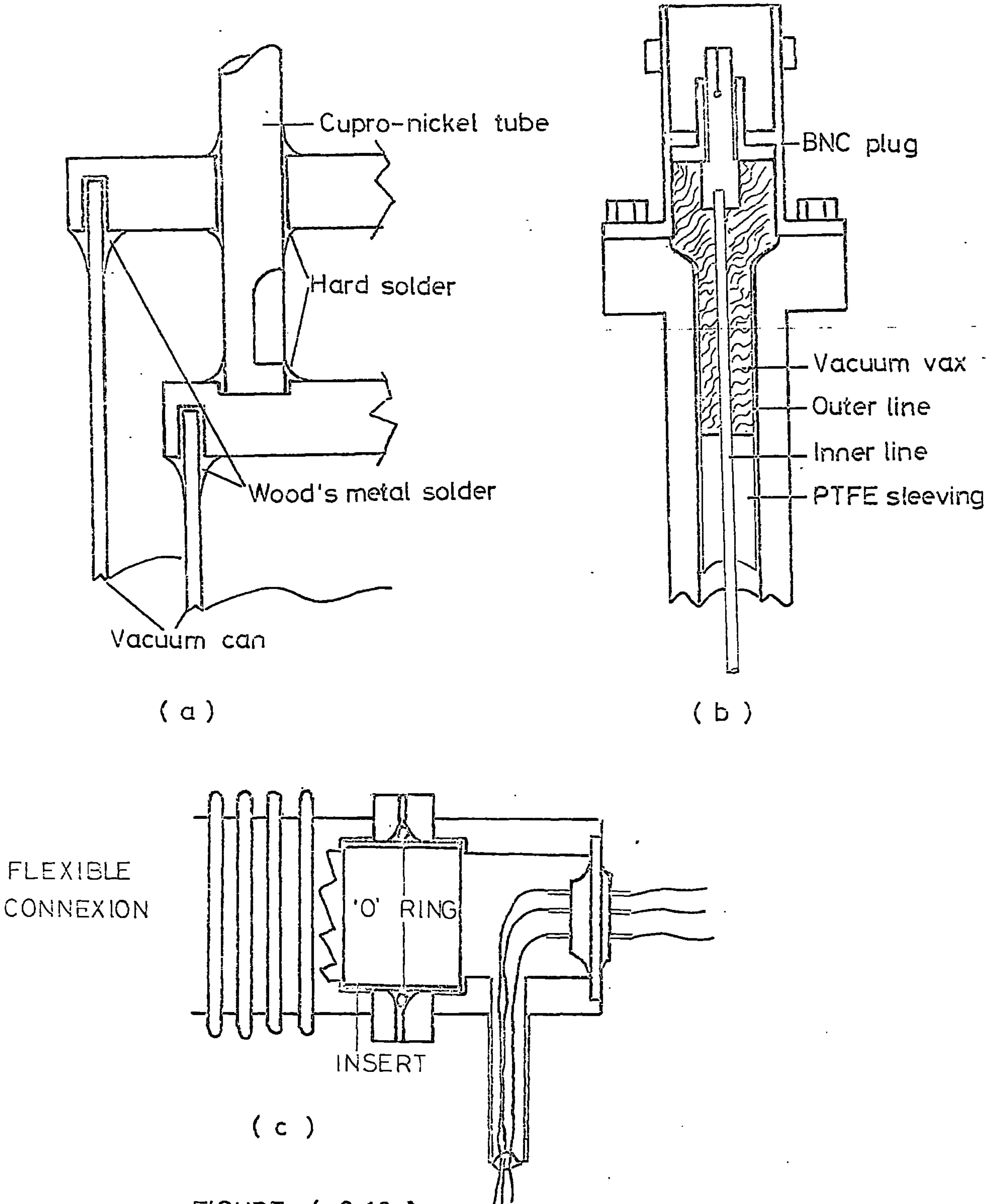

FIGURE (3.10) Various vacuum joints used in the sample holder.

satisfactory vacuum-tight joints unaffected by repeated cooling to liquid helium temperature. A vacuum tight coaxial, also illustrated in Figure (3.10b) was fitted on the cryostad head to prevent air leakage down the coaxial line. Heater and thermocouple leads were taken out through the vacuum lines to the cans and the method of insuring vacuum tightness is illustrated in Figure (3.10c). The inner can pumping line had a T-junction outside the cryostat to allow attachment of a helium gas filling system. Cryostatic equipment is shown in Figures (3.11) and (3.12).

The top of the glass liquid helium dewar was located to a rubber gasket and vacuum tightness achieved by a rubber sleeve. The inner space of the dewar was joined, through the cryostat head, to a manometer system and to a large mechanical pump. To release any built-up pressure in the dewar, as shown in the Figure (3.12), the inner space connected to a mercury protection valve. The other arms of the manometers, and the interspace of the helium dewar were pumped by a further mechanical pump. The vacuum spaces were monitered by Pirani gauges.

A superconducting gauge (Figgins et al. 1964) was used to measure the liquid helium level in the dewar. This was made from a coil of constantan wire tinned with 60% Sn - 40% Pb solder, using phosphoric acid as flux. The location position at the top of the sample holder is shown in Figure (3.11). A constant electric current is passed through the coil. In the liquid helium, the wire is superconducting with a transition temperature of $T_c \simeq 7^{\circ}K$. By observing the voltage drop across the wire, the level of the liquid helium could be monitered.

FIGURE (3.11).

CRYOSTAT HEAD AND SAMPLE HOLDER

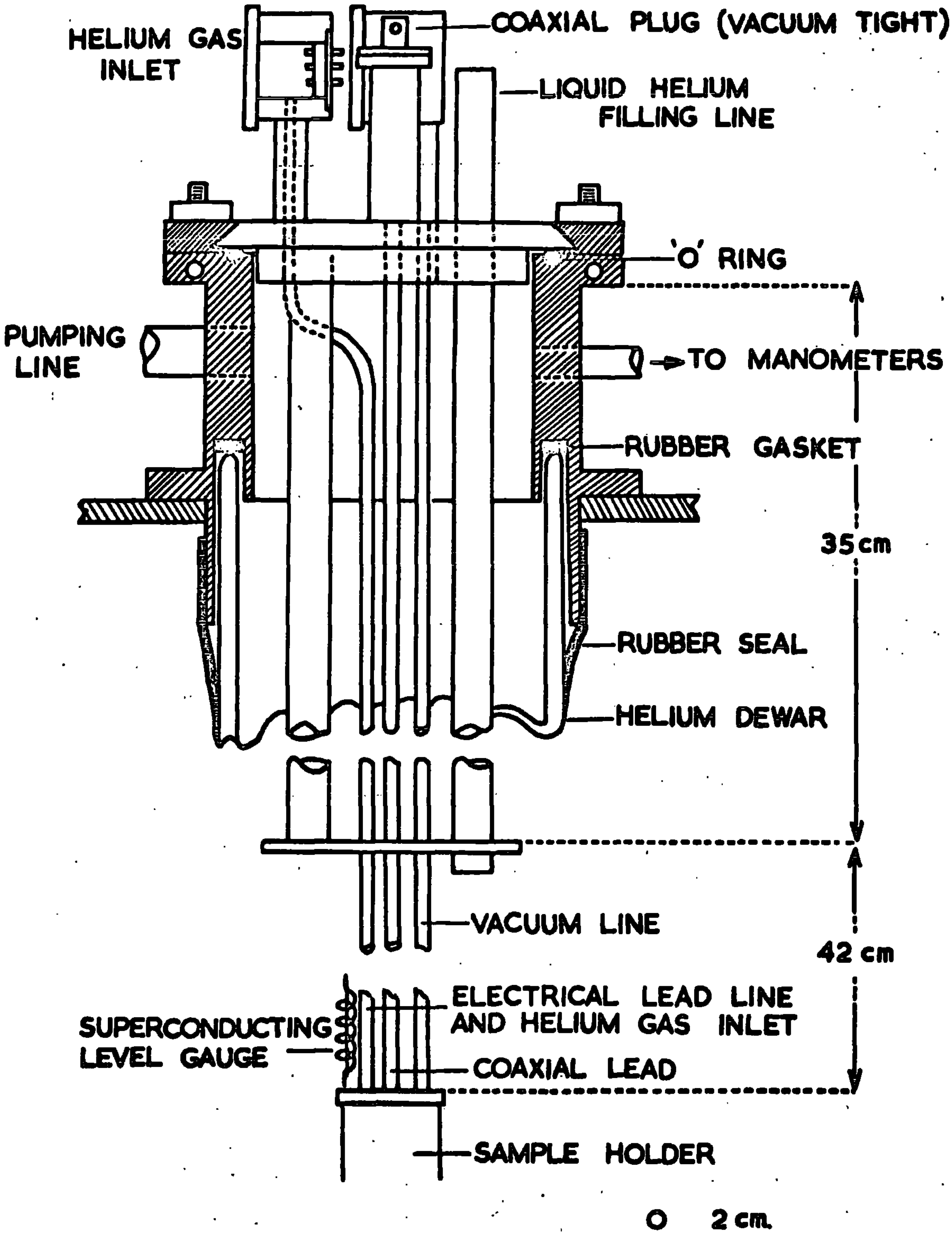

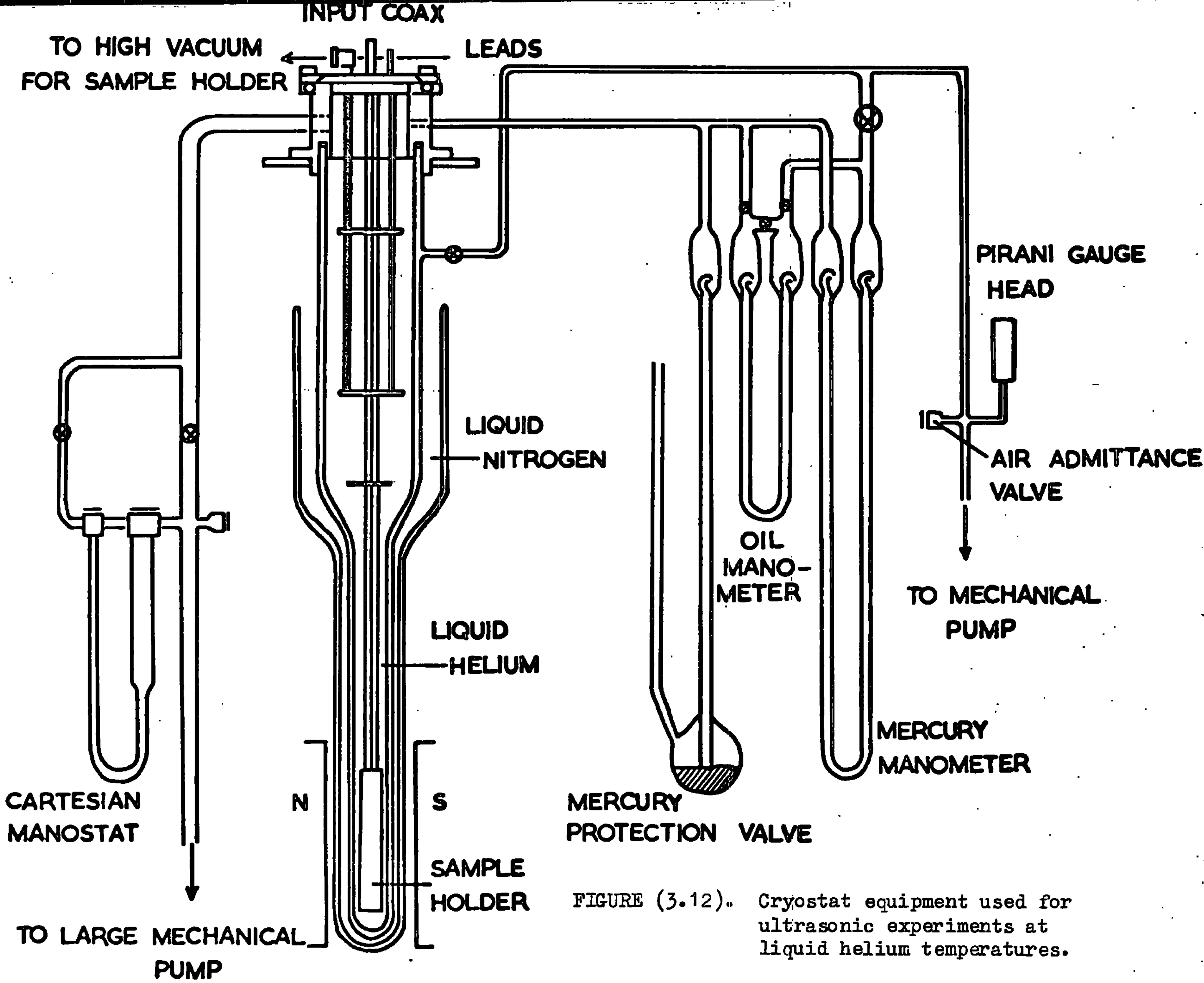

FIGURE (3.12). Cryostat equipment used for ultrasonic experiments at liquid helium temperatures.

To measure and control the sample temperature, two copper-constantan, and one 0·03 at.% gold/iron-chromel thermocoupler were used. 40 gauge (0·01219 cm diameter) copper and constantan, 0·008 cm diameter gold/iron and 0·009 cm diameter chromel wiring were used to make these thermocouples. For insulation, the pairs were inserted into thin sleeve, carried all the way through the cupro-nickel tubing.

The joints of the copper constantan thermocouple were prepared in the standard way. The gold/iron and chromel wire were fused together by silver soldering.

The reproducibility of the thermocouples depends upon very much the quality of the alloy wire and the junction, even mechanically straining effects the reading. Because of these reasons each thermocouple was calibrated. For calibration of the copper-constantan thermocouples the reference temperatures were: ice and water ($0^{o}C$), dry ice and acetone ($196^{o}K$) and liquid nitrogen ($77^{o}K$). The gold/iron-chromel thermocouple was calibrated against the manometer thermometer.

Above $40^{o}K$ the copper-constantan thermocouples were used while between $4{\cdot}2^{o}K$ and $40^{o}K$ the gold/iron-chromel thermocouple was employed.

To read the thermocouple potentials a "Tinsley" decade potentiometer, capable of reading 1 μV, and a spot light galvanometer was employed. The reference junction of the copper constantan thermocouple, immersed according to the temperature range in, ice and water or liquid nitrogen. As the reference junction of the gold/iron-chromel thermocouple's, a specially prepared, long junction arm of 1·0 mm diameter thin walled cupro-nickel tube was directly immersed to the liquid helium dewar.

Temperatures below $4{\cdot}2^{o}$K were measured with manometers. The vapour pressure of a liquified gas is a rapidly varying function of the temperature, and therefore the pressure over the liquid is a measure of temperature. In the range between 760-40 torr a mercury manometer was used and for the lower pressures an oil manometer was employed. The density of the oil (silicone fluid MS705) in the manometer 14•0 times less than that of the mercury. Both manometers were calibrated for the vapour pressure of liquid helium and liquid nitrogen. Tables can be found in White(1959, p.104-5.)

The cryostat was designed to give a temperature control accuracy to better than ± 0•5 degree, Preliminary experiments had shown that this adequate. Different temperature ranges required different techniques:

a - Control by electrical heating

b - Charcoal desorption control

c - Vapour-pressure control

In all these methods the required accuracy was achieved readily.

<u>a - Control by electrical heating</u>:

The usual method is by controlling the supply of electrical energy to preserve a temperature (T) in the space which is to be above that of the surroundings (at To). As the loss of heat, to the surroundings by radiation, conduction, etc., is a monotonically increasing function of (T-To), so the electrical input, must increase similarly with (T-To). In the present experiment, temperature was controlled, over a wide temperature range between $4{\cdot}2^{o}$K and room temperature. Electrical control was used solely between 77^{o}K and 300^{o}K successfully by this method. The arrangement used is shown in Figure (3.13). The inner vacuum jacket of around the

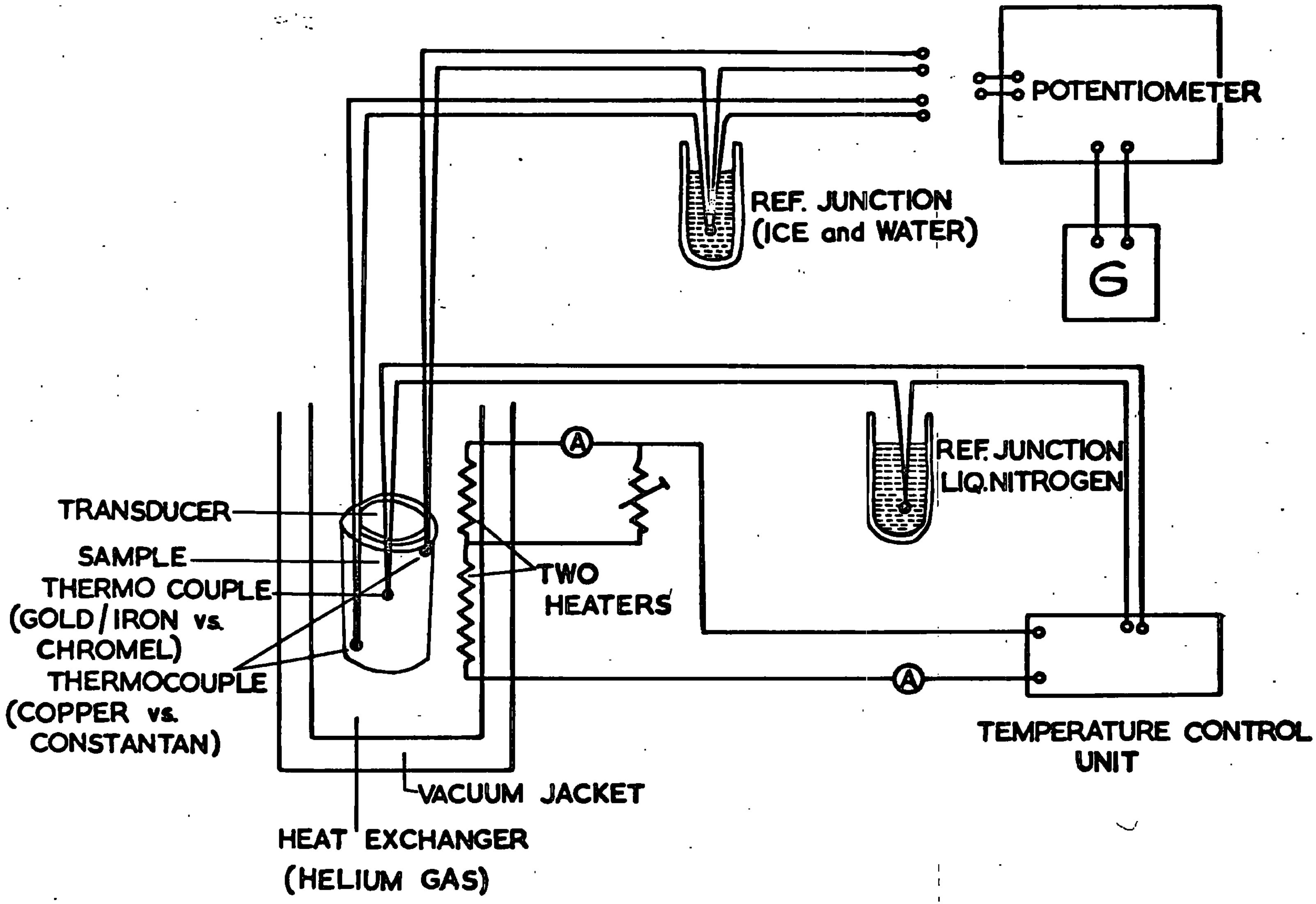

FIGURE (3.13). TEMPERATURE CONTROL AND MEASURING CIRCUIT sample was filled with a controlled pressure of helium gas as heat exchanger, and this assembly was isolated from the refrigerant liquid by evacuating the outer can. A temperature gradient, measured by the two copper-constantan thermocouples, developed along the sample due to heat flow in the support rods and electrical leads. This gradient was compensated for by adjustment of current to two independently controlled, heater coils of constantan wire wound around the sample holder bars, concentrically with the sample. Control was carried out by a solid state control unit, similar to that used for control of temperature in the crystal growth furnace (see page 11). The heaters were fed by the output of the controller, which is proportional to the difference between thermocouple and a reference voltage, which can be set on the unit. The setting which had been calibrated for rhodium/platinum-platinum thermocouples. With this arrangement the sample temperature could be held at room temperature, when liquid nitrogen was used as a refrigerent liquid, to better than that ± 0·5 degree accuracy for a long time.

To attain temperatures below 77°K liquid helium was used as coolant. To reach thermal equilibrium, using the electrical heater control system, was about 30 minutes. Thus to take a reasonable number of measurements between 4·2°K and 77°K took many hours. To keep the liquid helium level high for this time was uneconomical.

c - Charcoal desorption control:

(Rose-Innes and Broom 1956). A simple desorption system was therefore used for obtaining temperatures between 4·2°K and 77°K. The space in the inner dewar surrounding the sample holder was filled with activated charcoal. After measurements at $4{\cdot}2^{o}$K were completed, the liquid helium in the inner dewar was boiled off at atmospheric pressure by an electrical heater, leaving the charcoal saturated with absorbed helium. When all the liquid helium had gone the temperature of the sample rose: this rise could be accelerated by the heater or the temperature held constant, when required, by pumping on the inner dewar. An additional advantage of this system is that the saturated charcoal has a large heat capacity and so the temperature rises very slowly even when the charcoal is not being pumped. In the Figure (3.14) temperature variation of the sample is shown. In the region between $4{\cdot}2^{o}$K and 30^{o}K average temperature rise is 12 minutes per degree, in this range, readings were taken, while temperature rises. The temperatures between 30^{o}K and 60^{o}K were held steady by pumping on the inner dewar.

c - Vapour pressure control:

The temperatures below $4{\cdot}2^{o}$K and between 60^{o}K and 77^{o}K were obtained by reducing the vapour pressure over the liquid helium and nitrogen by pumping with a fast pump. The inner space of the dewar was pumped through a cartesian manostat to control the vapour pressure over the liquid and this gave a steady temperature during measurements.

FIGURE (3.14). Temperature change with time of the sample when charcoal is used.

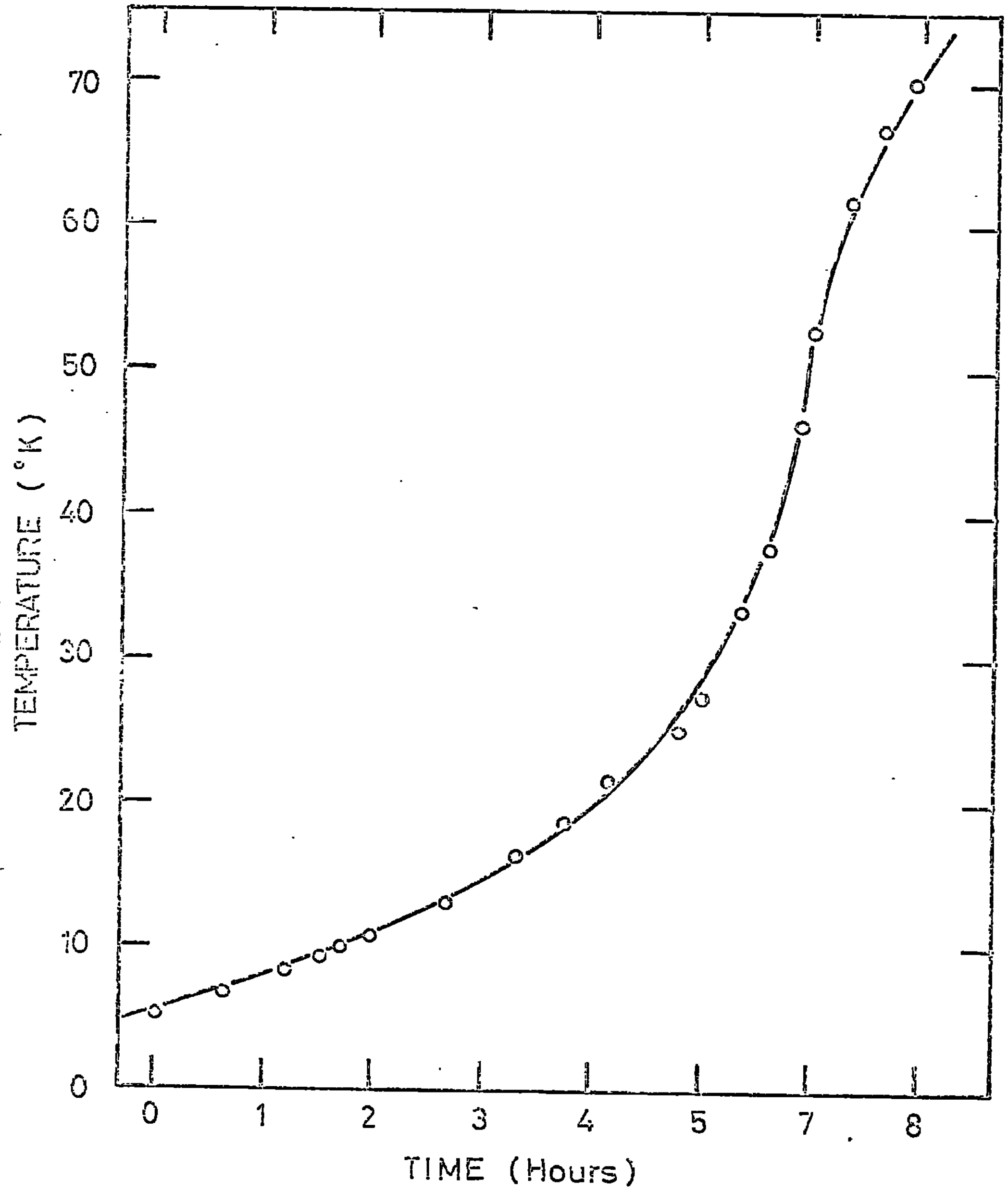

CHAPTER 4

ELASTIC CONSTANTS OF MERCURY TELLURIDE

4.1 INTRODUCTION

The elastic constants of single crystals furnish basic mechanical and thermodynamic information in solids. During the study of ultrasonic wave propagation the adiabatic elastic constants C_{11}, C_{12} and C_{44} of mercury telluride have been obtained. Preparation of stoichiometric mercury telluride presents a problem (see Section 2.1) and serious discrepancies exist between published data, especially on electron transport properties: carrier densities and mobilities are particularly sensitive to excess of either component in such a semimetal with a very small band overlap. Stoichiometry is also relevant to ultrasound wave propagation and crystals prepared in different ways have been examined for any effects of non-stoichiometry and possible relationship to mechanical properties.

In II-VI compounds the ionicity, the proportion of ionic component in mixed covalent-ionic bond, plays an important role. One aim of the present work was to estimate the ionicity in mercury telluride through the elastic constants. In zinc blende materials, due to their piezoelectric nature, sound velocities in some directions can be modulated. However, in the present work no effect of piezoelectricity on sound velocities in mercury telluride was detected. The applicability of Born's relation and the three-force constant model are tested in mercury telluride. Although Born's relation is found to be a reasonable approximation, the three-force constant model should not be rigidly applied to compounds. From the comparison of results with those of neighbouring substances, it is concluded that the elastic constants, like other intrinsic lattice properties of materials belonging the same crystallographic classes, exhibit remarkable similarities; mercury telluride shows no anomalous behaviour. Relevant parameters such as the Debye temperature has been calculated from the elastic constants data.

4.2 THE VELOCITY OF ELASTIC WAVES IN CRYSTALLINE SOLIDS.

Since the strains encountered in ultrasonic measurements are of the order of 10^{-6} to 10^{-8}, calculations based upon the classical theory of linear elasticity are valid. Hooke's law, which has been defined for a linear, one dimensional solid in Section (1.1) and given as Equation (1.1), is applicable. This equation for three dimensional, crystalline, real solids takes the following form:

$$\sigma_{ij} = C_{ijkl}\,\epsilon_{ij} \qquad (4.1)$$

Here stress (σ) and strain (ϵ) are second rank tensors and the proportionality constant (C), defined as an elastic modulus, is a fourth rank tensor.

Elastic constants can be determined not only from the stress-strain relation (Equation 4.1) but also from sound velocities. The procedure for obtaining the elastic constants from sound velocities in a dynamic experiment will now be outlined.

__The stress tensor__ (σ_{ij}) represents the components of force per unit area. The first subscript denotes the plane on which the stress component acts. The second subscript denotes the direction of the stress component.

__The strain tensor__ (ϵ_{ij}) defines the deformation in the neighbourhood of a point in the undeformed medium by the position vector X. The strain for small deformations may be written in terms of displacement gradient in the form.

$$\epsilon_{ij} = 1/2\ (S_{j,i} + S_{i,j}) \tag{4.2}$$

Here the commas show the differential with respect to position vector. The ϵ_{ij} defined by this equation have a simple geometrical meaning such that ϵ_{ij} for $i=j$ ($\epsilon_{ii} = \delta S_i/\delta X_i$) is the change in length per unit length of a straight line segment. For $i \neq j$, ϵ_{ij} is twice the change in an angle whose sides were originally parallel to the X_j and X_i axis.

The equation of motion for an elastic body can be derived from Newton's second law. Equating the force components to the acceleration components for a medium of density ρ, one obtains

$$\rho \ddot{S}_i = \sigma_{ij,i}\ (i=1,2,3) \tag{4.3}$$

Here $\ddot{S}_i$ is the second derivative of the displacement vector with respect to time; that is the acceleration. Then on combining Equations (4.3), (4.2) and (4.1) one obtains the following equation.

$$C_{ijkl}\ (S_{l,kj} + S_{k,lj}) = 2\rho\ddot{S}_i \tag{4.4}$$

and, since $C_{ijkl} = C_{ijlk}$, this equation simplifies to

$$C_{ijkl}\ S_{l,kj} = \rho\ddot{S}_i \tag{4.5}$$

This equation admits solution of the form

$$S_l = S_{ol} \exp i(\omega t - kr) \quad (l = 1,2,3) \tag{4.6}$$

which is an elastic plane wave. Here S is the particle displacement and k is the wave vector defined as $k = \frac{\omega}{v} n$.

Therefore

$$S_{l,kj} = -n_k n_j s_{ol} \left(\frac{\omega}{v}\right)^2 \exp i(\omega t - kr) \tag{4.7}$$

and

$$\ddot{S} = \omega -{}^{2} S_{oi} \exp i(\omega t - kr) \tag{4.8}$$

The equation of motion, given in Equation (4.5) becomes

$$C_{ijkl} S_{ol} n_k n_j = \rho v^2 S_{oi} \quad (i = 1,2,3) \tag{4.9}$$

In this form the equations constitute the basis for the "long wavelength" (no dispersion) method that Born and his coworkers used to develop the elastic constants from lattice theory. (see Born and Huang 1954). Hence, a nontrival solution of the form of Equation (4.6) requires that the determinant of the coefficient in the system of Equation (4.9) must vanish.

$$\therefore \quad \left| C_{ijkl} n_k n_j - \rho v^2 \right| = 0 \tag{4.10}$$

For applications to actual situations in which elastic constants are determined from plane wave propagation, it is usually preferable to transform to a co-ordinate system in which the direction of propagation is one of the axes. Elastic constants may be transformed from one axial system to another by means of the tensor transformation equations

$$C'_{ijkl} = \frac{\delta X'_i}{\delta X_m} \cdot \frac{\delta X'_j}{\delta X_n} \cdot \frac{\delta X'_k}{\delta X_o} \cdot \frac{\delta X'_l}{\delta X_p} \; C_{mnop} \tag{4.11}$$

The partial derivatives appearing in this equation are direction cosines and, if one goes from a crystallographic set of axes to a rotated set designated by primes, or vise versa, the direction cosines are related to the partial derivatives as

$$\begin{array}{c|ccc} & X_1 & X_2 & X_3 \\ \hline X_1' & \frac{\delta X_1'}{\delta X_1} & \frac{\delta X_1'}{\delta X_2} & \frac{\delta X_1'}{\delta X_3} \\ X_2' & \frac{\delta X_2'}{\delta X_1} & \frac{\delta X_2'}{\delta X_2} & \frac{\delta X_2'}{\delta X_3} \\ X_3' & \frac{\delta X_3'}{\delta X_1} & \frac{\delta X_3'}{\delta X_2} & \frac{\delta X_3'}{\delta X_3} \end{array} \qquad (4.12)$$

Hence, there are only 21 independent constants C_{ijkl} of the possible 81. The usual matrix notation giving the elastic constants as C_{ij} is obtained by replacing

1 by 11 ; 2 by 22 ; 3 by 33 ; 4 by 23 ; 5 by 13 ; 6 by 12.

In cubic materials, due to the high crystal symmetry, there are only three independent elastic constants. These are:

$$C_{11} = C_{22} = C_{33}$$

$$C_{12} = C_{21} = C_{13} = C_{21} = C_{23} = C_{32}$$

$$C_{44} = C_{55} = C_{66}$$

There are three orientations ([100], [110] and [111] directions) for which a pure longitudinal and two pure shear waves can be transmitted in a cubic material. Following the transformation of Equation (4.10) for these particular crystallographic directions by the transformation law of fourth rank tensors, given in Equation (4.11), and choosing the direction cosines of these directions (Equation 4.12), sound velocities propagating along these major crystallographic directions can be obtained. These are:

For the [100] direction

$$v_{long.} = (C_{11}/\rho)^{\frac{1}{2}} \tag{4.13}$$

$$v_{shear} = (C_{44}/\rho)^{\frac{1}{2}} \text{ polarised along either [001] or [010] direction} \tag{4.14}$$

For the [110] direction

$$v_{long.} = [(C_{11} + C_{12} + 2\,C_{44})/2\rho]^{\frac{1}{2}} \tag{4.15}$$

$$v_{shear} = (C_{44}/\rho)^{\frac{1}{2}} \text{ polarised along [001] direction}$$

$$v_{shear} = [(C_{11} - C_{12})/2\rho]^{\frac{1}{2}} \text{ polarised along [110] direction}$$

For the [111] direction

$$v_{long.} = [(C_{11} + 2C_{12} + 4C_{44})/3\rho]^{\frac{1}{2}} \tag{4.18}$$

$$v_{shear} = [(C_{11} - C_{12} + C_{44})/3\rho]^{\frac{1}{2}} \text{ polarised any direction in the (111) plane} \tag{4.19}$$

It is interesting to note that in cubic materials all three elastic constants can be obtained from the longitudinal and two shear velocities of waves propagated in the [110] direction. In the present work sound velocities have been measured along [100], [110], and [111] (major) crystallographic directions and linear combinations of the elastic constants have been obtained from these velocities using Equations (4.13-19).

The preceding treatment is based upon Hooke's law of elasticity, but most real solids, even for strains of 10^{-8}, do not obey Hooke's law exactly. Thus, as previously discussed in Section (1.1) in an anelastic solid, sound waves are attenuated and velocities are frequency dependent. On the other hand the velocity changes, due to most of the relaxation phenomena encountered in solids, are less than 1%. This is about the error in velocity measurements in the present work. Thus, the approximations made to obtain Equations (4.13-19) are reasonable. Because of the small change of velocity, the anelastic properties of mercury telluride are much more important in sound attenuation rather than the velocity change. This is left to subsequent chapters.

4.3 RESULTS

The temperature dependences of ultrasound velocities were measured between 1.4°K and 300°K for wave propagation along [100], [110] and [111] crystallographic directions in several crystals. The appropriate relationships between the velocities and linear combinations of the elastic constants C_{11}, C_{12} and C_{44} for those directions of either pure longitudinal or pure shear waves propagation has been given in the preceding section. In Figure (4.1) and (4.2) are presented linear

FIGURE (4.1). The temperature dependence of the elastic constants of an as-grown crystal of HgTe oriented along the [100] direction. The units are 10^{11} dynes/cm^2.

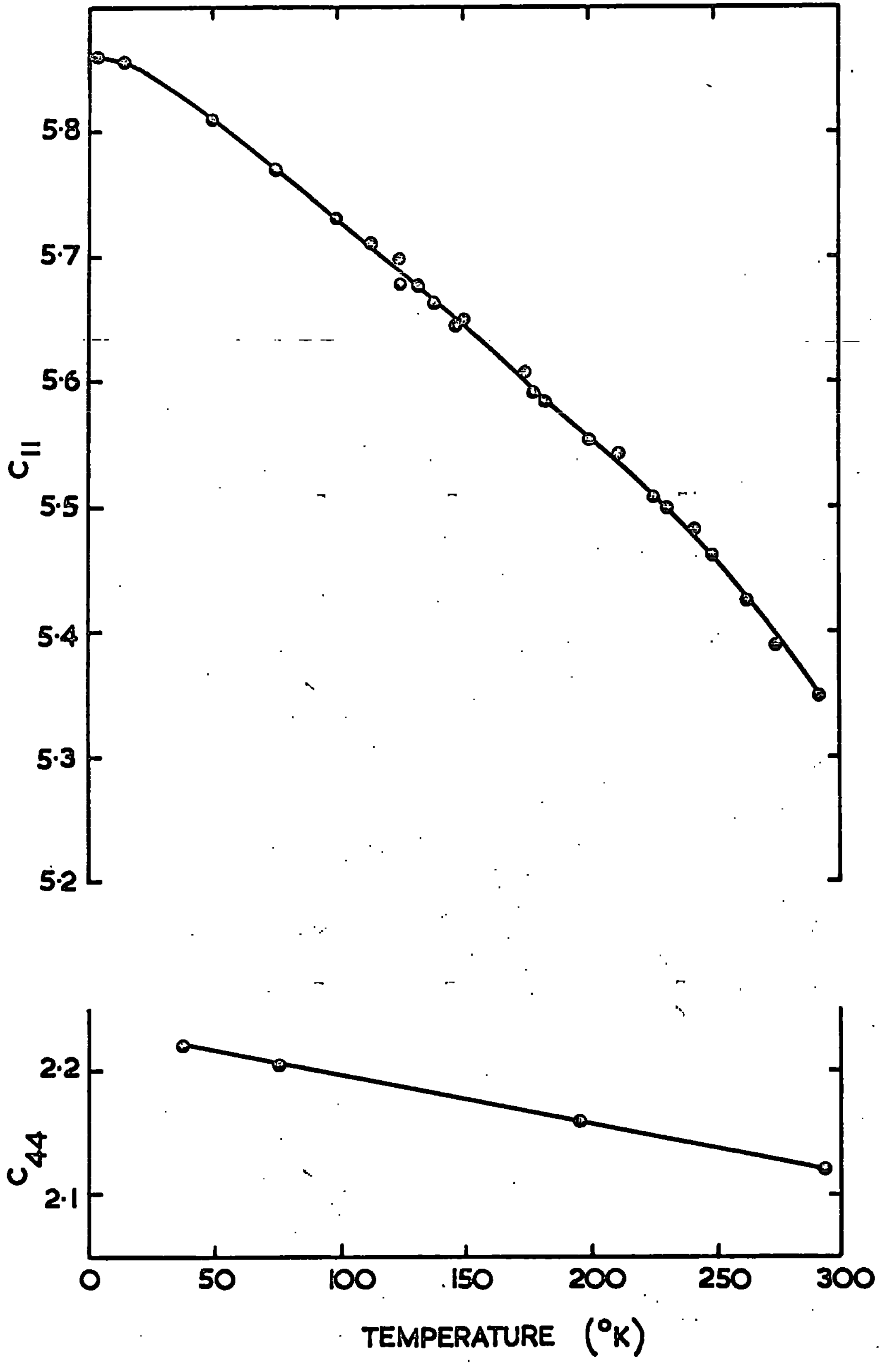

FIGURE (4.2). The elastic constants of an as-grown HgTe oriented along the [111] direction. The units are 10^{11} dynes/cm^2.

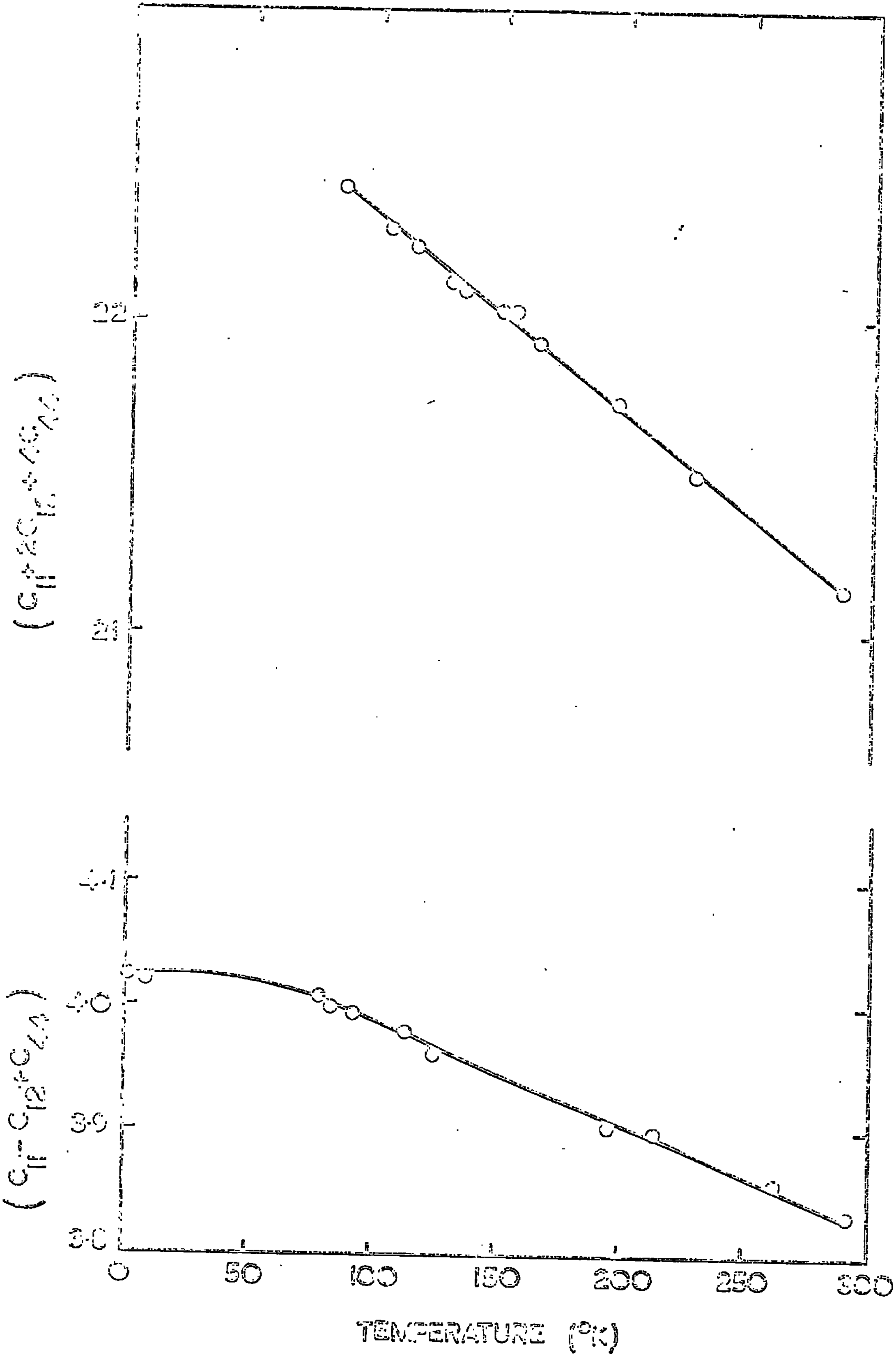

combinations of the elastic constants derived, using Equations (4.13-14) and (4.18-19), from the ultrasonic wave velocities measured in (100) and (111) samples. Linear combinations of the elastic constants, obtained from the ultrasonic wave velocities measured in (110) samples, before and after annealing in mercury vapour, are illustrated in Figure (4.3). Calculated (Equations 3.15-17) values of the three elastic constants C_{11}, C_{12} and C_{44} obtained from ultrasonic wave velocities measured in (110) sample, before and after annealing are shown in Figure (4.4) and tabulated for selected temperatures in Table (4.1), together with the bulk modulus and the mean results of (100) and (111) samples. Changes in the elastic constants (ΔC_{ij}) before and after annealing are small (see Table 4.2, ~1·5% at 4·2°K and ~ 2% at 300°K) and are of similar magnitude for each constant, although ΔC_{44} is negative in contrast to ΔC_{11} and ΔC_{12}. Crystal preparation and history modify the elastic constants of mercury telluride: this would explain the discrepancy between the present result and those of Mavroides and Kolesar (1964) (see Appendix A) measured at room temperature only; these workers give no details of crystal preparation so that further comparison cannot be made. The thermal variation of elastic constants is characterized by two general features; a) an approach with zero slope to the T = 0°K and b) a negative slope at high temperatures. The results on mercury telluride show this normal behaviour.

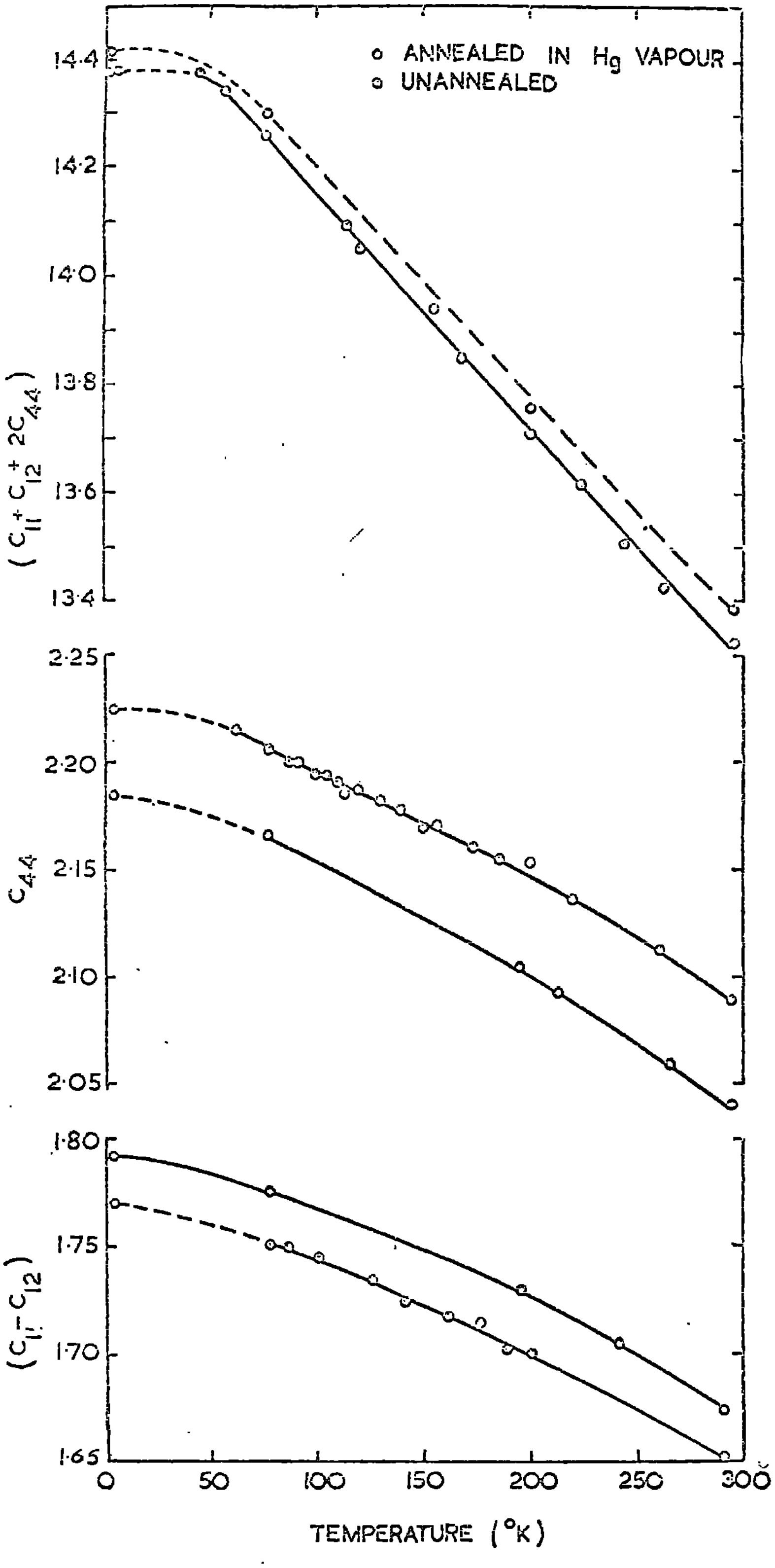

FIGURE (4.3). The temperature dependence of the measured linear combinations of the elastic constants of a crystal oriented along the [110] direction both as grown and after annealing at 300° for 100 hr in mercury vapour. The units are 10^{11} dyn/cm^2.

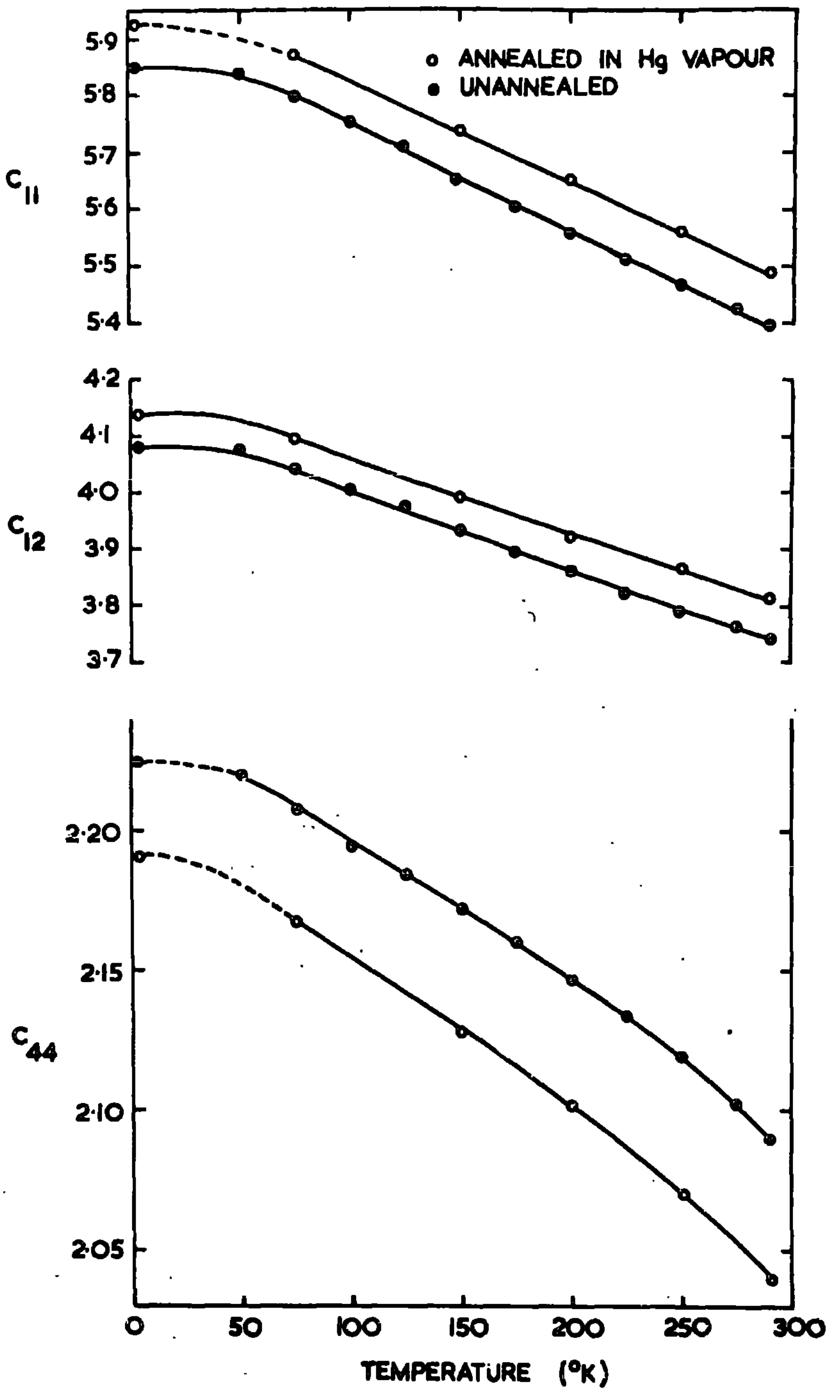

FIGURE (4.4). The elastic constants C_{11}, C_{12} and C_{44} calculated from the data in Figure (4.3). The units are 10^{11} dynes/cm^2.

TABLE (4.1) Adiabatic Elastic constants and bulk modulus $(C_{11} + 2C_{12})/3$ for HgTe crystals at selected temperatures T. Units are 10^{11} dynes/cm^2. Maximum errors are ± 0·5%

T(°K)	Elastic modulus	[110] Sample (unannealed)	[110] Sample (annealed)	Mean results from [100] and [111] samples
4·2	C_{11}	5·85	5·92	5·86
	C_{12}	4·08	4·14	4·03
	C_{44}	2·22	2·19	2·22
	$(C_{11} + 2C_{12})/3$	4·67	4·73	4·63
77	C_{11}	5·80	5·87	5·77
	C_{12}	4·04	4·10	3·96
	C_{44}	2·21	2·17	2·20
	$(C_{11} + 2C_{12})/3$	4·62	4·69	4·56
196	C_{11}	5·57	5·65	5·57
	C_{12}	3·87	3·94	3·78
	C_{44}	2·15	2·10	2·16
	$(C_{11} + 2C_{12})/3$	4·44	4·51	4·38
290	C_{11}	5·39	5·48	5·35
	C_{12}	3·74	3·81	3·64
	C_{44}	2·09	2·04	2·12
	$(C_{11} + 2C_{12})/3$	4·30	4·37	4·21

TABLE (4.2) The change in elastic constants of mercury telluride after annealing.

Temperature (^oK)	ΔC_{11}	% change	ΔC_{12}	% change	ΔC_{44}	% change
4·2	(+) 0·07	1·2	(+) 0·06	1·4	(-) 0·03	1·4
77	(+) 0·07	1·2	(+) 0·06	1·5	(-) 0·04	1·8
196	(+) 0·08	1·4	(+) 0·07	1·8	(-) 0·05	2·3
290	(+) 0·09	1·6	(+) 0·07	1·8	(-) 0·05	2·4

4.4. DISCUSSION

Before the significance of the elastic constants is discussed, it is useful to look at the changes produced by annealing. Then the magnitude of the difference between the results on the crystals and those which would be measured on perfect crystals can be assessed.

The small changes in the elastic constants produced by annealing in mercury vapour probably do not stem from variations in carrier densities and energies. Keyes (1961) has shown from the deformation model that in n-type germanium only C_{44} is effected by electronic energy changes and consequent fluctuations in carrier density. In general the shape of the arrangement in k-space of the energy surface extrema determine which of the elastic constants will be modified by doping. Annealing of mercury telluride effects all three elastic constants proportionately, although ΔC_{44} is different in sign from ΔC_{11} and ΔC_{12}. This is consistent with the single, almost spherical, electron Fermi surface centred on $k = 0$: in the deformation potential approximation the elastic constants are independent of carrier density, when the carriers are contained within only one Fermi surface extremum. The slight effects of annealing must find their source elsewhere, plausibly in lessening of the crystal internal strain. Similar velocity strain behaviour is consonant with dislocation damping theory. Annealing mercury telluride removes microheterogeneous regions containing excess tellurium (see Section 2.6) and furthermore, the dislocation density is reduced. The effects of the dislocations on the elastic constants are small. This will be discussed later, in Chapter 8. The measured values are probably very close to those in the perfect crystal. We turn now to discuss their physical meaning.

4.4.1. The force constants in mercury telluride

Born's two-force constant model has been applied to mercury telluride. In this model Born assumes that atoms in crystalline solids are rigid and are connected together by Hookian springs. The two Hooke's radial (α) and angular (β) forces are obtainable from

$$\begin{aligned} C_{11} &= \alpha/2r_o \\ C_{12} &= \alpha/2r_o\ (2\beta/\alpha - 1) \\ C_{44} &= \alpha/2r_o\ (1 - \beta^2/\alpha^2) \end{aligned} \tag{4.20}$$

Here r_o is the nearest neighbour distance. For mercury telluride the force constants α and β are calculated as $3{\cdot}8 \times 10^4$ dyn/cm and $3{\cdot}2 \times 10^4$ dyn/cm respectively. In these equations three elastic constants are related by two force constants and by eliminating α and β, Born's relation between the elastic constants may be obtained.

$$[4C_{11}(C_{11} - C_{44})]/(C_{11} + C_{12})^2 = 1 \tag{4.21}$$

The left hand side of this equation is 0·86 for mercury telluride. This result is compared in Table (4.3) with other neighbouring group substances. From this table it may be seen that, although deviation from unity for purely covalent materials is small (1% for germanium and 7% for silicon), the deviation for mercury telluride is rather high (14%). Nevertheless, TABLE (4.3) Comparison between the two force constant model of Born and ionicity. Results, other than those for mercury telluride, are from Potter (1957)

	Si	Ge	lnSb	ZnS	HgTe
$\frac{4C_{11}(C_{11} - C_{44})}{(C_{11} + C_{12})}$	1·07	1·01	0·90	0·89	0·86
Effective charge e^{*}	0	0	0·2	0·65	0·66

Born's two-force constant model appears to be reasonably applicable to mercury telluride. The three force constant model which brings into consideration a central force between next nearest neighbours is also tested for mercury telluride. This model was originally developed by Nagendra Nath (1934) and later by Smith (1948) and gives

$$8A(A + 8C_{11} - 16C_{44})/(3A - 8C_{11} + 16C_{12}) = 1 \tag{4.22}$$

Here $A = \omega^2 M/a_0$, M is the average atomic mass and ω is the angular frequency of the principle optical absorption. Although this equation holds for germanium to 6% and for silicon to 12% but for mercury telluride it gives an imaginary answer. Herman (1959) has extended the argument, to fit the results, out to fifteen independent force constants. Even for the simple covalent semiconductors, the above procedures do not lead to satisfactory agreement between theory and experiment. In all the theories, the atomic polarisation is neglected and, therefore results hold better for covalent materials than for the mixed, covalent-ionic compounds. For the two-force constant model, deviation from unity may be used to indicate the extent of the covalent character of a compound. However, this is better considered from the viewpoint of ionicity, to which we now turn.

4.4.2. Ionicity of mercury telluride

The fundamental lattice absorption (restrahlen) frequency represents the frequency at which the rigid Bravais lattices vibrate relatively each other. For zinc-blende lattices the two Bravais lattices are face-centred cubic. Interatomic repulsive forces largely determine the optical absorption frequency and the compressibility, which are then related by the Szigeti (1950) relation, based on a dipolar term in the Lorentz force approximation. This equation forms a useful link between elastic and optical properties and is

$$B = \frac{r_o^2}{3U} \; \frac{p + 2}{p_\infty^2 + 2} \; \bar{m} \; \omega_r^2 \tag{4.23}$$

Here U is the volume occupied by an ion pair. For zinc-blende lattices U is $a_o^3/4$. r_o is the nearest neighbour distance. p and p_∞ are the static and high frequency (optical) dielectric constants respectively. $\bar{m}$ is the reduced mass which for compounds is

$$\frac{1}{\bar{m}} = \frac{1}{m_1} + \frac{1}{m_2} + \frac{1}{m_3} + \cdots \tag{4.24}$$

For mercury telluride m_1 and m_2 are the masses of the mercury and tellurium atoms respectively. In terms of atomic weights, $\bar{m}$ can be expressed in the following form

$$\bar{m} = m_{Te} \cdot m_{Hg} / [(m_{Te} + m_{Hg})N] \tag{4.25}$$

Here N is the Avogadro's number. The reduced mass of mercury telluride turns out to be $1 \cdot 2945 \times 10^{-22}$ gm. From the measurements of the restrahlen reflection of mercury telluride by Dickey and Mavroides (1964) (see Appendix A), the static (p) and optical (p_∞) dielectric constants are 20 and 14 respectively. Taking the bulk modulus as $4 \cdot 67 \times 10^{11}$ dyn/cm^2 (see Table 4.1), $\bar{m}\,\omega_r^{\,2}$ turns out to be $8 \cdot 8 \times 10^4$ cgs units and $\nu_r (= \omega_r / 2\pi)$ is $(4 \cdot 1 \pm 0 \cdot 1) \times 10^{12}$ Hz. This is in reasonable agreement with the result obtained from optical reflectivity by Dickey and Mavroides ($3 \cdot 45 \times 10^{12}$ Hz).

The effective charge e^* is related to the change of dielectric constants on passing through the restrahlen band by the Szigeti (1949) relation

$$p - p_\infty = \frac{16\pi (p_\infty + 2)^2}{9\bar{m}\,\omega_r^{\,2} a_o^{\,3}} (se^*)^2 \tag{4.26}$$

Introducing the necessary data, the ionicity of mercury telluride is obtained as $(se^*) = 0 \cdot 65e$. s is a short-range factor and in the Lorentz approximation is equal to unity. Should the charge distribution around the ions not be spherical, or non-electrostatic, short range-forces distort the ions, or there be displacement, then s is not unity. However, for a variety of cubic materials s seems to be $0 \cdot 9 \pm 0 \cdot 2$

[Szigeti, Table 1, p.163, 1949]. Thus, recognizing both these effects of distortion and experimental error, e^* is assessed as $(0{\cdot}65 \pm 0{\cdot}05)e$.

In heteropolar, tetrahedrally-bonded compounds the molecular wave-functions Ψ are formed by overlap of sp^3 tetrahedral, hybrid orbitals ϕ on nearest neighbour atoms (Coulson et al. 1962).

$$\Psi = \phi_a + \lambda\phi_b \quad \text{(Bonding orbital)} \tag{4.27}$$

$$= \lambda\phi_a - \phi_b \quad \text{(Antibonding orbital)} \tag{4·28}$$

where λ is a parameter, describing the polarity of the bond. The bonding orbital Ψ corresponds to fractions of electrons $1/(1+\lambda^2)$ on the hexavalent atom (A) and $\lambda^2/(1+\lambda^2)$ on the bivalent atom (B). The net charge, measured in electrons, associated with the atom A is for a compound $A^N B^{8-N}$

$$e^* = \frac{N\lambda^2 - (8-N)}{1+\lambda^2} \tag{4.29}$$

or $(6\lambda^2 - 2)/(1+\lambda^2)$ for a II-VI compound where N is 6. When $e^* = 0{\cdot}65e$, λ becomes $0{\cdot}7$: any valence electron remains on a mercury atom about 30 per cent of the time. This result compares with those of other zinc-blende structure materials. Other direct comparison between the elastic constants of these materials with mercury telluride will now be discussed.

4.4.3. Comparison of the elastic constants of compounds.

Keyes (1962) showed that the reduced elastic constants

$$c^*_{ij} = c_{ij}/c_o \tag{4.30}$$

of the $\bar{4}3m$ compounds and diamond structure elements fall within a few percent of the same value for each group of materials. To reduce the elastic constants, he defined a constant

$$C_o = e^2/r_o^4 \qquad (4.31)$$

which is $0{\cdot}376 \times 10^{12}$ dyn/cm^2 for mercury telluride. The reduced adiabatic elastic constants and the bulk and shear moduli of mercury telluride are:

$$C^*_{11} = C_{11}/C_o = 1{\cdot}43$$

$$C^*_{12} = C_{12}/C_o = 0{\cdot}993$$

$$C^*_{44} = C_{44}/C_o = 0{\cdot}555$$

$$B^* = (C_{11} + 2C_{12})/3C_o = 1{\cdot}139$$

and

$$C^*_s = (C_{11}-C_{12})/2C_o = 0{\cdot}219$$

Keyes' method has been extended over a whole range of IV group elements, III-V, II-VI and I-VII compounds. Results are shown in Table (4.4). $a_o/2$ has been used as the nearest neighbour distance (r_o) for I-VII compounds (sodium chloride crystal structure). It may be concluded that the reduced parameters of I-VII compounds as well as the $\bar{4}3m$ compounds and the diamond structure elements fall within a few percent of the same value for each material group. Mercury telluride shows no anomalous elastic behaviour. Thus this table may be used to provide an approximate estimate of the elastic constants for unmeasured substances if their lattice spacing is known. Averaged values of the reduced quantities was also tabulated in

TABLE (4.4) Reduced elastic constants and the sheer and bulk moduli of IV group elements, III-V, II-VI and I-VII compounds

Material	Ref. 1*	a_o Å	C_o X10^{11} dyn/cm^2	C^*_{11}	C^*_{12}	C^*_{44}	C^*_s	B^*
Diamond	a	3·57	40·52	2·65	0·308	1·42	1·17	1·09
Ge	b	5·66	6·39	2·02	0·756	1·05	0·63	1·18
Si	b	5·43	7·55	2·19	0·877	1·05	0·67	1·30
GaAs	c	5·65	6·41	1·85	0·840	0·925	0·503	1·17
lnAs	c	6·06	4·86	1·71	0·930	0·814	0·391	1·19
GaSb	c	6·09	4·74	1·87	0·853	0·910	0·506	1·19
AlSb	c	6·14	4·63	1·93	0·952	0·895	0·488	1·28
lnSb	c	6·48	3·72	1·79	0·981	0·812	0·376	1·27
ZnS	d	5·41	7·64	1·41	0·945	0·539	0·234	1·10
ZnSe	e	5·67	6·35	1·27	0·768	0·694	0·253	0·937
ZnTe	e	6·10	4·74	1·50	0·858	0·658	0·323	1·074
CdTe	f	6·48	3·73	1·43	0·987	0·535	0·224	1·137
HgTe	g	6·46	3·76	1·43	0·993	0·555	0·219	1·139
LiF	1	4·03	14·00	0·80	0·34	0·45	0·23	0·47
LiCl	1	5·14	5·27	0·93	0·42	0·47	0·25	0·56
LiBr	1	5·50	4·02	0·98	0·46	0·47	0·25	0·59
LiJ	1	6·00	2·84	1·00	0·49	0·47	0·25	0·60
NaF	1	4·63	7·99	1·21	0·30	0·35	0·45	0·58
NaCl	1	5·64	3·64	1·34	0·33	0·35	0·50	0·66
NaBr	1	5·98	2·84	1·41	0·40	0·34	0·50	0·70
NaJ	1	6·47	2·95	1·03	0·30	0·24	0·36	0·51

Table (4.5) which indicates that averaged values of the reduced quantities decrease in the sequence

IV ⟶ III - V ⟶ II - VI ⟶ I - VII

This gradual decrease of the reduced quantities suggests that the amount of ionic bond is responsible for this behaviour.

[1*] References for elastic constants in Table (4.4)

a. McSkimin and Bond (1957)
b. McSkimin (1953)
c. Drabble (1966, p.112)
d. Zarembovitch (1963)
e. Berlincourt, Jaffe and Shiozawa (1963)
f. McSkimin and Thomas (1962)
g. Present work
l. Anderson (1965, Appendix 1)

TABLE (4.5) Averaged values of reduced parameters of IV group elements and III-V, III-VI and I-VII compounds

Reduced parameters	IV [1≠]	III-V	II-VI	I-VII
C^*_{11}	2·10	1·83	1·40	0·92
C^*_{12}	0·80	0·91	0·91	0·38
C^*_{44}	1·05	0·87	0·60	0·30
$[(C_{11}-C_{12})/2]^*$	0·65	0·45	0·25	0·34
$[(C_{11}+2C_{12})/3]^*$	1·24	1·22	1·08	0·58

[1≠] in average diamond is omitted.

4.4.4. Polycrystalline elastic modulus and anisotropy of mercury telluride.

The averaged polycrystalline bulk and sheer modulus are useful parameters to describe solids. In terms of single crystalline elastic modulus, in Voigt's and Reuss' approximation, for cubic material, they are given by

$$K_V = \frac{C_{11} + 2C_{12}}{3}$$

$$K_R = K_V$$

and

$$G_V = \frac{C_{11} - C_{12}}{5} + \frac{3C_{44}}{5} \tag{4.32}$$

$$G_R = \frac{5(C_{11} - C_{12})C_{44}}{3(C_{11} - C_{12})+4C_{44}}$$

By comparing these relations with experimentally measured polycrystalline bulk and sheer moduli, it appears that the true values of K and G lie between two theoretical extremes

$$K_R < K < K_V$$
$$G_R < G < G_V \tag{4.33}$$

Hence Hill (1952) suggests using the following values

$$K_H = \frac{1}{2}(K_R + K_V)$$
$$G_H = \frac{1}{2}(G_R + G_V) \tag{4.34}$$

In this type of approximation the accuracy very much depends upon the degree of anisotropy. Following Hill the degree of anisotropy δ is (Anderson 1963)

$$\delta = \frac{1}{2}\,\frac{G_V - G_R}{G_H} = \frac{G_V - G_R}{G_V + G_R} \qquad (4.35)$$

or in terms of elastic constants for cubic materials

$$\delta \text{ (per cent)} = 100\,\frac{3[2C_{44}-(C_{11}-C_{12})]^2}{12C_{44}^{2}+38C_{44}(C_{11}-C_{12})+3(C_{11}+C_{12})^2} \qquad (4.36)$$

The usual anisotropy factor A defined by the ratio of two shear constants

$$A = 2C_{44}/(C_{11}-C_{12}) \qquad (4.37)$$

is still a useful parameter. However, it is ambiguous in that any departure from unity is said to correspond to the degree of elastic anisotropy. δ is more convenient and practical than A. Chung and Buessem (1967) obtained the following relation between δ and A

$$\delta \text{ (per cent)} = 100\,\frac{3(A-1)^2}{3(A-1)^2+25A} \qquad (4.38)$$

δ is zero for isotropic crystals; for an anisotropic material δ is a single-valued measure of the elastic anisotropy regardless of whether $A < 1$ or $A > 1$. δ allows comparison of materials.

The averaged polycrystalline elastic parameters and anisotropy factor of annealed mercury telluride at 4·2°K are:

$K_V = K_R = 4{\cdot}67 \times 10^{11}$ dyn/cm^2

$G_V = 1{\cdot}67 \times 10^{11}$ dyn/cm^2

$G_R = 1{\cdot}38 \times 10^{11}$ dyn/cm^2

$K_H = 4{\cdot}67 \times 10^{11}$ dyn/cm^2

$G_H = 1{\cdot}53 \times 10^{11}$ dyn/cm^2

$A = 2{\cdot}51$

and

$\delta = 9{\cdot}8\%$

In Figure (4.5) the degree of anisotropy of some of the diamond and zinc blende materials are shown. The anisotropy factor (δ) increases through the sequence of group IV elements, III-V and II-VI compounds. In the II-VI compounds zinc selenide and telluride show slightly anomalous behaviour. But the anisotropy of mercury telluride resembles that of other II-VI compounds.

4.4.5. The Debye temperature of mercury telluride

The Debye theory of specific heat has proved very useful because it is a single-parameter theory which describes the experimental observations remarkably well. The Debye temperature θ can be calculated from the sound velocities as well as from the specific heat. However, the theoretical model of Debye assumes the solid to be an elastic continuum in which all the sound waves travel at the same velocity independent of their wavelength; there is no dispersion. Such a model is satisfactory

FIGURE (4.5). Graphical representation of the elastic anisotropy in cubic crystals.

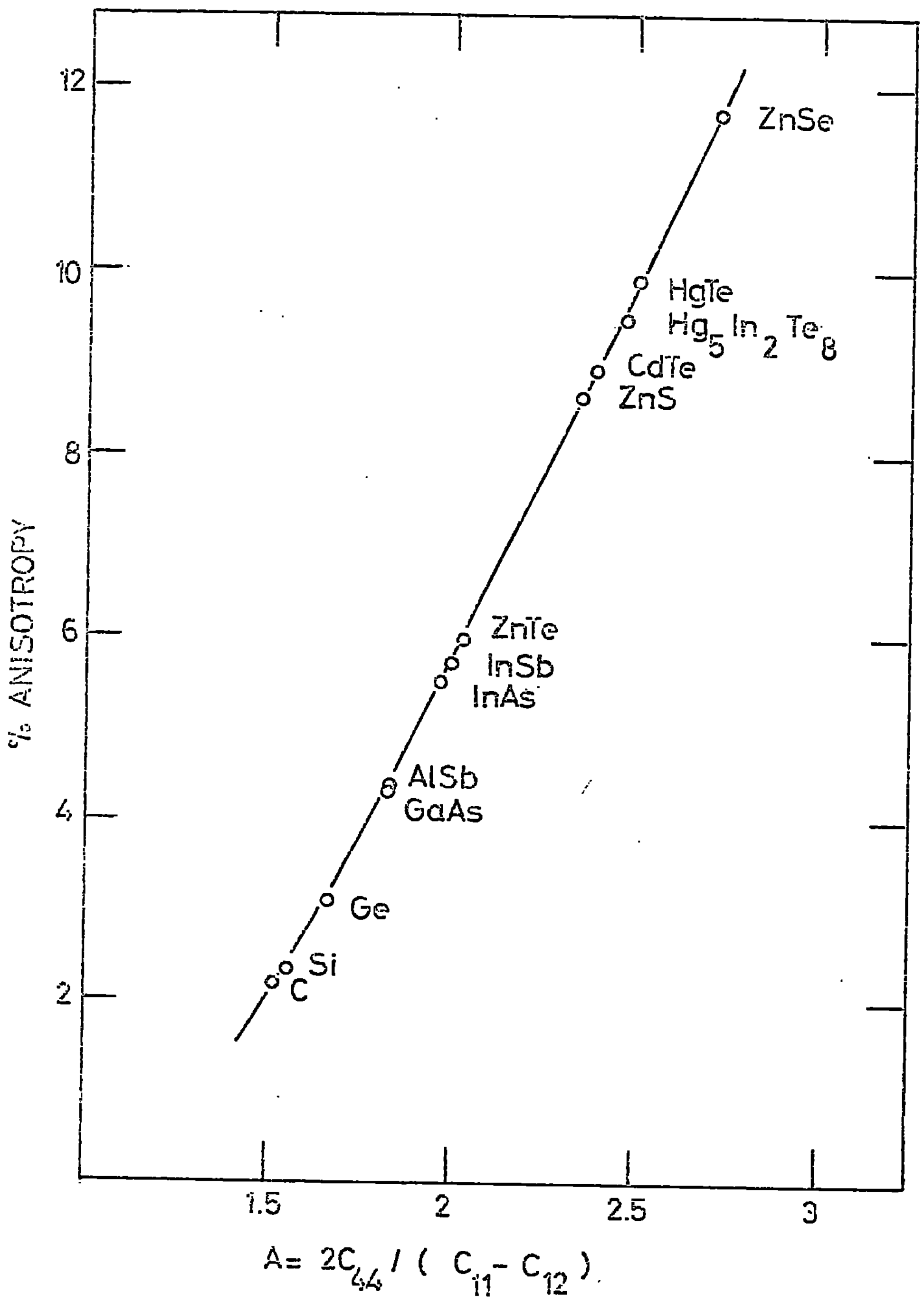

only in the limit of long wavelength or low temperatures.

In the Debye model the number of identical frequencies does not exceed the 3N degrees of freedom available to N discrete mass points. Thus,

$$\int_0^{\nu_m} N(\nu)d\nu = 3N = \frac{4}{3}\pi V\nu_m^3 \int\left(\frac{1}{v_1^3}+\frac{1}{v_2^3}+\frac{1}{v_3^3}\right)\frac{d\Omega}{4\pi} \qquad (4\cdot39)$$

Here $d\Omega$ is the element of solid angle, ν_m is a parameter specifying the highest frequency possible in a system with a finite number of particles (the cut off frequency). The Debye temperature θ in terms of frequency is defined as $\frac{h}{k}\nu_m$, inserting ν_m from Equation (4.39)

$$\theta_D = \frac{h}{k}\left(\frac{9}{4\pi}\frac{N}{V}\right)^{1/3}\left\{\int\left(\frac{1}{v_1^3}+\frac{1}{v_2^3}+\frac{1}{v_3^3}\right)\frac{d\Omega}{4\pi}\right\}^{-1/3} \qquad (4.40)$$

here h and k are the Planck's and Baltzmann's constants respectively, $\frac{N}{V}$ is the volume occupied per atom, which is $8/a_0^3$ for zincblende and diamond lattices. The calculation of θ from sound velocities or elastic constants involves the solution of the last term on the right hand side which leads to a single velocity called the average velocity of solid (v_m):

$$3^{1/3}\left\{\int\left(\frac{1}{v_1^3}+\frac{1}{v_2^3}+\frac{1}{v_3^3}\right)\frac{d\Omega}{4\pi}\right\}^{-1/3} = v_m \qquad (4.41)$$

For diamond and zincblende lattices the average Debye velocity may be obtained from Equations (4.40) and (4.41) as

$$v_m = 1\cdot6795 \times 10^{10}\cdot\theta\cdot a_0 \qquad (4.42)$$

The evaluation of the surface integral of Equation (4.40) involves solution of the secular equation (Equation 4.10)

$$\left| C_{ijkl}\, n_k\, n_j - \rho v^2 \right| = 0 \qquad (4.43)$$

by subdividing the surface into triangles defined by direction cosines. In cubic materials, because of the high symmetry, it is sufficient to consider only direction cosines confined to 1/48 of the sphere, i.e., those directions bounded by the triangle formed by the [100], [110], and [111] crystallographic directions. Subdividing this sphere into equal areas and from the determined direction cosines for this subdivision, secular equations can be solved for these points. After each integrand has been multiplied by its associated area element $d\Omega$ and summed, the integration is complete and the value of θ determined. The accuracy of this method can be made as high as required by subdividing the areas more finely. Even for very highly anisotropic cubic materials θ can be obtained to better that 0·1% by subdividing just 1/16 of the sphere into only twenty areas.

Other than numerical integration, there are indirect methods in which, tables or graphs of the value of the integral as a function of certain ratios of the elastic moduli have been prepared using computers. Also, several series of expansions of the integral have been worked out; these methods are detailed in a review by Alers (1965).

In the present work the Debye temperature of mercury telluride has been calculated by several methods from the low temperature elastic constants extrapolated to $0^{\circ}K$. The values for different methods are listed below.

1.	de Launay's method	$141{\cdot}07^{\circ}K$
2.	Marcuss' and Kennedy's method	$141{\cdot}20^{\circ}K$
3.	Leibfried's method	$141{\cdot}48^{\circ}K$
4.	Anderson's method	$142{\cdot}40^{\circ}K$

Now we can compare this Debye temperature for mercury telluride with that of related materials. Steigmeier (1963), using Keyes' observations, found a method to estimate the unknown Debye temperature θ of III-V compounds from just the parameters mass and lattice spacing. To establish this method, he rewrote a relationship derived by Marcuss and Kennedy (1959) in the following form

$$\theta_D(0) = \frac{4{\cdot}19 \times 10^{-8}}{\left(a_o^3 M\right)^{\frac{1}{2}}} Y \qquad (4.44)$$

Here M is the mean atomic weight and the quantity Y is defined by the relation

$$Y = \left(\frac{C_{11}}{C_o}\right)^{\frac{1}{2}} f\,(r_1,r_2) \qquad (4.45)$$

We now extend this procedure to other II-VI and I-VII compounds and the IV group elements. In Table (4.6) the calculated Y values from Equation (4.44) are tabulated. For this calculation the quantities of $f(r_1,r_2)$ have been deduced from Marcuss' graphs. Figure (4.6) gives a plot of Y against the lattice spacing. The variation of Y is very small within a given group. The solid lines in this figure can be used to estimate the Debye temperatures through Equation (4.44).

Mercury telluride fits well into the scheme.

TABLE (4.6) Mean atomic weight (M), Y values for Steigmeier's method and Debye temperatures of IV group elements and III-V, II-VI and I-VII compounds.

Materials	M	G	θ (°K)
Ge	72·60	1·01	370
Si	28·09	1·03	648
GaAs	72·31	0·94	344
lnAs	94·91	0·87	250
GaSb	95·75	9·93	266
AlSb	74·45	0·92	295
lnSb	118·40	0·87	206
ZnS	48·72	0·73	346
ZnSe	72·17	0·75	273
ZnTe	96·49	0·77	220
CdTe	120·00	0·69	158
HgTe	164·10	0·71	141
LiF	12·97	0·51	735
NaI	74·94	0·56	165
LiCl	21·19	0·50	390
LiBr	43·42	0·50	247
LiI	66·92	0·50	175
NaCl	29·22	0·52	303

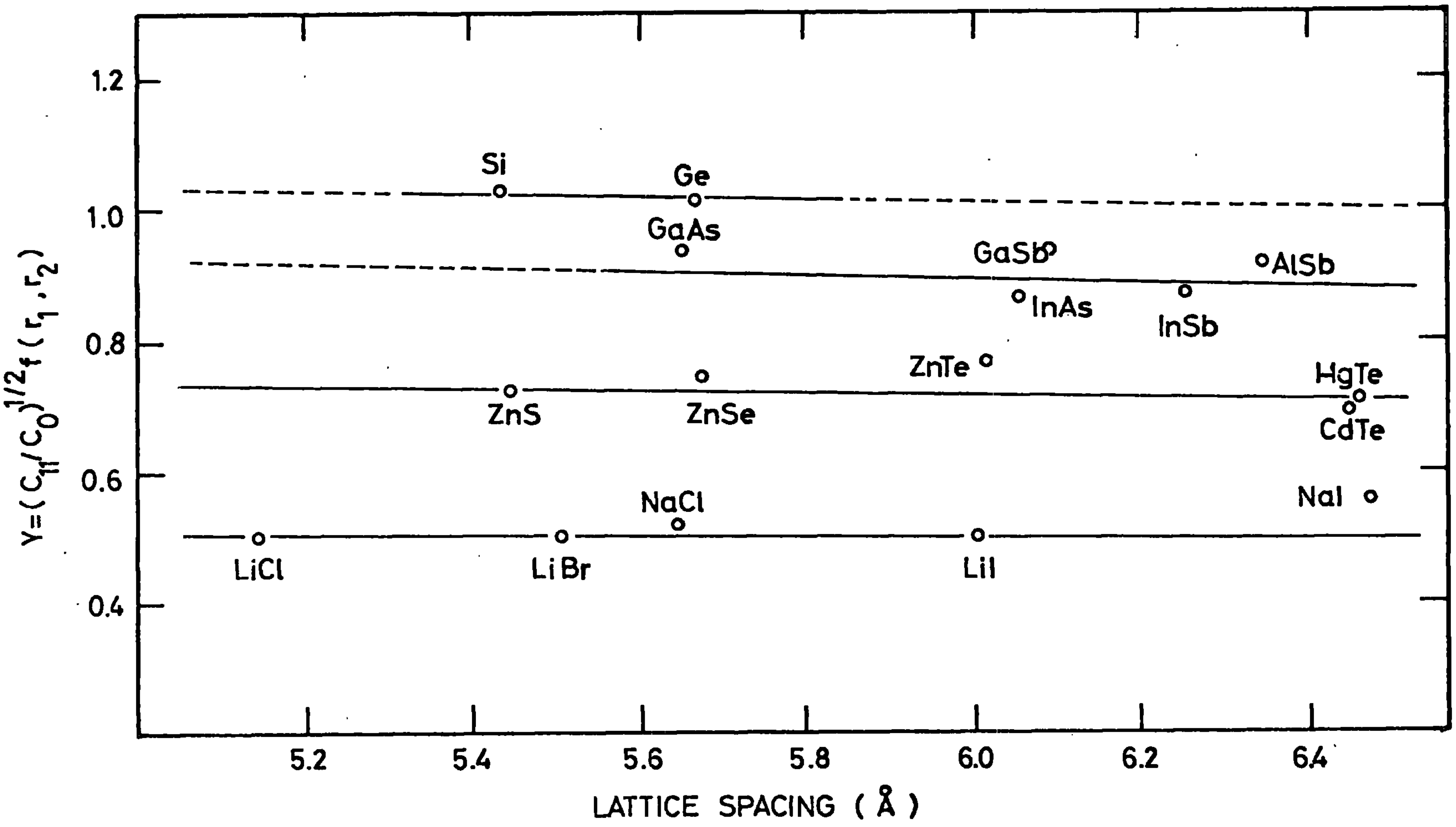

FIGURE (4.6). The parameter Y giving the Debye temperature of group IV elemental semiconductors and III-V, II-VI and I-VII compounds.

The elastic constants agree with result found from theories of the crystalline interatomic forces. When compared with those of other II-VI, III-V and I-VII compounds and IV group elements, the elastic properties of mercury telluride correspond closely to those of cubic zinc sulphide and exhibit no anomalous behaviour. It has been shown that, mercury telluride like other of those II-VI compounds form a link between the semiconducting elements of fourth column of the periodic table and the I-VII compounds. From the Szigeti relationship, the ionicity e^* is estimated as 0·65e ± 0·05e and the restrahlen frequency as $(4{\cdot}1 \pm 0{\cdot}1) \times 10^{12}$ Hz. The Debye temperature, calculated from the elastic constant data, is $141^{\circ}K \pm 4^{\circ}K$, which is the lowest among the related materials, thus mercury telluride might be expected to show some interesting ultrasonic properties.

Now the anelastic properties of mercury telluride will be investigated through the sound attenuation measurements.

CHAPTER 5

ULTRASOUND ATTENUATION IN MERCURY TELLURIDE: RESULTS.

5.1. INTRODUCTION TO THE RESULTS

Different ultrasonic energy dissipation mechanisms in solids can contribute, simultaneously to the measured attenuation. In general, each energy loss mechanism is due to a relaxation phenomenon, which has a characteristic relaxation time (see Section 1.1). Relaxation times encountered in solids are mainly temperature dependent. Thus, the ultrasonic wave attenuation measurements as a function of temperature can facilitate separation of the different contributions. In addition to temperature dependence of attenuation measurements, frequency and stress dependent measurements help to complete the knowledge of energy loss mechanisms. During the present work, the attenuation of longitudinal and shear ultrasonic waves has been measured in the wide temperature range 1·4°K to 400°K and in the frequency range between 10 MHz to 300 MHz along the three major crystallographic directions, namely [100], [111] and [110]. Now examples of the temperature, frequency and applied stress dependent ultrasonic wave attenuation in mercury telluride will be given, firstly the general features of the temperature dependence.

The temperature dependence of ultrasonic wave attenuation in single crystals of mercury telluride exhibits some characteristic features in certain temperature regions and may best be considered in three ranges: the low temperature region (1·4°K to about 70°K), an intermediate temperature region (about 70°K to 180°K) and the high temperature region (above 180°K). Now to give some examples of these characteristic features.

5.2 THE TEMPERATURE DEPENDENCE OF ATTENUATION

Firstly the general temperature spectrum of ultrasonic wave attenuation is illustrated in Figure (5.1) the general features of longitudinal wave attenuation along the [100] crystallographic direction over the whole temperature region (4·2°K to 388°K) are shown. The specimen used in these measurements is not annealed and is grown from stoichiometric melts in a smaller bore crucible (see p. 12). The measurements have been made with a 10 mm diameter, X-cut quartz transducer whose fundamental frequency is 10 MHz. Starting from the low temperature side, the features of the attenuation are as follows: the measurements at 10 MHz and 50 MHz have been made down to 4·2°K and the 70 MHz measurements to 22°K. The behaviour of the attenuation in low temperature region can be seen on the 50 MHz and partially on the 70 MHz measurements; it decreases sharply below about 40°K. As seen on the 50 MHz measurements this sharp decrease ends at about 20°K and below this the attenuation is almost temperature independent. These features are barely discernible in the 10 MHz measurements. The ultrasound attenuation for temperatures higher than 50°K decreases slightly with increasing temperature until about 80°K.

As seen from these four sets of measurements in this figure, in the intermediate temperature region (80°K to about 170°K) the attenuation of ultrasonic waves is almost temperature independent.

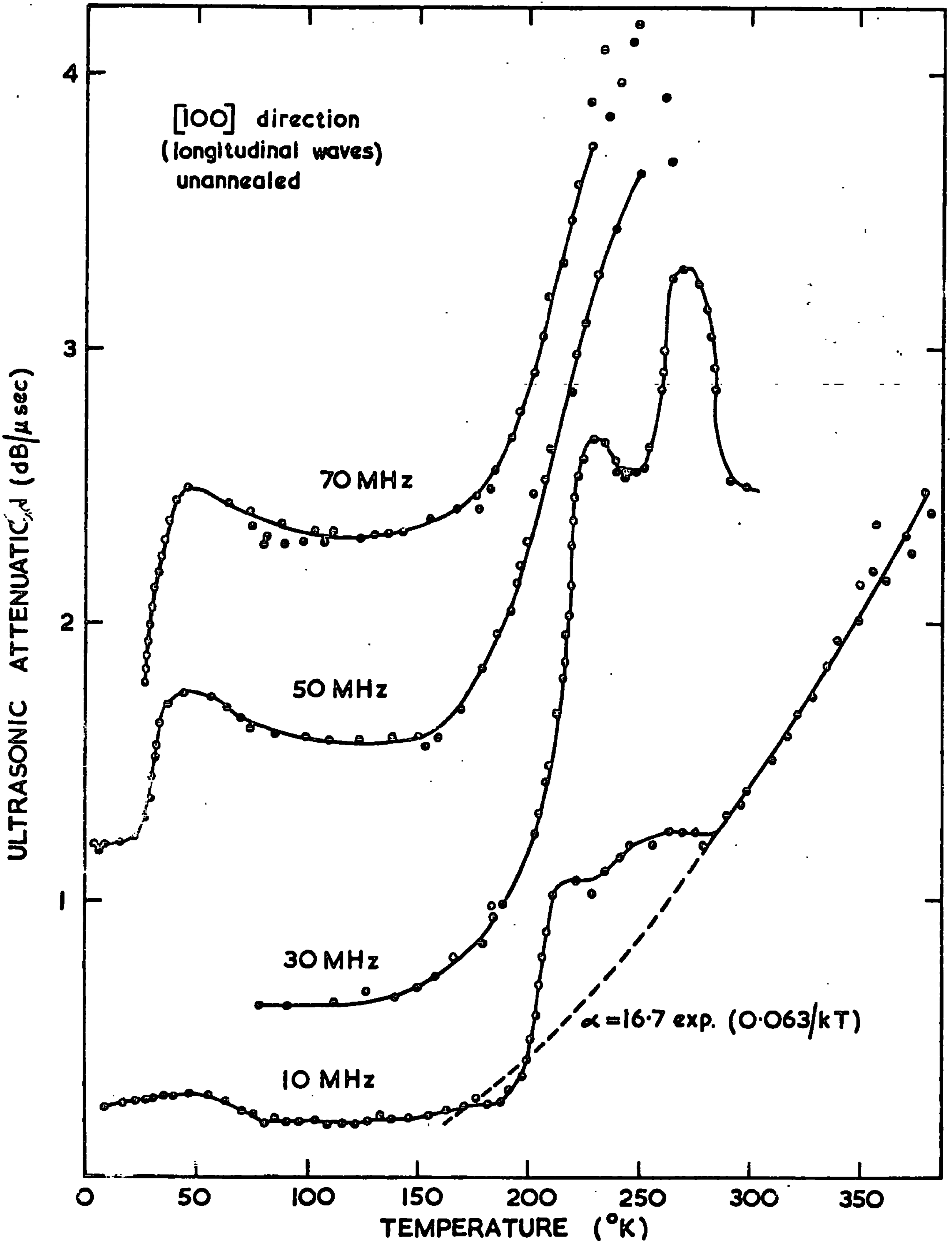

FIGURE (5.1). The temperature dependence of attenuation in an as-grown HgTe single crystal.

In the high temperature region (above 180°K) the temperature dependence of attenuation exhibits peaks superimposed on the background attenuation which increases with increasing temperature. In the 30 MHz and 10 MHz measurements, two peaks are observed. These two peaks are very distinct at 30 MHz while at 10 MHz they are close to each other. The background attenuation reaches 4 dB/μsec at about 250°K at 50 MHz and 70 MHz. This is the maximum attenuation measurable in the equipment used. Thus at 50 MHz and 70 MHz peaks cannot be looked for. To check whether the background attenuation increases monotonically with temperature or is the low temperature side of a very broad peak, attenuation measurements at 10 MHz in this specimen have been extended above room temperatures. For these measurements an oil bath with thermostatically controlled temperature ($\pm 0{\cdot}5^{\circ}$C) has been used. The attenuation does increase monotonically with temperature up to 388°K, the limit of the oil bath. The temperature dependence of the background attenuation can be formulated as

$$\alpha = 16{\cdot}7 \exp (0{\cdot}063/kT)$$

where kT is the thermal energy.

Another example of the temperature dependence of ultrasonic wave attenuation from $1{\cdot}8^{\circ}$K to about 250°K is illustrated in Figure (5.2). Two sets of measurements are shown for longitudinal waves along the [110] direction and shear waves along the [111] direction. The longitudinal wave frequency is 70 MHz. This measurement has been made on the annealed specimen with a 6 mm diameter, fundamental frequency 10 MHz, X-cut quartz

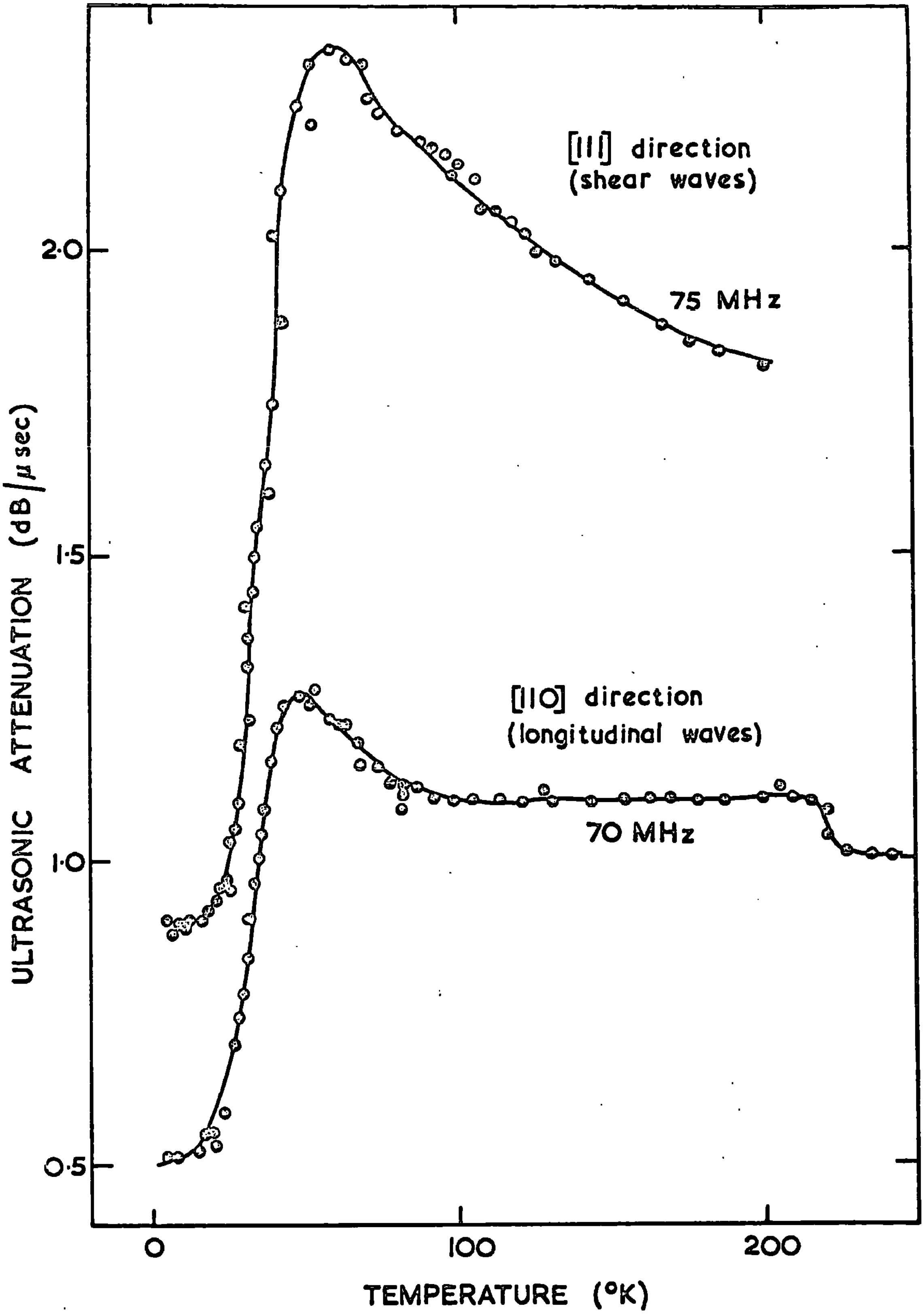

FIGURE (5.2). The attenuation of longitudinal and shear waves in HgTe at low and intermediate temperatures.

transducer. The general features of the temperature dependence of ultrasonic wave attenuation are as follow. Attenuation is temperature independent till about 20°K; then it increases sharply between 20°K and about 50°K. A decrease inversely proportional to temperature is then observed until the attenuation becomes almost temperature independent at about 90°K. For temperatures higher than 200°K the attenuation reaches the region of the peaks. Thus the general low and intermediate temperature characteristics of temperature dependent ultrasound attenuation in this specimen are very similar to those illustrated in Figure (5.1).

The features of shear wave attenuation along the [111] direction in the low and the intermediate temperature region (1·8°K to 200°K) are also illustrated in Figure (5.2). This specimen is unannealed. The experiment has been performed with a 10 mm diameter, 15 MHz fundamental frequency, Y-cut quartz transducer. The low temperature characteristics of shear ultrasonic wave attenuation in this specimen are also given, later in Figure (5.5). The low temperature characteristics are very similar to those illustrated in previous figures. The behaviour of shear wave attenuation in the intermediate temperature region in this specimen and propagation direction is not quite similar to those of longitudinal ultrasonic wave attenuation along [110] and [100] directions given in this and the previous figure (Figures 5.1 and 5.2). The characteristic feature of shear wave attenuation in the intermediate temperature region is that it decreases smoothly with increasing temperature.

The observations given in these two figures can be summarised as follows. The temperature dependence of ultrasound attenuation in single crystal mercury telluride exhibits three characteristic features in different temperature regions: a sharp rise between about 20°K and 40°K followed by a decrease continuing until about 80°K, then a temperature independent region (except for shear waves along the [111] direction) followed by peaks at temperatures higher than 200°K. These features have been observed in all the samples studied. Now other specific examples will be given. First the low temperature region will be discussed.

The temperature dependence of longitudinal wave attenuation along the [100] and [111] crystallographic axis below 77°K on unannealed specimens is shown in Figure (5.3). In all these measurements, 10 mm diameter, fundamental frequency 10 MHz, X-cut quartz transducers have been employed. The measurements belonging to the [100] direction have been transferred from Figure (5.1). All of these measurements have the same characteristic features. The attenuation below about 20°K is almost temperature independent and is assumed to be not intrinsic and is called the residual attenuation. In many cases a small, barely measurable rise has been observed below about 10°K. This could be due to an electronic interaction as found in Metals (Morse 1959). But this effect is so small that it has not yet been followed up. The attenuation increases sharply above 20°K as about the third or fourth power of temperature. This sharp rise ends at about 35°K and is followed by a smooth decrease. The effect of frequency on this effect can also be seen from the measurements made along the [111] direction at 30 MHz and 50 MHz. The effect is enhanced at higher frequencies.

FIGURE (5.3). The temperature dependence of ultrasonic attenuation in as-grown HgTe at low temperatures.

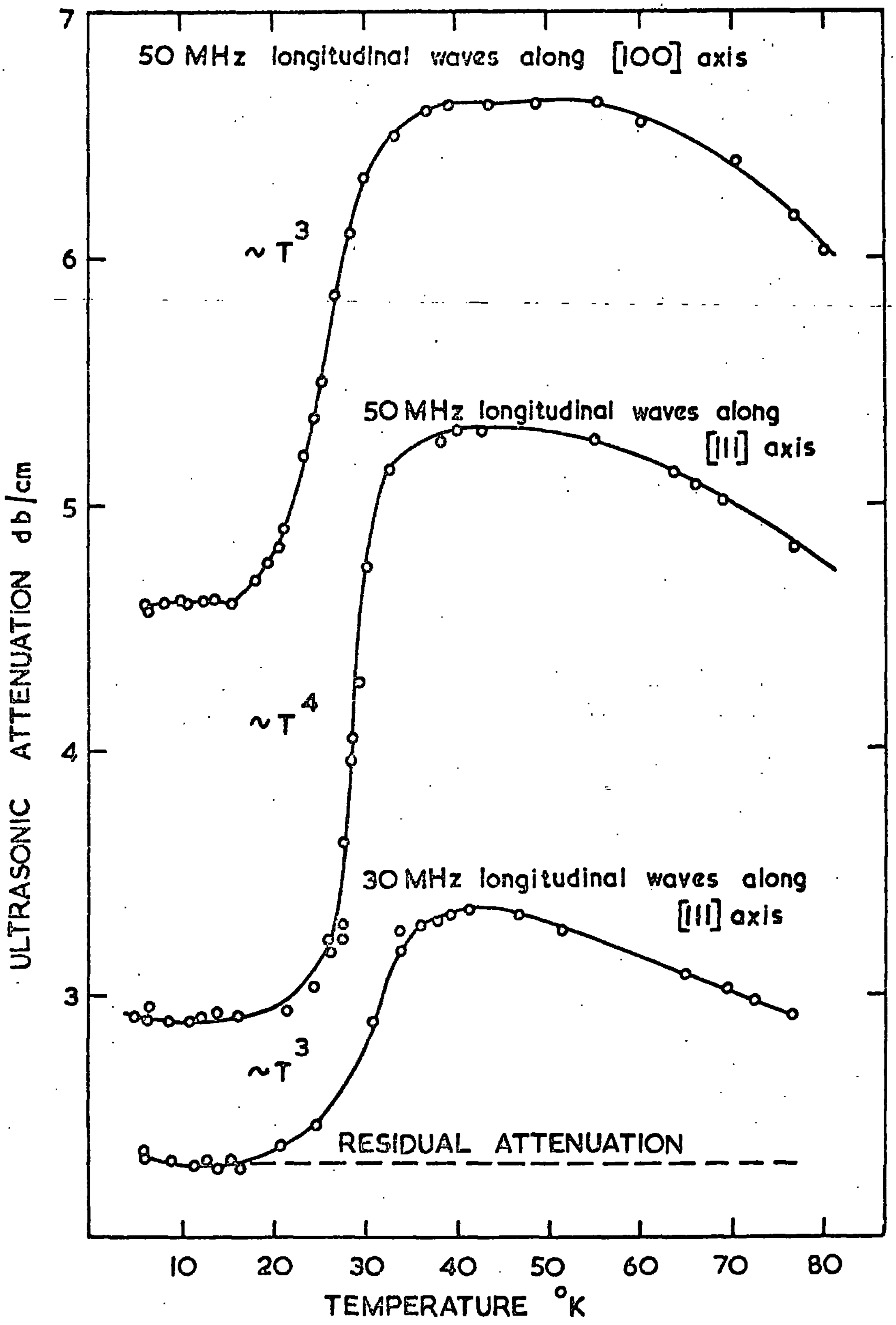

The temperature dependence of longitudinal wave attenuation along the [110] direction on an annealed specimen is shown in Figure (5.4). Here a 6 mm diameter, 10 MHz fundamental frequency, X-cut quartz transducer has been used. The general features are closely similar to those given in the previous figures. Again attenuation is almost temperature independent below 20°K (the residual attenuation) and then increases very sharply up to about 45°K followed by a smooth decrease with a slope of almost T^{-1}. Here again the enhanced effect at higher frequencies is shown.

Shear wave attenuation shows the same effect. Figure (5.5) gives the temperature dependence of shear wave attenuation along the [111] crystallographic direction on an unannealed specimen. Here a 10 mm diameter, 15 MHz fundamental frequency, Y-cut quartz transducer has been used. Again three distinct attenuation characteristics in the low temperature region are observed: the almost temperature independent attenuation below 25°K and then a sharp increase to a "peak type" maximum in this case at about 60°K, followed by a smooth decrease. The extension to the intermediate temperature region has been presented already in Figure (5.2). Except for the peak-type maximum, the general features for shear wave attenuation along the [111] direction in the low temperature region are very similar to those for the longitudinal waves given in previous figures. Now we turn to detail the temperature dependence of attenuation in the high temperature region.

The temperature dependence of longitudinal ultrasonic wave attenuation along the [111] direction in the temperature range 180°K to 300°K is shown

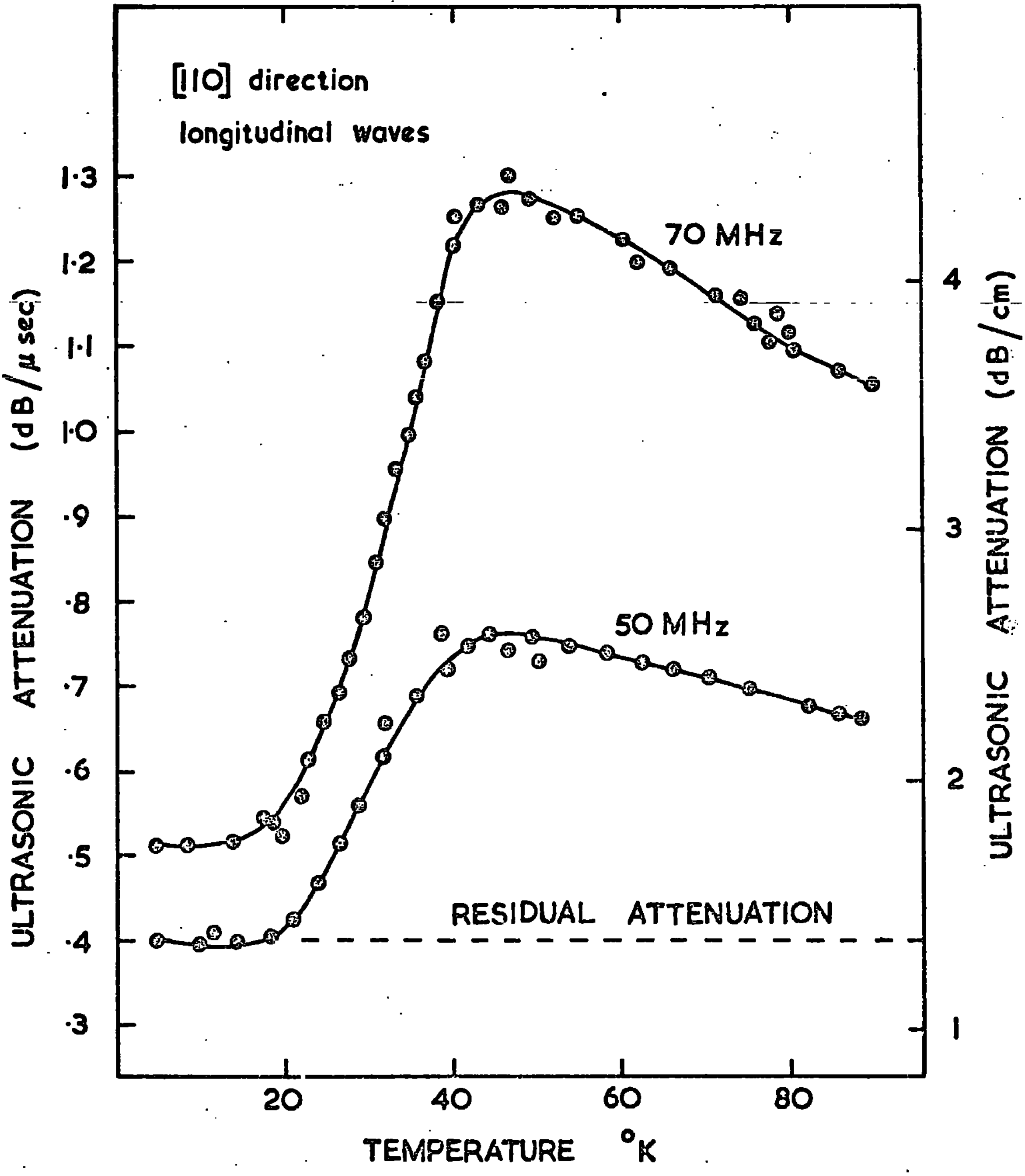

FIGURE (5.4). The temperature dependence of ultrasonic attenuation in annealed HgTe.

FIGURE (5.5). The temperature dependence of shear wave attenuation in as-grown HgTe at low temperatures.

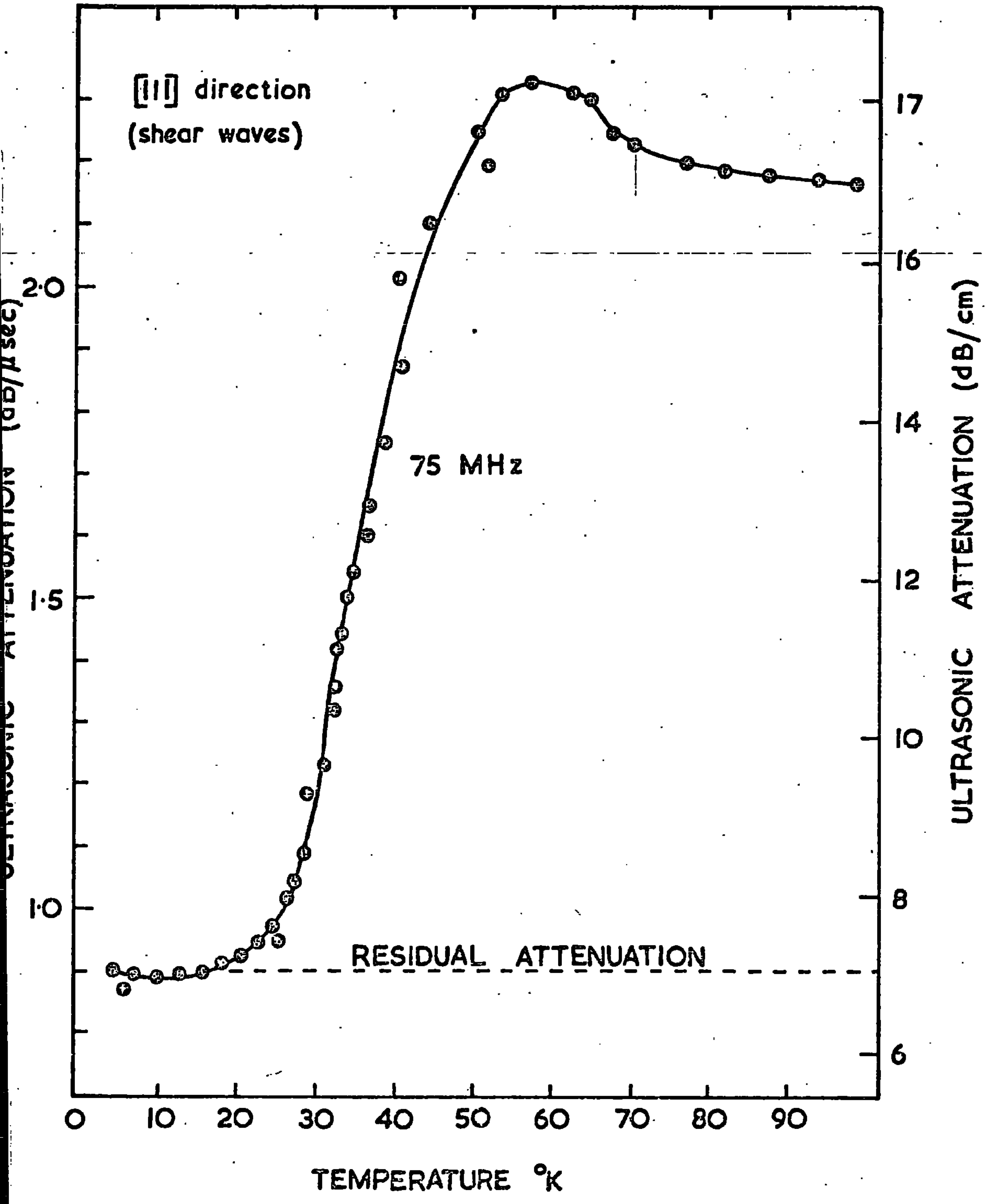

in Figure (5.6). In these measurements 10 mm. diameter X-cut quartz transducers have been used. The fundamental frequencies of the transducers for the 12 MHz and 36 MHz measurements is 12 MHz and for the 40 MHz and 56 MHz measurements is 8 MHz. Here each measurement exhibits peaks, whose magnitude increases with increasing frequency. Another interesting feature is that the temperature at which the maximum takes place increases with increasing frequency. These peaks are quite similar to those obtained along the [100] direction (Figure 5.1) except that they are not split and are not superimposed on an exponential background attenuation.

In Figure (5.7) the temperature dependent attenuation of shear waves along the [110] direction between 150°K to 240°K is shown. The polarisation of the shear waves is along the $[1\bar{1}0]$ direction. The ultrasonic wave frequency used in both measurements is 10 MHz. The general behaviour of the two sets of measurements 'A' and 'B' is quite similar, except that the measurements marked 'B' have a much higher attenuation. The amount of shift is about 150%. Both sets exhibit a peak at 200°K. The measurements marked 'A' were taken with a 10 mm diameter Y-cut quartz transducer on a freshly prepared, as grown mercury telluride crystal. The measurements marked 'B' are the repetition of the first after annealing the specimen and subjecting it to repeated cooling down to 4·2°K. For these measurements a 6 mm. diameter, Y-cut transducer has been used. Two years passed between the two sets of measurements. Thus several sources might contribute this change in attenuation: namely, the effect of annealing, the size of the transducer and the handling of the specimen.

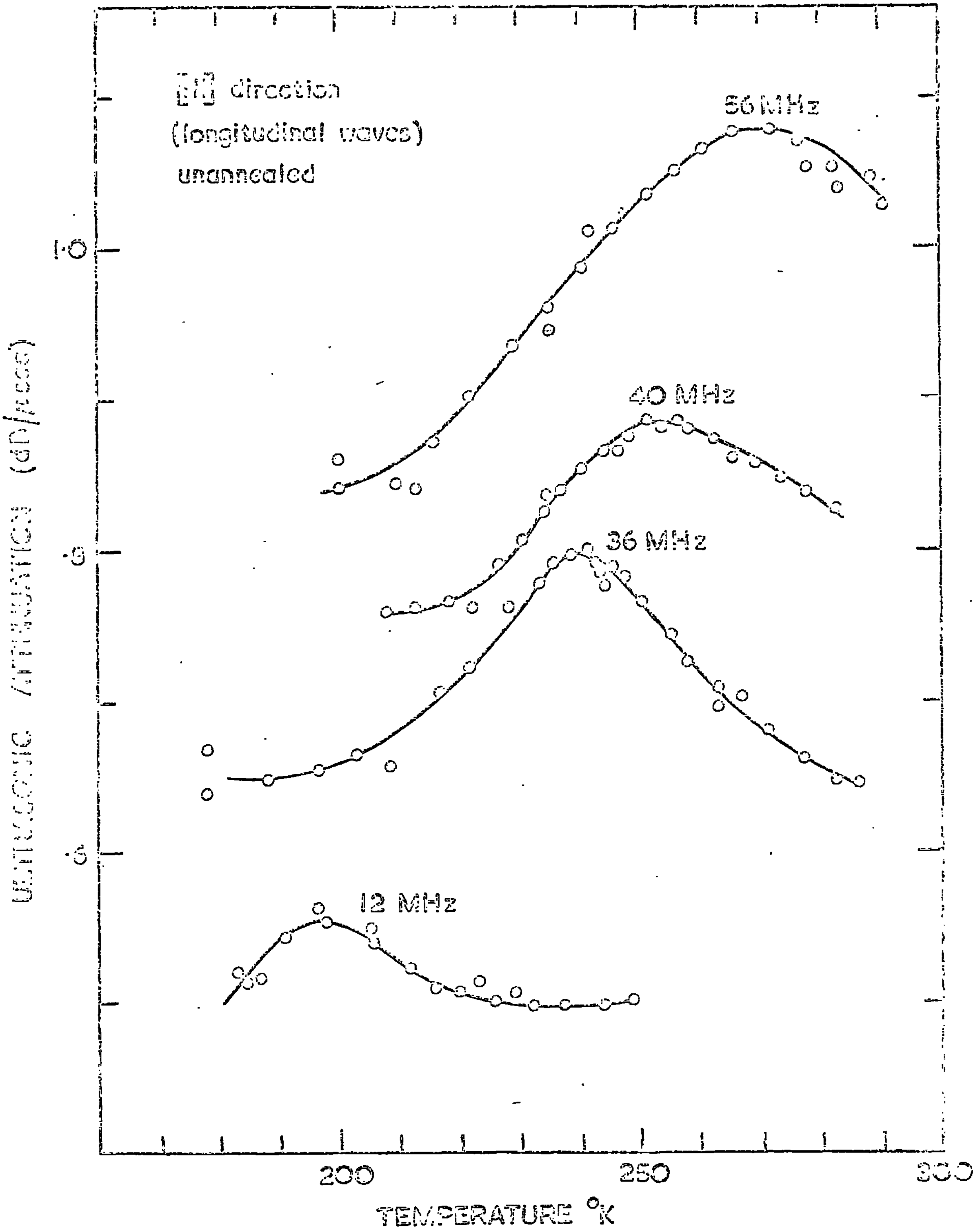

FIGURE (5.6). The temperature and frequency dependence of the peaks in the attenuation of longitudinal waves propagated along the [111] direction in as-grown HgTe.

FIGURE (5.7). The temperature dependence of shear wave attenuation showing a peak at about 200°K and the effects of handling and transducer size.

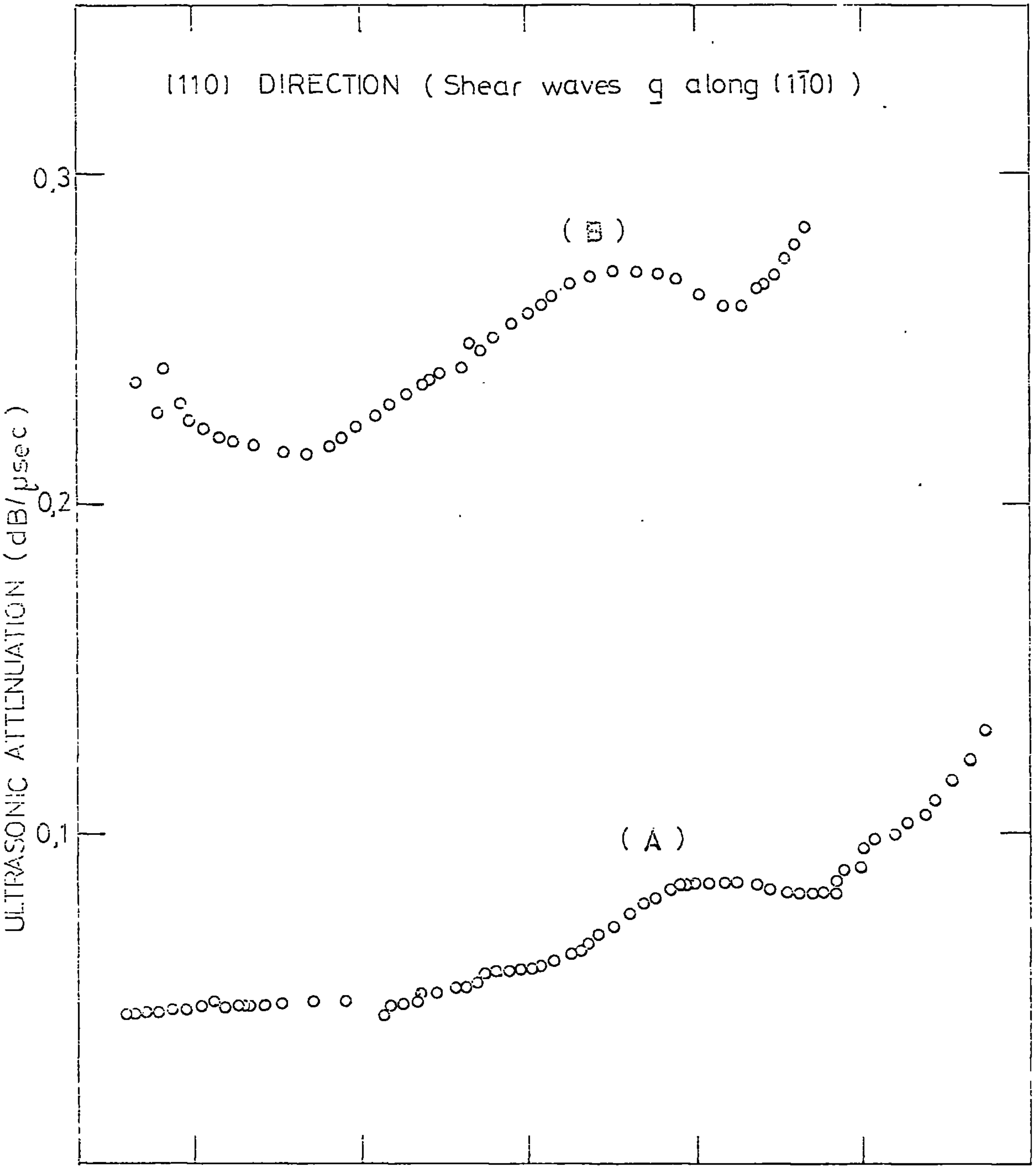

The size of the transducer is important: it effects the diffraction losses (see p. 32) given approximately by one decibel per a^2/λ. Here a is the transducer radius and λ is the wavelength of the sound wave (= V/f where V is the velocity and f is the frequency). Diffraction losses can also be expressed as

$$\alpha_{\text{diff.loss}} = \frac{\alpha_{\text{meas.}} V}{f^2 . a^2} \qquad (5.1)$$

Since here the same frequency is used in both measurements, diffraction losses due to the different size of transducer are:

$$100. \frac{2(a_1^2 - a_2^2)}{a_1^2 + a_2^2} \; \% \qquad (5.2)$$

Inserting the values of a_1(10 mm) and a_2(6 mm), difference in attenuation due to diffraction losses turn out to be 95% which does not account for all the attenuation difference (140%) between the two sets. Handling and annealing the specimen are probably responsible for the remainder of the difference. Now, a further example of the effect of annealing on the temperature dependence of ultrasonic attenuation will be given.

The effect of annealing on the temperature dependence of ultrasonic attenuation is shown in Figure (5.8). The bold lines in this figure have been transferred from Figure (5.1) and belong to the unannealed specimen. The measurements repeated after annealing under the same experimental conditions with the same transducer show about 50% increase in attenuation. The peak heights change on annealing but their position does not.

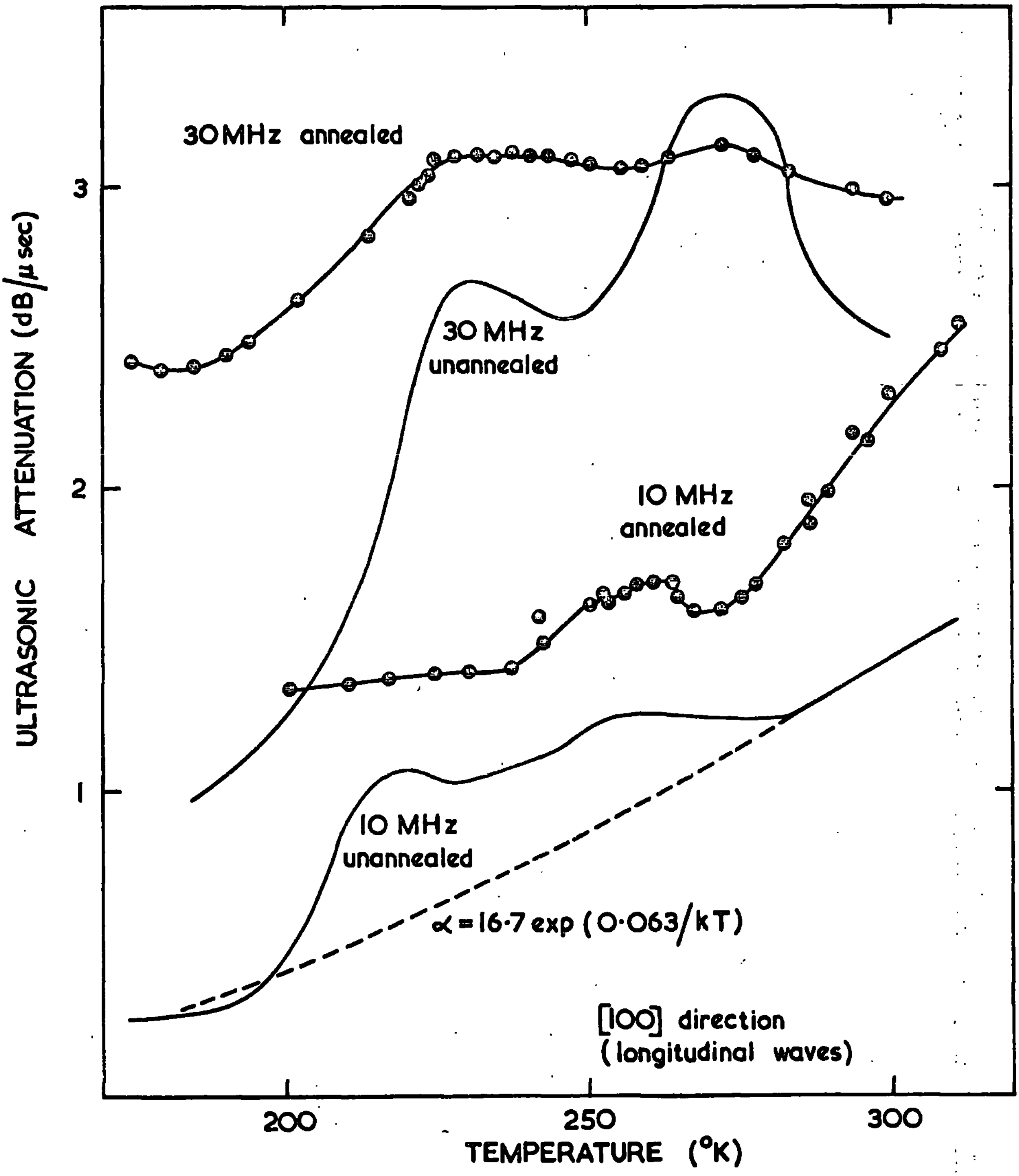

FIGURE (5.8). The effect of annealing on the attenuation at higher temperatures. The solid lines are obtained in unannealed material and are results from Figure (5.1), while the experimental points are the data taken after annealing.

5.3 THE FREQUENCY DEPENDENCE OF ATTENUATION

The frequency dependence of ultrasound attenuation provides a great deal of information about the energy loss mechanism in solids. This has been studied extensively in mercury telluride. Here examples of the frequency dependence of attenuation in mercury telluride are given. Figure (5.9) shows the frequency dependence of longitudinal ultrasonic wave attenuation along the [110] crystallographic direction. In these measurements 6 mm diameter, 10 MHz fundamental frequency, X-cut quartz transducers have been employed. In all sets of measurements the frequency dependence exhibits the same characteristic features. Starting from the low frequency side, the attenuation versus frequency curve for low frequencies is inversely proportional to frequency, then it passes through a minimum at about 25 MHz. Beyond the minimum the slope for the 4.2°K measurements approaches a frequency squared region higher than about 100 MHz. The attenuation above 200 MHz is constant. The measurements at 4.2°K have been repeated under the same experimental conditions after annealing the specimen. Once again annealing produces an increase of about 50% in ultrasound attenuation.

The exponent of the frequency of dependence can be estimated from the general relaxation equation (Equation 1.8, p.3). For $\omega\tau \ll 1$, the exponent is two, while in the region where $\omega\tau$ is close to unity, the exponent is less than two; but it can never take the negative values shown in the low frequency region in present case. Thus from this consideration it might be concluded that the behaviour of the inverse

FIGURE (5.9). The frequency dependence of attenuation in HgTe. The dotted lines are for results taken in the region of high diffraction losses.

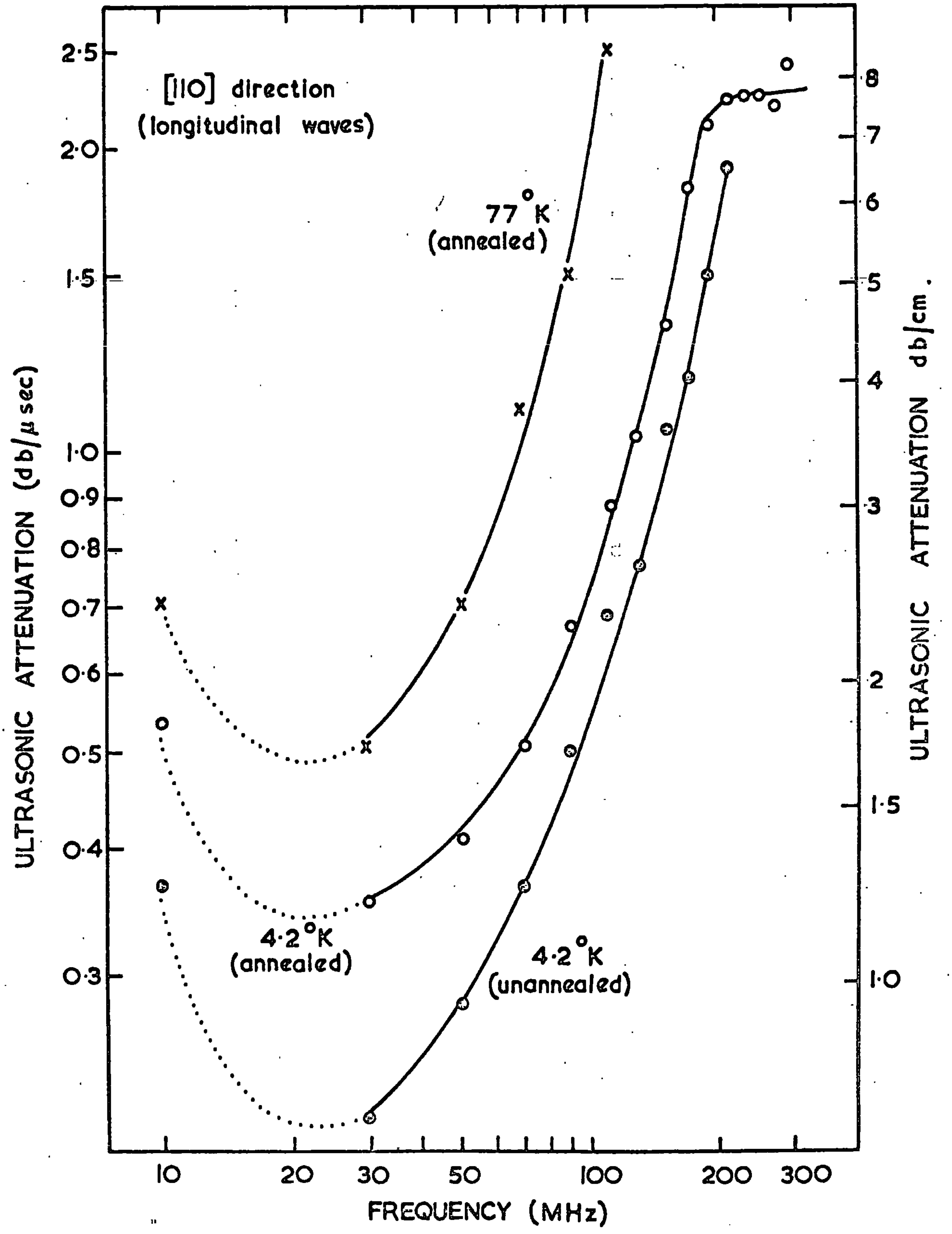

frequency dependence is not intrinsic. It is due to diffraction losses. Although the relation for diffraction losses given in Equation (5.1) is not strictly quantitative, it does predict the inverse frequency dependence found. Thus in mercury telluride when smaller diameter transducers are used for the lower frequencies, the diffraction losses are mainly responsible for the apparent ultrasound attenuation. Diffraction losses decrease with increasing frequency. The effect has been shown to be negligible for the frequencies higher than 30 MHz.

The frequency dependence of shear wave attenuation along the [110] direction will be illustrated in Figures (8.6) and (8.7) in Chapter 8. These exhibit similar features.

The frequency dependence of shear wave attenuation along the [111] crystallographic direction is illustrated in Figure (5.10). In these measurements 10 mm diameter, Y-cut quartz transducers have been used. The exponent of frequency is about unity in the 77°K measurements while at 4.2°K it decreases with increasing frequency. Here the diffraction losses are negligible due to the bigger diameter of transducer.

In Figure (5.11) the frequency dependence of longitudinal ultrasonic wave attenuation along the [100] crystallographic direction before and after annealing is illustrated. Again it can be seen that annealing produces an increase of about 50% in the attenuation. Due to the large sound attenuation (2.5 dB/μsec at 70 MHz) in this propagation direction, the frequency dependence of attenuation for higher frequencies could not be followed further. The general feature of the frequency dependence of attenuation in this direction is an increase with increasing frequency in the slope of

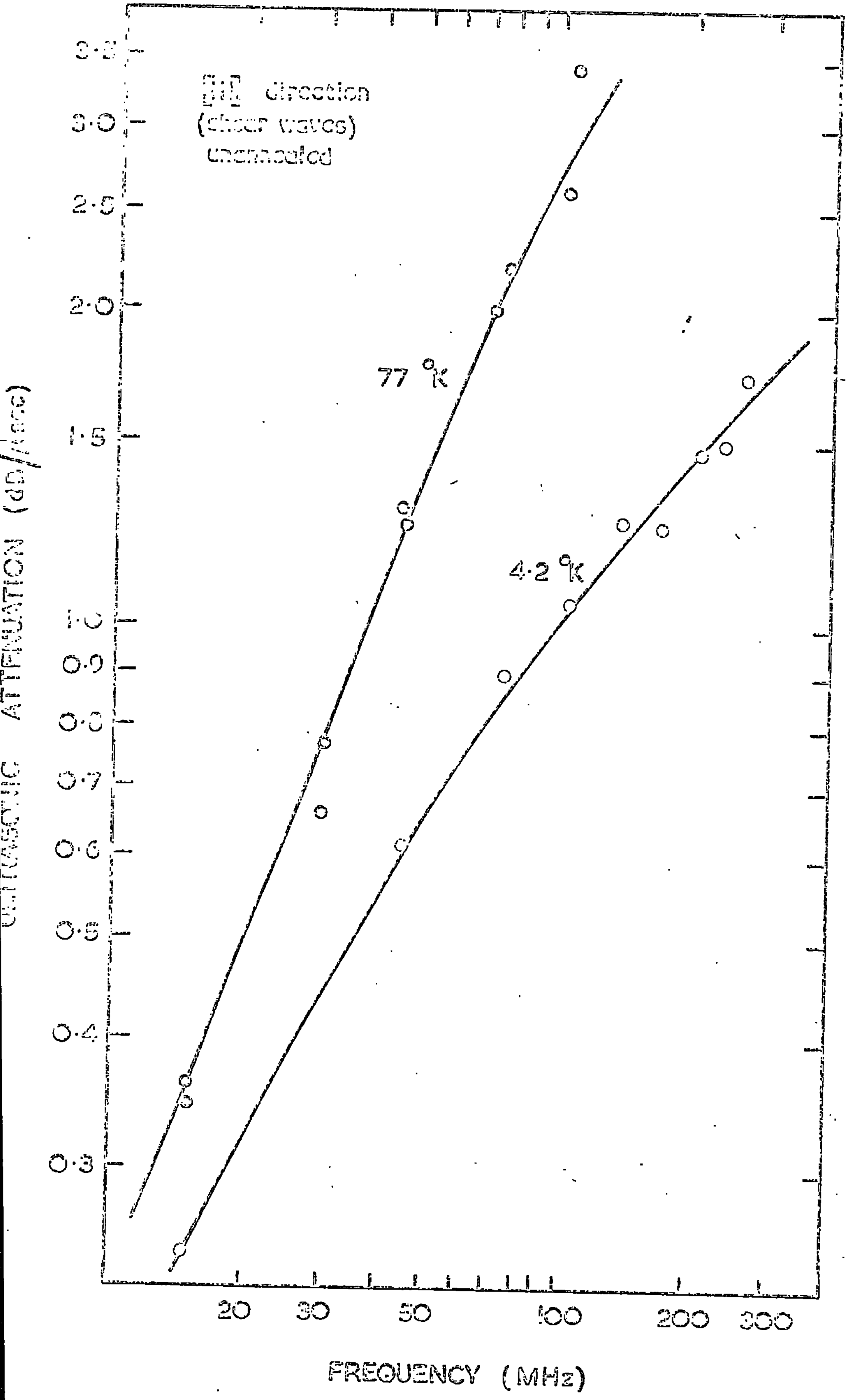

FIGURE (5.10). Frequency dependence of attenuation at two temperatures.

FIGURE (5.11). Frequency dependence of attenuation in as-grown and annealed HgTe at 77^{o}K.

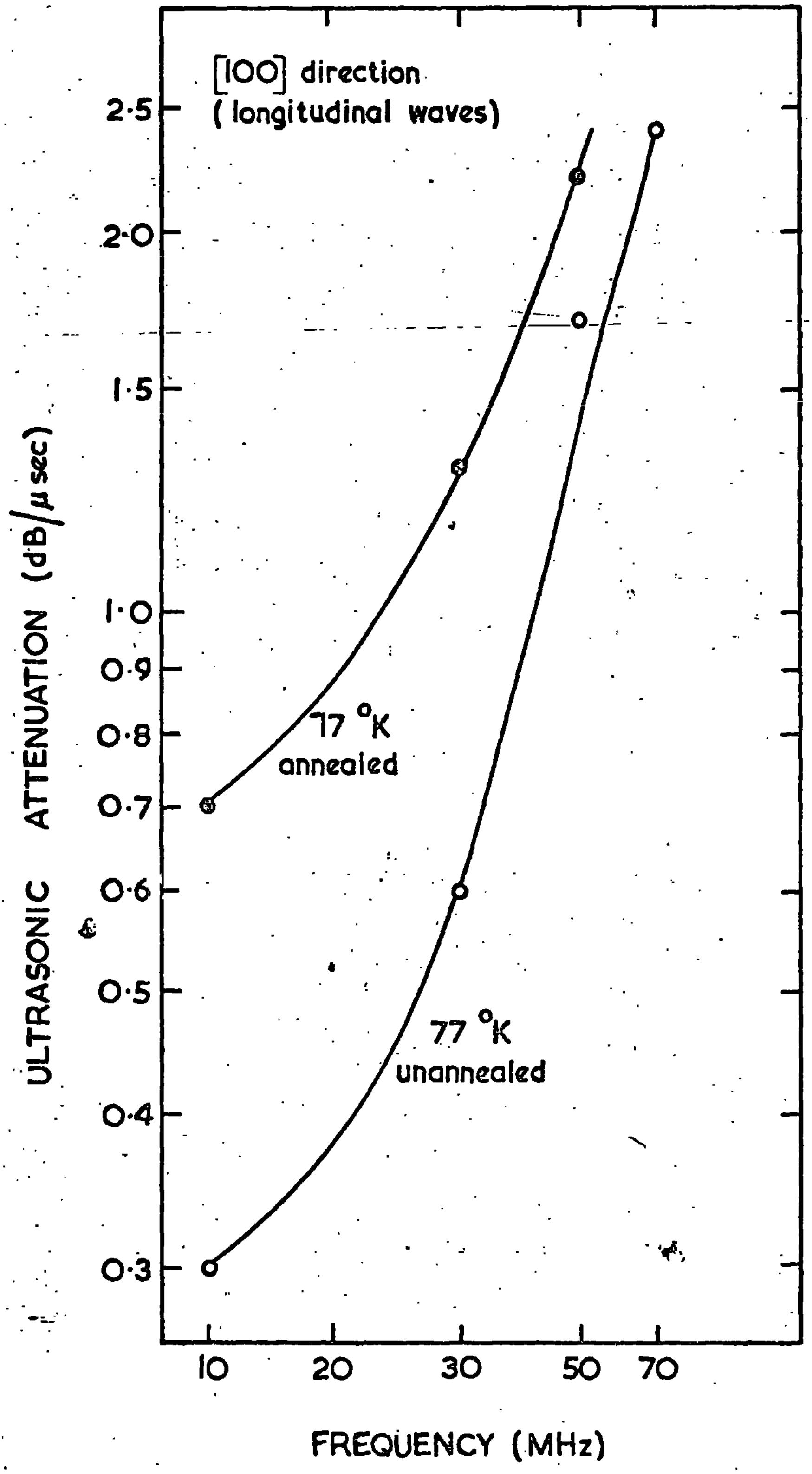

the attenuation versus frequency curve. Although in these measurements a larger diameter transducer is used, the effect of diffraction losses still exist at lower frequencies.

The frequency dependence of shear wave attenuation along the [100] direction of the same crystal used in the measurements discussed in the last paragraph is presented in Figure (5.12). The polarisation of the shear waves is in the [010] direction. In these measurements an unannealed specimen is used. The frequency dependence of shear wave attenuation is quite different from that of longitudinal waves. The slope of the attenuation versus frequency curve decreases with increasing frequency. There is no indication of diffraction losses even at lower frequencies. In these measurements the same size transducer (10 mm diameter) is used; the absence of diffraction losses can be explained by making use of Equation (5.1) from which diffraction losses can be expressed as

$$\alpha_{\text{diff.loss}} \propto \frac{V}{f^2}$$

The shear and longitudinal ultrasonic wave velocity along [100] crystallographic direction at 77^{o}K are $1\cdot654 \times 10^{5}$ cm.sec^{-1} and $2\cdot679 \times 10^{5}$ cm.sec^{-1} respectively. Thus, for each fixed frequency, about 24% more diffraction losses could be expected for the longitudinal ultrasonic waves.

Diffraction losses contribute to the background attenuation measurements and they do not effect the general shape of any relaxation losses. Diffraction losses only shift the overall features of the characteristic attenuation to higher attenuation.

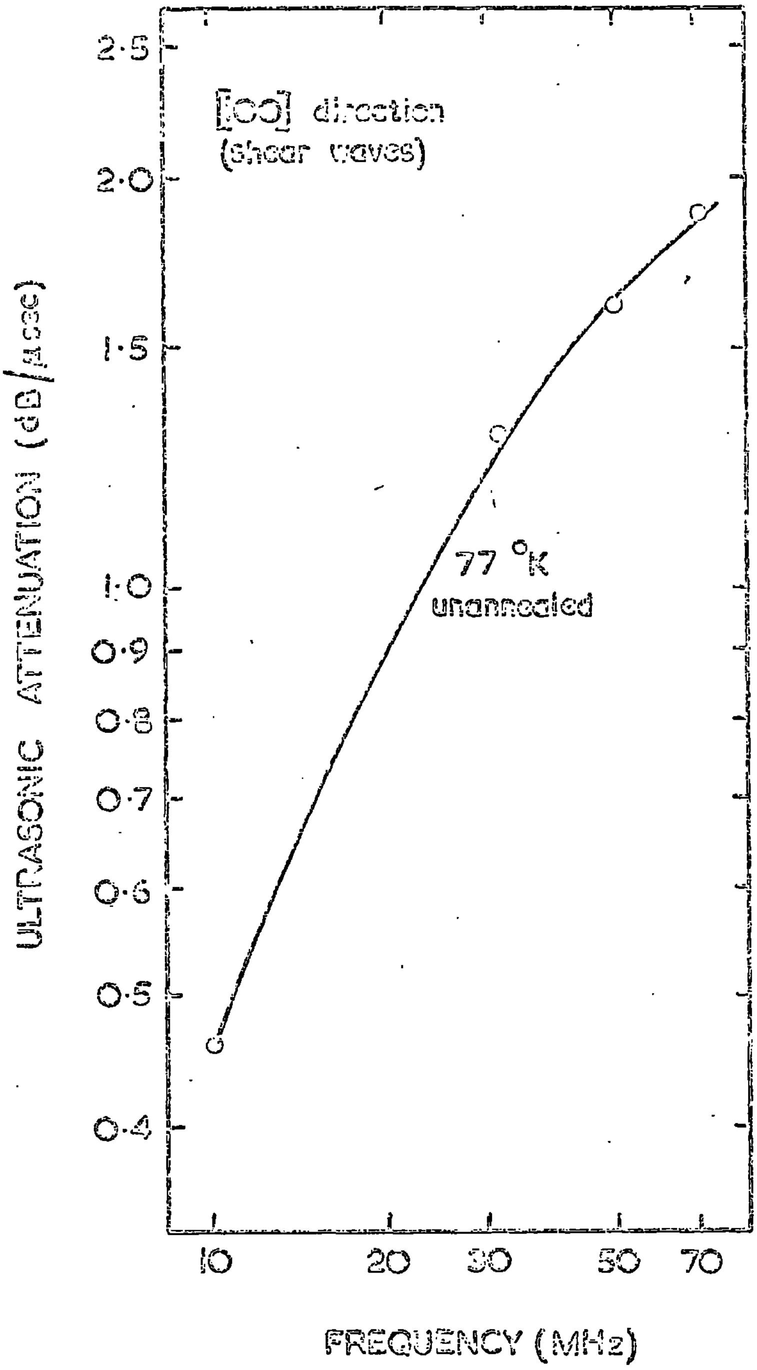

FIGURE (5.12). Frequency dependence of attenuation of shear waves propagated along the [111] crystallographic direction in unannealed HgTe.

5.4. THE STRESS-DEPENDENCE OF ATTENUATION

The effect of annealing and handling of specimens on the measured attenuation implies that dislocations might play an important role. Dislocations are very sensitive to applied stresses. Thus as part of the work, the applied stress dependence of attenuation has also been assessed. The characteristics of this kind of measurement will now be given.

In Figure (5.13) the effect of applied stress on the measured attenuation is illustrated for longitudinal, 10MHz ultrasonic waves propagated along the [110] crystallographic direction. The specimen is squeezed along the $[1\bar{1}0]$ direction with a "Hounsfield 'W' type tensometer". For these measurements a rectangular parallelopiped specimen with surfaces normal to the [110] and $[1\bar{1}0]$ crystallographic directions has been prepared by spark erosion. Ultrasonic waves are generated and detected with a 10 mm diameter, 10 MHz fundamental frequency X-cut quartz transducer. The sample holder for the stress dependence of attenuation measurements and the experimental arrangement is sketched in Figure (5.14). The specimen has been squeezed up to pressures of 2×10^8 dyn/cm^2. The strain on the specimen is much smaller than the strain on the tensometer. Therefore, accurate strain measurements could not be made. However the strain can be estimated from the stress-strain relation given by Hooke's law.

$$\epsilon = \sigma/(C_{11}+C_{12}+2C_{44}) \tag{5.3}$$

The stress dependence of longitudinal wave attenuation in single crystals of mercury telluride exhibits the following characteristic

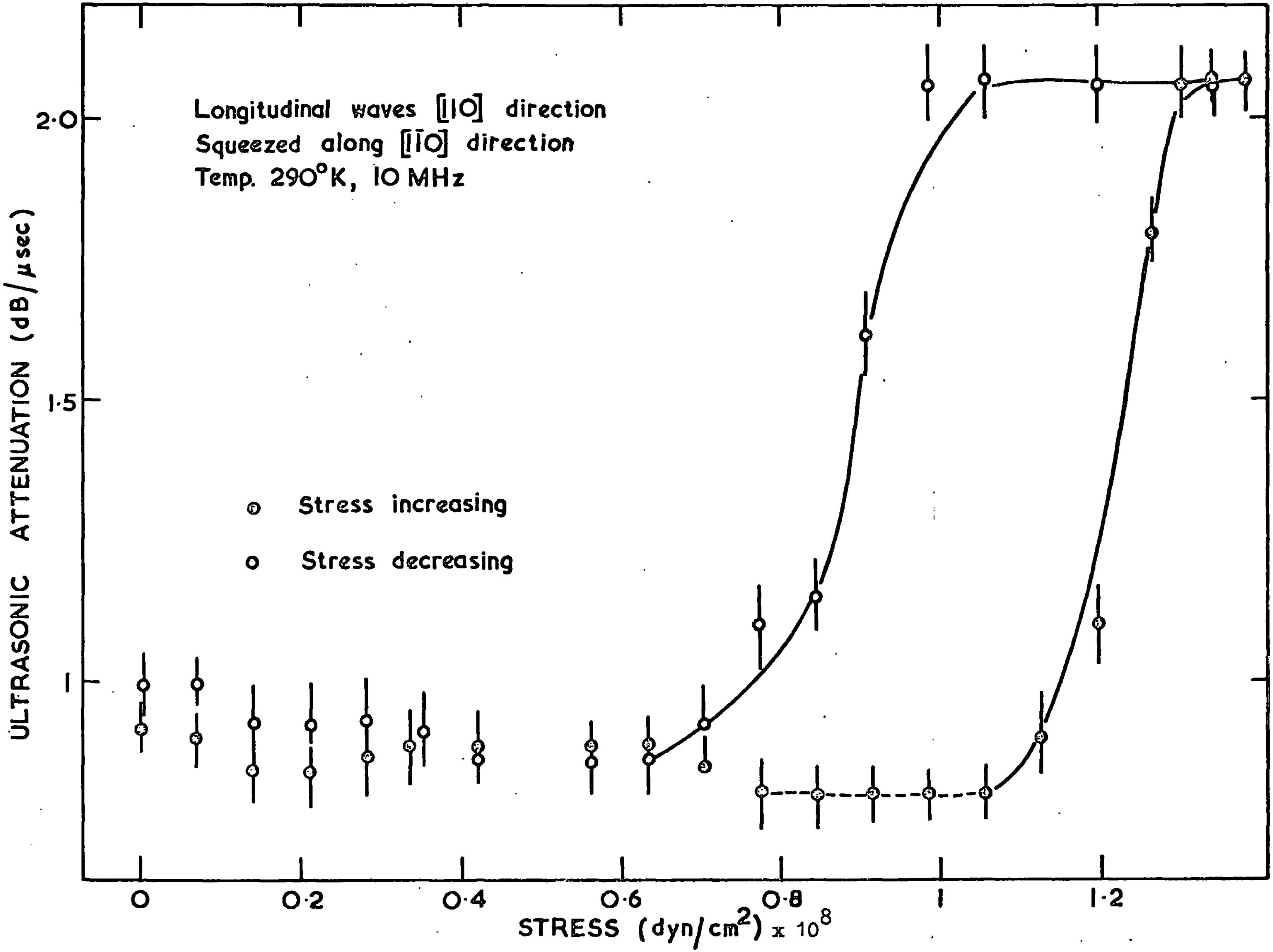

FIGURE (5.13). The stress dependence of attenuation of longitudinal waves in HgTe.

FIGURE (5.14). The sample holder used to measure the stress dependence of attenuation.

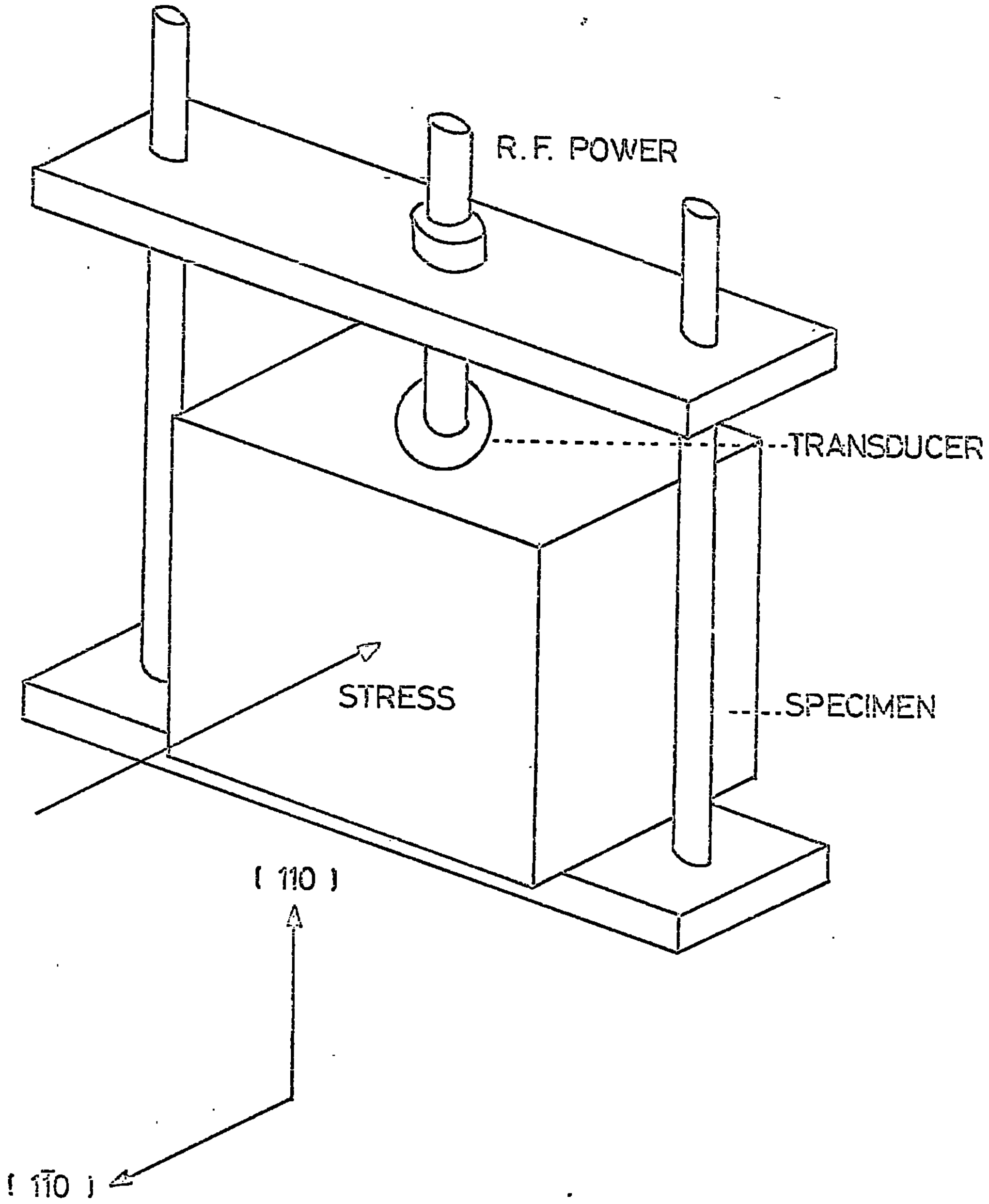

features. Attenuation is almost stress independent for stresses below about $1{\cdot}5 \times 10^{8}$ dyn.cm^{-2}, but after this value attenuation increases very sharply. On the way to releasing the applied stress the attenuation is stress independent for the short stress interval (10^{8} dyn.cm^{-2} - $1{\cdot}4 \times 10^{8}$ dyn.cm^{-2}), then it sharply decreases with decreasing stress and it reaches at about $6{\cdot}5 \times 10^{7}$ dyn.cm^{-2} the initial state and again is stress independent. Thus, the stress dependence of longitudinal wave attenuation exhibits hysteresis.

The effect of the amplitude of the driving sound waves on the mechanical loss at low frequencies (few Hz to low kHz regions) has been well known for years. However, due to the experimental uncertainties of determining the strain or stress of the driving ultrasonic waves, there have been only few studies of the effect of the amplitude on the attenuation of megahertz ultrasonic waves. In Figure (5.15) the amplitude dependence of the attenuation of longitudinal ultrasonic waves along [110] direction in mercury telluride is illustrated. No attempt has been made to estimate the magnitude of the stress or strain induced by the transducer. The relative heights of the sound waves given along the abscissa are calculated from

$$\text{Amplitude (dB)} = 20 \log \frac{I}{I_o} \qquad (5.4)$$

Here I_o is the amplitude of the first pulse for the lowest power. I_o and the other I's are measured by comparing the first pulse height on the oscillascope.

Both sets of measurements in this figure exhibit similar behaviour; the attenuation increases with decreasing ultrasonic wave amplitude. The difference in the attenuation for the lowest and highest amplitude of sound

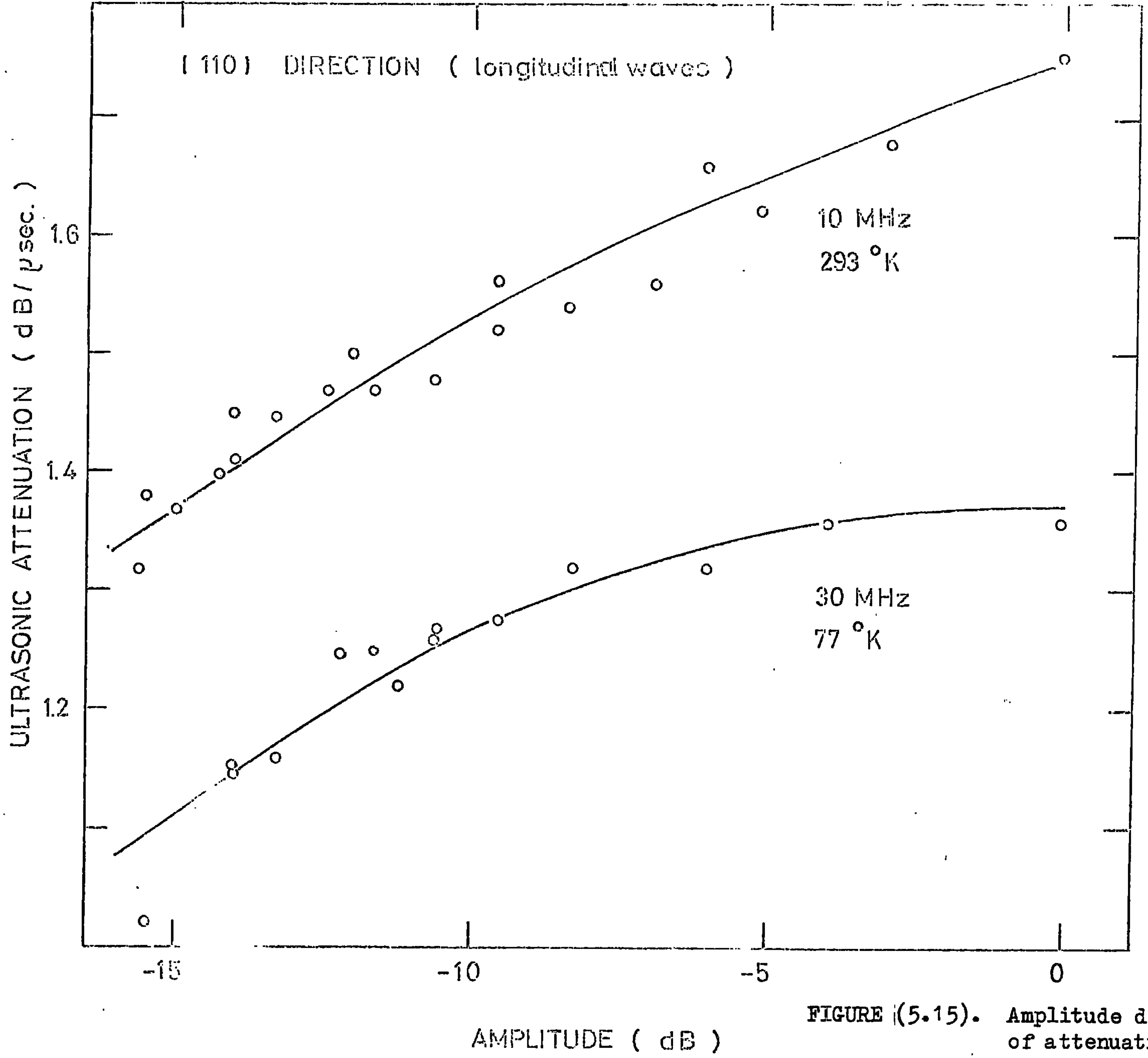

FIGURE (5.15). Amplitude dependence of attenuation.

waves are about 26% for the measurements made with 30 MHz at 77°K and about 30% for those made with 10 MHz at room temperature.

The ultrasonic waves amplitude effects are very important. In the measurements of the temperature dependence of attenuation this is minimised by keeping the amplitude constant. On the other hand the bonding material between the transducer and the specimen changes its character somewhat, the transducer to specimen coupling alters and thus the amplitude of sound waves in the material will change a little over the temperature range. This effect is unavoidable but it should be very small and well within the experimental error of 10% in the relative attenuation measurements.

5.5. SUMMARY OF THE RESULTS

The examples of temperature, frequency, stress and amplitude dependence of shear and longitudinal ultrasonic wave attenuation in different propagation direction in mercury telluride single crystal have been illustrated. The general features of attenuation exhibits similarities throughout and give easily recognisable set. These features will now be summarized.

(i) Temperature dependence of ultrasound attenuation in mercury telluride: In different temperature ranges some characteristic features are exhibited. Starting from the low temperature side, the attenuation of both shear and longitudinal waves is almost temperature independent for temperatures lower than 20°K. Then it sharply increases as the third or fourth power of temperature until about 40°K, followed by a smoothly decrease inversely proportional to temperature to about 70 or 80°K. Attenuation in temperature range 80°K to 170°K is almost temperature independent. In the temperature range between 170°K to 300°K attenuation of both shear and longitudinal waves exhibits some peaks. In some crystallographic directions the peaks are superimposed on background attenuation which increases exponentially with increasing temperature. In some directions the peaks are split.

(ii) Frequency dependence of ultrasound attenuation in mercury telluride: The slope of the attenuation versus frequency curve is usually less than two but for the measurements of 4·2°K along the [110] direction the slope at higher frequencies reaches two and for frequencies higher than 170 MHz the attenuation reaches a maximum value. The diffraction losses are appreciable at low frequencies, especially when smaller diameter transducers are used.

(iii) Applied stress dependence of attenuation in mercury telluride: The attenuation of ultrasonic waves in mercury telluride is dependent upon both the applied stress and the wave amplitude. Annealing increases the attenuation. Effects of handling the specimen are also observed.

The general features of temperature dependence of ultrasonic wave attenuation in the low temperature region below 80°K indicate a relaxation effect. This curve is characteristic of a mechanism involving a temperature dependent relaxation time. The features are those shown by direct conversion of acoustical waves into heat energy; this is the ultrasonic phonon-lattice phonon interaction or Akhieser effect. This portion will be discussed in Chapter 7.

The effect of annealing and the handling of the specimens on the attenuation of the ultrasonic waves indicate that dislocations contribute strongly to the sound energy loss mechanism in mercury telluride. The applied stress and amplitude of driving sound wave dependence measurements also provide further confirmation and information of the dislocation effects. The attenuation of shear ultrasonic waves along the [111] crystallographic direction always exhibits slight differences compared with that in the other directions. This provides further indications of dislocation interactions: the (111) plane is the most probable slip plane in zincblende lattices. The losses caused by dislocations will be analysed in Chapter 8.

The peaks in the temperature dependence of attenuation in the high temperature region are considered to be Bordoni-type relaxation peaks due to a different form of dislocation motion. The discussion of the peaks will take place in Chapter 9.

Some of the relaxation-type losses have their own characteristic features and they can be distinguished. But this becomes difficult if $\omega\tau \ll 1$. In the next chapter the effect of possible sound energy loss mechanism on the attenuation of ultrasonic waves in mercury telluride and their magnitude will be analysed to sort out the important contributions. These major effects will be discussed in subsequent chapters.

CHAPTER 6

MECHANISM CONTRIBUTING TO ULTRASONIC ATTENUATION IN MERCURY TELLURIDE

Before discussion of the ultrasound attenuation mechanism in single crystal of mercury telluride it is necessary to estimate the magnitudes of the possible contributions. In different frequency and temperature regions the effects on the measured attenuation would be different. Due to complex frequency dependence it is often difficult to identify and separate experimentally the possible mechanism.

Mercury telluride is piezoelectric and this could be an important contribution. So too could the thermoelastic loss. Both these mechanism have been considered in some detail to ascertain their magnitudes. It turns out that neither is of importance.

6.1. PIEZOELECTRIC COUPLING

In piezoelectric solids stress waves accompany electromagnetic waves and vice versa. Depending on the piezoelectric tensor and the mode of propagation, each acoustic wave causes bunching of the mobile carriers. This creates an internal electric field whose relaxation is determined by the conductivity and the dielectric properties of the medium in which the sound waves are propagated. Like other relaxation phenomena, the piezoelectric effect also causes sound attenuation and a velocity change.

The contribution of the internal electric field to the sound velocities was originally pointed out by Voigt (1910). This effect has been analysed in more detail by Kyame (1949) and (1954) and Hutson and White (1962) and the others. In the first treatment Kyame showed that analysis of wave propagation in piezoelectric materials involves the combined use of the mechanical-piezoelectric equations of state and Maxwell's equations. The stress-strain relation contains an additional stress term caused by the internal electric field (E) arising from the applied stress. Thus Equation (4.1, p.44) given for the elastic solid takes the following form:

$$\sigma_{ij} = C_{ijkl}\epsilon_{kl} - e_{ijr}E_r \qquad (6.1)$$

where e_{ijr} is the piezoelectric tensor and E_r is the component of the electric field vector. The other parameters have already been defined in Section (4.2, p.44.) The expression for the electric displacement (D_j) caused by the strain and the electric field is

$$D_j = e_{ikl}\epsilon_{kl} + p_{jr}E_r \qquad (6.2)$$

Here p_{jr} is the component of the dielectric tensor. Following a similar procedure to that in Section (4.2) and making use of Maxwell's equations for the plane wave propagating in the X_1 direction, the equation of motion in piezoelectric materials is obtained:

$$\omega^2\rho S_i = k^2 C'_{i11k} S_k - ik\, e'_{i1l} E_l$$

$$i,k = 1,2,3 \text{ and } l = 2,3 \qquad (6.3)$$

Here S_i and S_k are the elastic plane wave (Equation 4.6, p.46), E_1 is the plane electric field equation $[E_1 = E_{01}\, e^{i(\omega t - kX_1)}]$ and k is the wave vector $(k = \frac{\omega}{v} n)$ Equation (6.3) specifies the elastic behaviour of piezoelectric materials and the modified elastic constants can be deduced from the secular determinant:

$$\left| C'_{i\,11\,k}\, k^2 - \omega^2 \rho \right| = 0 \tag{6.4}$$

$$i,k = 1,2,3$$

where

$$C'_{i\,11\,k} = C_{i\,11\,k} + \frac{e_{i\,11}\, e_{11\,k}}{p_{11} + i\,\frac{b_{11}}{\omega}} \tag{6.5}$$

Here b is the electrical conductivity. Equation (6.4) has been written for the propagation of plane waves in X_1 direction of an orthogonal coordinate system. For the case that wave propagation is not along the crystallographic X_1 direction, elastic and piezoelectric coefficients can be obtained from the usual ones by a coordinate rotation.

As shown from Equation (6.5) the elastic constants of piezoelectric materials have real and imaginary parts and are frequency dependent. In the limit where the piezoelectric coefficients vanish or the medium is a nearly perfect conductor, the effective elastic constants are equal to the conventional constants that is

$$C'_{i\,11\,k} = C_{i\,11\,k}$$

for either $e's \longrightarrow 0$ or $b's \longrightarrow \infty$

It is interesting that piezoelectric coupling does not effect all the sound velocities measured in different directions and polarisations. The magnitude of this effect may be seen from comparison of the shear wave velocities along the [100] direction (polarised in either the [010] or the [001] directions) with that along the [110] direction (polarised [001] direction). For Hookeian solids both velocities give the same elastic constant. But in piezoelectric materials the piezoelectric tensor component is absent in the [100] direction, while the second velocity is effected by piezoelectric coupling:

$$v_{[100]} = (C_{44}/\rho)^{\frac{1}{2}} \quad \text{polarised along either (010] or [001] direction} \qquad (6.6)$$

and

$$v_{[110]} = (C'_{44}/\rho)^{\frac{1}{2}} \quad \text{polarised along [001] direction} \qquad (6.7)$$

Here

$$C'_{44} = C_{44} + \frac{e^2_{14}}{p+i\,\frac{b}{\omega}} \qquad (6.8)$$

and p is the dielectric permittivity and b is the conductivity.

Thus, for zincblende structure compounds, it is required to measure the sound velocities in at least two directions. In the present work the effect of piezoelectric coupling on sound velocities in mercury telluride has been estimated by comparing these two velocities.

In Table (6.1) two particular velocities are tabulated for selected temperatures.

TABLE (6.1) Comparison of two sound velocities from which the same elastic constant is derived, thus showing piezoelectric coupling is negligible.

Temperature °K	v along [110] direction polarised along the [001] direction	v along [100] direction polarised along the [010] or the [001] direction
4·2	1·66 x 10^5 cm/sec	1·66 x 10^5 cm/sec
77	1·65 "	1·65 "
196	1·63 "	1·63 "
290	1·61 "	1·62 "

From this table it may be concluded that the effect of piezoelectric coupling on sound velocities is undetectable within the limits of the experimental error. Due to high conductivity of mercury telluride, the second term in Equation (6.8) is negligible; the usual sets of equations can be used to compute the elastic constants from velocities.

On the basis of the preceding treatment, Hutson and White (1962) derived a theory of ultrasonic attenuation in piezoelectric semiconductors. Their result for low megahertz frequencies takes the following form (Lord and Truell 1966).

$$\alpha = \frac{\omega}{V} \; \frac{L^2}{2} \; \frac{\omega_{c/\omega}}{1 + (\omega_{c/\omega})^2} \qquad (6.9)$$

where α is in Nepers/cm, v is the velocity of sound, $L = \left(\frac{e}{c \cdot p}\right)^{\frac{1}{2}}$ is the electromechanical coupling coefficient, with e, the piezoelectric coefficient, C, the particular elastic constant, and p the dielectric permittivity, $\omega_c = {}^{b}\!/_{p}$ is the conductivity frequency, with b, the conductivity. This is a relaxation-type of attenuation and reaches its maximum value when $b/p = \omega$. In the limit where the piezoelectric coefficient vanishes ($e = 0 \therefore L = 0$) or the medium is a nearly perfect conductor ($b = 0$), Equation (6.9) shows that the medium does not absorb sound energy.

Equation (6.9) has been used to estimate the effect of piezoelectric coupling on ultrasonic attenuation in mercury telluride. At $4{\cdot}2^{\circ}$K the lowest conductivity (b) is 3000 $(\Omega.\mathrm{m})^{-1}$ (Dziuba et al. 1964) and the dielectric permittivity (p) is $1{\cdot}8 \times 10^{-10}$ Farads.m^{-1} (Dickey and Mavroides 1964); for this case, the frequency $(\omega_c/2\pi)$ for maximum attenuation is estimated to be of the order of 3×10^{12} Hz, well beyond that of the present experiment. The magnitude of piezoelectric coupling effect in the frequency range used can be estimated. The electro mechanical coupling coefficient (L) seems to be of the order of 10^{-2} for most of the III-V and II-VI compounds (Arlt et. al. 1968), taking 5×10^{-2} for mercury telluride even using the highest frequency available and lowest conductivity known, the attenuation due to the piezoelectric coupling effect is of the order of 10^{-4} to 10^{-3} dB/µsec.

It may be concluded that piezoelectric nature of mercury telluride, due to high conductivity, does not contribute to any of its anelastic properties.

6.2. THE THERMOELASTIC LOSS.

Direct conversion of acoustic energy to thermal energy is called the thermoelastic effect. When a solid is subjected to a stress, the resulting strain is in general accompanied by a change in temperature. If the strain is homogeneous, the temperature change will be the same everywhere in the specimen. If the strain is not homogeneous, as, for example, when a longitudinal ultrasonic wave is propagated through a solid, a temperature gradient will be set up between regions of expansion and of compression. This will lead to a flow of heat from the hotter (compressed) part to the cooler (expanded) part, accompanied by a production of entropy and a dissipation of energy, which will result in an attenuation. Lücke (1956) has discussed this effect in a standard linear viscoelastic solid, taking into account the anisotropy of the elastic properties. At high frequencies the time per cycle is insufficient for appreciable heat to flow between the adjacent regions and the thermoelastic damping should be small. At very low frequencies thermal equilibrium between regions is approached and again no attenuation occurs. When the period of the applied stress becomes comparable with the relaxation time (τ) of the heat transfer process, attenuation is observed and reaches a maximum when $\omega\tau = 1$.

As the thermoelastic loss is relaxation type, the general form of the relaxation equation (Equation 1.8, p.3) can be used.

$$\alpha' = \frac{1}{2\tau} \frac{\Delta M}{M_o} \frac{\omega^2\tau^2}{1+\omega^2\tau^2} \tag{6.10}$$

An adiabatic elastic deformation, with a longitudinal component, leads to a change in temperature (thermoelastic effect). Because of the thermal expansion due to this temperature change, the adiabatic elastic modulus ($M_{ad.}$), appears to be different from that for isothermal deformation (M_T). Some time is required for a flow of heat to occur; hence, when the deformation is sufficiently fast, it can be considered adiabatic, even when the solid is not isolated from its surroundings.

In Equation (6.10) $\Delta M/M_o$ is the fractional change of the adiabatic and isothermal elastic modulus ($= \frac{M_{ad}-M_T}{M_T}$) and τ is the relaxation time of this effect and is given by

$$\tau = \frac{K}{\rho c_p v^2} \qquad (6.11)$$

Here K is the thermal conductivity, ρ is the density c_p is the specific heat at constant pressure and v is the velocity of sound in this particular direction.

In cubic symmetry it may be shown that (Bhatia 1967, p.40).

For propagation in the [100] direction

$$\frac{\Delta M}{M_o} = \frac{(C_{11}+2C_{12})^2\,\alpha^2 T}{C_{11}\;\rho\,c_p}$$

For propagation in the [110] direction

$$\frac{\Delta M}{M} = \frac{2(C_{11}+2C_{12})^2\,\alpha^2 T}{(C_{11}+C_{12}+2C_{44})\rho\,c_p}$$

For propagation in the [111] direction

$$\frac{\Delta M}{M_o} = \frac{3(C_{11}+2C_{12})^2\,\alpha^2 T}{(C_{11}+2C_{12}+4C_{44})\rho c_p}$$

Here α is the thermal expansion coefficient.

Even for the best conductors of heat, τ is of the order of 10^{-11} sec and, therefore, for the Megahertz frequencies $\omega\tau \ll 1$. Equation (6.10) thus can be simplified to (with the units of dB/cm):

$$\alpha' = \frac{8 \cdot 68}{V} \; 2\pi^2 \frac{\Delta M}{M_o} \; \tau f^2 \tag{6.12}$$

Therefore, the thermoelastic loss for $\omega\tau \ll 1$ is frequency square dependent. The room temperature values of elastic constants C_{11}, C_{12} and C_{44} of mercury telluride are given in Table (6.2) together with other necessary parameters. Calculated values of the relaxation time (τ) and $\Delta M/M_o$ are presented; these results were used to estimate from Equation (6.12) the thermoelastic attenuation in single crystal mercury telluride; details are shown in Table (6.2) together with data obtained by Lücke (1956) for germanium and silver for comparison. The latter results have been transformed to the form (attenuation)/(frequency)^2.

The frequency (f) at which the thermoelastic loss has maximum ($\omega\tau = 1$) is

$$f = 1/2\pi\tau \tag{6.13}$$

or inserting the value of relaxation time

$$f = \rho c_p v^2/2\pi K \tag{6.14}$$

For mercury telluride at room temperature this frequency is of the order of 10^{11} Hertz which is far beyond the limit of present day ultrasonic equipment. However, if we look at the terms in Equation (6.14), as the temperature decreases, c_p may decrease by a ratio of 1000 to 1 while

TABLE (6.2) Comparison between the calculated thermoelastic losses in silver, germanium and mercury telluride. The results are quoted as α/f^2 (dB cm^{-1} Hz^{-2})

Material	DIRECTION OF ULTRASONIC WAVE PROPAGATION								
	[100]			[110]			[111]		
	τ (sec)	$\Delta M/M_o$	α/f^2	τ (sec)	$\Delta M/M_o$	α/f^2	τ (sec)	$\Delta M/M_o$	α/f^2
Ag	15×10^{-12}	$3{\cdot}2\times10^{-2}$	$2{\cdot}4\times10^{-16}$	12×10^{-12}	$3{\cdot}9\times10^{-2}$	$1{\cdot}4\times10^{-16}$	11×10^{-12}	$1{\cdot}3\times10^{-2}$	$0{\cdot}58\times10^{-16}$
Ge	$1{\cdot}5\times10^{-12}$	$0{\cdot}21\times10^{-2}$	$1{\cdot}1\times10^{-18}$	$1{\cdot}2\times10^{-12}$	$0{\cdot}26\times10^{-2}$	$0{\cdot}68\times10^{-18}$	$1{\cdot}5\times10^{-12}$	$0{\cdot}27\times10^{-2}$	$0{\cdot}33\times10^{-18}$
HgTe	$0{\cdot}30\times10^{-12}$	$0{\cdot}19\times10^{-2}$	$0{\cdot}38\times10^{-20}$	$0{\cdot}24\times10^{-12}$	$0{\cdot}15\times10^{-2}$	$0{\cdot}22\times10^{-20}$	$0{\cdot}23\times10^{-12}$	$0{\cdot}14\times10^{-2}$	$0{\cdot}19\times10^{-20}$

Elastic constant and sound velocity data used in the calculation								
Material	Reference	Elastic constants (dyn cm^{-2} x 10^{11})			Longitudinal sound wave velocity (cm sec^{-1} x 10^5)			Density ($g.cm^{-3}$)
		C_{11}	C_{12}	C_{44}	U [100]	U [110]	U [111]	
Ag(293^oK)	Bacon and Smith (1956)	12·40	9·34	4·61	3·43	3·83	3·95	10·53
Ge(273^oK)	McSkimin (1953)	12·93	4·85	6·72	4·93	5·41	6·14	5·323
HgTe (300^oK)	Present work, see Table 4.1, p.51)	5·39	3·74	2·09	2·58	2·87	2·96	8·08

Further data used for mercury telluride: Thermal expansion 5×10^{-6} $^oK^{-1}$ (Novikova and Abrikosov 1964)

Debye temperature 141 ± 4^oK (Present work, see Chapter 4, p.67)

Thermal conductivity $2{\cdot}5 \times 10^5$ erg cm^{-1} $^oK^{-1}$ (Carlson 1958)

Specific heat $1{\cdot}53 \times 10^6$ erg gm^{-1} $^oK^{-1}$ (Present work, see Appendix A).

K may increase by a hundred times. Then this frequency reduces to a measureable value. Here an attempt has been made to estimate the thermoelastic loss in low temperatures. In Table (6.3) the temperature variation of $\Delta M/M_o$, τ, and α/f^2 for longitudinal waves in the [110] direction with the necessary parameters used in this calculation are tabulated and in Figure (6.1) temperature dependence of $\Delta M/M_o$, τ and α/f^2 are shown. Although the relaxation time (τ) of this effect rises sharply at low temperatures, due to a decrease of thermal expansion faster than the specific heat, $\Delta M/M_o$ decreases very sharply. Thus the product, which gives the attenuation (Equation 6.12), has the features shown in this figure. This argument could not be extended for lower temperatures (lower than 77°K) due to lack of experimental data on thermal conductivity in this temperature region.

The thermoelastic loss is large for metals because both the thermal conductivity and the thermal expansion are large. For instance Lücke finds that the attenuation of longitudinal sound waves in zinc single crystals between 10 and 150 MHz largely comes from thermoelastic losses. But in mercury telluride over the frequency range 10 to 300 MHz this loss component is negligible. Calculation of the contribution of the thermoelastic loss over the temperature range 77°K to 290°K confirms that this effect is negligible in mercury telluride.

These preliminary arguments show that in mercury telluride the damping of ultrasonic waves does not come from either piezoelectric coupling or from thermoelastic losses. The experiments demonstrate that the dominant

TABLE (6.3). The temperature variation of $\Delta M/M_o$, τ and α/f^2 for mercury telluride

T (°K)	$\Delta M/M_o$	τ (sec)	α/f^2 (dB/cm Hz^2)
290	$1\cdot52 \times 10^{-3}$	$2\cdot62 \times 10^{-13}$	$1\cdot2 \times 10^{-19}$
196	$8\cdot60 \times 10^{-4}$	$3\cdot7 \times 10^{-13}$	$1\cdot9 \times 10^{-19}$
150	$4\cdot67 \times 10^{-4}$	$5\cdot2 \times 10^{-13}$	$1\cdot4 \times 10^{-19}$
77	2×10^{-5}	$2\cdot74 \times 10^{-12}$	$3\cdot2 \times 10^{-20}$

Temperature variation of elastic constants, thermal expansion coefficient and thermal conductivity data used in this calculation

T(°K)	Elastic constants (dyn cm^{-2} x 10^{11})			α ther. expansion coeff.	c_p erg/gm °K	K erg/cm °K
	C_{11}	C_{12}	C_{13}			
290	5·4	3·76	2·05	5×10^{-6}	$1\cdot49 \times 10^{6}$	$1\cdot6 \times 10^{5}$
196	5·6	3·90	2·15	$4\cdot5 \times 10^{-6}$	$1\cdot48 \times 10^{6}$	$3\cdot7 \times 10^{5}$
150	5·7	4·0	2·15	$3\cdot7 \times 10^{-6}$	$1\cdot46 \times 10^{6}$	$5\cdot2 \times 10^{5}$
77	5·85	4·04	2·20	1×10^{-6}	$1\cdot28 \times 10^{6}$	$2\cdot5 \times 10^{6}$
	Present work (Table 4·1, p.51			Appendix A		

FIGURE (6.1). Temperature dependence of thermoelastic attenuation and related parameters.

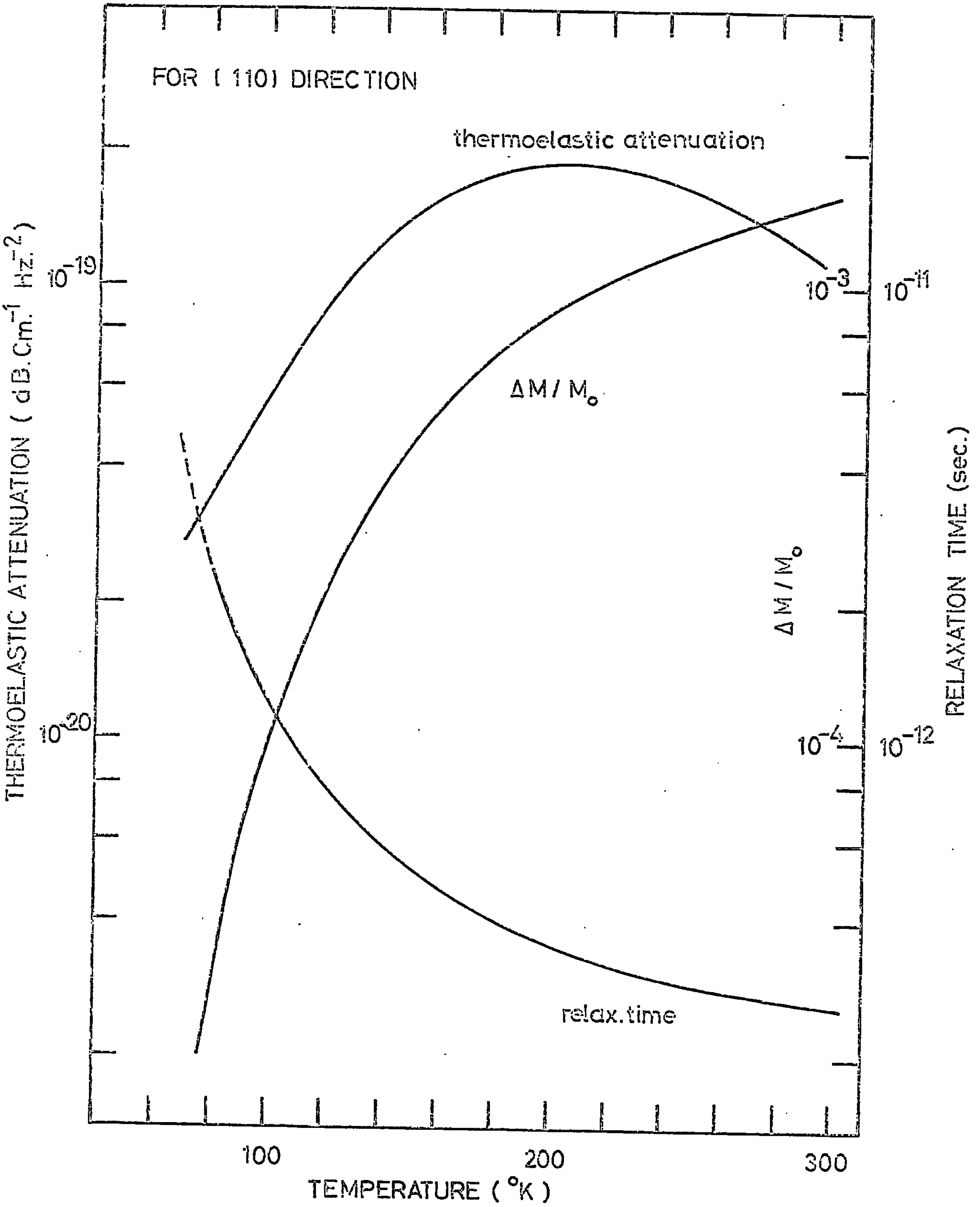

interactions giving rise to ultrasonic attenuation are those with lattice phonons and with dislocations. These effects will now be detailed in the next three chapters.

CHAPTER 7

ULTRASONIC WAVE INTERACTION WITH THERMAL ELASTIC WAVES: THE ULTRASONIC PHONON-THERMAL PHONON INTERACTION

7.1. INTRODUCTION

Ultrasonic waves in solids have, in principle, the same nature as the lattice waves which describe thermal vibrations. The former are available as coherent beams and are induced artificially; the latter constitute background noise. Thus an interaction can be expected between the two kinds of waves. The attenuation of the ultrasonic waves can be studied directly; the attenuation or scattering of thermal waves must be induced from conduction properties. Information obtained from the interaction between the waves adds greatly to knowledge, deduced from conduction experiments, of thermal waves. Unfortunately it has not yet been possible to establish good contact between these two methods of getting information. Reasons for this failure include a two orders of magnitude difference between the highest ultrasonic frequency and the thermal wave frequency at liquid helium temperature and the difficulty of separation of other contributions to ultrasonic wave attenuation.

A given ultrasonic wave interacts with thermal lattice waves by virtue of the anharmonic nature of interatomic forces in a solid. The bulk of this interaction is with thermal waves of approximate frequency kT/h. The lattice waves are also subject to interaction processes and have a mean free path (l). If the wavelength (λ) of the driving ultrasonic waves is less than that mean free path (l) of the thermal waves ($\lambda << l$), one can assume the wave to interact with individual lattice modes. This condition is met when one is considering the attenuation of ultrasonic waves in very low temperatures. However, for ultrasonic waves, this condition is not fulfilled, except at the lowest temperatures and at the highest frequencies. In the other extreme, when the wavelength (λ) of the driving ultrasonic wave is greater than the mean free path (l) of the thermal waves ($\lambda >> l$), one can treat the interaction as taking place not with individual thermal modes but with the entire assembly of lattice waves or the phonon gas.

The effects of absorption by the lattice itself will always be present. It can be best studied in dislocation-free, insulating crystals, in which the other contributions are negligible, and at low temperatures where the mean free path of the lattice waves (l) is comparable with the wavelength of ultrasonic waves (λ). In other types of material, such as mercury telluride, the difficulty is to separate the contributing effects.

The works of Bömmel and Dransfeld (1960) on ultrasonic attenuation in quartz opened the field of sound absorption in insulating crystals. They measured the temperature dependence of ultrasonic attenuation at the frequency of 1000 MHz for temperatures below about 140^{o}K. Similar measurements have followed in quartz and other insulating crystals, alkali halides, elemental semiconductors and some III-V compounds. Experiments in quarts include those of Nava, Azrt, Ciccarello and Dransfeld (1964) in the frequency range 500 MHz to 10,000 MHz at temperatures below 40°K, and those of Lewis and Patterson (1967) at 9,000 MHz and temperatures below about 30°K. Hanson (1967) looked at lithium fluoride between 500 MHz and 2,500 MHz at temperatures below 50°K. Germanium has been studied by Dobbs, Chick and Truell (1959) in the frequency range 333 MHz to 508 MHz below room temperatures, silicon by Mason (1965, p.250) at 495 MHz below room temperature, galium arsenide by Pomerantz (1965) at 9000 MHz. All these measurements exhibit similar characteristic features in crystals with low dislocation content. Let us note some of these features of the experimental results on the temperature dependence of ultrasonic attenuation. In the range below about 30°K, the attenuation is low and almost temperature independent. At some higher temperature the attenuation increases steeply with temperature and then, in some of the measurements, the attenuation decreases slightly with increasing temperature followed by a region of temperature independence. These features are quite similar to those found for mercury telluride in the present experiment. Now the mechanism of ultrasonic attenuation due to the acoustic phonon-lattice phonon interaction will be summarised.

7.2. THEORY OF THE PHONON VISCOUS DRAG.

7.2.1. Anharmonicity and Phonon-phonon scattering.

For ultrasonic waves to be attenuated by thermal phonons, there must be coupling. The origin of this coupling is the change in the elastic properties of a medium by the strain imposed by the sound wave. This may be seen explicitly by expanding the potential energy (U) of a solid in powers of strain components

$$U = U_o + \frac{1}{2} \sum_{i,j=1}^{6} C_{ij}\epsilon_i\epsilon_j + \frac{1}{6} \sum_{i,j,k=1}^{6} C_{ijk}\epsilon_i\epsilon_j\epsilon_k + \cdots \qquad (7.1)$$

Here U_o is the potential energy of the solid, when all strains are zero. If the first two terms only in the expansion are retained, we have an approximation corresponding to the perfectly elastic or harmonic solid, and the small amplitude sound waves propagate without interacting each other. In Chapter 4 this situation has been discussed. The third and higher order terms, known as the anharmonic terms, give rise to interactions between these waves.

If the first anharmonic term is considered to be much larger than the others, then the constants C_{ijk} determine the strength of the anharmonic interactions. These C_{ijk} are known as the third-order elastic constants. Because of the anharmonic terms in Equation (7.1), the velocity of an elastic wave changes, if the solid is strained. Hence by measuring the sound velocity in a solid under different static stresses, one can determine experimentally the third-order elastic constants (C_{ijk}).

The thermal phonon velocity is altered by scattering by amounts which differ for phonons of different polarization ($\underline{j}$) and different propagation vector ($\underline{k}$). The relation between the fractional velocity change $(\Delta v/v)_{j,k}$ for a branch (j,k) and the relative density change $(\Delta\rho/\rho)$ is given by

$$\left(\frac{\Delta v}{v}\right)_{j,k} = \gamma_{j,k}\left(\frac{\Delta \rho}{\rho}\right) \qquad (7.2)$$

The constant $\gamma_{j,k}$ is also a measure of the strength of the anharmonic interaction and is linearly related to third-order elastic constants.

A useful assumption often made in the theory of solids, gives a rough measure of the strength of the anharmonic interactions. If the $\gamma_{i,j}$ are assumed to be the same for all the branches and are set equal to γ (the Grünersen constant), then

$$\gamma = \frac{3\,\alpha\,\beta}{c} \qquad (7.3)$$

Here α is the thermal expansion coefficient, β is the bulk modulus and c is the specific heat per unit volume.

In the absence of coupling, the sound wave can be described by its angular frequency ω and its wave vector $\underline{k}$, which is in the direction of propagation of equal phases, and $\underline{k} = 2\pi/\lambda$. These are related by $\omega = \underline{k}/v$, where v is the velocity of sound in the direction of the wave vector. Thermal phonons are similarly described, but their velocity is a function of $\underline{k}$ for the large values of k; that is the lattice is dispersive, when the wavelength of sound approaches interatomic distances. A phonon has energy $E(=\frac{h}{2\pi}\omega)$ and momentum $P(=\frac{h}{2\pi}k)$.

In the theory of ultrasonic attenuation due to phonon-phonon interactions, the scattering of a sound wave with a single phonon to produce another phonon is calculated. Then a summation over all the phonons is made. The energies and momenta of the waves are well defined and their totals are conserved. In a typical event

$$\begin{aligned} \frac{h}{2\pi}\,\omega + \frac{h}{2\pi}\,\omega_1 &= \frac{h}{2\pi}\,\omega_2 \\ \frac{h}{2\pi}\,k + \frac{h}{2\pi}\,k_1 &= \frac{h}{2\pi}\,k_2 \end{aligned} \tag{7.4}$$

Here ω, k describe the impressed ultrasonic phonon, ω_1, k_1 and ω_2, k_2 describe the initial and the resulting thermal phonon. Equation (7.4) describes a three-phonon process. Interactions involving four or more phonons are also possible in higher order theory.

7.2.2. Attenuation of Ultrasonic Waves.

There are two types of ultrasonic phonon-lattice phonon interactions leading to attenuation. One is the thermoelastic loss, which has been discussed in Section (6.2, p.92), negligible in insulating and semiconducting crystals. The other mechanism is the lattice phonon viscous drag effect which is largely responsible for the ultrasonic attenuation; a number of attempts have been made to calculate the attenuation due to this effect. Two approaches are particularly useful, one is due to Bömmel and Dransfeld (1960) and the other to Woodruff and Ehrenreich (1961); both are based on the original suggestions of Akhieser (1939). The interpretation given in the theories is not entirely quantitative because only rough values of some of the parameters entering the theory are available at present; so the theories do not fully account for the observed behaviour.

Akhieser first introduced the concept of a new process different from the thermoelastic loss. To explain this process he pointed out that a sound wave passing through a crystal would cause a disturbance of the distribution of thermal phonons, so that the phonons corresponding to the thermal lattice vibrations have no longer an equilibrium Planck distribution. The re-establishment of equilibrium in the phonon gas requires an increase of entropy and, therefore, leads to the absorption of sound at finite temperatures.

In the region of present interest, the wavelength of a thermal phonon is always shorter than the ultrasonic wavelength ($l \ll \lambda$). In this case it may be considered that the thermal phonon travels through a uniform medium which is being slowly modulated by the sound wave.

Both Bömmel and Dransfield and Woodruff and Ehrenreich use similar approximations to apply their theoretical results to experimental data. Namely; (i) they consider that the medium in which the sound waves are propagated is a simple isotropic Debye solid. As a consequence of this, dispersion is ignored and phonons of all frequencies in a single branch have the same velocity change for a given strain. (ii) due to lack of sufficient data on the anharmonicity parameter ($\gamma_{j,k}$), both theories consider only the general features of absorption processes, while taking simply an average anharmonicity parameter (γ). (iii) Woodruff and Ehrenreich considered the total or combined relaxation (τ) defined by

$$\frac{1}{\tau} = \frac{1}{\tau_U} + \frac{1}{\tau_N} \qquad (7.5)$$

for their theoretical derivation. Due to the difficulties in separating out the relaxation times for normal phonon scattering processes (τ_N)

and for umklapp processes (τ_U), both theories consider only phonon-phonon umklapp processes. Then the relaxation time can be deduced from thermal conductivity data.

$$K = \frac{1}{3}\, cvl \tag{7.6}$$

Here v is the average phonon velocity and l is the phonon mean free path between collisions equal to $v\tau$.

To calculate the attenuation coefficient Bömmel and Dransfeld consider that if a longitudinal sound wave propagates through the crystal, a periodic temperature difference will be set up. A relaxation time (τ) is assumed for the heat exchange which takes place; this exchange in time leads to an increase in entropy corresponding to absorption of the ultrasonic waves. Since this effect is a relaxation process, the absorption coefficient can be calculated as

$$\alpha = \frac{c\ \ T\ \ \gamma^2_{\text{Ave.}}}{\rho v^3} \left(\frac{\omega^2 \tau}{1+\omega^2\tau^2} \right) \tag{7.7}$$

At high enough temperatures the relaxation time (τ) is much shorter than the sound period, $\omega\tau \ll 1$, and the absorption coefficient given in Equation (7.7) reduces to:

$$\alpha = c\ \ T\ \ \gamma^2_{\text{Ave.}}\, \omega^2 \tau / \rho v^3 \tag{7.8}$$

The effect of the temperature dependent factors cancel and it turns out that ultrasonic attenuation is practically temperature independent at these high temperatures. In this region the attenuation is frequency square dependent.

For $\omega\tau >> 1$, the Woodruff and Ehrenreich result, following the approximations mentioned above reduces to

$$\alpha = \frac{8 \cdot 68\, \gamma^2_{\mathrm{Ave.}}\, \omega T K}{\rho\, v^5}\; \frac{\tan^{-1}(2\omega\tau)}{2\omega\tau} \quad (\mathrm{dB/cm}) \qquad (7 \cdot 9)$$

Their result, for $\omega\tau << 1$ is exactly the same as that given by Bömmel and Dransfeld (Equation 7.8).

7.2.3. The applicability of the theories to the measurements.

Both theories for $\omega\tau << 1$ give the same result: temperature independent attenuation. This behaviour has been observed by many workers (see Bömmel and Dransfeld measurements above 60°K, Figures 4, 5 and 6). Verma and Joshi (1961) used Equation (7.7) to calculate the ultrasonic attenuation as a function of temperature for germanium and compared the result with measured values (Dobbs, Chick and Truell 1959). For this theoretical assessment, they deduced the relaxation time for phonon-phonon umklapp processes from thermal conductivity. The average anharmonicity constant was obtained by choosing it such that the theoretical value of ultrasonic attenuation was equal to the experimental value at a certain temperature. The agreement between the experimental values and the theoretically calculated values is good.

Miller (1963) has used Equation (7.9) given by Woodruff and Ehrenreich for the case where $\omega\tau >> 1$, to calculate the ultrasonic attenuation as a function of temperature so as to compare the theoretical estimation with experiments on germanium. For this analysis, he estimated the anharmonicity parameter in several ways. Firstly, he assumed that γ is temperature independent. This procedure was also previously used by Verma and Joshi (1961) and explained in last paragraph. The temperature independent γ yielded a strong peak, in disagreement with the experimental results. Next by taking the temperature dependence of the thermal expansion Grünersen constant (Equation 7.3), he obtained slightly better agreement (see Figure 7 in Miller 1963).

Although the Bömmel and Dransfeld approach is based upon very simple arguments, it seems to give a better fit to the temperature dependence of ultrasound attenuation due to phonon-phonon interaction for $\omega\tau >> 1$. But, as indicated by Woodruff and Ehrenreich, neither theory is really valid for $\omega\tau >> 1$.

The main difficulty in applying these theories to the experimental measurements comes from the assessment of the anharmonicity parameter γ. As acoustical waves in solids are involved with particular phonon branches, the thermal expansion Grüneisen parameter cannot be a true measure of lattice anharmonicity for the ultrasonic attenuation. The thermal expansion Grüneisen constant, given in Equation (7.3) is the total measure of bulk anharmonicity of the lattice. Furthermore, it does not give any explanation of shear wave losses.

Mason and Bateman (1964) have been able to account for the ultrasonic attenuation for all values of temperature using a relaxation model derived from Equation (7.7). They attempted to deduce the anharmonicity parameter (γ) using third order elastic constants. Mason and Bateman obtained agreement within about 30% for longitudinal wave attenuation and within about 50% for shear waves in both germanium and silicon. It was noted, however, that the relaxation time that gave good agreement with the experiments was twice the thermal conductivity relaxation time τ for longitudinal wave attenuation. Here the limitation at present is that the third order elastic constants have been measured for only a few materials.

The theory of absorption of ultrasonic waves due to their interaction with the thermal phonons is extremely complex and only qualitative at present. Now the ultrasonic wave attenuation in mercury telluride single crystals due to ultrasonic phonon-lattice phonon interaction will be discussed.

7.3 RESULTS AND DISCUSSION

The low temperature characteristics of ultrasound attenuation shown in Figures (5.1), (5.2), (5.3), (5.4) and (5.5) in mercury telluride single crystals imply that one of the dominating sound energy dissipation mechanism is the ultrasonic phonon-lattice phonon interaction. This effect, previously observed in insulators and semiconductors in high ultrasonic frequencies (above 500 MHz) is large in the semimetal mercury telluride and it is observable at relatively low frequencies (30 MHz).

When the thermal phonon mean free path is small compared with the sound wavelength ($l \ll \lambda$ or $\omega\tau \ll 1$), both theories give the same result (Equation 7.8). Deducing the relaxation time (τ) from thermal conductivity data (Equation 7.6) an expression giving ultrasonic attenuation due to this effect takes the following form

$$\alpha = \frac{8\cdot 68\ \gamma^2_{\text{Ave.}}\ \omega^2 KT}{\rho\ v_m^5} \quad (\text{dB/cm}) \tag{7.10}$$

Here v_m is the averaged Debye velocity which can be deduced from the elastic constants. In terms of Debye temperature (θ_D) and lattice spacing (a_o), v_m has been given in Equation (4·42, p.65):

$$v_m = 1\cdot 6795 \times 10^{10}\ \theta_D\ a_o \tag{7.11}$$

Inserting the value of 141°K for Debye temperature (θ_D) (see p.67) and 6·462Å for lattice spacing (a_o) (see p.18), average sound velocity in the Debye sense for mercury telluride turns out to be $1\cdot 53 \times 10^5$ cm/sec, considerably less than that of germanium ($3\cdot 55 \times 10^5$ cm/sec), silicon ($5\cdot 87 \times 10^5$ cm/sec) and quartz ($4\cdot 39 \times 10^5$)(Mason 1965, p. 269 and 272). Since ultrasonic attenuation due to phonon-phonon interaction is proportional to the inverse fifth power of the average sound velocity, a stronger ultrasonic attenuation at a given frequency would therefore be expected in mercury telluride. The effect can be observed at comparatively low frequencies.

In the vicinity of the Debye temperature the temperature dependence of thermal conductivity of mercury telluride is inversely proportional to temperature (Carlson 1958 and see Appendix A). Thus Equation (7.12) gives a temperature independent attenuation. This behaviour is found in most of the measurements in the temperature region of about 70°K to about 150°K (see Figures 5·1 and 5·2). Although there is no experimental data on the temperature dependence of thermal conductivity of mercury telluride below

77^{o}K, it is not difficult to deduce the low temperature behaviour of thermal conductivity by analogy with similar materials. In general the slope of thermal conductivity versus temperature curve is greater than (T^{-1}) thus, from Equation (7.10), attenuation of ultrasonic waves is temperature dependent and it decreases with increasing temperature. This behaviour is observed in all the cases and shown in Figures (5.1), (5.2), (5.3), (5.4) and (5.5). The temperature dependence of thermal conductivity, in general, increases sharply with decreasing temperature until about $\theta_D/20$. So the mean free path of thermal phonons begins to be comparable with the sound wavelength. This is the region where relaxation starts and Equation (7.10) is no longer applicable. At low temperatures where the mean free path of thermal phonons begin to be comparable with the sound wavelength ($l \approx \lambda$ or $\omega\tau \approx 1$) or even greater ($l \gg \lambda$ or $\omega\tau \gg 1$) both the Bömmel and Dransfeld (Equation 7.7) and Woodruff and Ehrenreich (Equation 7.9) theories predict a sharp decrease in attenuation with decreasing temperature. This feature is also observed and shown in Figures (5.1), (5.2), (5.3), (5.4) and (5.5). This sharp decrease ends at low temperatures and the attenuation is temperature independent. As this behaviour is not intrinsic, none of the theories can take this range into account. Thus, the general features of ultrasonic attenuation at low temperature in single crystals of mercury telluride are understandable qualitatively. But, due to lack of experimental data on thermal conductivity at low temperatures, no attempt can be made to calculate the temperature dependence of ultrasonic attenuation due to the phonon-phonon process.

The Grüneisen parameter (γ) which describes the anharmonicity of the lattice, is not available from third-order elastic constants which are not known. However, here γ is treated as an adjustable parameter and assuming the theories are correct for the temperature region where $\omega\tau \ll 1$, are deduced from the experimental measurements. For this assessment γ (the acoustical Grüneisen parameter) is expressed from Equation (7.10) in the following form.

$$\bar{\gamma}^2 = \frac{\rho \; v_m^5}{8 \cdot 68 \; 4 \; \pi^2 \; KT} \; \frac{\alpha}{f^2} \tag{7.12}$$

The values of the acoustical Grüneisen constant have been obtained by choosing it such that the theoretical value of the ultrasonic attenuation is equal to experimental value at 40°K. The thermal conductivity of mercury telluride at 40°K has been obtained as $3 \cdot 4 \times 10^7$ (ergs/sec.cm°K) by extrapolating the Carlson (1958) data using the relation (Rosenberg 1963, p.58):

$$K = y(\theta_D / gT) \tag{7.13}$$

Here y and g are constants, which are deduced to be $1 \cdot 176 \times 10^{-2}$ and $0 \cdot 617$ respectively and θ_D is the Debye temperature. Inserting the values of the related parameters into Equation (7.12), the acoustical Grüneisen parameter in terms of sound attenuation and the frequency turns out to be

$$\bar{\gamma} = 3 \cdot 8 \times 10^7 \; \frac{\alpha^{\frac{1}{2}}}{f} \tag{7.14}$$

Here α is the intrinsic ultrasonic attenuation with units of dB/cm which is defined as the attenuation at 40°K minus the residual attenuation (α_o). In Table (7.1) the intrinsic ultrasonic attenuation at 40°K and the acoustical Grüneisen parameter are tabulated. In most of solids $\bar{\gamma}$ calculated in a similar manner falls within the limits for $\bar{\gamma} = 0{\cdot}6$ and $\bar{\gamma} = 1{\cdot}2$ (Oliver and Slack 1966). Mercury telluride, except for the shear wave propagating along [111] crystallographic direction, shows similar behaviour. For comparison, the thermal expansion Grüneisen parameter is estimated as $0{\cdot}65 \pm 0{\cdot}10$ from the Equation (7.3).

Here for both shear and longitudinal waves the same relaxation time is used. However, in reality, longitudinal waves can interact with both longitudinal and shear phonons of the same frequency range. Thus, they have longer relaxation times. Experiments indicate that the relaxation time for longitudinal waves is about twice that for the thermal relaxation time (Mason 1965, p.268). Thus the acoustical Grüneisen parameters ($\bar{\gamma}$) for mercury telluride, presented in Table (7.1), even considering the errors involved in the extrapolation of the thermal conductivity are probably high. This fact is also clearly shown in the value of the acoustical Grüneisen parameter calculated from shear wave attenuation along [111] crystallographic direction (Figure 5.5). Therefore, it is considered that another energy dissipation mechanism, other than of due to ultrasonic phonon-lattice phonon interaction, contributes to the sound attenuation in mercury telluride at low temperatures. Further, both theories predict that a frequency square dependence of attenuation for $\omega\tau << 1$. This is not (see Figures

TABLE (7.1) The acoustical Grüneisen parameters estimated from the ultrasonic attenuation of longitudinal waves propagated in mercury telluride single crystals.

Direction of Propagation	Velocity of sound at $4\cdot2^{o}K$ (cm/sec)	Frequency (MHz)	Intrinsic ultrasonic attenuation $(\alpha-\alpha_{o})$db/cm	Acoustical Grüneisen parameter $\overline{\gamma}$	Data source
$[111]_{long.}$	$3\cdot073\text{x}10^{5}$	50	2·44	1·19	Figure (5.3)
		30	1·02	1·28	Figure (5.3)
$[100]_{long.}$	$2\cdot961\text{x}10^{5}$	50	2·04	1·07	Figure (5.3)
$[110]_{long.}$	$2\cdot982\text{x}10^{5}$	70	2·48	0·86	Figure (5.4)
		50	1·16	0·81	Figure (5.4)
$[111]_{shear}$	$1\cdot284\text{x}10^{5}$	75	10·7	5·25	Figure (5.5)

8.5, 8.6 and 8.7 in Chapter 8). The phonon-phonon mechanism suggests a temperature independent attenuation around the Debye temperature where thermal conductivity is inversely proportional to temperature. Figures (5.1), (5.2), (5.6), (5.7) and (5.8) show that this is not so. Thus not only the phonon-phonon interaction is responsible for the ultrasonic attenuation in mercury telluride at low temperatures. This further contribution will be discussed in subsequent chapters.

CHAPTER 8

DISLOCATION CONTRIBUTION TO THE MEASURED ATTENUATION IN MERCURY TELLURIDE

8.1. INTRODUCTION

The pronounced lattice phonon-ultrasonic wave interaction (Akhieser effect) occurs in the intermediate temperature range 20°K to 40°K. For higher temperatures ($\omega\tau \ll 1$) this effect should result in a temperature independent attenuation. This is found only over a limited temperature range (see Figures 5.1, 5.6, 5.7 and 5.8). Another energy dissipation mechanism must be extant. Evidence that this is dislocation damping is strong. In the crystals under study the dislocation density of 10^7 pits per square centimetre is as high that in cold worked metals; dislocation effects can be expected. The frequency dependence of the attenuation exhibits the characteristics expected of dislocation damping. Further confirmation comes from measurements of the strain dependence of attenuation.

8.2. THE VIBRATING STRING MODEL OF DISLOCATION DAMPING

To explain the plastic or anelastic behaviour of solids, line lattice imperfections known as dislocations which extend over many thousands of atoms, were introduced into the theory of solids as early as fifty years ago. The interaction of sound waves with dislocations causes energy dissipation (Read 1941). Although Read's work and similar investigations had early established the importance of dislocations in mechanical damping, it was not until recently that a detailed picture of at least some aspects began to emerge. Two main reasons are responsible for the slow progress. Firstly, mechanical damping in single crystals is most sensitive to static stresses. Therefore, as reported by Mason and Rosenberg (1967) and other investigators, internal friction measurements are extremely dependent on handling damage. In the present work, increases in attenuation due to handling have been observed. Secondly, mechanical damping depends on the amplitude of the alternating stress employed in the measurement. Nevertheless damping experiments do provide an excellent method of studying dislocations.

Sound absorption due to dislocation movement may be classified as follows:

1. Resonance losses
2. Hysteresis losses
3. Relaxation losses

Considerable success has been achieved in explaining dislocation damping, resonance losses by a model, which considers the dislocation as vibrating strings, proposed by Koehler (1952) and extended by Granato and Lücke (1956). Although the qualitative features of the interaction have been well demonstrated in many experiments, due both to experimental difficulties and to the problems of resolving and estimating theoretical parameters, quantitative agreement with experiment is rather poor.

This model considers the dislocation lines in a crystal to be pinned by impurities or vacancies or dislocation nodes at various points along their length (see Figure 8.1a). The distance between two pinning points is called the loop length L_c. In addition it is assumed that the interaction of the dislocation with the lattice and also dislocation interactions can be neglected.

If an external stress is now applied, there will be, in addition to the elastic strain, an additional dislocation strain. The stress-dislocation strain relationship corresponding to this model is shown in Figure (8.2). For a very small stress (A-B), the loops (L_c) bow out and continue to bow out until the breakaway stress is reached (C). Now, for further increases in the stress, the network length L_N bows out (D-E). It is assumed that the network pinning is so strong that no breakaway of network length occurs. However, further increases in the applied stress may lead to an activation of Frank-Read sources and, therefore, to irreversible dislocation strain, which is the plastic strain. This stress region will not be considered.

A hysteresis arises because during the unloading part of the stress cycle (D-A in Figure 8.2), the long loops collapse elastically. When the loops have completely collapsed, they again become pinned and the same type of path (A ⟶ B ⟶ C ⟶ D) is followed in the other half cycle. For small enough stresses, hysteresis does not occur because the breakaway from the pinning points cannot take place.

In this model dislocation lines are treated as extensible strings

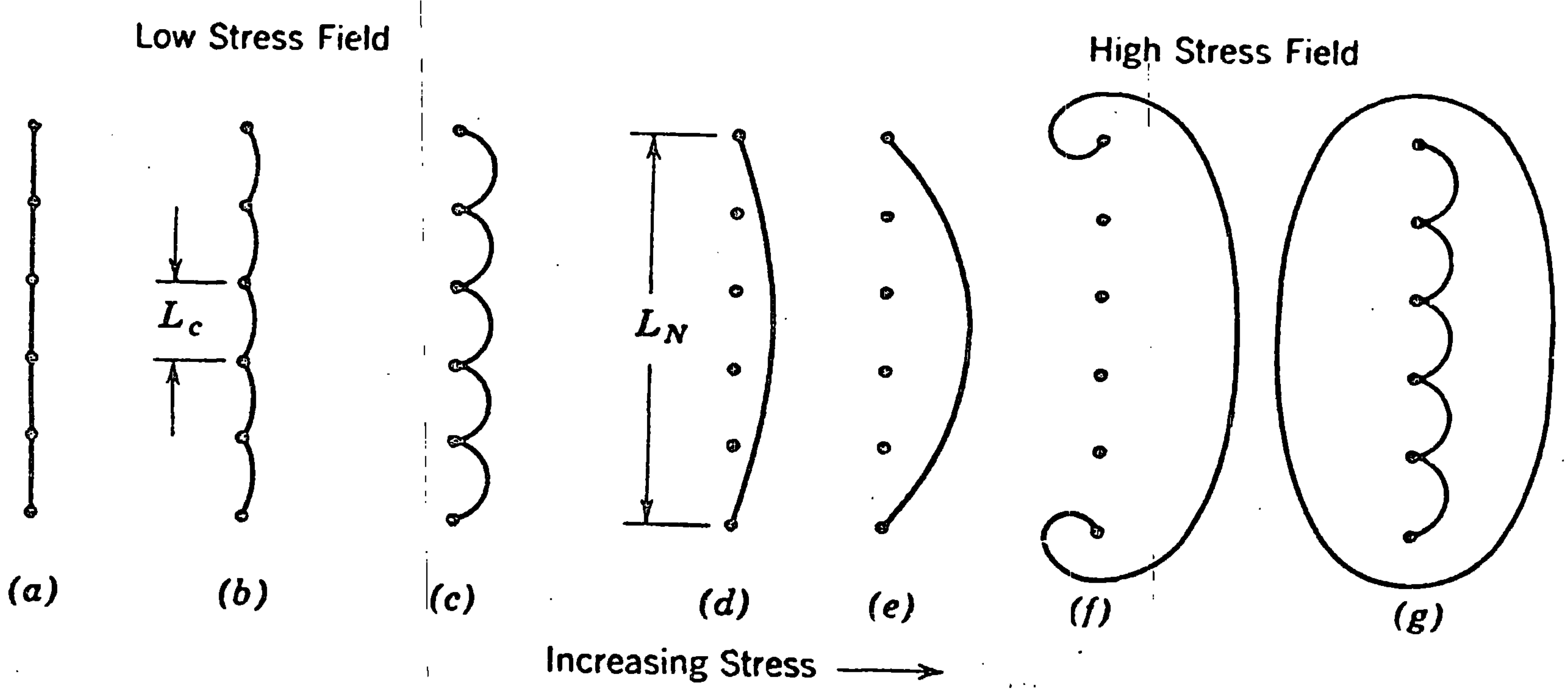

FIGURE (8.1). Pinned dislocation model used in the Granato and Lücke theory. The loop length determined by impurity pinning is denoted by L_c, and that determined by the network by L_N. As the stress increased, the loops L_c bow out (b and c) until breakaway occurs (d). For very large stresses, the dislocations multiply according to the Frank-Read mechanism (f and g) (After Granato and Lücke 1956).

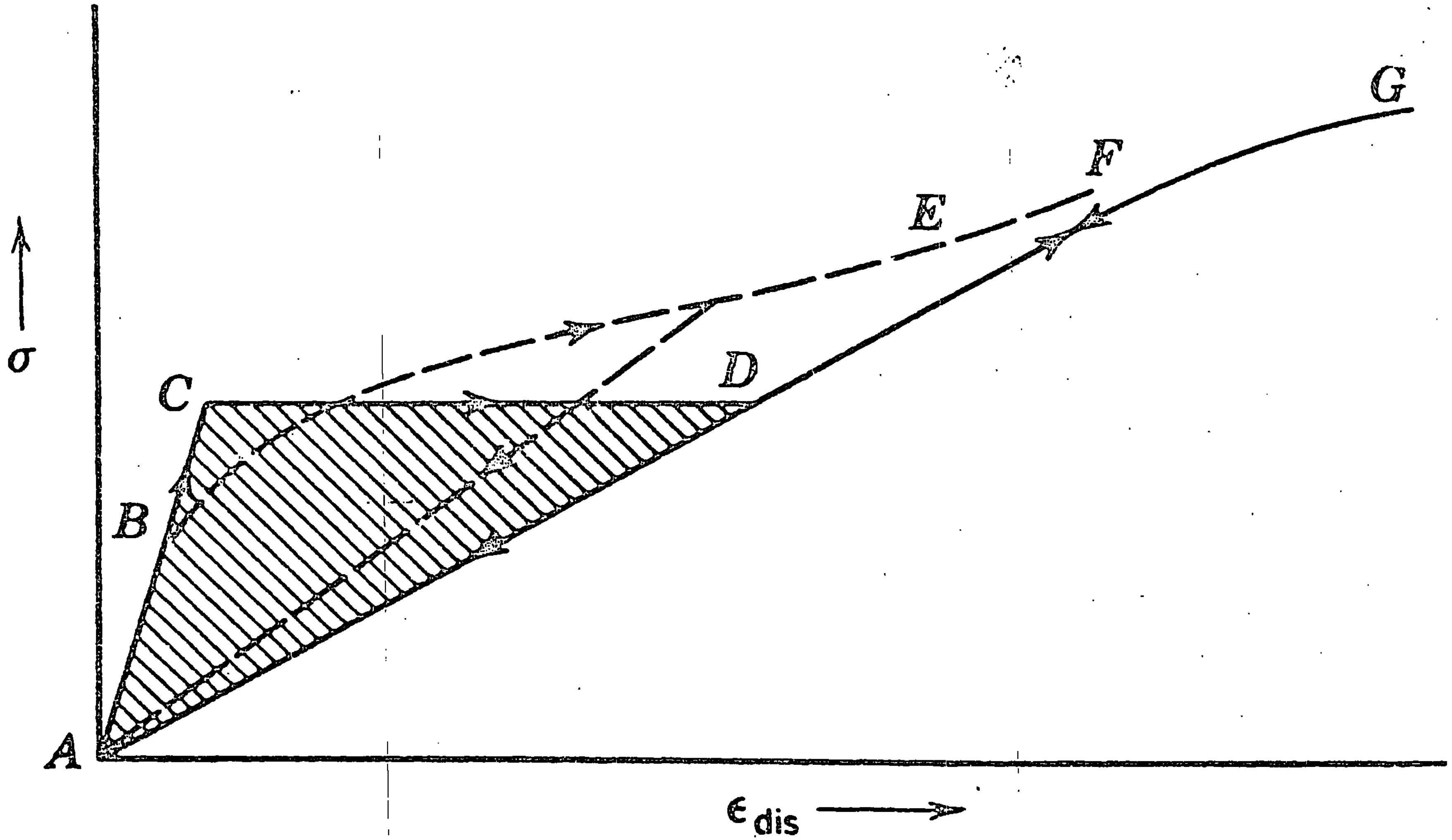

FIGURE (8.2). Stress-dislocation strain curve for the dislocation segment shown in Figure (8.1) (solid line). The dashed line curve is that which would result if not all the loops have the same length. (After Granato and Lücke 1956).

with a line tension and a mass. They can undergo resonance, if the frequency f of an applied alternating stress coincides with the characteristic frequency f_o of the dislocation string. As will be fully discussed later, such a resonance may or may not be observed, depending upon the damping forces of dislocations.

For stresses below that required for breakaway, the equation of motion for a loop of length l, perpendicular to the applied stress, is given by

$$A \frac{\delta^2 S}{\delta t^2} + B \frac{\delta S}{\delta t} - C \frac{\delta^2 S}{\delta y^2} = b\sigma \qquad (8.1)$$

here S = S(x,y,t) is the displacement of the dislocation from its equilibrium position, which is zero at y=o and y=l (nodal points), and the parameters in the equation have the following meanings:

A is the effective mass of dislocation per unit length, which is given approximately by

$$A = \rho b^2 \qquad (8.2)$$

Here ρ is the density of the material and b is the Burger's vector.

B is the damping or friction force coefficient on unit length of dislocation travelling with unit velocity.

C is the force per unit length due to the effective tension in a bowed-out dislocation and is given by

$$C = \frac{2 G b^2}{\pi(1-\nu)} \qquad (8.3)$$

Here G is the shear modulus, and ν is Poisson's ratio.

$b\sigma$ is the driving force per unit length of the dislocation exerted by the applied stress.

The mechanical damping caused by dislocations may be calculated by starting from Newton's equation of motion

$$\frac{\delta^2 \sigma}{\delta x^2} = \rho \frac{\delta^2 \epsilon}{\delta t^2} \tag{8.4}$$

Here ϵ is the total strain and contains the dislocation part, as well as the elastic part.

$$\therefore \epsilon = \epsilon_{el} + \epsilon_{dis} \tag{8.5}$$

The elastic strain (ϵ_{el}) is σ/G, while the dislocation strain (ϵ_{dis}) produced by a loop of length l may be represented by

$$\epsilon_{dis} = \bar{S}\, l\, b \tag{8.6}$$

where $\bar{S}$ is the average displacement of a dislocation and is given by

$$\bar{S} = \frac{1}{l} \int_0^l S\,(y)\, dy \tag{8.7}$$

If Λ is the total length of movable dislocation line in the unit cube, the dislocation strain can be obtained using Equations (8.6) and (8.7)

$$\epsilon_{dis} = \frac{\Lambda b}{l} \int_0^l S\,(y)\, dy \tag{8.8}$$

This equation together with the Equation (8.4) leads to following equation:

$$\frac{\delta^2\sigma}{\delta x^2} - \frac{\rho}{G}\,\frac{\delta^2\sigma}{\delta t^2} = \frac{\Lambda\rho b}{l}\,\frac{\delta}{\delta t^2}\int_0^l S\,(dy) \tag{8.9}$$

As shown by Granato and Lücke, Equation (8.9) and (8.1) form a system of two simultaneous partial differential integral equations. A trial solution of the form

$$\sigma = \sigma_0\, \exp(-\alpha x)\exp[i\omega(t-x/v)] \tag{8.10}$$

leads to an equation for the vibrational amplitude S and then using the expression S and σ, the attenuation and velocity can be deduced. Following Granato and Lücke, the mechanical damping and modulus change due to the dislocation mechanism are:

$$\Delta = \Omega\,\Delta_0\,\Lambda L^2\,\frac{\omega/\omega_0 D}{[1-(\omega/\omega_0)^2]^2+(\omega/\omega_0 D)^2} \tag{8.11}$$

$$\frac{\Delta M}{M} = \frac{\Omega\,\Delta_0\,\Lambda L^2}{\pi}\,\frac{[1-(\omega/\omega_0)^2]}{[1-(\omega/\omega_0)^2]^2+(\omega/\omega_0 D)^2} \tag{8.12}$$

where the parameters in these equations have the following meanings:

Ω is an orientation factor, which takes into account the fact that the mechanical damping should be sensitive to the crystal orientation and the distribution of the dislocations over the various slip systems.

Δ_0 is a constant for a given material and is given by

$$\Delta_0 = 8Gb^2/\pi^3 C \tag{8.13}$$

Here the significance of G, b and C have already been indicated.

Λ has been defined as the total length of dislocation lines per unit volume. The number of dislocations in a solid is specified by the density N: the number of dislocation lines that cross a unit area perpendicular to them. Thus N represents the total length of the dislocation line per unit volume of the solid.

L is the dislocation loop length.

D is the normalized damping constant and is given by

$$D = \omega_o A/B \tag{8.14}$$

ω is the angular frequency of the driving sound waves.

The frequency dependence of mechanical damping, obtained in this way, has some interesting features. In Figure (8.3) the normalised decrement ($\Delta/\Omega\Delta_o\Lambda L^2$) is plotted (after Granato and Lücke) as a function of normalised frequency (ω/ω_o). As shown from this figure, the decrement very much depends on the constants D or B ($D = \omega_o A/B$), which determine whether a resonance or a relaxation type loss should occur. For very small damping (B), the dependence is linear nearly up to the resonant frequency; next it passes through a maximum at $\omega/\omega_o = 1$ and then sharply decreases. The resonant frequency of dislocations is given by

$$\omega_o^2 = \pi^2 C/AL^2 \tag{8.15}$$

For larger damping, the initial response is linear up to a maximum value which occurs at a lower frequency than ω_o. Beyond the maximum, the decrement decreases as the inverse of frequency. After the true resonant frequency, it decreases very sharply.

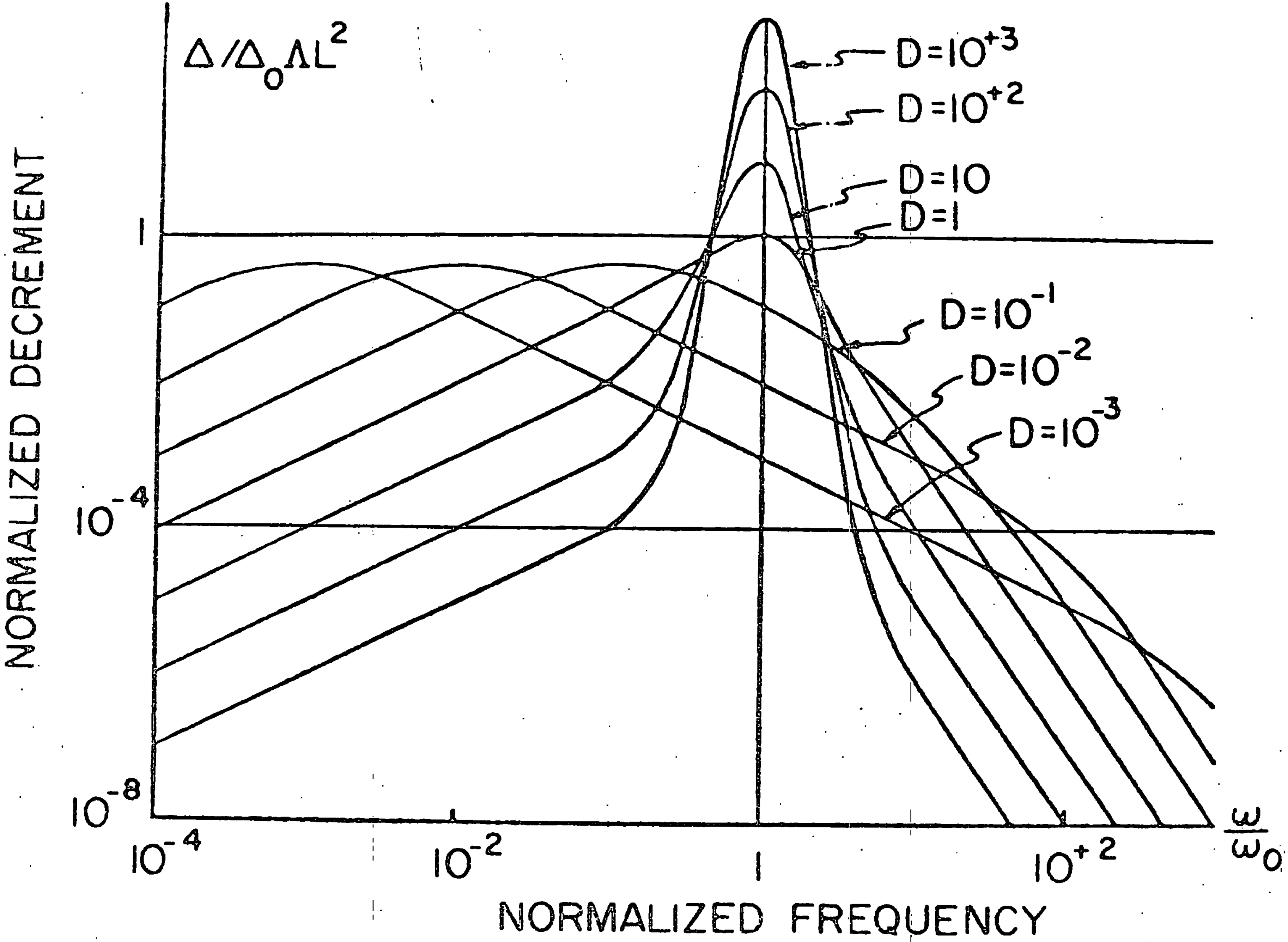

FIGURE (8.3). A plot of Equation (8.11).

For sufficiently low frequencies i.e. $(\omega/\omega_o)^2 << 1$, Equation (8.11) may be written in the form

$$\Delta = \Omega \Delta_o \Lambda L^2 \frac{\omega\tau}{1+\omega^2\tau^2} \tag{8.16}$$

Here τ, the relaxation time of a vibrating dislocation is

$$\tau = BL^2/\pi^2 C \tag{8.17}$$

When $\omega\tau = 1$, Equation (8.16) has a maximum given by

$$\Delta_m = \Omega \Delta_o \Lambda L^2/2 \tag{8.18}$$

This maximum occurs at the frequency

$$\omega_m = \tau^{-1} = \pi^2 C/BL^2 = \omega_o^2 A/B \tag{8.19}$$

For frequencies much greater than ω_m $(\omega\tau >> 1)$, Equation (8.16) may be written as

$$\Delta = \Omega \Delta_o \Lambda L^2/\omega\tau \tag{8.20}$$

or inserting the values of Δ_o and τ

$$\Delta = \frac{8 \Omega G b^2 \Lambda}{\pi B} \frac{1}{\omega} \tag{8.21}$$

This equation implies that, for sufficiently high frequencies the decrement varies with the inverse first power of the frequency, so that the attenuation α $(= \omega \Delta/2\pi)$ approaches a limiting value α_∞, which is

$$\alpha_\infty = 4 \Omega G b^2 \Lambda/\pi^2 B \tag{8.22}$$

This equation shows that the limiting value of attenuation is frequency independent and simply depends upon material properties only.

It must be expected that loop lengths are not equal in any real solid, but rather are distributed at random. The effect of a random (exponential) distribution is to shift the maximum to lower frequencies and higher values (Granato and Lücke, 1966).

$$\Delta_m = 2{\cdot}2\ \Omega\,\Delta_o\,\Lambda L^2 \tag{8.23}$$

$$\omega_m = 0{\cdot}084\ \pi^2 C/L^2 B \tag{8.24}$$

In this case, the high frequency asymptotes of the curves remain unchanged.

Now this model will be applied to the results of mercury telluride.

8.3. APPLICATION OF THE VIBRATING STRING MODEL TO MERCURY TELLURIDE

The results for mercury telluride best considered first are those taken at $4{\cdot}2^{o}$K, where the Akhieser effect is negligible. The frequency dependence of longitudinal waves propagated along the [110] direction is shown in Figure (5.9). At about 200 MHz the attenuation reaches a maximum. This is shown more clearly with expanded scales in Figure (8.4). The position of the maximum frequency ω_m is sharply defined by the plot of the decrement $\Delta(= \frac{2\pi\alpha}{\omega})$ in the same figure. This direct observation of the resonance peak provides strong evidence for Granato-Lücke dislocation damping in mercury telluride. Previously such a maximum has been reported for copper (Alers and Thomson 1961; Stern and Granato

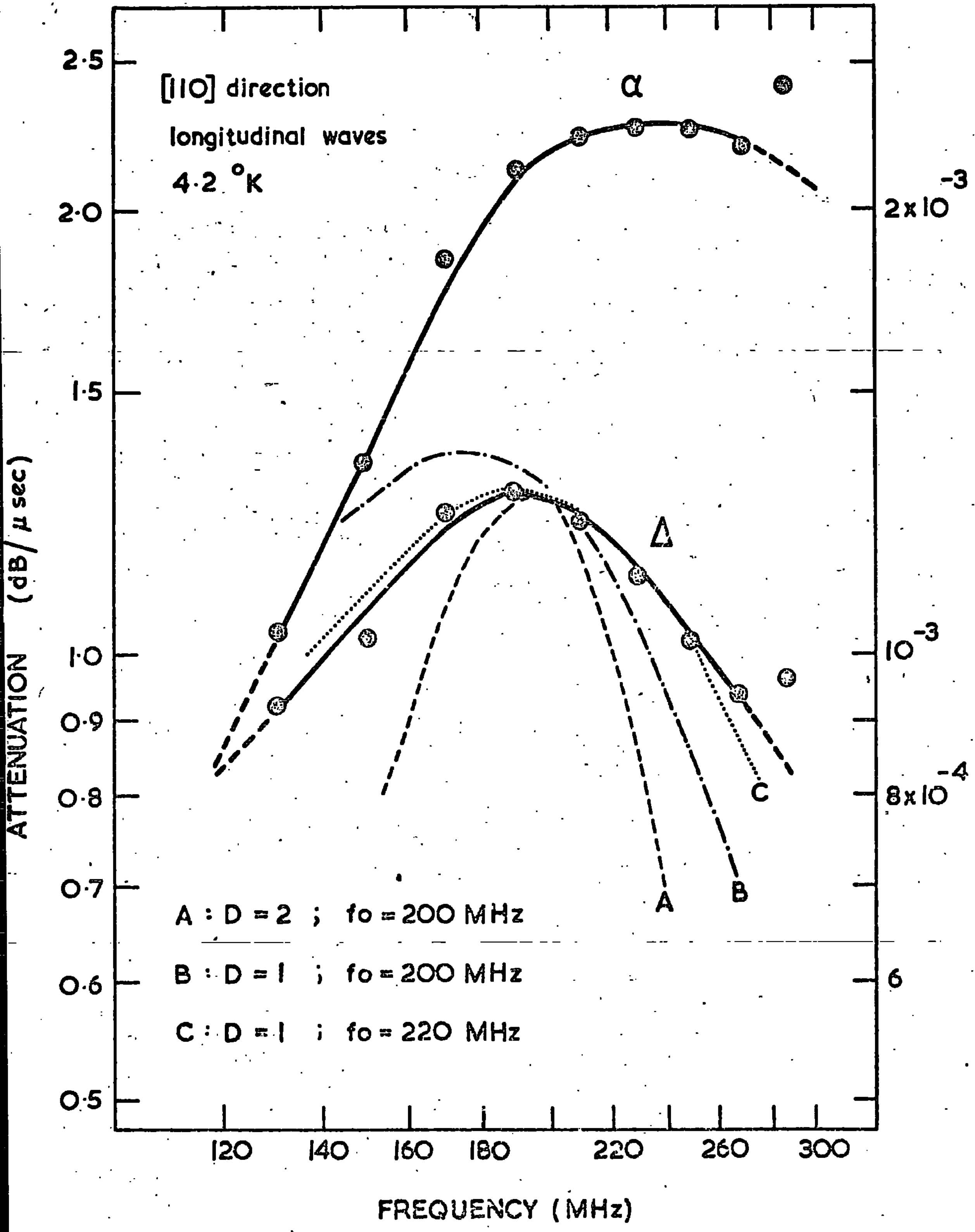

FIGURE (8.4). Frequency dependence of ultrasonic attenuation (α) and decrement (Δ) in annealed HgTe A, B and C are theoretical fits using Equation (8.11).

1962) and for sodium chloride (Merkulov and Yakovlev 1960).

Before the finding of a maximum in the attenuation can be used to assess dislocation parameters for mercury telluride, the proximity of the maximum to the resonance frequency must be ascertained. It can be seen from Figure (8.3) that as the normalized damping constant D decreases, so the maximum goes to lower frequencies below that of resonance (ω_o). The effective mass A of a dislocation is a constant and, therefore, $D(=\omega_o A/B)$ becomes larger and resonance is more closely approached as the drag coefficient B decreases. Leibfried (1950) has predicted that B should be very small at low temperatures. Experimental evidence for this has been provided for copper by Alers and Thomson (1961). This then is assumed. The frequency of the measured maximum in mercury telluride at 4·2°K must be very close to ω_o. The parameters D and ω_o are then assessed by taking them as variable parameters in the Granato and Lücke theory (Equation 8.11) and finding the best fit (see Figure 8.4). The general shape of the curve is not affected by the constant $(\Omega \Delta_o \Lambda L_c^2)$. The frequency at which the maximum is observed is $2\pi.190$ MHz. If this is the resonance frequency ω_o, then since ω_m is equal to $\omega_o D$, when the damping is low, D must be unity. However the best match between the measured points and the theoretical curves from equation (8.11) is obtained for D equal to unity and $f_o(=\omega_o/2\pi)$ equal to 220 MHz. This suggests that, even at 4·2°K, the frequency at which maximum attenuation is found is slightly lower than the true resonance frequency.

Once a value for the resonance frequency has been obtained, the temperature variation of the normalised damping constant D, and hence B, can be estimated by using the same matching procedure at other temperatures. It is not possible to carry this out with any accuracy over the whole temperature range because separation of the other contributing mechanisms is difficult. Liquid nitrogen temperature is the most convenient: the most pronounced effect of the phonon viscous drag occurs below this temperature ($\omega\tau = 1$ around 40°K) and Bordoni-type peaks are found above 200°K. The method of separation is now described.

The exponent of the frequency dependence of attenuation in mercury telluride is much less than two: behaviour consonant with damping due to dislocation motion. In those temperature ranges where peaks are absent, the measured attenuation can be formulated as

$$\alpha_{\text{measured}} = \alpha_{\text{Akhieser}}(\omega^2) + \alpha_{\text{dislocation}}(\omega^n)$$

The loss can be separated into a frequency square loss, associated with direct conversion of acoustic energy into heat, and the dislocation contribution. This procedure has been verified by Granato and Truell (1956) and by Mason and Rosenberg (1966, 1967). During the present work this procedure has been adopted. Typical examples of the separation method are illustrated in Figures (8.5), (8.6) and (8.7). For the large damping case at higher frequencies the dislocation contribution to the attenuation approaches a frequency independent region: the asymptote at high frequencies to the measured points at higher temperatures gives a

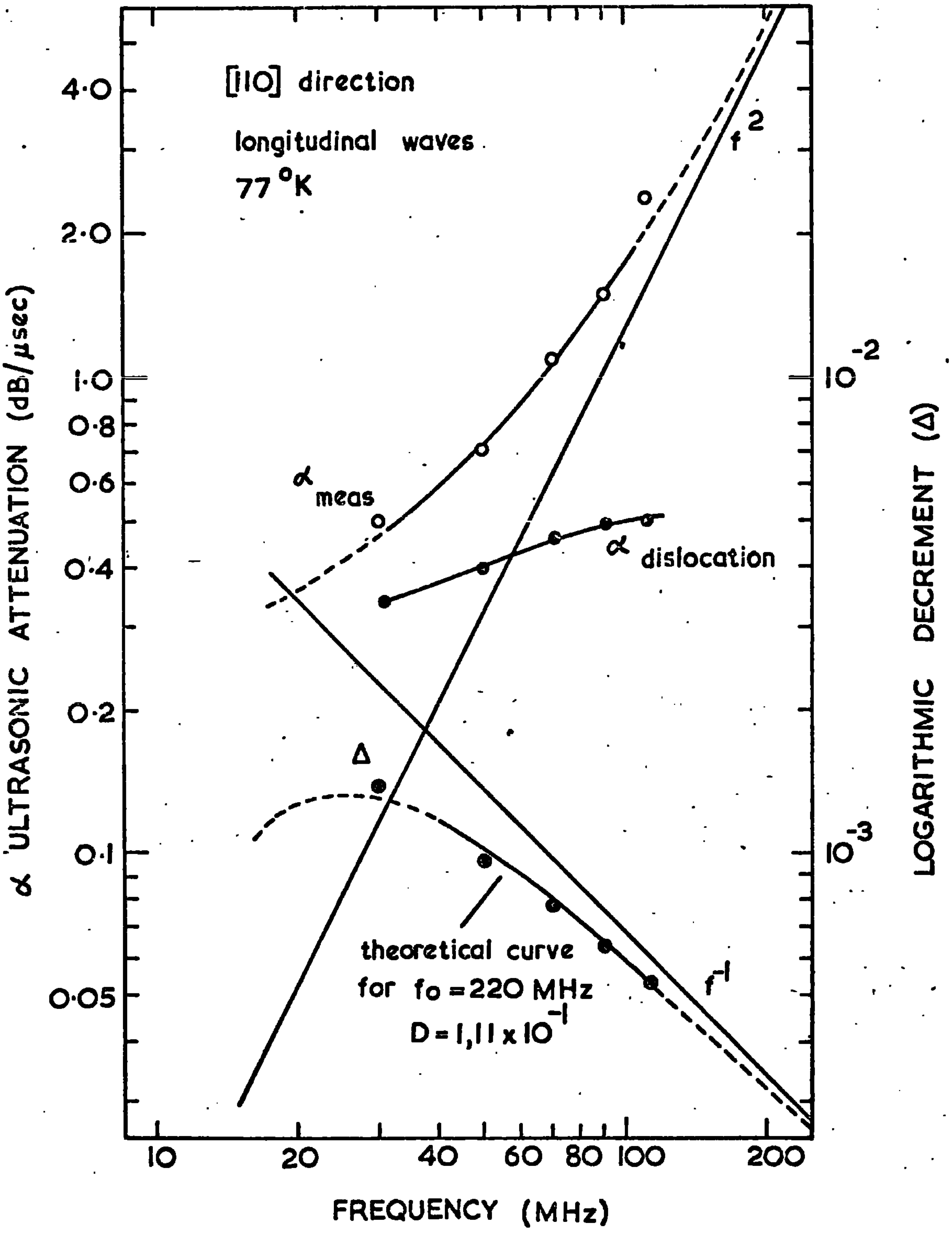

FIGURE (8.5). Separation of measured attenuation into the dislocation part and the square-law term.

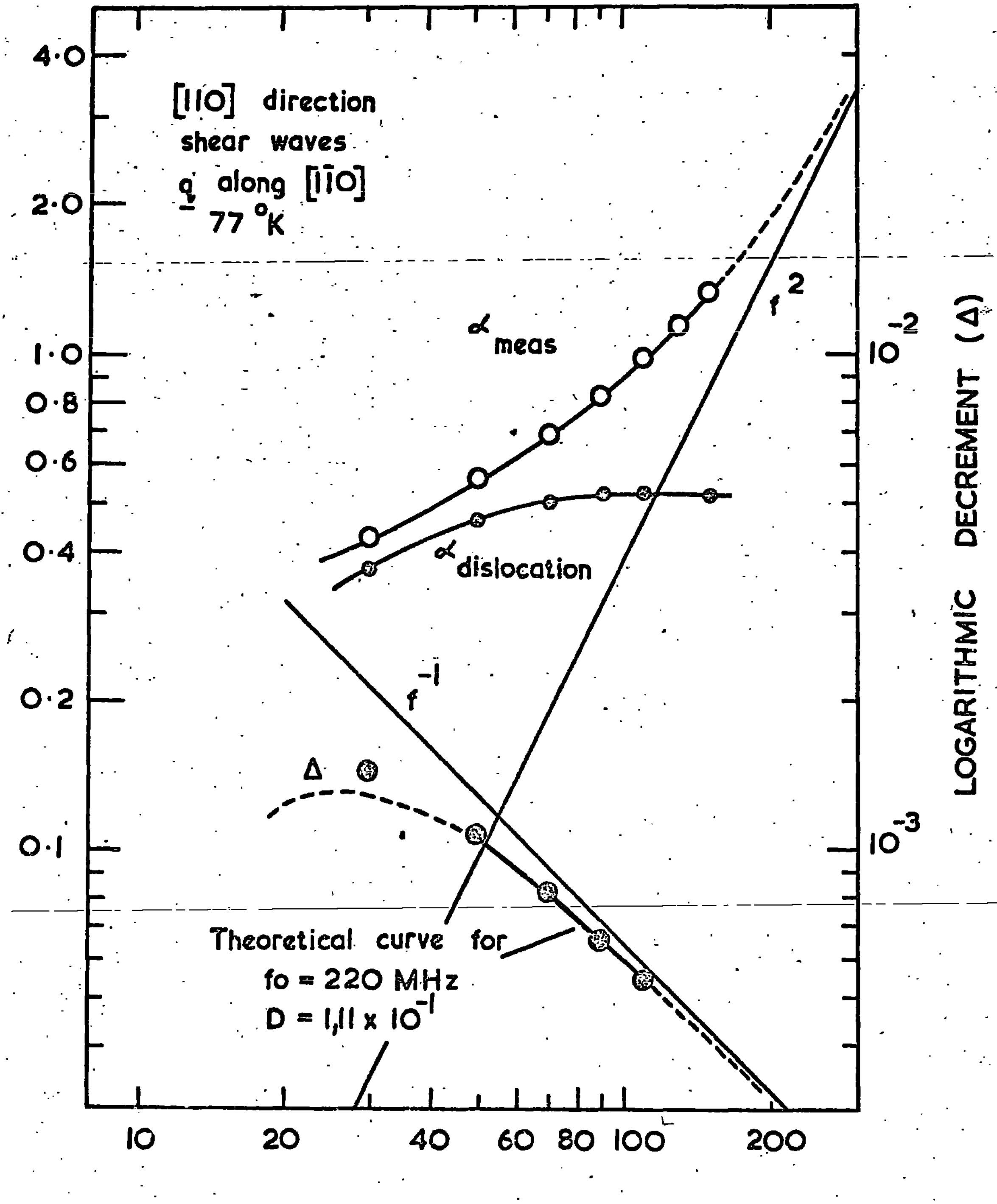

FIGURE (8.6) Separation of measured attenuation into the dislocation part and the square-law term.

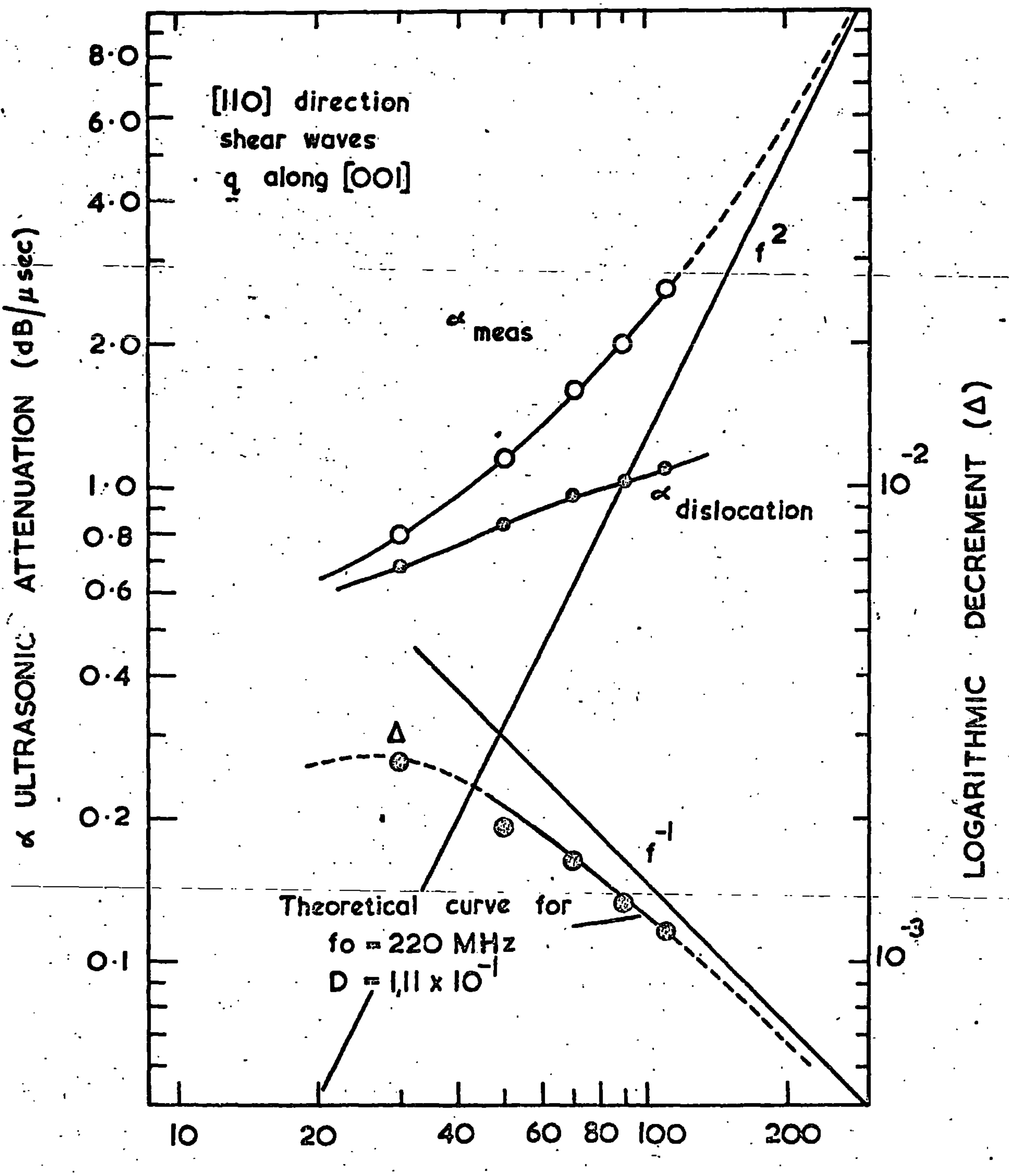

FIGURE (8.7). Separation of measured attenuation into the dislocation part and the square-law term.

frequency square law. As the dislocation contribution to the attenuation approaches the frequency independent region, as predicted by the Granato and Lücke theory, so the logarithmic decrement $\Delta(=\omega/2\pi\alpha)$ begins to vary inversely with frequency, as shown.

Once the dislocation contribution to the damping has been separated off, it can be compared with the predictions of the Granato and Lücke theory in the condition that D is small. In Figure (8.8) the predicted normalised decrement $(\Delta/\Omega \Delta_0 \Lambda L^2)$ is plotted as a function of frequency for a range of values of D. The resonance frequency f_0 is taken between 200 MHz and 220 MHz, as found from the results at 4·2°K. The measured dislocation contributions for the longitudinal and the two transverse ultrasonic waves propagated along the [110] direction are also presented. The best match occurs in each case for D equal to 0·11 and f_0 equal to 220 MHz.

Interactions with thermal phonons damp the dislocation motion in a crystal. The drag coefficient B can be determined from (Equation 8.14)

$$B = \omega_0 A/D$$

using the experimental data for ω_0 and D at 4·2°K and 77°K and taking the effective mass A per unit length of dislocation as $1{\cdot}69 \times 10^{-19}$ g.cm^{-1} (see Appendix B). Results are shown in Table (8.1). There is an order of magnitude discrepancy between the measured values of B and those predicted by Leibfried by a consideration of phonon scattering of the moving dislocations, assuming a linear dependence of B on temperature.

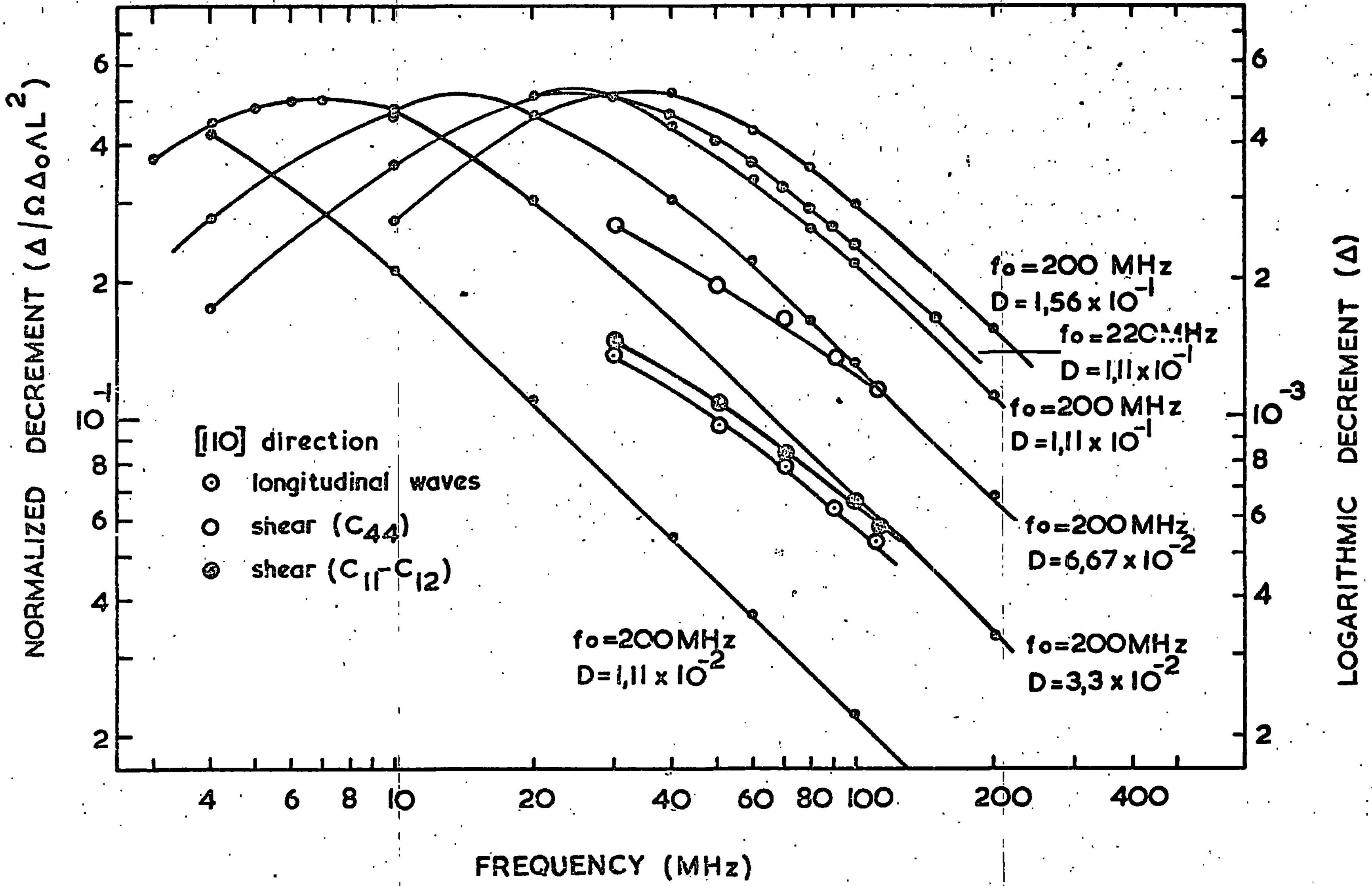

FIGURE (8.8). Theoretical fit to the dislocation part of the measured decrement.

TABLE (8.1) Dislocation parameters for the mercury telluride single crystals.

Temperature ^{o}K	Resonance Frequency f_o (MHz)	Normalised Damping Constant D	Drag Coefficient B (dyn. sec. cm^{-2})		
			Measured	Theoretical	
				a	b
4·2	220	1·00	$2{\cdot}3\text{x}10^{-5}$	$0{\cdot}8\text{x}10^{-6}$	
77	220	0·11	$2{\cdot}1\text{x}10^{-4}$	$1{\cdot}45\text{x}10^{-5}$	$1{\cdot}5\text{x}10^{-4}$

a. Theoretical prediction of Leibfried (1950)

b. Theoretical prediction of Mason and Rosenberg (1967)

The values of B determined for copper by Alers and Thomson (1961) are also much higher than the theoretical calculations. But the predicted linear dependence of B comes from a high temperature approximation not applicable below room temperature. Recently Mason and Rosenberg (1967) have shown that the experimental values for lead support a combination of two effects, namely phonon viscosity as well as phonon scattering, as being the likely source of the drag on dislocations. From the magnitude of the drag coefficient B obtained for mercury telluride, which is the same as that in copper, it seems likely that this situation applies here too.

In a real solid the loop lengths are not all the same, but the use of a single effective loop length affords a useful basis for comparison. The relationship between the loop length L_c and the resonance frequency ω_o is given by Granato and Lücke as (Equation 8.19)

$$L_c^2 = \pi^2 C/A\omega_o^2$$

From the finding of f_o as 220 MHz, L_c turns out to be $2\cdot8 \times 10^{-4}$ cm. for annealed mercury telluride. Granato and Lücke (1966, p.263) estimate values for copper of $0\cdot49 \times 10^{-4} < L < 2\cdot9 \times 10^{-4}$ cm. from the data of Thompson and Holmes (1956). Other workers find loop lengths of this magnitude in copper. Truell and Elbaum (1962, p.194) give $1\cdot3 \times 10^{-4}$ cm. for a sodium chloride crystal. The value obtained for mercury telluride is reasonable.

The effective dislocation loop length is reduced by the addition of impurities and defects; studies of the effects of radiation-induced defects on ultrasonic attenuation have proved of great value in assessing the validity of the Granato and Lücke theory. During the present work, a considerable number of experiments have been performed to determine the effect of annealing in mercury vapour on the attenuation of both longitudinal and shear waves propagated along the [100], [110] and [111] directions. In all cases the attenuation increased markedly after annealing. Typical results can be seen in Figures (5.7), (5.8), (5.9) and (5.11). The effect of annealing as-grown mercury telluride is to reduce excess tellurium content. The ultrasonic experiments point to an increase in the dislocation loop length due to removal of some pinning points during annealing. The results in these figures show about a 50% increase in attenuation after annealing. A change in loop length from $2\cdot3 \times 10^{-4}$ to $2\cdot8 \times 10^{-4}$ cm. is required to produce this increase. This corresponds to a decrease in the total number of pinning points ($\Lambda/L = 10^7/L$) from $4\cdot3 \times 10^{10}$ cm^{-3} by 8×10^9 cm^{-3} to $3\cdot5 \times 10^{10}$ cm^{-3}. The total number of electrons ($\sim 10^{17}$ cm^{-3}) introduced during annealing is much greater. Clearly most of the mercury atoms diffusing in do not go into dislocation pinning sites and only a few of the defects present interact with the dislocations.

The stress-induced dislocation motion also leads to a modulus change (ΔM): the elastic constants are smaller for a sample containing mobile dislocation segments than for a perfect crystal by an amount

$$\frac{\Delta M}{M} = \frac{6\Omega}{\pi^2} \Lambda L^2 \tag{8.25}$$

according to the Granato and Lücke theory. The effect of the annealing process on the elastic constants of mercury telluride has been given in Chapter 4. The changes induced in $(C_{11} + C_{12} + 2C_{44})$ and $(C_{11} - C_{12})$ are too small to be distinguished with certainty from the experimental error. But (C_{44}) decreases by 2·5% after annealing. If the elastic moduli before and after annealing are written as M_u and M_a respectively then

$$(M-M_u)/M = \frac{6\Omega}{\pi^2} \Lambda L_u^2 \tag{8.26}$$

$$(M-M_a)/M = \frac{6\Omega}{\pi^2} \Lambda L_a^2 \tag{8.27}$$

and

$$(M-M_u)/(M-M_a) = L_u^2/L_a^2 \tag{8.28}$$

Using the values of $2{\cdot}3 \times 10^{-4}$ cm. for L_u and $2{\cdot}8 \times 10^{-4}$ cm. for L_a, then at 4·2°K the elastic constant C_{44} of dislocation-free mercury telluride would be $2{\cdot}28 \times 10^{11}$ dyne cm^{-2} in contrast to that of $2{\cdot}22 \times 10^{11}$ dyne cm^{-2} and $2{\cdot}19 \times 10^{11}$ dyne cm^{-2} for as-grown and annealed crystals respectively. Problems connected with the study of crystal internal forces require accurate elastic constant data. The deviations due to dislocation strain may be responsible for the discrepancies between quoted data for elastic constants of crystals. The orientation factor $\Omega_{C_{44}}$ for a transverse wave propagated along the [110] with the particle velocity vector along [001] is estimated from the annealing experiment to be 0·16. This is excellent agreement with that calculated from $\frac{1}{3} C_{44}/(C_{11}-C_{12}+C_{44})$ (Alers and Thomson 1961) of 0·18. The orientation factor $\Omega_{(C_{11}-C_{12})/2}$ for the other transverse wave with velocity vector along the $[1\bar{1}0]$ is $\frac{1}{2}(C_{11}-C_{12})/(C_{11}-C_{12}+C_{44})$ equal to 0·22. But the value of $(C_{11}-C_{12})/2$ of 0·88 dyne cm^{-2} is nearly an order of magnitude smaller than C_{44} and the change on annealing cannot be observed. The orientation factor for the longitudinal wave is only 0·068. Thus the finding of that only C_{44} is altered measurable on annealing is consistent with the postulate of a strong dislocation interaction of ultrasonic waves in mercury telluride.

Further confirmation comes from experiments which demonstrate breakaway of the dislocations from the weak pinning points. When a stress large enough to induce breakaway is applied, the attenuation should increase markedly. This is shown in Figure (5.13).

CHAPTER 9

BORDONI-TYPE RELAXATION PEAKS IN MERCURY TELLURIDE

9.1. INTRODUCTION

Peaks are observed in the temperature dependence of ultrasound attenuation measurements in single crystals of mercury telluride. (see Figures 5.1 and 5.6). These show characteristics of Bordoni peaks and the results will be interpreted in terms of the theories of the Bordoni peak, particularly that due to Seeger (1956). The great importance of Bordoni peaks is that they give direct information about the motion of dislocations; some parameters of dislocation movement, such as the Peierls stress, can be deduced. Here first the qualitative and quantitative features of the source of Bordoni peaks will be surveyed and then the theories tested by application to the measurements in mercury telluride.

Bordoni (1949, 1954) first observed characteristic peaks in the temperature dependence of mechanical loss in certain face-centred cubic metals. Extensive studies of these Bordoni peaks have subsequently been carried out by numerous investigators; similar peaks have also been observed in other types of solids; for example, in body-centred cubic metals, covalent semi-conductors and in some alkali halides. The topic has been reviewed by Bordoni (1960), Truell and Elbaum (1962, p.203) and more recently by Niblett (1966, p.77).

The main characteristics shown by these peaks can be summarized as follows:

1. The peak occurs in both single crystals and polycrystalline materials.

2. The peak height increases with increasing plastic deformation until saturation at about two to three per cent plastic deformation.

3. The height of the peak decreases on annealing.

4. Impurities reduce the peak height; similar effects result from neutron irradiation.

5. In addition to the main peak, a smaller subsidiary peak is frequently observed on the low temperature side.

6. The temperature at which the maximum occurs increases as the frequency of the driving wave is raised.

7. The temperature at which the peak occurs is not very much dependent on prestrain, annealing and impurities.

Before turning to the mathematical theories, let us discuss these qualitative features of the Bordoni peaks.

9.2. THEORY OF BORDONI PEAKS

From the main features of the Bordoni peaks outlined above in (1) to (7), the following facts have been concluded:

a. The general behaviour of the peaks suggests that they arise from dislocation motion.

b. The changing peak temperature with frequency suggests that the peak originates from a thermally activated, relaxation effect, associated with a characteristic time τ which depends on temperature according to an Arrhenius equation.

$$\tau = \tau_o \exp (W/kT) \qquad (9.1)$$

Here W is the activation energy of the process, τ_o gives the limiting value of the characteristic time for very high temperatures and kT is the thermal energy.

c. Since the peak temperature does not depend greatly on prestrain, annealing and impurities, the activation energy is not generally related to the pinning of the dislocation line by impurities and the density of dislocations. From this it may also be concluded that the mechanism of the Bordoni peaks is mainly related to intrinsic properties of dislocations.

The general conclusions made are that Bordoni peaks are due to relaxation processes involving dislocations, which run parallel to one of the close-packed directions. We now turn to discuss the dislocation motion.

Consider a dislocation line lying in the position of minimum energy along a close-packed direction denoted by x (see Figure 9.1). If the dislocation line behaves as a rigid rod with no kinks, as is possible at 0^oK, a stress equal to the Peierls stress (σ_p^o) is required to displace it by an atomic distance, parallel to a close-packed direction. If a small bulge is formed, as shown in Figure (9.1), as a result of thermal fluctuation, a quite small stress will cause it to spread out by sideways

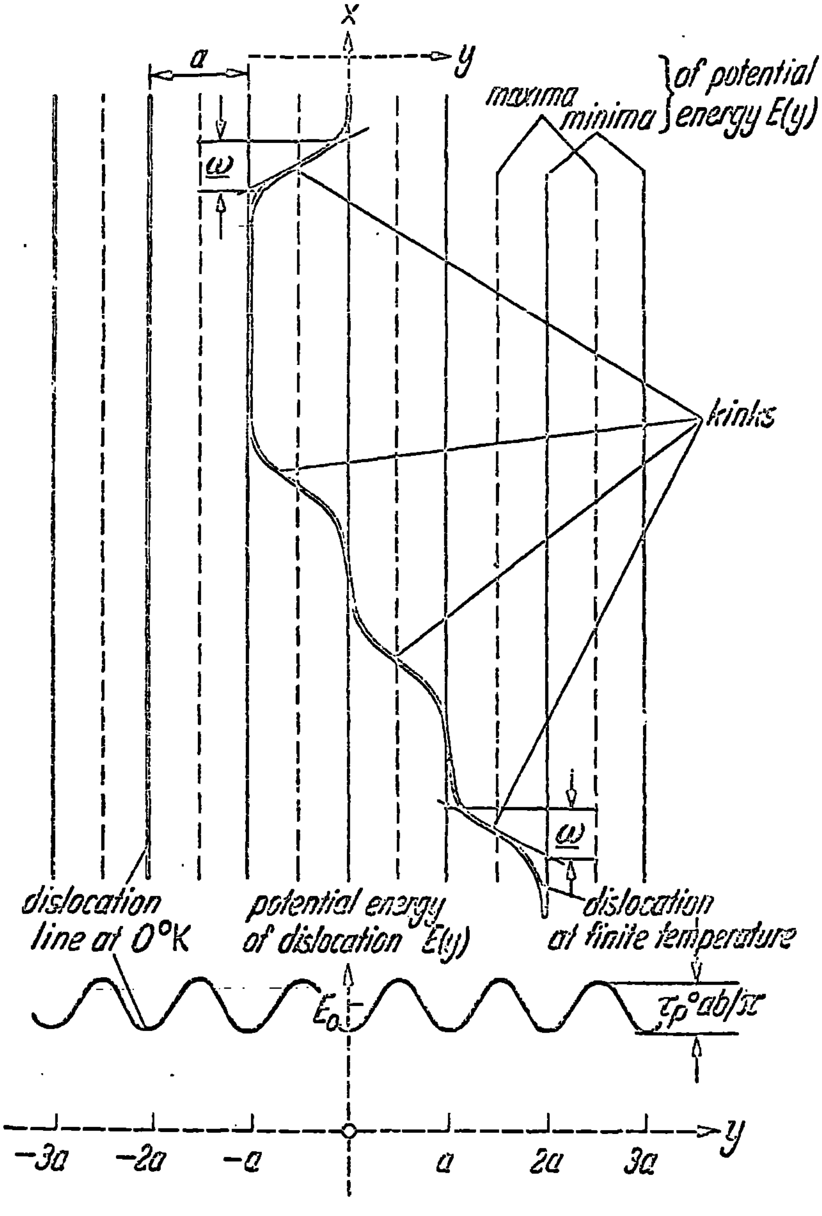

FIGURE (9.1). Potential energy of a dislocation line due to Peierls stress σ_p^o (After Seeger, Donth and Pfaff 1957).

motion; due to the periodic structure of crystals, the potential barriers along the close-packed direction are very much lower than those in directions parallel to the close-packed direction. The bulge can be considered as a pair of kinks. In the absence of any stress, these two kinks will attract and annihilate each other, but an applied stress will tend to move them apart and increase the slipped area. Under the action of stress, there exists a critical separation (l_{cr}) between the pairs, which corresponds to unstable equilibrium. If $l \ll l_{cr}$, the kinks annihilate each other. But when $l \gg l_{cr}$, the pairs will separate further and become non-interacting. An internal friction component arises because of the formation of these bulges.

The first attempt to give a theoretical model for this type of dislocation motion was made by Mason (1955), who assumed that a bulged dislocation line is pinned by impurity atoms. In order to move the bulge to the next equilibrium position, a dislocation must overcome a potential barrier (H). To compute the height of this barrier, Mason assumed that the complete dislocation segment between the pinning points moves.

The potential energy per unit length E(y), which opposes the motion of the dislocation line, is a periodic function of its position and is given by (see Figure 9.1).

$$E(y) = E_o - \frac{\sigma_p^o \, b^2}{2\pi} \cos \frac{2\pi y}{a} \qquad (9.2)$$

here b is the Burgers vector, a is the lattice spacing in the y direction ($\approx$ b) and σ_p^o is the Peierls stress. The dislocation line of length l has to overcome the energy (H_m)

$$l[E(y=\frac{a}{2}) - E(y=o)]$$

required for the jump to the next energy minimum position. This energy (H_M) is responsible for the activation energy (W) of the relaxation process, which is

$$H_M = \sigma_p^o\, b^2\, l/\pi \qquad (9.3)$$

This would lead a strong dependence of the peak temperature on the parameters which control the length of the dislocation line (l), such as prestrain, annealing and impurity content. This is contradicted by the experimental evidence because, according to this model, the formation of a kink pair is not an intrinsic property. Thus, some modification to Mason's model must be introduced, by considering types of dislocation motion not controlled by the dislocation length.

Weertman (1956) considered that, it is not necessary for the whole dislocation bulge to move at once in going from one equilibrium position to another. A small bulge of length l may move over the potential barrier and by sideways motion go into the next equilibrium position. A lower limit to l is given by the length of a kink pair ($2\underline{\omega}$). Taking Mason's estimate for $\underline{\omega}$

$$\underline{\omega} = b(G/\sigma_p^o)^{1/2} \qquad (9.4)$$

where G is the shear modulus, and inserting $\underline{\omega}$ instead of l in Equation (9.3), one obtains

$$H_W = \frac{2}{\pi} \; G \; b^3 \; (\sigma_p^o/G)^{1/2} \tag{9.5}$$

According to this equation, the formation of a kink pair has an intrinsic character, its energy being independent of the particular length of dislocation lines and of their interaction with impurity atoms. However, as pointed out by Bordoni (1960), the derivation of Equation (9.5) lacks somewhat in mathematical rigour; so the maximum value of potential, used in Equation (9.2), is applied, in this case, to a kinked line that is not parallel to the direction of maximum energy. Moreover, the approximate value in Equation (9.4) is taken as the length of a kink, and the changes in dislocations length are neglected.

A more satisfactory computation of the energy associated with the formation of kinks has been given by Seeger (1956). The starting point is a differential equation for the shape of an unpinned dislocation line, whose minimum energy position is parallel to the x-axis (see Figure 9.1)

$$E(y) \frac{\delta^2 y}{\delta x^2} = \frac{\delta E(y)}{\delta y} - boy + A \frac{\delta^2 y}{\delta t^2} \tag{9.6}$$

Here σ is the resolved shear stress in a glide system and A is the density per unit length of the dislocation line. The periodic potential E(y) may be represented by Equation (9.2). Following Seeger, the energy of single kink is

$$H_K = \frac{2a}{\pi} (2 \; a \; b \; E_o \; \sigma_p^o/\pi)^{1/2} \tag{9.7}$$

Here a is the separation of close-packed rows of atoms. Using the value of $Gb^2/5$ for E_o (Seeger 1956 and Bordoni 1960) and assuming that a is very close to b, the equation can be formed as

$$H_K = \frac{2}{\pi} (2/5\pi)^{1/2} G\, b^3 (\sigma_p^o/G)^{1/2} \tag{9.8}$$

As previously explained, the potential barrier in the x-direction is small compared to that in the y-direction. Once again below some critical distance, the pair of kinks will attract and annihilate each other, but an applied stress will tend to move them apart. To obtain the total energy barrier (H_S) that opposes the formation of a kink pair, the energy associated with the attraction must be added to the energy of a single kink (H_K). An approximate computation of l_{cr} gives for the total energy (H_S).

$$H_S = H_K[1 + \frac{1}{4} \ln (16\, \sigma_p^o/\pi\sigma)] \tag{9.9}$$

As shown from this equation H_S tends to infinity, when the applied stress tends to zero. This does not mean that kink pairs are not formed when there is no applied stress, but that they annihilate very soon after their formation. In the Seeger's model the energy barrier H_S depends on applied stress. Estimation of this applied stress from ultrasonic measurements is difficult and inaccurate. However, a reasonable approximation can be made (Bordoni 1960). The value of strain usually encountered in the ultrasonic measurements lies between 10^{-8} or 10^{-6}, while the ratio of σ_p^o/G is generally found to be 10^{-4}. Therefore the ratio σ_p^o/σ in the equation must lie between 10^2 and 10^4. Thus, the value of the last term in the Equation

(9.9) ranges from 2·0 to 3·0 and a value of 2·5 may be taken as a satisfactory average. Thus H_S becomes 3·5 H_K or inserting the approximate estimate of H_K (Equation (9.8)

$$H_S = 3{\cdot}5 \frac{2}{\pi} (2/5\pi)^{1/2} \; G \; b^3 \; (\sigma_p^o/G)^{1/2}$$

or

$$H_S = 1{\cdot}25 \frac{2}{\pi} G \; b^3 \; (\sigma_p^o/G)^{1/2} \qquad (9.10)$$

Here it is interesting to note that the final form of the energy barrier estimation only differs by a factor of 1·25 from the Weertman (1956) estimation (Equation 9.5).

Seeger (1956), following many other workers, in his preliminary study assumed for simplicity that the rate of formation of a kink pair ν might be represented by an Arrhenius equation. He also assumed that the theoretical prediction of the energy of the potential barrier opposing the dislocation motion (H), can be used for activation energy of the process.

$$\nu = \nu_o \exp(-H/kT) \qquad (9.11)$$

Where ν_o is the vibration frequency of a straight rigid dislocation line, near its position of minimum energy. Seeger's theory also predicts ν_o as

$$(\nu_o)_S = \frac{v_t}{b\sqrt{2\pi}} \; (\sigma_p^o/G)^{1/2} \qquad (9.12)$$

here v_t is the velocity of shear waves. $[= (G/\rho)^{1/2}]$.

This treatment yielded the right order of magnitudes, for face-centred cubic metals, but it was subsequently realized that the derivation was not correct, because the Arrhenius equation does not apply to formation of kink pairs. This is due to the fact that kink pair formation is a collective process involving thousands of atoms. A more complete treatment has subsequently been given by Seeger, Donth and Pfaff (1957). According to this theory, the peak frequency and temperature must satisfy the following equation

$$\ln \frac{\nu}{Z} = F_1(r,q) \qquad (9.13)$$

The function F_1 is given graphically, and the dimensionless variables r and q are defined by:

$$r = 2H_K/kT \qquad (9.14)$$

$$q = 1 - \frac{\pi}{8} \; \frac{\sigma_o}{\sigma_p} \qquad (9.15)$$

Here H_K is the energy of a dislocation kink (Equation 9.7) and σ is the shearing stress acting upon the dislocation. The parameter Z in this equation has the physical dimension of frequency and after approximations (Bordoni, Nuovo and Verdini 1959)

$$Z = \frac{\pi^2 k}{6b^4} \cdot (1/\rho G)^{1/2} T \qquad (9.16)$$

In this theory, the height of the potential barrier or the activation energy (H) is given by

$$H = - \frac{d(\ln\nu)}{d(1/kT)} = kT\, F_2(r,q) \qquad (9.17)$$

Here the function of $F_2(r,q)$ is presented graphically and the dimensionless parameters r and q are given as in Equations (9.14) and (9.15) respectively.

Bordoni (1960) has demonstrated that the more rigid development by Seeger, Donth and Pfaff (1957) provide little change to the original ideas of Seeger (1956) and give no further important improvement. On the other hand, this theory can be used to deduce the theoretical parameters from experimental data obtained from only one peak at one frequency. This is very useful, for instance, for our measurements on a (100) sample for which data could only be obtained accurately from 30MHz measurements.

In the next section, using these theories, the thermally activated dislocation movement in mercury telluride will be discussed. The applicibility of the theories to materials with different kinds of bonding will also be discussed.

9.3 RESULTS AND DISCUSSION

In the present measurements, distinct peaks have been observed in the attenuation in crystals of mercury telluride in the temperature region from 170°K to 260°K and at frequencies between 10 MHz and 60 MHz. As shown in Figure (5.1), the peaks are superimposed on a background attenuation, which in this case increases exponentially with increasing temperature. The peaks show certain characteristic features. The measurements made along [111] direction with longitudinal waves (see Figure 5.6) clearly show that the temperature at which the attenuation is a maximum (the peak temperature) decreases with decreasing frequency. In the measurements made at 30 MHz, along [100] direction (see Figure 5.1), in addition to the main peak another smaller peak appears on the low temperature side. This appearance of a second peak is common in other materials. These two peaks are almost superimposed at 10 MHz. Thus, identification of their position is rather difficult and subject to error. For this crystal at frequencies above 30 MHz the background attenuation has become so high by about 200°K that the peaks can not be observed.

The effect of annealing on the peaks is demonstrated in Figure (5.8). In this figure the bold lines have been taken from the experimental points shown in Figure (5.1).

This behaviour of the peaks observed in the attenuation in mercury telluride suggests that they are Bordoni-type peaks. For a simple relaxation process, the relaxation time (τ) depends on the temperature (T) according to the Arrhenius equation. The relation was given in Equation (9.1) as

$$\tau = \tau_o \exp(W/kT)$$

When measured at a frequency (ν) the mechanical loss or ultrasound attenuation arising from this process is a function of the product of $\omega\tau$ ($2\pi\nu\tau$), and has a maximum value when $\omega\tau$ is unity. Thus the temperature at which the maximum attenuation occurs can be related to the frequency of vibration by the equation

$$\nu = \nu_o \exp(-W/kT) \qquad (9.18)$$

Here $\nu_o = 1/2\pi\tau_o$ is called the attempt frequency.

The activation energy (W) and attempt frequency (ν_o) of the process leading to Bordoni peaks can be obtained from the experimental data by making use of Equation (9.18). This equation implies that the plot of the logarithm of frequency at which a maximum in attenuation takes place (relaxation frequency), against the inverse of the peak temperature should be linear. Thus the slope and the intercepts of this straight line give both the activation energy (W) and the attempt frequency.

Peak temperatures and frequencies, obtained from the experimental data in Figures (5.1) and (5.6) are tabulated in Table (9.1). Using this experimental data, the plot of the logarithm of the relaxation frequency against the inverse temperature is shown in Figure (9.2). From the slope and intercepts of this straight line belonging to this (111) sample, the activation energy (W) and the attempt frequency (ν_o) of mercury telluride for the [111] crystallographic direction are found to be $(0{\cdot}094 \pm 0{\cdot}004)$eV, and $(4 \pm 1) \times 10^9$ Hz. respectively. Due to uncertainties of estimation of the peak temperature and absence of sufficient experimental points no attempt has been made to deduce these parameters from the experimental data obtained from (100) sample. The activation energy and the attempt frequency of mercury telluride are compared with those of other materials in Table (9.2). The activation energy for mercury telluride falls in the same range as that for other materials.

For a relaxation process involving a single relaxation time, the attenuation varies with temperature in the manner (Bhatia 1967, p.368):

$$\frac{\alpha}{\alpha_m} = \frac{2e^x}{1+e^{2x}} \quad , \quad x = \frac{W}{k}\left(\frac{1}{T_m} - \frac{1}{T}\right) \qquad (9.19)$$

TABLE (9.1) The data for peaks in mercury telluride

Peak Frequency (MHz)	Peak Temperature (^oK)	Direction of Propagation	Data Source
10	~ 218 (1st peak)	$[100]_{long.}$	Figure (5.1)
10	~ 260 (2nd peak)	"	"
30	230 (1st peak)	"	"
30	270 (2nd peak)	"	"
12	196	$[111]_{long.}$	Figure (5.6)
36	240	"	"
40	253	"	"
56	270	"	"

1st peak (Subsidiary peak

2nd peak (Main peak)

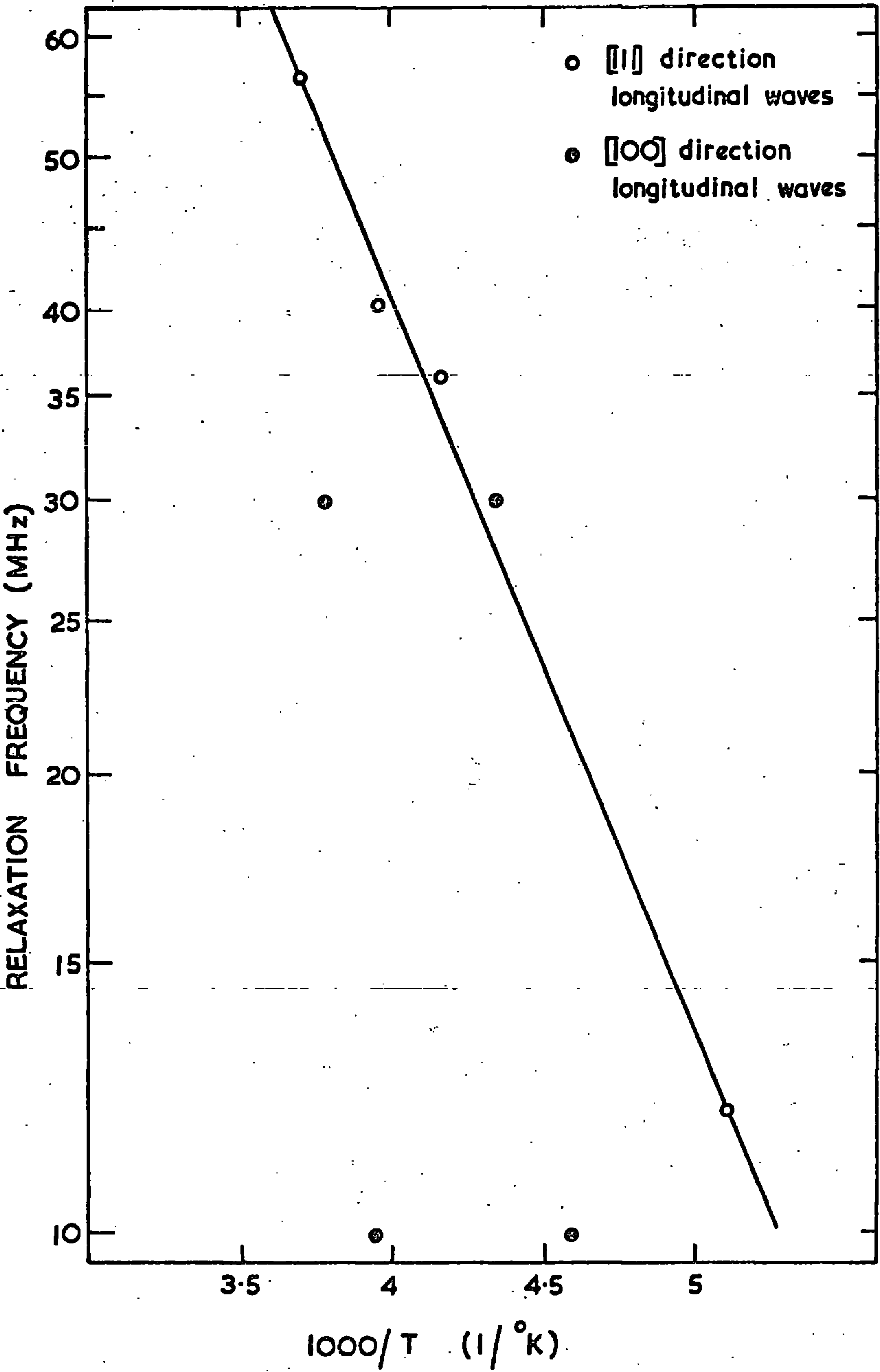

FIGURE (9.2). Frequency dependence of the temperature of maximum attenuation in mercury telluride.

TABLE (9.2) Dislocation relaxation parameters for some cubic materials

Material	Activation energy (eV)	σ_p^o/G $\times 10^4$	Attempt frequency $\nu_o \times 10^{11}$ (Herzt)		Reference
			Measured	Calculated	
Al	0·107	3·1	0·13	0·45	Bhatia (1967,
Cu	0·122	2·6	3·8	0·33	Table 13.2,
Ag	0·124	3·7	40·0	0·24	page 367)
Au	0·158	5·2	0·7	0·21	"
Pb	0·043	3·3	0·008	0·08	"
Pd	0·26	6·4	12·0	0·42	"
Pt	0·192	1·9	0·06	0·19	"
HgTe	0·094	2·32	0·032	0·09	Present work (a)
		0·62		0·048	" " (b)
Si	0·162	[n-type Si (100)]			Kromer and
	0·120	[p-type Si (111)]			Khiznichenko
Ge	0·07				(1967)
LiF	0·15	5·8			Taylor (1962)
	0·09	2·1			Ikushima et al.(1961)
KCl	0·08	0·46			Ikushima and
	0·05	0·14			Zuzuki (1963)
MgO	0·18	0·72			"
PbS	0·43	2·2			"

(a) computed by the equations given in the text.

(b) computed by the equations given by Bhatia (1967)

Here T_m is the temperature at which the peak occurs and α_m is the value of attenuation at T_m. Figure (9.3) shows a plot of $2e^x/(1+e^{2x})$ and α/α_m as a function of $W/k(1/T_m-1/T)$ using α/α_m values obtained from 36 MHz measurements given in Figure (5.6). It appears to give a good fit for the single relaxation curve. Furthermore half-widths of the peaks obey, within the experimental error the expression

$$\Delta\left(\frac{1}{T}\right) = \frac{k}{W} \log\left(\frac{2+\sqrt{3}}{2-\sqrt{3}}\right) \tag{9.20}$$

expected for a single relaxation process (see Niblett 1966, p.118). However too much emphasis must not be placed on these procedures: the difficulty of separating the peak from background makes for considerable error.

9.3.1 Application of Seeger's theory to the results.

The measured activation energy (W) is that required to surmount the potential barrier. The total energy barrier that opposes the dislocation motion has been estimated by Mason (1955) and is given in Equation (9.3), by Weertman (1956) (Equation 9.5) and by Seeger (1956) (Equation 9.10) among others. Seeger's theory seems to be the most reasonable explanation of the mechanism resulting in Bordoni peaks: it explained the peaks in face-centred cubic metals successfully. Thus, here, this theory will be the first to be applied to the results. The potential barrier (H_S) is assumed to be that obtained as the activation energy W (equal to 0·094 eV). From the following equation, which is given as Equation (9.10 p. 140)

FIGURE (9.3). Comparison of the normalized attenuation for HgTe (B, Figure 5.6, 36 MHz) with the theoretical attenuation curve assuming a single relaxation time (A).

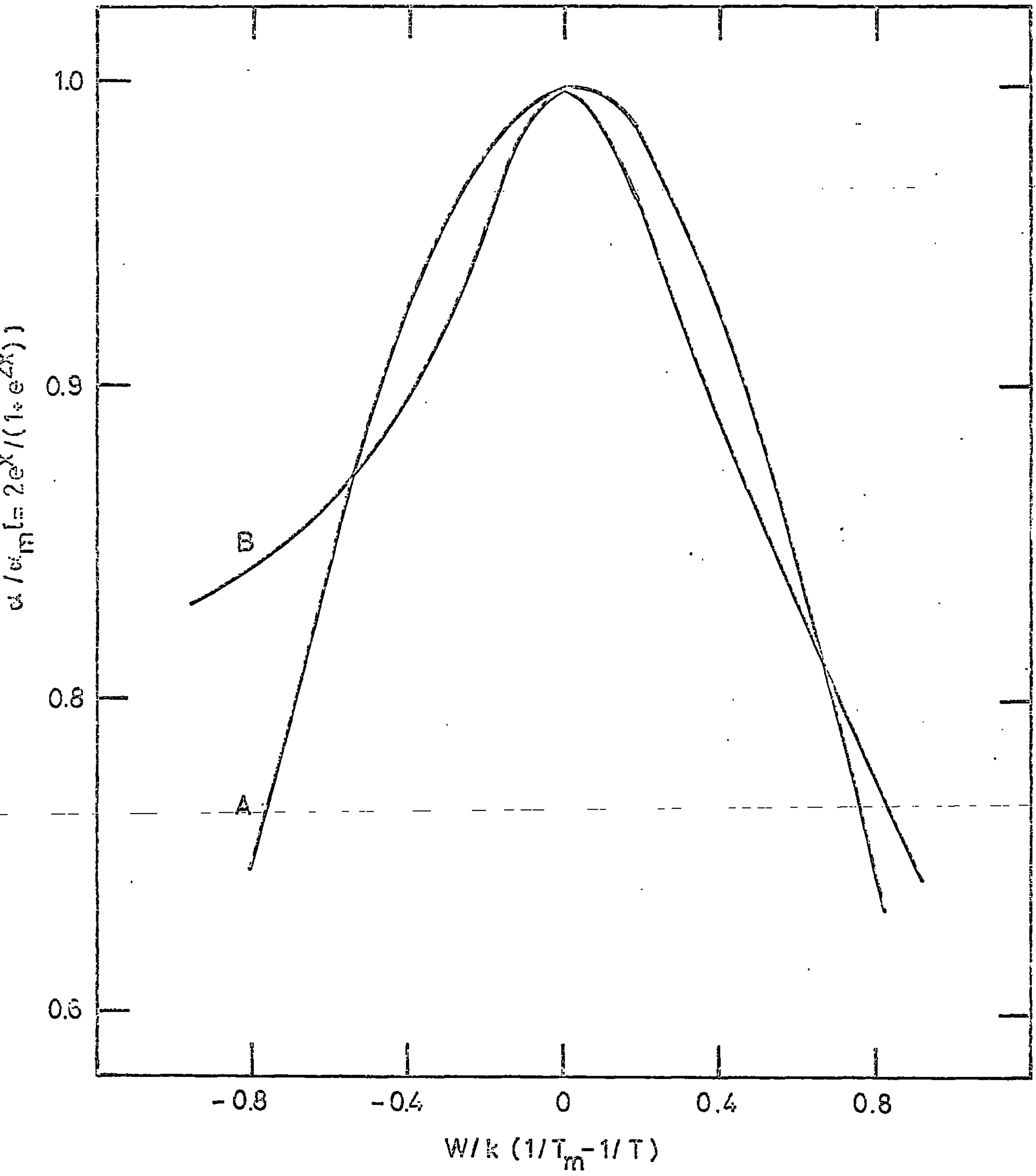

$$H_S = 1{\cdot}25\,\frac{2}{\pi}\,G\,b^3\,(\sigma_p^o/G)^{1/2}$$

the ratio (σ_p^o/G) of the Peierls stress (σ_p^o) to shear modulus (G) then turns out to be $2{\cdot}3 \times 10^{-4}$. Therefore, the Peierls stress is 3×10^7 dyn.cm^{-2}. The attempt frequency (ν_o) has been estimated from the prediction of Seeger's theory (Equation 9.12, p.140):

$$(\nu_o)_S = \frac{v_t}{b\sqrt{2\pi}}\,(\sigma_p^o/G)^{1/2}$$

as 9×10^9 Hz; this is of the same order of magnitude as the experimental value of $3{\cdot}2 \times 10^9$ Hz: effects are consistent with the Seeger's theory. A comparison between the theoretical and experimental values of attempt frequency (ν_o) for various materials is given in Table (9.2). The values for face-centred cubic metals are taken from Bhatia (1967, Table 13.2, p.367). His approximations are slightly different from those made here (for example, he has taken 3 as the average value of the last term in the Equation 9.9). Therefore, for easier comparison, the parameters of mercury telluride computed, using the equations given by Bhatia, are also given in Table (9.2).

As shown here, the discrepancies between the measured and calculated attempt frequencies of face-centred cubic metals, especially platinum, palladium and silver can be almost two orders of magnitude; the agreement for mercury telluride is better. There are both experimental and theoretical difficulties. The frequency depends exponentially on temperature and the temperature of peak is often not well defined experimentally. A wide range of experimental values is quoted in literature for given metals and plausibly comes from the experimental difficulties rather than the use of varied material by different workers. Bordoni peaks are essentially due to intrinsic properties of the dislocations. For example, the smallest activation energy for copper has been reported by Niblett and Wilks (1956) as 0·05 eV, while the highest value has been reported by Niblett (1961) as 0·14 eV. The difference between quoted attempt frequencies for the same materials is much worse because a few per cent change in the activation energy can lead an order of magnitude change in the attempt frequency. The disagreement for some materials reaches six orders of magnitude. Further, the basis of the theory is rather weak. The processes involved are certainly much more complicated than the theory suggests. The Arrhenius equation is not strictly applicable to the production of dislocation kink pairs, which is a collective process involving a large number of atoms. The derivation of Equations (9.10) and (9.12) is not strictly accurate.

9.3.2 Application of the theory of Seeger, Donth and Pfaff to the results:

A modified form of Seeger's theory aimed at resolving some of the difficulties is that of Seeger, Donth and Pfaff (1956); this will now be applied to the results for mercury telluride. Using this theory the energy of a single kink (H_K), the ratio (σ_p^o/G) and the activation energy have been estimated for mercury telluride in the following manner.

In the theory, the relation of the temperature dependence of relaxation frequency is

$$\ln(\nu/Z) = F_1\ (r,q)$$

(Equation 9.13, p.141). This can be rewritten more explicitly as

$$\ln \nu = F_1\ (r,q) + \ln\ (Z/T) + \ln T \qquad (9.21)$$

where the ratio of Z/T from Equation (9.16, p.141) is

$$\frac{Z}{T} = \frac{\pi^2 k}{6b^4}\ (1/\rho G)^{1/2} \qquad (9.22)$$

and only depends the physical properties of the material. It is $5{\cdot}1 \times 10^7$ $\sec^{-1}$ $\deg^{-1}$ for mercury telluride. Thus knowing only the peak temperature (T) and frequency (ν) the value of the function $F_1\ (r,q)$ can be deduced. Hence, using the graph the parameter r can be found for different q values. Once r is known, the energy of a single kink H_K ($= r\frac{kT}{2}$ Equation 9.14, p.141) can be estimated. Knowing H_K, the ratio of σ_p^o/G can next be deduced from (Equation 9.8, p.139).

$$H_K = \frac{2}{\pi} \left(\frac{2}{5\pi}\right)^{1/2} G\ b^3\ (\sigma_p^o/G)^{1/2}$$

In this procedure the only unknown is q. As a reasonable approximation, since the applied stress (σ) in an ultrasonic experiment is very much smaller than the Peierls' stress (σ_p^o), the ratio of σ/σ_p^o in Equation (9.15, p.141) ($q = 1 - \frac{\pi}{8}\ \sigma/\sigma_p^o$) can be neglected. Thus q is unity. The effect of this approximation will be examined later.

In this theory the activation energy is given by (Equation 9.17, p.141).

$$H = -\frac{d(\ln\nu)}{d(1/kT)} = kT\,F_2(r,q)$$

which shows that, H can be deduced not only from the slope of the straight line through the experimental points but also from the value of function F_2 (r,q). Once the r value for each peak has been found, the function F_2 $(r,1)$ is known. The parameters obtained are shown in Table (9.3).

The following remarks can now be made. 1. The theory gives a higher activation energy than that of the simple Arrhenius plot. 2. The parameters estimated by this theory are frequency dependent. 3. The magnitude of the Peierls stress for mercury telluride deduced from this theory are of the same order as the value obtained from Seeger's theory. Now let us discuss these remarks in more detail.

1. To look more closely at the source of higher theoretical activation energy, the relation (Equation 9.13)

$$\ln\frac{\nu}{Z} = F_1\ (r,q)$$

has been replotted from the experimental points. At the same time using two extremum values of q in this plot, the $\sigma/\sigma_p^o \simeq 0$ approximation is also tested. First an arbitrary point S has been chosen on the best fit to experimental points in Figure (9.4). For this point the energy of a single kink (H_K) is deduced as before, for two extremum values of q (1 and 0·9). The temperature variation of r ($= \frac{2H_K}{kT}$ Equation 9.14) and the value of the function F_1 (r,q) at different temperatures can be found. Now $\ln\frac{\nu}{Z} = F_1$ (r,q) can be plotted. This is also shown in the

TABLE (9.3) Evaluation of the experimental data on the Bordoni peak in mercury telluride using the theory of Seeger, Donth and Pfaff

		ν_m (MHz)	T_m (^oK)	F_1	r	H_K (eV)	σ_p^o/G x 10^4	F_2	H eV
Longitudinal waves along [111] direction		12	196	-6•72	4•00	0•034	3•7	8•58	0•145
		36	240	-5•82	3•50	0•036	4•2	7•34	0•152
		40	253	-5•78	3•46	0•038	4•6	7•23	0•158
		56	270	-5•50	3•30	0•038	4•8	6•84	0•159
Longitudinal waves along [100]direction	Main Peak	10	260	-7•18	4•20	0•047	7•1	9•08	0•203
		30	270	-6•19	3•70	0•043	6•0	7•83	0•182
	Subsidiary peak	10	218	-7•00	4•10	0•038	4•8	8•83	0•166
		30	230	-5•96	3•60	0•036	4•1	7•58	0•150

FIGURE (9.4). The modification of the simple Arrhenius theory by the approach of Seeger, Donth and Pfaff.

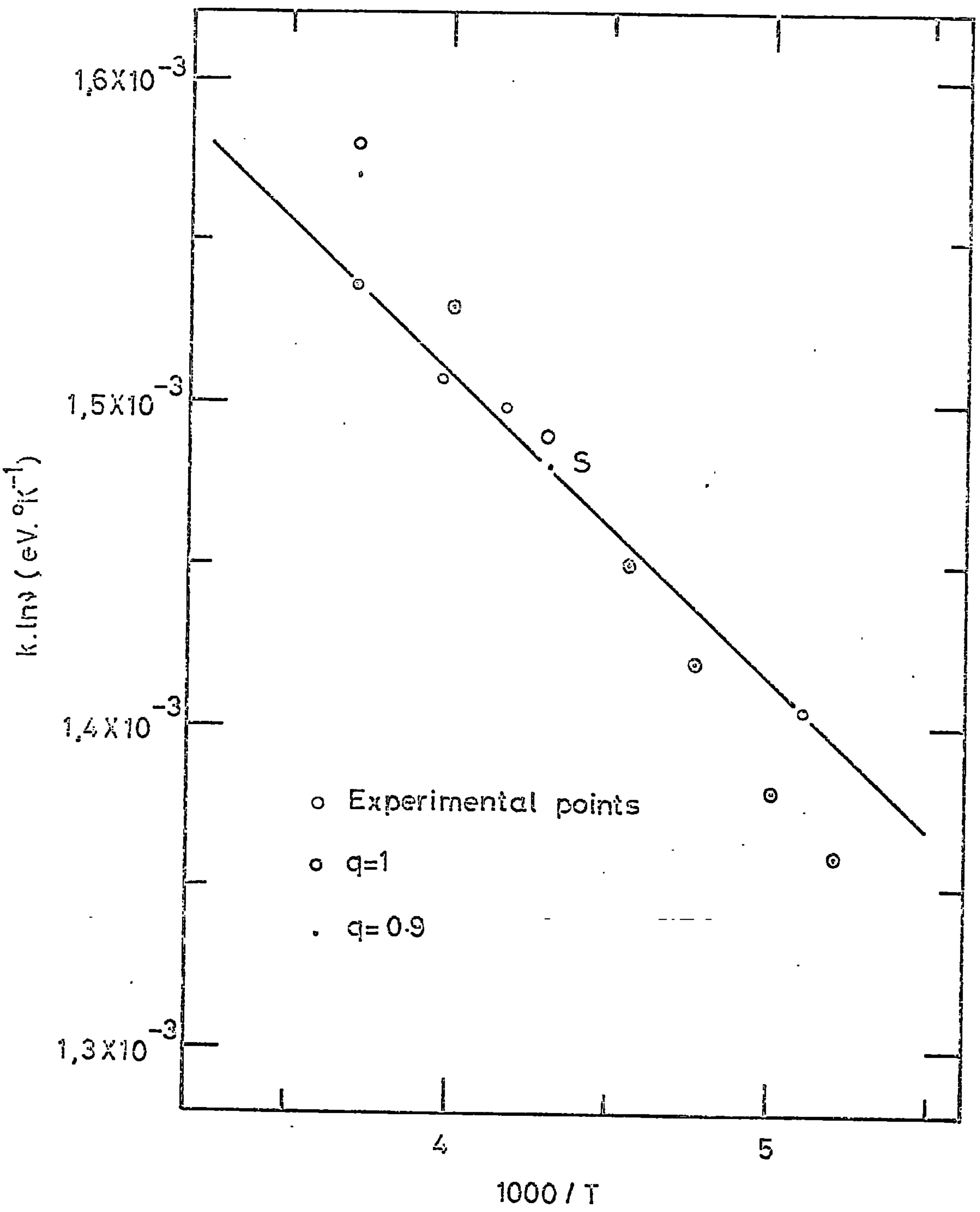

same figure (Figure 9.4). The plots of this function for the two q values are almost identical. Therefore, the approximation made that q is unity seems to be reasonable. In this figure it is clearly shown that this theory gives a slightly higher activation energy: the slopes are different. Either the simple Arrhenius equation does not hold over a wide frequency range or the theoretical model is not strictly valid. The present measurements have been performed at rather high frequencies. It is at high frequencies that such a discrepancy might be expected. Bordoni, Nuovo and Verdini (1959) has measured the internal friction of copper over a very wide frequency range (from 1 kHz to 10 MHz) on the same specimen. His results are reproduced here and shown in Figure (9.5) from which a slight deviation from linearity above 1 MHz may be seen. The reason for this frequency dependence might be, as implied by Seeger, Donth and Pfaff (1957), an unsatisfactory representation of the energy barrier shape.

2. The frequency dependence of parameters: there appears to be a systematic deviation in the sense that the measurements at higher frequencies give larger parameters. Similar behaviour has also been observed by Seeger, Donth and Pfaff on collected experimental data for some face-centred cubic metals. Here, as an example, the peak frequency, temperature and the value of σ_p^o/G for lead, obtained from Seeger, Donth and Pfaff is presented in Table (9.4). This is a consequence of the behaviour discussed above.

FIGURE (9.5). Frequency dependence of the peak temperature in copper. A deviation from linearity is shown for the frequencies higher than 1 MHz. (After Bordoni, Nuovo and Verdini 1959). This gives rise to higher calculated activation energies at megahertz frequencies than would be expected from the simple Arrhenius equation.

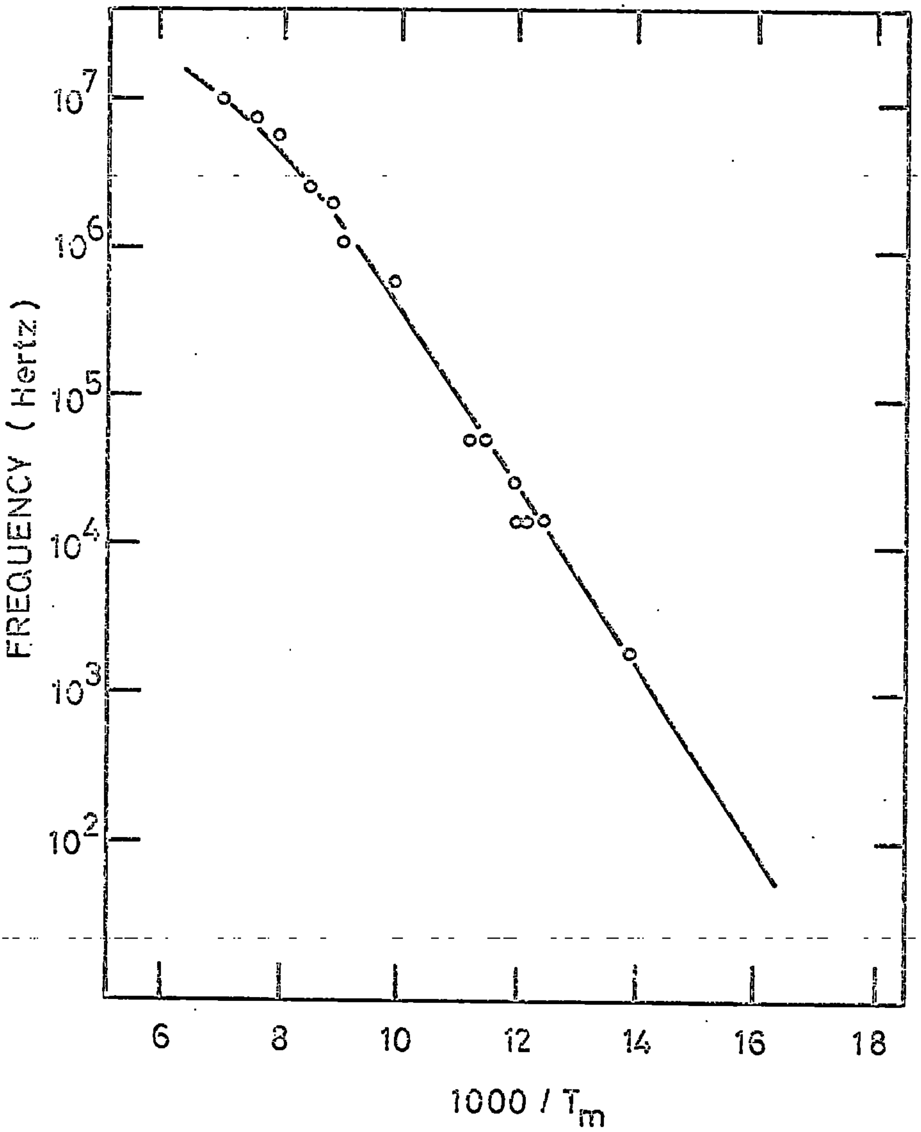

TABLE (9.4) Evaluation of experimental data on the Bordoni peak in lead

ν_m (Hz)	T_m (^oK)	σ_p^o/G $\times 10^4$
10334	36	3·5
10163	36	3·5
10348	36	3·5
20500	43	4·6
29500	47·5	5·4
50000	50	5·6
$10{\cdot}1 \times 10^6$	120	14·6
$26{\cdot}5 \times 10^6$	140	16·5

(Table 1 in Seeger, Donth and Pfaff, 1957)

3. Now we can turn to discuss the magnitude of the Peierls stress. Neglecting the frequency dependence of the parameters in Table (9.3) and from comparison with the parameters deduced from the Seeger (1956) theory (Table 9.2) it can be said that, within the framework of the approximations made, these two theories give almost similar results. Here it is important to mention that for mercury telluride the ratio σ_p^o/G, and the Peierls stress (σ_p^o) obtained by both the Seeger (1956) and the Seeger, Donth and Pfaff (1957) theories, is approximately 40×10^{-5} and 3×10^{7} dyn.cm^{-2} respectively and is almost the same as that for face-centred cubic metals. This value appears to be very small for a compound with the zinc-blende structure. No theoretical estimation of the Peierls stress could be traced for mercury-telluride or similar compounds. However, by considering related materials the results of the theories may be criticised. First, the purely covalent elements silicon and germanium may be looked at as being related. The theoretical value of Peierls stress for these elements is approximately 50×10^{9} dyne.cm^{-2} (Suzuki 1963). As demonstrated by Suzuki, the germanium crystal should have an internal friction peak at around 1300°K for 40 kHz due to Seeger mechanism. This is above the melting point. (The melting point of germanium is 1231°K). Silicon has a higher Peierls stress and the internal friction peak could be expected at temperatures higher than 1300°K for 40 kHz. However, internal friction peaks have been observed in both germanium and silicon by Kromer and Khiznichenko (1967) at much lower temperatures. The conclusion is that the Seeger model is not

applicable to elemental semiconductors. Secondly, the purely ionic, I-VII group compounds can be considered as being related to mercury telluride. Ikushima and Suzüki (1963) have demonstrated for some alkali halides a two order of magnitude discrepancy in the Peierls stress obtained from theoretical values and those deduced by Seeger's theory from experiment. From the comparison and taking into account the bonding properties of mercury telluride, a partially ionic and partially covalent compound, it may be concluded that Seeger's theory gives a small value of the Peierls stress for mercury telluride. Therefore, it is possible that dislocations in mercury telluride do not behave as considered in Seeger's model.

The origin of the double peaks observed on the (100) sample can be interpreted qualitatively in the following manner. The most probable slip planes in zinc-blende lattice matrices are the {111} and {110} forms. The resolved shear stress component of the longitudinal ultrasound waves will be different on different slip planes. The longitudinal elastic waves propagating along the [100] direction have a resolved shear stress component on both slip planes, while those propagating along the [111] direction have a shear stress component only for the (110) plane. As shown in Table (9.3), the ratio of the Peierls stress to shear modulus of the subsidiary peak is quite similar to that obtained from the (111) sample. The parameters belonging to the main peak are rather higher than those of the subsidiary peak. This is further confirmation of this argument.

The conclusions may now be summarized. The peaks observed in mercury telluride with an activation energy 0·09 eV and $3 \cdot 2 \times 10^9$ Hz attempt frequency are probably Bordoni-type of peaks involved with the dislocation motion. Theories of the phenomenon are at present not quantitative.

CHAPTER 10

SUMMARY AND CONCLUSIONS

Elastic properties of mercury telluride have been studied through sound velocity measurements in a wide temperature range. Attention has been paid to possible effects of non-stoichiometry in the crystals and the results correlated with ultrasound attenuation data. Materials belonging to the same crystallographic classes usually exhibit similarities in their lattice properties. Therefore, the results have been compared with those of other II-VI compounds and with III-V compounds, group IV elemental semiconductors and I-VII compounds: the elastic properties of mercury telluride correspond closely to those of cubic zinc sulphide and fall into the general scheme. From the comparisons, it is concluded that the elastic properties follow the sequence

$$\text{IV} \longrightarrow \text{III-V} \longrightarrow \text{II-VI} \longrightarrow \text{I-VII}$$

Elastic constant data of mercury telluride have been discussed in terms of the crystalline interatomic forces, founded by Born and co-workers: as the polarisation of atoms, which is important in partially ionic and partially covalent compounds like mercury telluride are neglected, in these derivations, the agreement the lattice dynamic theory and experiment is not completely satisfactory. From the Szigeti relationships, the ionicity e^{*} is estimated as $0{\cdot}65 \pm 0{\cdot}05$ e and the restrahlen frequency as $(4{\cdot}1 \pm 0{\cdot}1) \times 10^{12}$ Hz. From the elastic constant data, extrapolated to absolute zero, the limiting value of the Debye temperature for mercury telluride has been calculated as (140 ± 4)°K and the averaged sound velocity in Debye sense is $1{\cdot}53 \times 10^{5}$ cm.sec^{-1}; these are the lowest reported values in the whole group of related materials. The elastic properties of mercury telluride are found to be quite anisotropic (~ 10%), like other II-VI compounds.

Anelastic properties of mercury telluride have been deduced from the temperature, frequency and applied stress dependence of ultrasound attenuation measurements. The important ultrasound dissipation mechanisms include the viscous drag of lattice phonons and forced dislocation motion.

The effect of piezoelectricity and thermoelasticity on sound absorption is negligible in mercury telluride. The thermoelastic loss is large for metals because both the thermal conductivity and the thermal expansion are large. But in the semimetal mercury telluride, over the frequency range 10 to 300 MHz, this loss component is negligible. Calculations of the contribution over the temperature range 77°K to 300°K confirm that this is so over the temperature range.

One of the main energy dissipation mechanisms in single crystal, mercury telluride is the lattice phonon-ultrasonic phonon interaction. Attenuation at low temperatures where the other mechanisms are less dominant exhibits the characteristic features of this effect. The effect is stronger in mercury telluride due to the low Debye temperature and has been observed at relatively low frequencies.

Another loss mechanism is found to be due to the forced vibration of dislocation segments. At $4{\cdot}2^{o}$K a maximum has been observed in the frequency dependence of attenuation. The resonance frequency is 220 MHz, the dislocation loop length is about 3×10^{-4} cm and the dislocation drag coefficient is $2{\cdot}3 \times 10^{-5}$ dyn.sec.cm^{-2} at $4{\cdot}2^{o}$K, $2{\cdot}1 \times 10^{-4}$ dyn.sec.cm^{-2} at 77^{o}K. The effect of annealing as-grown mercury telluride is to reduce excess tellurium content.

The measurements point to an increase in the dislocation loop length due to removal of some pinning points during annealing. A change in loop length from $2{\cdot}3 \times 10^{-4}$ to $2{\cdot}8 \times 10^{-4}$ cm. is required to produce about a 50% increase in attenuation after annealing. From this it is also predicted that at $4{\cdot}2^{o}$K the elastic constant C_{44} of dislocation-free mercury telluride would be $2{\cdot}28 \times 10^{11}$ dyn.cm^{-2} in contrast to that of $2{\cdot}22 \times 10^{11}$ dyn.cm^{-2} and $2{\cdot}19 \times 10^{11}$ dyn.cm^{-2} for as-grown and annealed crystals respectively. Problems connected with the study of crystal internal forces require accurate elastic constant data. The derivations due to dislocation strain may be responsible for the discrepancies between quoted data for elastic constant of crystal. Data for the ultrasonic wave velocity and attenuation before and after annealing and under stress are in agreement with the dislocation mechanism.

The peaks on temperature dependence of ultrasound attenuation have been accounted for as Bordoni-type of relaxation peaks. The activation energy is about $0{\cdot}15$ eV and the attempt frequency is about 4×10^{9} Hz.

Ultrasound is useful tool for studying the solids. Most of the intrinsic and extrinsic properties can be studied directly. Experimental difficulties, other than instrumentation, come from the quality of specimen ; the sound energy loss mechanism especially is very sensitive to the dislocation content. Even for silicon and germanium, which can be grown almost perfectly due to advanced technology of the semi-conductor industry, the differences between quoted attenuation measurements is almost 150-200%. The situation is worse in compounds containing volatile elements. However for mercury telluride, due to lack of any other measurements on sound propagation, no comparison can be made. Progress in crystal growing methods, especially that of pulling from melt by the liquid encapsulation technique (Hiscocks and Hurle 1968), should provide better crystals. Measurements made on crystals with low crystal imperfections will allow to study other intrinsic effects more precisely; it should then be possible to observe the effect of electrons on the sound attenuation.

APPENDIX A

THE THERMAL AND LATTICE PROPERTIES OF MERCURY TELLURIDE

The thermal conductivity has been measured between 90°K and 240°C by several workers. This property is particularly relevant to an understanding of ultrasonic wave propagation. Carlson (1958), Kelemen, Cruceanu and Niculescu (1965) and Wagini and Reiss (1966) have found that the thermal conductivity follows approximately the usual inverse temperature dependence between 100°K to 300°K. In Figure (A.1) all the available experimental data up to 1966 on the thermal conductivity is presented.

The room temperature thermal expansion coefficient for mercury telluride has been reported by Blair and Newnham (1961) as 4×10^{-6} $(^{\circ}K)^{-1}$. Novikova and Abrikosou (1965) have measured temperature dependence of the coefficient of thermal expansion between 20°K and 320°K. This is shown in Figure (A.2).

Dickey and Mavroides (1964) have observed the restrahlen reflection at 85 μ. By fitting the experimental points with a classical Lorentz oscillator, they have found that the fundamental lattice absorption frequency is $3{\cdot}45 \times 10^{12}$ Hz., the high frequency dielectric constant p_{∞} is 14 and the static dielectric constant p is 20.

Mavroides and Kolesar (1964) have reported the room temperature elastic constants as, in units of 10^{11} dyn/cm^{2}, $C_{11} = 5{\cdot}05$,

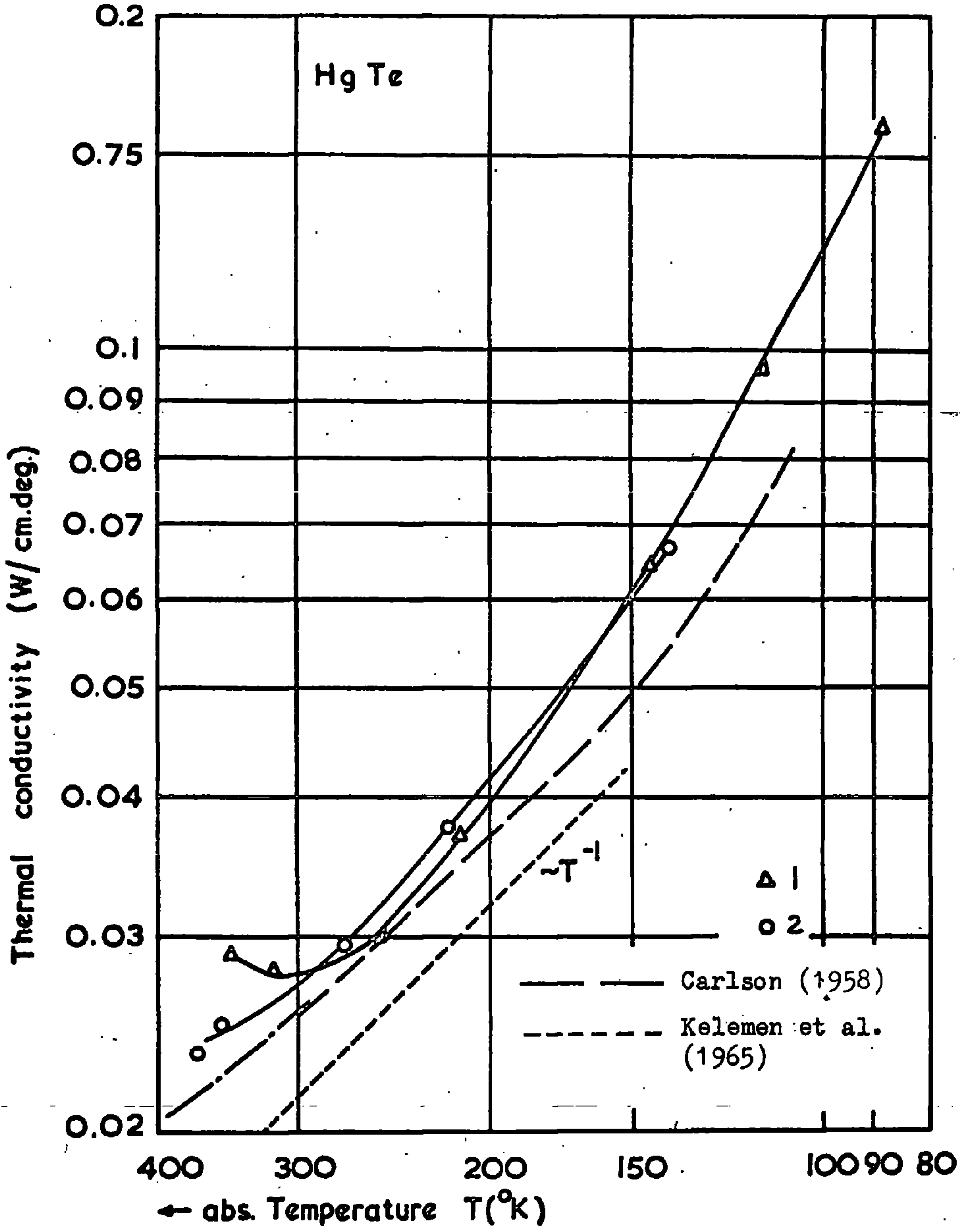

FIGURE (A.1). Temperature dependence of thermal conductivity of mercury telluride (After Wagini and Reiss 1966).

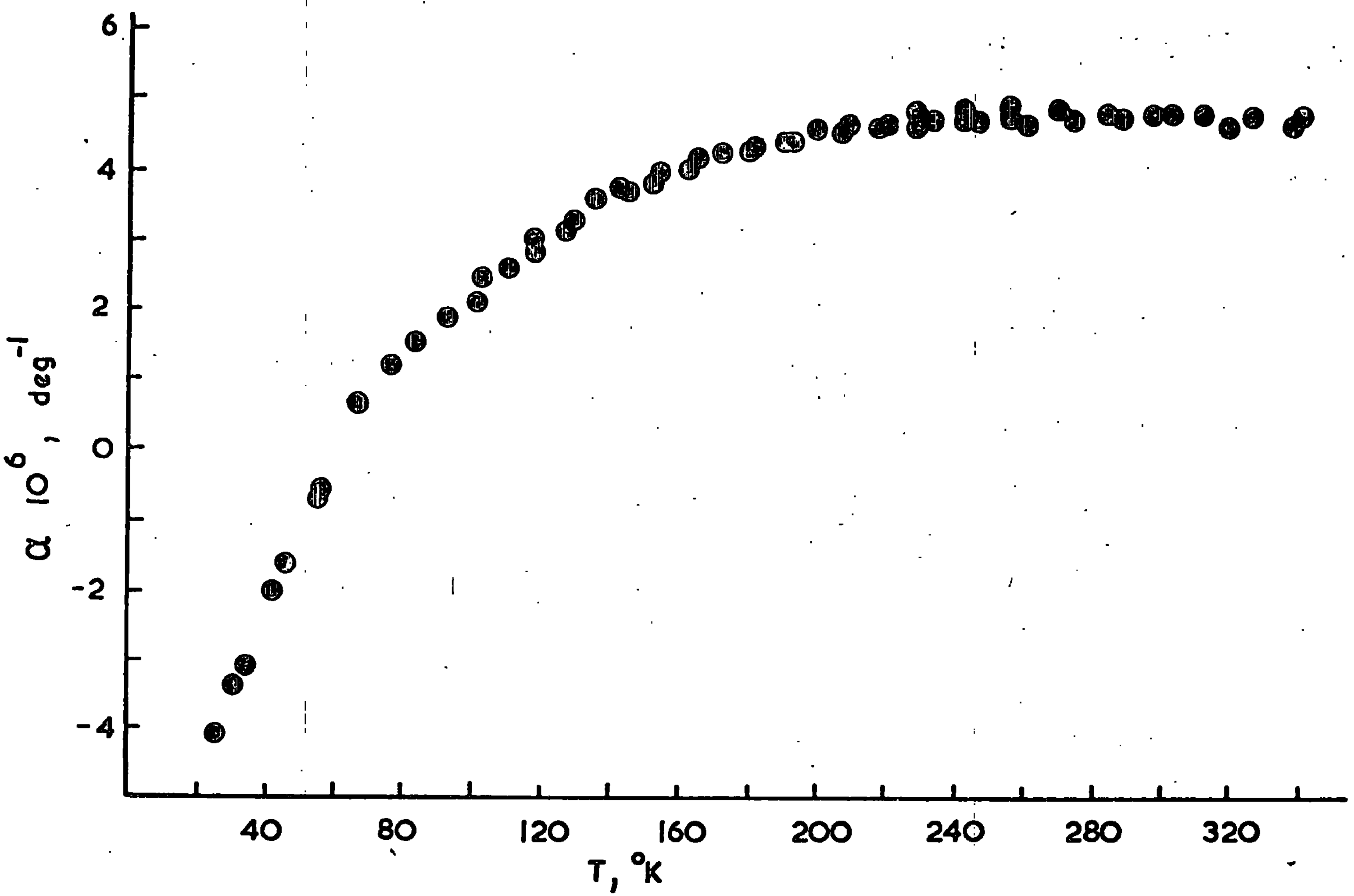

FIGURE (A.2). Experimental values of thermal expansion coefficient of mercury telluride (After Navikova and Abrikosov 1964).

$C_{12} = 3{\cdot}58$ and $C_{44} = 2{\cdot}05$.

Kelemen et al. (1965) have measured the specific heat of mercury telluride between 20°C to 240°C. They reported the room temperature value as 0·039 (cal. $g^{-1}\ {}^{o}K^{-1}$). However in this thesis the temperature dependence of specific heat of mercury telluride has been deduced from Debye's expression for various values of θ/T (Figure A.3). The table giving c_v as a function of θ/T has been taken from White (1959, p.316, Table XXVII).

The specific heat at constant volume c_v is related to the quantity which is usually measured, namely the specific heat at constant pressure c_p, by the thermodynamic equation

$$c_p - c_v = 9\,\alpha^2\, T\, B/\rho \tag{A.1}$$

Here α is the coefficient of linear thermal expansion, T is the absolute temperature, B is the bulk modulus and ρ is the density of material. At 290°K, c_v is 15×10^5 erg.$g^{-1}\ {}^{o}K^{-1}$ and c_p is $14{\cdot}97 \times 10^5$ erg. $g^{-1}\ {}^{o}K^{-1}$ for mercury telluride. Therefore, c_p can be accepted as being equal to c_v for temperatures lower than room temperature. At higher temperatures the difference $(c_p - c_v)$ increases.

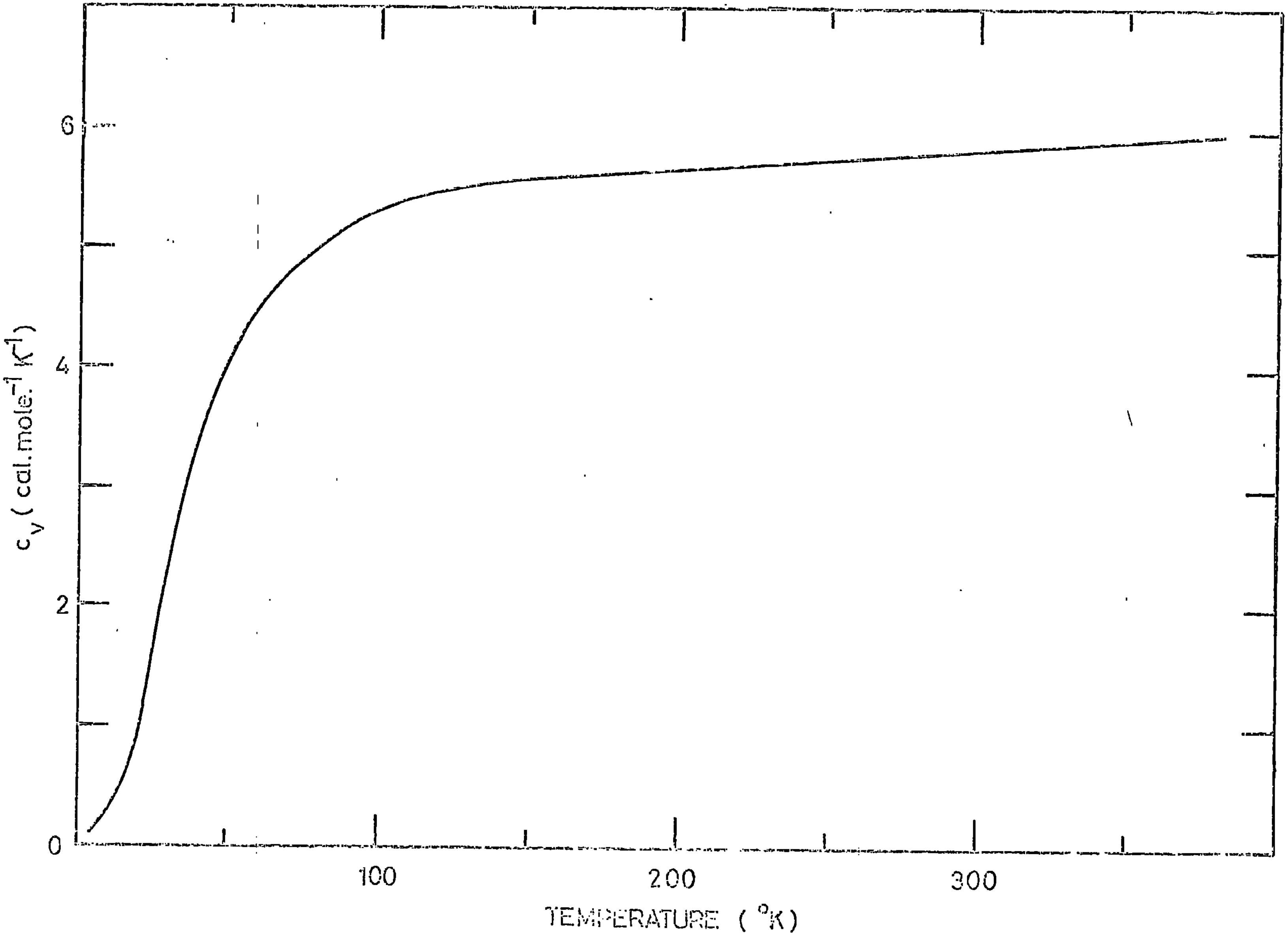

FIGURE (A.3). Temperature variation of the specific heat of HgTe computed from the Debye theory.

APPENDIX B

CONSTANTS IN MERCURY TELLURIDE RELATED TO DISLOCATION MOTION

The Burgers vector (b)

In zinc-blende crystals the shortest lattice vector that is allowed as the Burgers vector is $\frac{1}{2}\langle 110 \rangle$ or $\langle \frac{1}{2}\frac{1}{2}0 \rangle$ i.e. half the diagonal of a cube face (Holt 1962)

$$\therefore \quad b = \tfrac{1}{2}\sqrt{2}\, a_o$$

Inserting the value of a_o ($6{\cdot}462 \times 10^{-8}$ cm see page 12) Burgers vector for mercury telluride is found to be $4{\cdot}569 \times 10^{-8}$ cm.

The Shear modulus (G)

Since the motion of the dislocation lines produces a strain in addition to elastic strain, the apparent shear modulus (G) is lower than the true modulus (G_o). The shearing modulus in the glide plane is (Alers and Thompson 1961)

$$G = \frac{1}{3}\,(C_{11} - C_{12} + C_{44})$$

Inserting the values of elastic constants from Table (4.1, p.51), the shear modulus (G) for mercury telluride at 290°K is found to be $1{\cdot}25 \times 10^{11}$ dyn cm^{-2}.

Poisson's ratio (ν)

Poisson's ratio (ν) is defined as

$$= C_{12}/[2(C_{12} + G)]$$

(Bhatia 1967, p.338). Inserting the values of C_{12} ($3{\cdot}8 \times 10^{11}$ dyn.cm^{-2}, Table 4.1), p.51) and G($1{\cdot}25 \times 10^{11}$ dyn.cm^{-2}). Poisson's ratio (ν) for mercury telluride at 290°K is found to be 0·375.

The effective tension (C)

The force per unit length due to the effective tension in a bowed-out dislocation (C) is given by

$$C = 2\ G\ b^2/[\pi(1-\nu)]$$

(Granato and Lücke 1966, p.241)

C is $2{\cdot}66 \times 10^{-4}$ gm.cm.sec^{-2} for mercury telluride.

The effective mass of dislocation (A)

The effective mass per unit length of dislocation line is given

$$A = \rho\, b^2$$

(Granato and Lücke 1966, p.141)

Here ρ is the density ($8{\cdot}08$ gm.cm^{-3}). Therefore, A is $1{\cdot}69 \times 10^{-14}$ gm.cm^{-1} for mercury telluride.

REFERENCES

Akhieser, A., 1939, J.Phys. U.S.S.R., 1, 277.

Alers, G.A., 1965, Physical Acoustics, Vol.IIIB, Ed. W.P. Mason (New York: Academic Press), p.1.

Alers, G.A., and Thompson, D.O., 1961, J.Appl.Phys., 32, 283.

Anderson, O.L., 1963, J.Phys.Chem.Solids, 24, 909.

Anderson, O.L., 1965, Physical Acoustics, Vol.IIIB, Ed. W.P. Mason (New York: Academic Press), p.43.

Arlt, G., and Quadflieg, P., 1968, Phys.Stat.Sol., 25, 323.

Bacon, R., and Smith, C.S., 1956, Acta Met., 4, 337.

Berlincourt, D., Jaffe, H., and Shiozawa, L.R., 1963, Phys.Rev., 129, 1009.

Bhatia, A.B., 1967, Ultrasonic Absorption (Oxford: Clarendon Press).

Blair, J., and Newnham, R., 1961, (in Harman 1967, p.811).

Bobylev, B.A., and Kravchenko, A.F., 1967, Sov.Phys.-Acoustics, (English Trans.) 12, 315.

Bömmel, H.E., and Dransfeld, K., 1960, Phys.Rev., 117, 1245.

Bordoni, P.G., 1949, Ric.Sci., 19, 851.

Bordoni, P.G., 1954, J.Acoust.Soc.Am., 26, 495.

Bordoni, P.G., 1960, Nuova Cim.Suppl., 17, 43.

Bordoni, P.G., Nuovo, M., and Verdini, L., 1959, Nuova Cum., 14, 273.

Born, M., and Huang, K., 1954, Dynamic Theory of Crystal Lattices (Oxford: Clarendon Press).

Brebrick, R.F., and Strauss, A.J., 1965, J.Phys.Chem.Solids, 26, 989.

Carlson, R.O., 1958, Phys.Rev., 111, 476.

Chung, D.H. and Buessem, W.R., 1967, J.Appl.Phys., 38, 2010.

Coulson, C.A., Redei, L.B., and Stocker, D., 1962, Proc.R.Soc., A270, 357.

Delves, R.T., 1965, Brit.J.Appl.Phys., 16, 343.

Delves, R.T., and Lewis, B., 1963, J.Phys.Chem.Solids, 24, 549.

Dickey, D.H., and Mavroides, J.G., 1964, Solid State Commun., 2, 213.

Dobbs, E.R., Chick, B.B., and Truell, R., 1959, Phys.Rev.Letters, 3, 332.

Drabble, J.R., 1966, Semiconductors and Semimetals, Vol.2, Ed. R.K. Willardson and A.C. Beer (New York: Academic Press), p.75.

Dziuba, Z., and Zakrzewski, T., 1964, Phys.Stat.Sol., 7, 1019.

Figgins, B.F., Shepherd, T.A., and Snowman, J.W., 1964, J.Sci. Instrum. (Brit.), 41, 520.

Giriat, W., 1964, Brit.J.Appl.Phys., 15, 151.

Granato, A., and Lücke, K., 1956, J.Appl.Phys., 27, 583.

Granato, A., and Lücke, K., 1966, Physical Acoustics, Vol.IVA, Ed. W.P. Mason (New York: Academic Press), p.225.

Granato, A., and Truell, R., 1956, J.Appl.Phys., 27, 1219.

Hansen, M., 1958, Constitution of Binary Alloys (New York: McGraw-Hill).

Hanson, R.C., 1967, J.Phys.Chem.Solids, 28, 475.

Harman, T.C., 1967, II-VI Compounds, Ed. M.Aven and J.S. Prener (Amsterdam: North-Holland), p.767.

Harman, T.C., Logan, M.J., and Goering, H.L., 1958, J.Phys.Chem. Solids, 7, 228.

Herman, F., 1959, J.Phys.Chem.Solids, 8, 405.

Hill, R.W., 1952, Proc.Phys.Soc., A65, 349.

Hiscocks, S.E.R., and Hurle, D.T.J., 1968, Conf.Semimetals and Narrow Gap Semiconductors, Durham (unpublished).

Holt, D.B., 1962, J.Phys.Chem.Solids, 23, 1353.

Hutson, A.R., and White, D.L., 1962, J.Appl.Phys., 33, 40.

Ikushima, A., and Suzuki, T., 1961, J.Phys.Soc.Japan, 16, 2587.

Ikushima, A., and Suzuki, T., 1963, Proc. Intern. Conf. Crystal Lattice Defects; J.Phys.Soc.Japan, 18, suppl. 1, 163.

Kelemen, F., Cruceanu, E., and Niculescu, D., 1965, Phys.Stat.Sol., 11, 865.

Keyes, R.W., 1961, IBM Jl Res.Dev., 5, 266.

Keyes, R.W., 1962, J.Appl.Phys., 33, 3371.

Koehler, J.S., 1952, Imperfections in Nearly Perfect Crystals, Ed. W. Shockley, J.H. Hollomon, R.Maurer, and F.Seitz (New York: Wiley), p.197.

Kromer, P.F., and Khiznichenko, L.P., 1967, Phys.Stat.Sol., 21, 811.

Kyame, J.J., 1949, J.Acoust.Soc.Am., 21, 159.

Kyame, J.J., 1954, J.Acoust.Soc.Am., 26, 990.

Leibfried, G., 1950, Z.Physik, 127, 344.

Lewis, M.F., and Patterson, E., 1967, Phys.Rev., 159, 703.

Lord, A.E., and Truell, R., 1966, J.Appl.Phys., 37, 4631.

Lücke, K., 1956, J.Appl.Phys., 27, 1433.

Marcus, P.M., and Kennedy, A.J., 1959, Phys.Rev., 114, 459.

Mason, W.P., 1955, J.Acoust.Soc.Am., 27, 643.

Mason, W.P., 1965, Physical Acoustics, Vol.IIIB, Ed. W.P. Mason (New York: Academic Press), p.235.

Mason, W.P., and Bateman, T.B., 1964, J.Acoust.Soc.Am., 36, 644.

Mason, W.P., and Rosenberg, A., 1966, Phys.Rev., 151, 434.

Mason, W.P., and Rosenberg, A., 1967, J.Appl.Phys., 38, 1929.

Mavroides, J.G., and Kolesar, D.F., 1964, Solid State Commun., 2, 363.

McSkimin, H.J., 1953, J.Appl.Phys., 24, 988.

McSkimin, H.J., 1964, Physical Acoustics, Vol.1A, Ed. W.P. Mason (New York: Academic Press), p.271.

McSkimin, H.J., and Bond, W.L., 1957, Phys.Rev., 105, 116.

McSkimin, H.J., and Thomas, D.G., 1962, J.Appl.Phys., 33, 56.

Merkulov, L.G., and Yakovlev, L.A., 1960, Soviet Phys.-Acoust. (English Trans.), 6, 239.

Miller, B.I., 1963, Phys.Rev., 132, 2477.

Morse, R.W., 1959, Progress in Cryogenics, Vol.1, K. Mendelssohn (London: Heywood), p.220.

Nagendra Nath, N.S., 1934, Proc. Indian Acad.Sci., 1, 333.

Nava, R., Azrt, R., Ciccarello, I., and Dransfeld, K., 1964, Phys.Rev., 134, A581.

Nelson, J.B., and Riley, D.P., 1945, Proc.Phys.Soc., 57, 160.

Niblett, D.H., 1961, J.Appl.Phys., 32, 895.

Niblett, D.H., 1966, Physical Acoustics, Vol.IIIA, Ed. W.P. Mason (New York: Academic Press), p.77.

Niblett, D.H., and Willks, J., 1956, Conf.Phys.Basses Temp., Paris, 1955, p.484., Institut International du Froid, Paris.

Novikova, S.I., and Abrikosov, N.Kh., 1964, Soviet Phys.-Solid State, (English Trans.) 5, 1558.

Oliver, D.W., Slack, G.A., 1966, J.Appl.Phys., 37, 1542.

Pomerantz, M., 1965, Phys.Rev., 139, A501.

Potter, R.F., 1957, J.Phys.Chem.Solids, 3, 223.

Read, T.A., 1941, Trans. AIME, 143, 30.

Rodot, H., and Triboulet, R., 1962, C.R. Acad.Sci.Paris, 254, 852.

Rose-Innes, A.C., and Broom, R.F., 1956, J.Sci.Instrum., 33, 31.

Rosenberg, H.M., 1963, Low Temperature Solid State Physics (Oxford: Clarendon Press).

Seeger, A., 1956, Phil.Mag., 1, 651.

Seeger, A., Donth, H., and Pfaff, F., 1957, Discussions Faraday Soc., 23, 19.

Smith, H.M.J., 1948, Trans. Roy. Soc., A241, 105.

Steigmeier, E.F., 1963, Appl.Phys. Letters, 3, 6.

Stern, R.M., and Granato, A.V., 1962, Acta Met., 10, 358.

Strauss, A.J., and Brebrick, R.F., 1965, (in Harman 1967, p.773).

Suzuki, H., 1963, Proc. Intern. Conf. Crystal Lattice Defects; J.Phys.Soc. Japan, 18, Suppl. 1, 182.

Szigeti, B., 1949, Trans.Faraday Soc., 45, 155.

Szigeti, B., 1950, Proc.R.Soc., A204, 51.

Taylor, A., 1962, Acta Met., 10, 490.

Thompson, D.O., and Holmes, D.K., 1956, J.Appl.Phys., 27, 713.

Truell, R., and Elbaum, C., 1962, *Encyclopedia of Physics (Acoustics II), Vol. XI/2*, Ed. S. Flügge (Berlin: Springer-Verlag), p.153.

Verma, G.S., and Joshi, S.K., 1961, Phys.Rev., 121, 396.

Voigt, W., 1910, (in Hutson and White 1962).

Wagini, H., and Reiss, B., 1966, Phys. Stat.Sol., 15, 457.

Warekois, E.P., Lavine, M.C., Mariano, A.N., and Gatos, H.C., 1962, J. Appl.Phys., 33, 690.

Waterman, P.C., 1959, Phys. Rev., 113, 1240.

Weertman, J., 1956, Phys.Rev., 101, 1429.

White, G.K., 1959, *Experimental Techniques in Low-temperature Physics* (Oxford: Clarendon Press).

Wolff, G.A., and Broder, J.D., 1959, Acta Cryst., 12, 313.

Woodruff, T.O., and Ehrenreich, H., 1961, Phys.Rev., 123, 1553.

Woolley, J.C., and Ray, B., 1960, J.Phys.Chem.Solids, 13, 151.

Zarembovitch, A., 1963, J.Phys. (France), 24, 1097.

Zener, C., 1948, *Elasticity and Anelasticity of Metals* (Chicago: University of Chicago Press).

J. Phys. Chem. Solids Pergamon Press 1967. Vol. 28, pp. 1637–1642. Printed in Great Britain.

THE ELASTIC CONSTANTS OF MERCURY TELLURIDE

T. ALPER and G. A. SAUNDERS

Department of Applied Physics, the University of Durham, England

(*Received* 20 *March* 1967; *in revised form* 21 *April* 1967)

Abstract—The elastic constants C_{11}, C_{12} and C_{44} of mercury telluride have been measured by the pulse echo technique as a function of temperature between 1·4°K and 300°K, attention being paid to possible effects of non-stoichiometry in the crystals. Results are discussed in terms of the crystalline interatomic forces and are compared with those of other II–VI and III–V compounds with the zinc blende structure: the elastic properties of mercury telluride correspond closely to those of cubic zinc sulphide and exhibit no anomalous behaviour. From the Szigeti relationships, the ionicity e^* is estimated as $0{\cdot}65e \pm 0{\cdot}05e$ and the restrahlen frequency as $(4{\cdot}1 \pm 0{\cdot}1) \times 10^{12}$ cycles/sec. The Debye temperature, calculated from the elastic constant data, is 141°K ± 4°K.

INTRODUCTION

THE ELASTIC constants of single crystals furnish basic mechanical and thermodynamic information in solids. During a study of ultrasonic wave propagation and the electronic properties of semimetals, the adiabatic elastic constants C_{11}, C_{12} and C_{44} of mercury telluride HgTe have been obtained using the ultrasonic pulse echo technique. Preparation of stoichiometric HgTe presents a problem and serious discrepancies exist between published data, especially on electron transport properties: carrier densities and mobilities are particularly sensitive to excess of either component in such a semimetal with a very small band overlap. Stoichiometry is also relevant to ultrasound wave propagation and crystals prepared in different ways have been examined for any effects of non-stoichiometry and possible relationships to mechanical properties.

In II–VI and III–V compounds the ionicity, the proportion of ionic component in mixed covalent–ionic bonds, plays an important role: in materials with mixed bonds the resonance energy influences both bond strengths and band structure. One aim of the present work was to estimate the ionicity in HgTe through the elastic constants and to correlate the results with those for other binary compounds with the zinc blende ($\bar{4}3m$) structure. Two equal, interpenetrating, face-centred cubic lattices, each containing one atomic species only, and relatively displaced one quarter of the distance along a cube diagonal, compose this structure. The unit cell contains two atoms, one on each lattice, spaced by $a_0\sqrt{(3)}/4$, a_0 being the lattice constant. That optical frequency associated with $k = 0$ represents the frequency at which the rigid Bravais lattices vibrate relatively to each other. Interatomic repulsive forces largely determine the optical absorption frequency and the compressibility, which are then related by the Szigeti relation,(1) based on a dipolar term in the Lorentz force approximation. This equation forms a useful link between elastic and optical properties and is applied to the present results on HgTe, although its extension to the zinc blende lattice, in which each atom is not a centre of symmetry, is not strictly justifiable. If nearest–neighbour interactions are sufficient to represent the lattice dynamics, then the two force constant model(2) should be satisfied: thus the applicability of Born's relation is tested in HgTe and found to be a reasonable approximation. Assuming that the behaviour of thermal vibrations approaches that of acoustical waves with increasing wavelength, the Debye temperature has been calculated from the elastic constant data presented in the next section.

2. EXPERIMENTAL DETAILS AND RESULTS

Mercury telluride single crystals, as cylinders of diameter up to 2·5 cm and length about 2 cm, were grown from 99·999 per cent purity elements, by a technique, developed by DELVES(3) of directional freezing of melts of composition $Hg_{1{\cdot}00}$

annealing are small ($\sim 1{\cdot}5$ per cent at 4·2°K and $\sim 2{\cdot}0$ per cent at 300°K) and of similar magnitude for each constant, although ΔC_{44} is negative in contrast to ΔC_{11} and ΔC_{12}. Crystal preparation and history modify the elastic constants of HgTe: this would explain the discrepancy between the present results and those of MAVROIDES and KOLESAR(8) at room temperature only; these workers give no details of crystal preparation so that further comparisons cannot be made. The elastic constants show characteristic dependence on temperature, namely, an approach to 0°K with zero slope and a negative, almost linear, slope at higher temperatures: these features follow from the theory of the crystalline equation of state (see HUNTINGTON(9) for references and a review of this topic). Now to discuss the results in more detail.

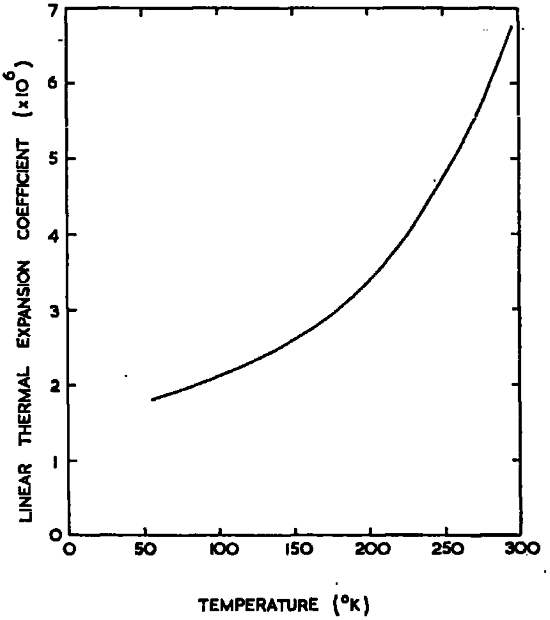

FIG. 1. The linear thermal expansion coefficient α of mercury telluride as a function of temperature. Errors are ±10 per cent at 77°K and ±4 per cent at 290°K.

DISCUSSION

Single crystal elastic constants can be expressed as the second derivative of the binding energy with respect to the appropriate strain. Contributing energy terms accrue from long range electrostatic forces between the ion cores and the valence electrons, from short range, ion core, repulsive interactions and from electronic effects. Satisfactory comparison with electron theories is not possible at present for HgTe because the pertinent band parameters and their strain dependences are unknown. The small changes in the elastic constants, produced by annealing in mercury vapour,

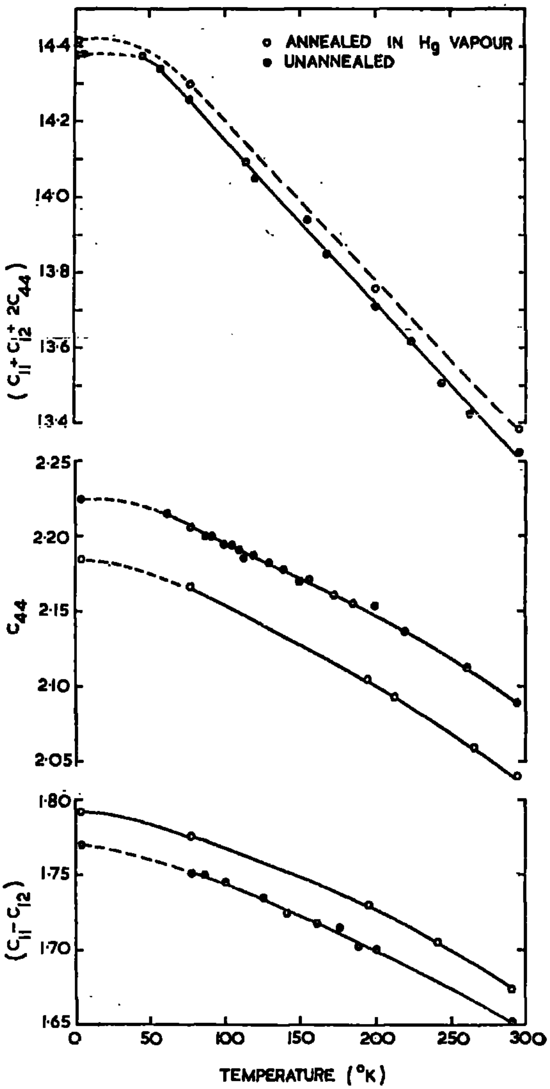

FIG. 2. The temperature dependence of the measured linear combinations of the elastic constants of a crystal oriented along the [110] direction both as grown and after annealing at 300° for 100 hr in mercury vapour. The units are 10^{11} dyn/cm^2.

$\overline{m}\omega_r^2$ turns out to be $8{\cdot}8\times10^4$ cgs units and ν_R is $(4{\cdot}1\pm0{\cdot}1)\times10^{12}$ c/s. As HgTe by no means obeys the Cauchy relation $C_{12} = C_{44}$ and the central force model is invalid, disagreement between this result and that measured from optical reflectivity$^{(14)}$ ($3{\cdot}45\times10^{12}$ c/s) is not surprising.

Giving considerable insight into the properties of solids are such chemical concepts as ionicity, cognate with the nature of the bonding. SZIGETI$^{(15)}$ has shown for a lattice of deformable ions that the effective charge e^* is related to the change in dielectric constants $\Delta\epsilon$ on passing right through the restrahlen band by

$$\Delta\epsilon = \frac{16\pi(\epsilon_\infty+2)^2(e^*)^2}{9\overline{m}\omega_r^2a_0^3} \tag{3}$$

Introduction of the elastic constant data into equations (2) and (3) gives the ionicity of HgTe as $0{\cdot}65\,e$. This value must be treated cautiously: included in Szigeti's work is a distortion parameter s (unity in the Lorentz approximation). The method really gives se^*. Should the charge distribution around the ions not be spherical, or the ions overlap, or non-electrostatic short-range forces distort the ions on displacement, then s is not unity. However, for a variety of cubic materials s seems to be $0{\cdot}9\pm0{\cdot}2$.$^{(15)}$ Thus, recognizing both these effects of distortion and experimental error, e^* is $(0{\cdot}65\pm0{\cdot}05)e$.

In the heteropolar, tetrahedrally bonded compounds the molecular wave-functions ψ are formed by overlap of sp^3 tetrahedral, hybrid orbitals ϕ on nearest neighbour atoms$^{(16)}$

$$\begin{aligned} \psi &= \phi_a+\lambda\phi_b \qquad \text{(Bonding orbital)} \\ \chi &= \lambda\phi_a-\phi_b \qquad \text{(Antibonding orbital)} \end{aligned} \tag{4}$$

where λ is a parameter, describing the polarity of the bond, obtainable by the variation method. The bonding orbital ψ corresponds to fractions of electrons $1/(1+\lambda^2)$ on the hexavalent atom (A) and $\lambda^2/(1+\lambda^2)$ on the bivalent atom (B). The net charge, measured in electrons, associated with the atom A is$^{(16)}$ for a compound A^NB^{8-N}

$$e^* = \frac{N\lambda^2-(8-N)}{1+\lambda^2} \tag{5}$$

or $(6\lambda^2-2)/(1+\lambda^2)$ for a II–VI compound where N is 6. When $e^* = 0{\cdot}65e$, λ becomes $0{\cdot}7$: any valence electron remains on a mercury atom about 30 per cent of the time.

Using Szigeti's work$^{(1,15)}$ as a foundation, POTTER$^{(17)}$ has demonstrated a close correspondence between the elastic constant ratio C_{11}/C_{12} and the ionicity in a number of compounds of the $\bar{4}3m$ structure. As the compounds become more ionic, the ratio C_{11}/C_{12} decreases from 2 for the purely covalent Si and Ge towards the lower limit of unity set by the critical conditions$^{(18)}$ for lattice stability

$$C_{11}-C_{12} > 0, \quad C_{44} > 0, \quad C_{11}+2C_{12} > 0 \tag{6}$$

The results ($C_{11}/C_{12} = 1{\cdot}41$, $e^* = 0{\cdot}65e$) for HgTe, similar to those for cubic ZnS($C_{11}/C_{12} = 1{\cdot}49$, $e^* = 0{\cdot}65e$), lie on Potter's theoretical curve (Fig. 1 in his paper): the general trends towards ionic character through the series of III–V and II–VI are followed by HgTe.

By reducing the elastic constants to dimensionless parameters,$^{(19)}$ comparison between the compounds can be extended; the normalizing elastic constant C_0

$$C_0 = \frac{e^2}{R^4} = \frac{256}{9}\cdot\frac{e^2}{a_0^4} \tag{7}$$

is $0{\cdot}376\times10^{12}$ dyn/cm^2 for HgTe. The reduced bulk and shear moduli are

$$\begin{aligned} B^* &= (C_{11}+2C_{12})/3C_0 = 1{\cdot}23\pm0{\cdot}03 \\ C_{44}{}^* &= C_{44}/C_0 = 0{\cdot}60\pm0{\cdot}01 \\ C_s{}^* &= (C_{11}-C_{12})/C_0 = 0{\cdot}24\pm0{\cdot}01 \end{aligned} \tag{8}$$

and the reduced average shear modulus

$$C^* = \frac{C}{C_0} = \frac{C_{11}-C_{12}+3C_{44}}{5C_0} = 0{\cdot}45\pm0{\cdot}02$$

These reduced moduli have a close affinity with those for cubic ZnS($B^* = 1{\cdot}11$, $C_{44}{}^* = 0{\cdot}56$, $C_s{}^* = 0{\cdot}24$, $C^* = 0{\cdot}43$). Keyes generalizations, concerning the elastic moduli of the $\bar{4}3m$ compounds and diamond structure elements, namely that $B^* \sim 1{\cdot}2$ and that the shear moduli decrease through the sequence group IV elements, III–V compounds and II–VI compounds, find further confirmation in HgTe, which shows no anomalous elastic behaviour.

BORN,$^{(2)}$ considering nearest neighbour interactions only, has developed a two constant model for

BRIT. J. APPL. PHYS. (J. PHYS. D), 1968, SER. 2, VOL. 1. PRINTED IN GREAT BRITAIN

The elastic constants of $Hg_5In_2Te_8$

T. ALPER, N. G. PACE and G. A. SAUNDERS

Department of Applied Physics, University of Durham

MS. received 6*th February* 1968, *in revised form* 19*th March* 1968

Abstract. The elastic constants C_{11}, C_{12} and C_{44} of the ternary compound semiconductor $Hg_5In_2Te_8$ are presented. The ionicity of this compound is estimated as 0·47 ± 0·05. The Debye temperature is 142 ± 6°K. The elastic properties are found to bear a marked resemblance to those of the related II–VI compounds, in particular HgTe.

1. Introduction

Details of the propagation of ultrasonic waves in ternary compound semiconductors are sparse. The phase diagram of the pseudo-binary system comprising mercury telluride and indium telluride indicates that a compound is extant at the composition 37·5 mol.% indium telluride (Spencer 1964). Valency requirements suggest that the compound is $Hg_5In_2\square Te_8$, where the symbol □ designates a vacancy. The present concern is to complement recent studies of the electrical properties (Spencer *et al.* 1962, Wright 1965, Wright and Dahake 1968) with knowledge of the elastic constants and of the nature of the crystal binding in this compound.

2. Experimental details and results

Single crystals of $Hg_5In_2Te_8$ have been grown by the Bridgman technique from elements of 99·999% purity. Back-reflection photographs show, within an experimental error of ±0·5°, that the compound is cubic with a point group belonging to either 432, $\bar{4}3m$ or m3m. Debye–Scherrer powder photographs reveal the marked resemblance of this ordered compound to mercury telluride. The measured lattice spacing of 6·33 ± 0·01 Å agrees with that found by Spencer *et al.* (1962). Each tellurium atom may have as nearest neighbours either four mercury atoms or two mercury atoms, an indium atom and a vacancy. The zinc blende structure is often depicted as a cube containing eight atoms. Eight such cubes form a large cube with 2^3 as many sites, accommodating $Hg_{20}In_8\square_4Te_{32}$, which exhibits the observed symmetries and gives a calculated x-ray density (7·30 ± 0·01 g cm^{-3}) in reasonable agreement with that measured by Archimedes' principle (7·23 ± 0·01 g cm^{-3}).

The elastic constants C_{11}, C_{12} and C_{44} were obtained from the velocities of longitudinal and transverse waves propagated along the [110] axis with wave polarization parallel to the [110], [001] and [$1\bar{1}0$] directions respectively. Ultrasonic-wave transit times were measured with an accuracy to better than 1% by the single-ended pulse-echo technique at a carrier frequency of 10 MHz. Further experimental details are given by Alper and Saunders (1967). Using back-reflection Laue photographs the crystals were aligned to within 1° of the pre-requisite axis and cut on a diamond wheel. The faces were lapped flat and parallel to within 10^{-4} in. The use of 10^6 cs silicone fluid as a transducer bonding material restricted the propagation and measurement of transverse waves to temperatures below 160°K. The elastic moduli, uncorrected for thermal expansion, are presented in the figure. The elastic moduli and compressibility data at selected temperatures are shown in table 1.

Direct comparison of the elastic moduli is best achieved by reduction to the dimensionless parameters (Keyes 1962) shown in table 2. A close similarity between the elastic constants of $Hg_5In_2Te_8$ and those of the II–VI compounds HgTe and ZnS is apparent. Keating (1966) found that for covalent diamond-structure materials $2C_{44}(C_{11}+C_{12})/(C_{11}-C_{12})(C_{11}+3C_{12})$ is unity. With increasing ionicity this parameter deviates from unity due to the increased importance of long-range Coulomb forces, being between 1·1 and 1·2 for III–V compounds, 1·38 for HgTe and 1·37 for $Hg_5In_2Te_8$. The two Hooke's-law constants α and β, resulting respectively from radial and angular forces, have been estimated from Keating's model, which predicts that

$$C_{11}=(\alpha+3\beta)/4a, \qquad C_{12}=(\alpha-\beta)/4a, \qquad C_{44}=\alpha\beta/a(\alpha-\beta).$$

For the ternary compound, α and β are $9{\cdot}5\times10^4$ and $1{\cdot}1\times10^4$ dyn cm^{-1} respectively, values close to those obtained for HgTe ($\alpha=1{\cdot}1\times10^5$ dyn cm^{-1}, $\beta=1{\cdot}1\times10^4$ dyn cm^{-1}).

Table 2. Reduced adiabatic elastic moduli of zinc blende type crystals†

	$Hg_5In_2Te_8$	HgTe	ZnS (cubic)
$(C_{11}+2C_{12})/3C_0$	$0{\cdot}95\pm0{\cdot}06$	$1{\cdot}23\pm0{\cdot}03$	1·11
C_{44}/C_0	$0{\cdot}51\pm0{\cdot}02$	$0{\cdot}60\pm0{\cdot}01$	0·56
$(C_{11}-C_{12})/2C_0$	$0{\cdot}21\pm0{\cdot}02$	$0{\cdot}24\pm0{\cdot}01$	0·24
$(C_{11}-C_{12}+3C_{44})/5C_0$	$0{\cdot}68\pm0{\cdot}04$	$0{\cdot}45\pm0{\cdot}02$	0·43

† The normalizing constant C_0 $(=256e^2/9a_0^4)=4{\cdot}08\times10^{11}$ dyn cm^{-2} for $Hg_5In_2Te_8$. Data taken at 77°K are used for computation.

Finally, the Debye temperature of 142 ± 6°K, estimated by the methods outlined by Alers (1965) from the elastic constant data extrapolated to 0°K, is in accord with that for HgTe, namely 141 ± 4°K (Alper and Saunders 1967).

Acknowledgments

The authors would like to thank Professor D. A. Wright, Department of Applied Physics, University of Durham, for many useful discussions.

References

ALERS, G. A., 1965, *Physical Acoustics*, Vol. III B (New York: Academic Press), pp. 1–42.

ALPER, T., and SAUNDERS, G. A., 1967, *J. Phys. Chem. Solids*, **28**, 1637–42.

KEATING, P. N., 1966, *Phys. Rev.*, **145**, 637–45.

KEYES, R. W., 1962, *J. Appl. Phys.* **33**, 3371–2.

POTTER, R. F., 1957, *J. Phys. Chem. Solids*, **3**, 223–8.

SPENCER, P. M., 1964, *Brit. J. Appl. Phys.*, **15**, 625–32.

SPENCER, P. M., PAMPLIN, B. R., and WRIGHT, D. A., 1962, *Proc. Int. Conf. on Physics of Semiconductors, Exeter*, 1962 (London: Institute of Physics and Physical Society), pp. 244–51.

WRIGHT, D. A., 1965, *Brit. J. Appl. Phys.*, **16**, 939–42.

WRIGHT, D. A., and DAHAKE, S. L., 1968, *Brit. J. Appl. Phys.* (*J. Phys.* D), ser. 2, **1**, 831–6.

(*Reprinted from Nature, Vol.* 218, *No.* 5136, *p.* 83 *only,*
April 6, 1968)

Phonon Viscosity Attenuation of Ultrasonic Waves in HgTe

ATTENUATION of ultrasonic waves arising from lattice phonon viscous drag is known in insulators such as quartz[1] and in semiconductors, notably germanium[2] and silicon[3]. Here we report that this damping effect is large in the semi-metal HgTe. When the thermal phonon mean free path is small compared with the sound wavelength ($\omega\tau_{th} \ll 1$), as in the present experiment, the lattice phonon damping for an isotropic solid is given by[4]

$$\alpha_L = 8{\cdot}68\bar{\gamma}^2\omega^2 KT/\rho\bar{v}^5 \text{ dB/cm} \qquad (1)$$

where $\bar{\gamma}$ is an average Gruneisen parameter and K the lattice thermal conductivity. For HgTe ($\Theta = 141°$ K)

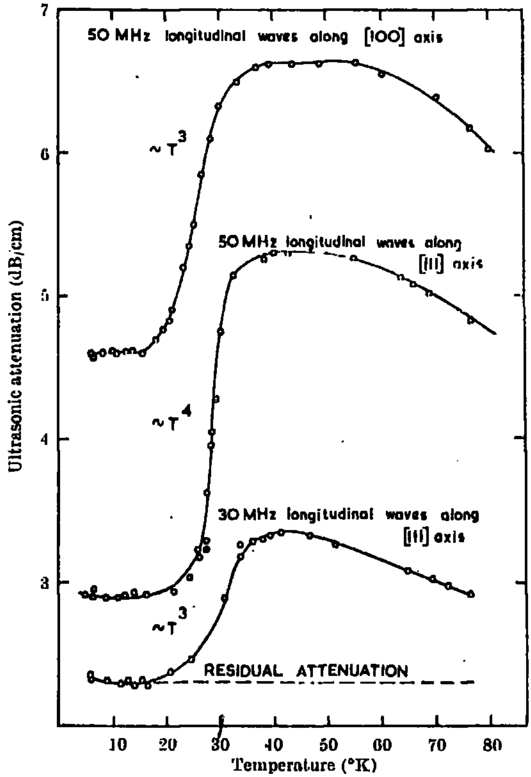

Fig. 1. The temperature dependence of ultrasonic attenuation in HgTe. The residual attenuation level is shown only for the lowest curve.

Table 1. ACOUSTICAL GRUNEISEN PARAMETERS ESTIMATED FROM THE ULTRASONIC ATTENUATION OF LONGITUDINAL WAVES PROPAGATED IN HgTe SINGLE CRYSTALS

Direction of propagation	Velocity of sound at 4·2° K (cm/s)	Frequency (MHz)	Intrinsic ultrasonic attenuation $(\alpha-\alpha_0)$dB/cm	Acoustical Gruneisen parameter $\bar{\gamma}$
[111]	$3{\cdot}073 \times 10^5$	50	2·44	1·19
		30	1·02	1·28
[100]	$2{\cdot}961 \times 10^5$	50	2·04	1·07
[110]	$2{\cdot}982 \times 10^5$	70	2·48	0·86
		50	1·16	0·81

frequency dependence of attenuation (Fig. 2) approaches ω^2 above 100 MHz but deviates at low frequencies, largely because of diffraction losses. The attenuation above 200 MHz is constant;[1] a similar effect in germanium has been attributed to dislocation damping[2].

A complete quantitative assessment awaits measurements of the third order elastic constants and thermal conductivity. But it is of interest to estimate the acoustic Gruneisen parameters $\bar{\gamma}$ (Table 1) using equation (1). For comparison, the thermal expansion Gruneisen parameter is estimated as 0·65 ± 0·10.

T. Alper
G. A. Saunders

Department of Applied Physics,
University of Durham.

Received February 22, 1968.

[1] Bömmel, H. E., and Dransfeld, K., *Phys. Rev.*, **117**, 1245 (1960).

[2] Dobbs, E. R., Chick, B. B., and Truell, R., *Phys. Rev. Lett.*, **3**, 332 (1959).

[3] Mason, W. P., *Physical Acoustics*, III B (1965), (edit. by Mason, W. P.), 235–86 (Academic Press, 1965).

[4] Woodruff, T. O., and Ehrenreich, H., *Phys. Rev.*, **123**, 1553 (1961).

[5] Alper, T., and Saunders, G. A., *J. Phys. Chem. Solids*, **28**, 1637 (1967).

Printed in Great Britain by Fisher, Knight & Co., Ltd., St. Albans.